Thermoplasmonic stimulation of gold nanorods for engineered living materials

Dissertation zur Erlangung des Grades
des Doktors der Naturwissenschaften
der Naturwissenschaftlich- Technischen Fakultät
der Universität des Saarlandes

von

M. Sc. Selim Basaran

Saarbrücken
2025

Tag des Kolloquiums: 19.08.2025

Dekan: Prof. Dr.-Ing. Dirk Bähre

1. Berichterstatter: Prof. Dr. Tobias Kraus

2. Berichterstatter: Prof. Dr.-Ing. Markus Gallei

Akad. Mitglied: Dr.-Ing. Andreas Tschöpe

Vorsitz: Prof. Dr. Dominik Munz

Abstract

Engineered Living Materials (ELMs) with living cells in polymer gels enable the synthesis and controlled release of therapeutic molecules. This thesis explores the optical triggering of ELMs using thermoplasmonic gold nanorods (AuNRs) embedded in Pluronic or polyvinyl alcohol hydrogels. Upon near-infrared (NIR) irradiation (808 nm), AuNRs generate localized heat, activating thermoresponsive bacteria.

Structured bilayer constructs with an AuNR-containing bottom layer and a bacteria-loaded top layer were developed. NIR light heated the lower layer, and the diffused heat induced mCherry expression in engineered *E. coli*. Temperature distribution and fluorescence analysis demonstrated controlled bacterial activation and the possibility to control protein production via light intensity. The system was then adapted to produce QK peptide, a VEGF-mimicking angiogenic factor, in a single-layer hydrogel, with secretion monitored via Nanoluciferase.

The approach was extended to NIR-sensitized nanocomposite PluDA hydrogels, incorporated in 3D-printed waveguides by a partner. Single- and double-segmented fibers enabled localized heating along the waveguide, with core-shell structures demonstrating confined plasmonic heating. This facilitates NIR-triggered bacterial activation in deep tissue environments, offering a pathway for advanced therapeutic ELMs.

Zusammenfassung

Engineered Living Materials (ELMs) mit lebenden Zellen in Polymergelen ermöglichen die kontrollierte Synthese und Freisetzung therapeutischer Moleküle. Diese Dissertation untersucht die optische Aktivierung von ELMs durch thermoplasmonische Goldnanostäbchen (AuNRs) in Pluronic- oder Polyvinylalkohol-Hydrogelen. Unter der Bestrahlung mit Nahinfrarotlicht (NIR, 808 nm) erzeugen AuNRs lokalisierte Wärme, die thermoresponsive Bakterien aktiviert.

Doppelschicht-Konstrukte mit einer AuNR-haltigen Bodenschicht und einer bakterienbeladenen Deckschicht wurden entwickelt. NIR-Licht erwärmte die untere Schicht, diffundierende Wärme induzierte mCherry-Expression in *E. coli*. Temperatur- und Fluoreszenzanalysen zeigten eine gezielte bakterielle Aktivierung und eine photothermisch steuerbare Proteinproduktion. Das System wurde zur Produktion des angiogenen QK-Peptids in einem einschichtigen Hydrogel adaptiert, und die Sekretion über Nanoluciferase verfolgt.

Der Ansatz wurde auf NIR-sensibilisierte nanokomposite PluDA-Hydrogele erweitert, die von einem Partner in 3D-gedruckte Wellenleiter integriert wurden. Segmentierte Fasern ermöglichten lokalisierte Erwärmung und zeigten gezielte plasmonische Erwärmung. Dies erlaubt eine NIR-gesteuerte bakterielle Aktivierung in tiefen Gewebeschichten und bietet einen neuen Ansatz für therapeutische ELMs.

Acknowledgment

I would like to express my gratitude to Prof. Dr. Tobias Kraus for his support throughout my doctoral research. His expertise in scientific writing and critical thinking has greatly improved my work, and I deeply appreciate his encouragement in refining my scientific language. He also provided me with the opportunity to participate in numerous international conferences, which were key experiences not only for my academic and professional growth but also on a personal level. I am particularly grateful for his open-minded and modern approach to research, as well as the pleasant working environment he fostered. I sincerely appreciate the opportunity to work on such an interdisciplinary and intellectually stimulating project in his group.

I would also like to thank Prof. Dr. Gallei, my second reviewer, for taking the time to evaluate my work and for his willingness to support my thesis.

A special thanks goes to Dr. Shrikrishnan Sankaran, head of Bioprogrammable Materials, for sharing his deep expertise in living materials. His insightful advice on bioengineering, synthetic biology, and laboratory techniques significantly contributed to my research. I greatly appreciated his constructive feedback and the time he dedicated to discussing ideas, which enhanced my understanding of bioengineering concepts and their integration into my project.

My work would not have been as interdisciplinary and diverse without the collaboration with research partners from different groups within the institute. I am particularly grateful to Sourik Dey and Anwesha Chatterjee from Bioprogrammable Materials for providing the engineered bacteria and their expertise in synthetic biology, from which I learned immensely. I also extend my gratitude to Zahra Kafrashian from Dynamic Biomaterials for including me in her fascinating project on optical waveguides, which enriched my knowledge in this field. A special thanks to Albenc Nexha from Structure Formation for the integration of nanothermometry into my research and for sharing his profound expertise, which significantly broadened my scientific perspective.

I am also deeply grateful to my long-time office colleagues, Tobias Knapp and Yannic Curto, for making the working atmosphere enjoyable and motivating. Their presence made day-to-day work much more pleasant.

A heartfelt thank you goes to the rest of the Structure Formation and Electrofluids group, with whom I shared not only an engaging research environment but also many fun moments. Our discussions, social gatherings, and outside of work activities made my time at the institute even more enjoyable.

Beyond work, I am incredibly grateful that many colleagues have become close friends, and that we have shared experiences even outside the institute, including memorable trips. A special thanks to Varun Tadimarri, Florian Riedel, Marc Asensio Blanch, Cansu Kök, Ketaki Deshpande, Kristela Shehu, Zahra Kafrashian, Anwesha Chatterjee, Anna Zimmermann, Long Zhang, David Iwanowitsch, and Hanuman Kalari for their friendship, support, and the great times we have had together.

Table of contents

List of Abbreviations and Symbols

3-D	3-dimensional
Ag_2S	Silver sulfide
AR	Aspect ratio
AuNR	Gold nanorod
B.subtilis	*Bacillus subtilis*
$BaYF_5$	Barium yttrium fluoride
BiT	Binary Technology
BSA	Bovines Serumalbumin
CBD	Chitin binding domain
CMT	Critical micelle temperature
CTAB	Cetrimonium bromide
CW	Continous Wave
DNA	Deoxyribonucleic acid
DOX	Doxorubicin
E.coli	*Escherichia coli*
EcN	*E.coli* Nissle 1917
EGFP	Enhanced green fluorescent protein
ELM	Engineered living material
EPR	Enhanced permeability and retention
Er^{3+}	Trivalent erbium ion
FA	Folic acid
FEM	Finite element modeling
GFP	Green fluorescent protein
HMC	Hydroxypropylmethylcellulose
HSP	Heat shock promoter

IR	Infrared
Irgacure 2959	2-Hydroxy-4′-(2-hydroxyethoxy)-2-methylpropiophenone
K^+	Potassium ion
K_2HPO_4	Dipotassium hydrogen phosphate
lacZ	Lactose Z
Laser	Light amplification by stimulated emission of radiation
LB media	Lysogeny broth media
LCGT	Lower critical gelation temperature
LED	Light-emitting diode
LgBiT	Large Binary Technology
L-LSPR	Longitudinal localized surface plasmonic resonance
LSP	Localized surface plasmons
LSPR	Localized surface plasmonic resonance
mCherry	Red fluorescent protein derived from *Discosoma sp*.
MMP	Matrix metalloproteinase
MPE	Maximum permissible exposure
mPECT	Methoxy poly(ethylene glycol)-b-poly(e-caprolactone-co-1,4,8-trioxa[4.6]spiro-9-undecanone)
Na^+	Sodium ion
NaCl	Sodium chloride
$NaYF_4$	Sodium yttrium tetrafluoride
$NaYF_4:Yb^{3+},Er^{3+}$	Sodium yttrium tetrafluoride doped with ytterbium and erbium
$Nd:BaYF_5$	Neodymium-doped barium yttrium pentafluoride
Nd^{3+}	Trivalent neodymium ion
NIR-I	Near-infrared I (range of wavelengths from 700 nm to 900 nm)
NIR-II	Near-infrared II (range of wavelengths from 1000 nm to 1400 nm)

NIR-light	Near infrared light
OD	Optical density
$OD_{808\ nm}$	Optical density at incident wavelength of 808 nm
PCE	Photothermal conersion efficiency
PCQ	PelB, CBD, and QK
PDMS	Polydimethylsiloxane
PEG	Poly(ethylene glycol)
PEI	Polyethyleneimine
PelB	Pectate Lyase B
PEO	Polyethylene oxide
Plu	Pluronic
PluDA	Pluronic-diacrylate
PPO	Polypropylene oxide
ptlpA	Promoter of TlpA
PTT	Photothermal therapy
PVA	Polyvinyl alcohol
PVA-VS	Polyvinyl alcohol-vinyl sulfone
QD	Quantum dot
QK	Synthetic peptide derived from the VEGF
RNA	Ribonucleic acid
ROS	Radical oxygen species
SiO_2	Silicon dioxide
SmBiT	Small Binary Technology
TC	Thermocouple
TEM	Transmission electron microscopy
TGF-β1	Transforming Growth Factor Beta 1

TlpA	Thermal labile protein A
TIR	Total internal reflection
T-LSPR	Transversal localized surface plasmonic resonance
UCNP	Upconverting nanoparticles
UV	Ultraviolet
VEGF	Vascular endothelial growth factor
VIS	Visible
VS	Vinyl sulfone
Y^{3+}	Trivalent yttrium ion

A	Area cross section
$A_{808\ nm}$	Absorbance at 808 nm
a, b, and c	Lengths of the ellipsoid
B	Constant rate of heat dissipation from the sample to the environment
c	Speed of light
$C_{abs,i}$	Absorption cross-section associated with the specific polarization direction i
C_{abs}	Absorbtion cross section
C_{ext}	Extinction cross section
C_p	Specific heat capacity at constant pressure
$c_{p,i}$	Specific heat capacity at constant pressure for component i
C_{scat}	Scattering cross section
D	Thermal diffusivity
d	Diameter of nanoparticle
E	Electric field
E^*	Complex conjugate of the electric field
E_{inc}	Incident electrical field

h	Heat transfer coefficient
h_r	Heat radiation heat transfer coefficient
I	Current
I_0	Intensity of incident light
Im	Imaginary part a complex quantity
J	Current density
k	Wavevector
k_0	Wave number in free space
L	Length of the region of size
l	Length of nanoparticle
L_{cond}	Condution length between system and surrounding
L_e	Maximum pentration depths
L_i	Depolarization factor
m	Cell mass
m_i	Mass of component i
P_J	Power of Joule heating
Q	Heat power
q	Electric power loss density
Q_0	Heat energy source term for baseline
Q_{abs}	Absorption efficiency
Q_{cond}	Conduction heat rate
Q_{out}	Heat dissipation to external environment
$Q_{plasmonic}$	Generated heat rate by plasmonic stimulation
Q_{rad}	Radiation heat rate
R	Resistance
r	Distance

Re	Real part of a complex quantity
R_{eff}	Effective radius
t	Time
T_{surface}	Surface temeprature
$T(\mathrm{r})$	Temperature at a given distance r
T_{amb}	Ambient temperature of surroundings
T_{IR}	Temperature recorded by infrared camera
T_{max}	Maximum temperature reached at steady state
T_{TC}	Temperature recorded by thermocouple
V	Volume
X	DA fractions
∇	Del operator
$\nabla \times$	Curl operator
α_{i}	Polarizability in directon i
B	Correction factor
Δr	Characteristic distance step
Δt	Characteristic time step
$\Delta T(R_{\mathrm{eff}})$	Temperature change at the effective radius
$\Delta T_{\mathrm{global}}$	Temperature rise at $L \sim 10$ mm
ΔT_{nano}	Temperature rise at $L \leq 50$ nm
$\Delta T_{\mathrm{segment}}$	Temperature rise at a segment in a waveguide
ε	Emissivity
ϵ_0	Vacuum permittivity
ε_1	Dielectric functions of the metal
ε_{m}	Dielectric functions of the surrounding
ϵ_{t}	Total permittivity

η	Photothermal conversion efficiency
θ	Electrical conductivity
θ_T	Dimensionless driving force temperature
κ	Thermal conductivity
λ	Wavelength
λ_{ex}	Irradiation wavelength
μ_r	Relative magnetic permeability
ρ	Density
σ_{SB}	Stefan-Boltzmann constant
τ_s	System rate constant
ω	Angular frequency

1 Introduction

Engineered Living materials (ELMs) are a type of advanced material that incorporates engineered living organisms (responsive function) into a matrix material (scaffold function). These materials are designed to exhibit biological functionality such as responsiveness to environmental stimuli to produce e.g. proteins or drugs. Living materials are an emerging area of research that is still in the early stages of development, but they hold great promise for the future of advanced material science and engineering. The living component can be bacteria, yeast, algae, and other microorganisms that can be engineered using techniques of synthetic biology. ELMs can be engineered through genetic modification and spatial patterning to control both the bulk structure mechanically and the chemical functionalization. These approaches enable the design of ELMs for a wide range of functions, including biofactories, self-healing materials, and dynamically responsive systems.[1] The genetic modification of ELMs is done depending on the desired application, such as biosensors, self-healing adhesives, smart drug delivery devices, and others.

This thesis focuses on aspects concerning the external triggering of Engineered Living Materials. So called stimuli-responsive ELMs are able to undergo controllable changes in material properties in response to external triggers.[2] To this end, genetically engineered cells can be incorporated to engender a range of biochemical and physical inputs, such as single chemicals, light, temperature, humidity and electrical fields, and programmed outputs, such as the production of enzymes or the expression of proteins.[2]

Potential applications of stimuli-responsive ELMs include environmental monitoring and biomedical fields. As biosensors and analytical devices, ELMs can sense and respond to environmental cues such as heavy metals, pesticides, and other pollutants.[2] In biomedical contexts, these ELMs can serve as biosensors, drug delivery vehicles, and components of soft biohybrid robots.[2] Stimuli-responsive ELMs offer advantages over conventional methods (e.g., precipitation, ion exchange, reverse osmosis, and ultrafiltration) due to their lower cost, renewability, and improved sensitivity, detection, and selectivity.[2]

Nanoparticles can be integrated into ELMs to introduce their unique optical properties to extend the functionality of ELMs. The strong optical responses of certain nanoparticles have been known for centuries. Already medieval alchemists created homogenous dispersions of metal oxides in glass to create colorful glazing. Reflection and refraction of the incident sunlight by these dispersions depends on the size of the particles, which alchemists controlled to obtain the desired color.[3] When particles are smaller than the incident wavelength of the electromagnetic

field (light), light–matter interactions and their optical properties significantly change compared to the bulk material. This effect is particularly strong in small particles of noble metals such as gold that are illuminated in the visible range of wavelengths.

Irradiation of gold nanoparticles with diameters below 100 nm induces the oscillation of conduction electrons on their surface. The oscillating conduction electrons (plasmons) are in phase with the electromagnetic field. At certain wavelengths, that depend on size, shape and composition of the particle, the incident field will be at resonance with the oscillating plasmons, leading to a significant increase of the absorption of the incoming light. This phenomenon is called localized surface plasmon resonances (LSPR).[3] The result is a strong optical absorption that produces vivid colors.

The absorbed energy is released as heat into the environment. Thus, plasmonic nanoparticles can serve as light to heat converters, or "nanoheaters". The heat flux can be triggered and controlled via the external irradiation: for instance, a laser may be activated momentarily to create a brief period of heating.

The photothermal conversion efficiency (PCE) of plasmonic materials depends on their composition, morphology, environment, and illumination wavelength.[4-6] Gold and silver have been the dominant materials in thermoplasmonic heating.[4] Gold nanoparticles are known for their chemical inertness, easy functionalization, low toxicity, and localized plasmon resonances in the visible-near infrared ranges, making them suitable for biomedical applications.[4, 7] In this thesis, I used gold nanorods (AuNRs) due to their easy accessibility and commercial availability. The synthesis of AuNRs is well-documented, with several methods available that allow for precise control over their size and shape facilitating their commercial production and availability.[8]

Gold nanorods are well-accepted in biomedical applications due to their biocompatibility, high absorption coefficients resulting from their plasmonic properties, tunable absorption wavelength into NIR range (biological transparency window) by changing their geometry, and high PCE.[9, 10] Their unique plasmonic properties are exploited for photothermal cancer therapy with reduced side effects, wound healing and remote control of gene regulation.[11]

More generally, the introduction of freely dispersed AuNR into a host body involves challenges such as insufficient retention and the need for specific surface functionalization for targeting and to prevent cytotoxicity.[11] These problems can be avoided by embedding AuNRs in hydrogels (AuNR hydrogel) to obtain nanocomposite hydrogels that retain the AuNR and enable spatiotemporal control by light.[12] AuNR hydrogels are utilized in photothermal

therapy (PTT) for localized heating, enabling hyperthermia and thermal ablation of cancerous tissues. Plasmonic heating of AuNR hydrogels with temperature increase to 45°C from initial body temperature are demonstrated to kill cancer cells.[10, 13] Additionally, they can facilitate drug delivery through material shrinkage or decomposition induced by heat, as well as support photodynamic therapy by incorporating dyes that generate reactive oxygen species (ROS).[12, 14] AuNR hydrogel consists mostly of water which will not be repelled by host bodies. Also mechanical properties for AuNR hydrogel are formulated to mimic human tissues and minimize immune rection.[12]

Light is an attractive stimulus for ELMs and AuNRs due to its versatility in terms of intensity, wavelength, and spatial dimensions. It is a low-cost, easy-to-handle, and non-invasive trigger that can be applied across a variety of applications. Light has been used for patterning, actuation and drug release in ELMs.[15] Existing systems typically use blue light with short wavelengths that act on optogenetic systems in bacteria.[15, 16] Blue light, however, exhibits low penetration depths *in vivo*, limiting e.g. translational potential for implanted ELMs.[17] NIR light is in biological transparency window, and thus it is important for biomedical applications due to its deep tissue penetration abilities without harming tissues and cells.[18] NIR-responsive optogenetic circuits have been reported but require co-factors that are not naturally present in most bacteria, and therefore need to be externally supplied or produced by the bacteria themselves through engineered complex enzyme cascades.[19-21]

In this thesis, I created ELMs that are triggered by NIR light. Thermoplasmonic AuNRs are exploited to activate ELMs. The living components of the ELMs were genetically engineered thermoresponsive *ClearColi* and *E. coli* Nissle 1917 bacteria, enclosed within hydrogels to create a thermoresponsive system.

A proof-of-concept model system utilized *ClearColi*, engineered to produce the fluorescent protein mCherry, within the hydrogel. Bilayer geometries combined separate AuNR-containing and bacteria-containing hydrogel layers. Upon NIR irradiation, thermoplasmonic heating in the AuNR layer diffused into the adjacent bacterial layer, stimulating mCherry production. The mCherry production in the ELM was analyzed by fluorescence spectroscopy and correlated with spatial temperature profiles obtained by infrared camera. By tuning the intensity of the incident light, it was possible to activate either the entire bacterial population or only a localized region.

Following this successful proof of concept, therapeutic ELMs were developed by encapsulating thermoresponsive *E. coli* Nissle, engineered to produce the angiogenic QK peptide, along with

AuNRs, in a single-layer cylindrical hydrogel. Upon photothermal stimulation, the ELM released QK peptide into the surrounding medium. As a VEGF-mimicking peptide, QK promotes angiogenesis and has potential applications in wound healing.

To explore the versatility of AuNR-based photothermal systems, AuNRs were encapsulated in segmented waveguide fibers without the inclusion of bacteria. Photothermal excitation in these fibers was evaluated for potential use in deep-tissue NIR treatments demonstrating the adaptability to different structural configurations. This plasmonic waveguide system also presents potential as a bacterial host in future designs, enabling bacterial-based therapeutic applications within deep tissues through NIR-triggered activation.

2 Motivation and Aim

There is an increasing demand for next-generation advanced materials that exhibit "smart" functional properties, such as the ability to adapt to environmental cues, dynamically switch between material states, and self-heal.[1] Traditional synthetic materials, while highly versatile in other respects, lack these adaptive and responsive capabilities. This limitation highlights the need for innovative platforms that leverage biological systems to produce programmable and advanced materials. A key challenge in designing such materials lies in their interaction with and response to their environment, particularly in achieving specificity to weak or poorly differentiated biochemical and physical stimuli.[2]

The emerging field of Engineered Living Materials (ELMs) addresses these challenges by integrating living cells with synthetic matrices, creating composites capable of dynamic, stimuli-responsive behavior. ELMs have demonstrated significant potential in developing materials that respond to diverse biochemical and physical stimuli with precision and specificity. These stimuli-responsive ELMs hold particular promise in biomedical applications, where they could enable sustained and long-term therapeutic delivery, outperforming traditional or purely synthetic counterparts.[2] Notably, ELMs can respond to a wide variety of stimuli to initiate drug delivery, while also synthesizing therapeutics *in situ*, offering a transformative approach to controlled and on-demand treatment strategies.[2, 22]

Living organisms bring a dynamic element to ELMs, as they can actively synthesize and release complex biomolecules, adapt to changing environments, and be sustained within a biocompatible matrix.[23] Bacteria are highly versatile, robust, and genetically tractable, making them ideal for ELMs.[1] Their ability to sense environmental cues and produce diverse biomolecules including proteins and peptides enables complex functions like drug delivery, self-healing, and environmental monitoring.[2] Genetic engineering allows precise programming of bacterial responses to external stimuli, while enabling them to simultaneously produce peptides and proteins. This dual functionality unlocks capabilities far beyond those of synthetic materials such as temperature-sensitive polymers[24, 25], shape-memory alloys[26], or photo-responsive gels[27], which are typically limited to single, predefined responses, making bacteria indispensable for designing advanced stimuli-responsive systems.

Thermoresponsive systems align well with the engineering of bacteria, as genetic circuits can be designed to reliably activate at specific temperature thresholds.[28] Thermoresponsive bacteria provide a significant advantage as their activation can be precisely controlled using

localized heating. This avoids the limitations of other stimuli, such as the need for complex biochemical inputs.[29]

The selection of *ClearColi* and *E. coli* Nissle 1917 as the bacterial components for this study is driven by their unique characteristics and relevance to the goals of developing thermoresponsive ELMs. *ClearColi* was chosen as a model system for its simplified endotoxin profile, which minimizes immune responses when used in experimental setups.[22] This makes it an ideal candidate for proof-of-concept studies in thermoplasmonic stimulation. *E. coli* Nissle 1917 is a probiotic strain with a well-documented safety profile, making it a suitable candidate for therapeutic applications.[22] Its robust growth in diverse environments and compatibility with the human microbiome make it a prime candidate for therapeutic ELMs.

The integration of plasmonic nanoparticles into ELMs as light-responsive components enables precise and non-invasive activation of biological systems. Gold nanorods (AuNRs) are biocompatible, and easy introducible into hydrogel matrices. They efficiently absorb and convert near-infrared (NIR) light into heat through a process called plasmonic heating.[10] By embedding AuNRs into ELMs, light can serve as a cheap, clean and non-invasive activation source,[30] activating thermoresponsive bacterial functions without direct contact or chemical additives. Plasmonic heating introduces several specific advantages to ELMs, particularly for therapeutic applications. First, it provides spatially and temporally controlled activation,[3, 31] enabling the targeted thermoplasmonic stimulation of bacterial activity within a defined region. This is critical for applications such as wound healing, where localized activation can enhance tissue regeneration while avoiding systemic side effects. Second, plasmonic heating enables on-demand activation, allowing users to trigger functions such as drug release or therapeutic molecule production precisely when and where they are needed.

Hydrogels, a class of soft, wet, and biocompatible materials, are widely utilized as matrices for engineered bacteria and AuNRs due to their high water content, tunable properties, and biocompatibility.[12, 23] In this thesis, ELMs were shaped into cylindrical geometries, including bilayer, single-layer, and fiber constructs, each tailored to specific experimental and functional needs. The bilayer and single-layer geometries allow controlled spatial separation or co-localization of bacteria and plasmonic nanoparticles, enabling precise investigation of heat transfer and bacterial response within the ELM system. These configurations are particularly important for understanding the interaction between thermoplasmonic heating and bacterial activation in controlled environments. Fiber-shaped hydrogels, on the other hand, were designed with waveguiding properties to facilitate the deep tissue penetration of NIR–light. The

integration of waveguiding hydrogels in this thesis serves a dual purpose: to enhance the delivery of NIR light for plasmonic heating and to extend the applicability of ELMs to scenarios where light needs to penetrate biological tissues.

The goal of this thesis is to integrate gold nanorods (AuNRs) into Engineered Living Materials (ELMs) to develop a cost-effective, light-responsive system for biomedical applications. AuNRs enable precise thermoplasmonic stimulation upon near-infrared (NIR) light irradiation, triggering thermoresponsive bacteria to produce therapeutic molecules. *ClearColi* was used to produce mCherry, a red fluorescent protein that provides a quantifiable output for evaluating thermoplasmonic activation. This system allows real-time correlation of heat delivery with bacterial responses. Additionally, *E. coli* Nissle 1917 was employed to produce QK peptide, a stable VEGF analog that promotes angiogenesis, essential for wound healing.

This thesis is structured to systematically investigate the integration of gold nanorods (AuNRs) into Engineered Living Materials (ELMs), focusing on their photothermal properties for precise and localized activation. The overall principle is to exploit the thermoplasmonic heating capabilities of AuNRs to stimulate engineered bacteria embedded within biocompatible hydrogel matrices. Three distinct approaches are explored to address specific biomedical challenges: (1) developing bilayer hydrogel systems, where AuNRs and bacteria are separated into distinct layers to control heat transfer and bacterial activation; (2) designing single-layer ELMs with AuNRs and bacteria mixed in the same hydrogel layer to enhance heat transfer efficiency and enable lower power density requirements; and (3) incorporating AuNRs into hydrogel-based optical waveguides to facilitate light-guided thermoplasmonic stimulation for deep tissue applications. The thesis systematically evaluates the colloidal stability, photothermal efficiency, and biocompatibility of AuNRs in various matrices, correlating these properties with their effectiveness in activating bacterial genetic circuits. The findings aim to establish a framework for the design of multifunctional ELMs with tailored thermoplasmonic properties for therapeutic applications, such as peptide production for wound healing and localized activation in advanced biomedical systems.

Chapter 3 provides the theoretical foundation and a comprehensive review of the state of the art. Since the combination of gold nanoparticles with ELMs for thermoplasmonic activation via NIR light has not yet been explored in the literature, the chapter addresses gold nanoparticles (specially AuNRs) and ELMs as separate topics. This approach highlights the distinct properties of each field, providing a foundation for understanding their potential integration and the innovative contribution of this work. Chapter 3 explores the plasmonic and thermoplasmonic

properties of single AuNRs (chapter 3.1 and 3.2) and the mechanisms of collective heating (chapter 3.3). The photothermal conversion efficiency (PCE) of collective AuNRs is a critical parameter for their application in biomedical contexts. Its calculation and influencing factors are thoroughly discussed in section 3.3.1. Additionally, accurately determining plasmonically generated temperatures is essential; thus, section 3.3.4 outlines various methodologies for temperature measurement. Chapter 3.4 explores the biomedical applications of thermoplasmonic nanoparticles, with particular emphasis on their roles in wound healing, photothermal therapy, and the fabrication of photothermal-responsive nanocomposite hydrogels. The relevance of stimuli-responsive ELMs is addressed in chapter 3.5, which delves into their design, preparation methods, and the pivotal role of hydrogels as functional matrices in these systems.

Chapter 4 outlines the author´s contribution for my thesis.

Chapter 5 presents the results, structured into introduction, materials and methods, results and discussion, and conclusion and outlook for each section. The first milestone of this thesis, presented in chapter 5.1, is the successful photothermal triggering and control of bacterial activity in ELMs. This chapter introduces the concept of thermoplasmonic activation using bilayer hydrogels, where the heat generated in a plasmonic layer is used to activate bacteria in an adjacent layer. These results provide proof-of-concept for the integration of AuNRs into ELMs and their potential for NIR-controlled bacterial stimulation. Chapter 5.2 expands on this by successfully developing therapeutic activable ELMs, marking a significant advancement in this work. These ELMs are engineered to produce QK peptides, a VEGF mimetic, under NIR illumination from both a continuous-wave laser and an LED lamp. Chapter 5.3 explores the photothermal response of AuNR composite hydrogel-based waveguides. This chapter investigates how various waveguide geometries, segment lengths, and core-shell structures influence the photothermal behavior, providing insights into optimizing light delivery systems for advanced applications. These results underscore the versatility of thermoplasmonic systems and their potential in controlled light propagation within living materials.

3 Theory and State of the Art

3.1 Plasmonic properties of gold nanorods

When plasmonic nanoparticles with typical diameters of 10 nm – 100 nm are irradiated with light, the conduction electrons on the surface of the nanoparticles collectively oscillate as localized surface plasmons (LSPs). At certain frequencies, the electromagnetic field is in resonance with the oscillations of the conduction electrons. This leads to a significantly increased absorption of the incoming light, and the phenomenon is called localized surface plasmon resonances (LSPRs). One part of the absorbed energy is released as heat, so that plasmonic nanoparticles can serve as light-to-heat converters.[3] The LSPR amplifies both the radiative and non-radiative processes of the nanoparticles, enabling diverse modalities for biological and medical applications, including cellular imaging, molecular diagnostics, and targeted therapy.[32]

The heating of plasmonic nanoparticles can be triggered and controlled by external irradiation, for instance, by a laser. Hence, plasmonic nanostructures have the property that their heating can be fine-tuned, turned on or off, and used for a large number of diverse applications like photothermal therapy (see chapter 3.4).[11] The absorption of light by plasmonic nanostructures and their associated temperature increase are exquisitely sensitive to the shape and composition of the structure and to the wavelength of light.[3] Gold nanoparticles have a facile synthesis and surface modification, strongly enhanced and tunable optical properties and biocompatibility feasible for biomedical applications.[32] Different shapes and structures like gold nanorods (AuNRs), silica/gold nanoshells and hollow gold nanoparticles can be synthesized. Among these shapes, gold nanorods (AuNRs) have garnered significant attention due to their unique properties, such as their tunable aspect ratios, which make them particularly suitable for applications in optical devices, biochemical sensors, and nanomedicine.[10]

AuNRs have a cylindrical symmetry and therefore exhibit two plasmon modes, a longitudinal LSPR (L-LSPR) associated with the electron oscillation along the length direction and a transverse LSPR (T-LSPR) mode arising from the transverse electron oscillations. Both modes are dipolar resonances and can be excited by electromagnetic waves.[10] To define the size and shape of AuNRs, the aspect ratio (AR) is introduced which is the ratio of length (longitudinal side) to diameter (transverse side). The LSPR effect makes AuNRs to strong light absorbers with very high extinction coefficients of $10^8 – 10^{10}\ M^{-1}\,cm^{-1}$ (for the L-LSPR at NIR-

wavelengths).[33] This is 10 000 times greater than strongly absorbing organic chromophores like rhodamine 6G with extinction coefficient in magnitude of 10^5 M^{-1} cm^{-1}.[33]

The excitation of plasmonic resonance results in rapid relaxation mainly by the generation of electron-hole pairs, thermalization with the lattice through Joule heating, and emission of photons.[3] Among these three plasmon damping mechanisms, thermalization is responsible for the plasmonic heating of nanostructures. When an electric current flows through a plasmonic nanostructure, it encounters resistance. The resistance is due to the phonons (lattice vibrations) of the metal structure. The interaction between the LSPs and the phonons leads to energy dissipation, where part of the absorbed plasmonic energy is converted into heat. This heat is transferred to the surrounding environment, resulting in an increase in the temperature of the AuNRs and the surrounding medium. The amount of heat generated by Joule heating depends on the properties of the nanostructure, such as its size, shape, and composition, as well as the properties of the surrounding medium. The thermal energy P_J generated by Joule heating is proportional to the square of the current I flowing through the conductor and to the resistance R.

$$P_J = I^2 \cdot R \tag{3- 1}$$

The coupling between incoming light and the LSP determines the photothermal conversion efficiency. It is strongly influenced by the extinction cross section C_{ext} of the AuNRs:

$$C_{ext} = C_{abs} + C_{scat} \tag{3- 2}$$

C_{scat} denotes the scattering cross section and C_{abs} the absorption cross section. As plasmonic heating primarily arises from non-radiative relaxation, C_{abs} is the key parameter for describing this process. C_{abs} is estimated by solving Laplace´s equation, which models the electric field distribution around the AuNR when exposed to incident light. The absorption cross section of "gold ellipsoids" excited along different axes can be obtained as:[10, 34]

$$C_{abs,i} = k\mathrm{Im}(\alpha_i) \tag{3- 3}$$

where k is the wavevector and α_i the polarizability.

The polarizability α_i of gold nanorods can be estimated using the quasi-static approximation of Gans Theory. It describes the rod shape as prolate spheroid and gives[10]

$$\alpha_i = 4\pi abc \frac{\varepsilon_i - \varepsilon_m}{3\varepsilon_m + 3L_i(\varepsilon_i - \varepsilon_m)} \tag{3- 4}$$

with a, b, and c the half lengths of the ellipsoid along the three major axes, ε_m and ε_1, the dielectric functions of the surrounding medium and the metal, respectively, and L_i the depolarization factor. The depolarization factor accounts for the fact that the electric field inside the gold nanorod is not uniform due to the induced charges on its surface. Equations (3- 3) and (3- 4) show that the plasmonic properties of metal nanocrystals depend strongly on their geometry, with polarizability (α_i) playing a key role in determining resonance wavelengths. Gans theory, specifically applied to AuNRs, reveals that their absorption cross section and plasmon wavelengths vary with size and shape. Increasing the aspect ratio (AR) of the AuNRs with a constant diameter leads to an enlargement of the extinction cross-sections of both the longitudinal and transverse plasmon modes. The plasmon wavelengths of these two modes also change, with the transverse mode exhibiting a small blue shift and the longitudinal mode exhibiting a much more sensitive behavior with a red-shift of up to several hundred nanometers (see also chapter 3.4.1).[10] The higher polarizability α_i of the AuNR at the longitudinal plasmon resonance is responsible for the larger dependence of the longitudinal plasmon wavelength on the aspect ratio, and hence is the more sensitive mode. Additionally, the light absorption of L-LSPR is higher than the T-LSPR. In consequence, the L-LSPR mode is more commonly exploited in thermoplasmonic biomedical applications (see chapter 3.4). In this thesis, the AuNRs with a L-LSPR at about 808 nm is used, within the biological transparency window.

The above section explains the interaction of light with AuNRs and how their plasmonic properties can be mathematically described. The next section connects the absorption cross section with the generated temperature profiles of plasmonically stimulated AuNRs.

3.2 Thermoplasmonic properties of gold nanorods

When gold nanorods (AuNRs) are irradiated by light at resonant frequencies, surface plasmons on the nanoparticles transduce the radiation to thermal energy, resulting in an increase in temperature in the AuNR and in its surrounding medium. This chapter explains this mechanism for individual AuNRs. The relevant equations describing the thermoplasmonic properties of AuNRs are presented, and the key parameters influencing plasmonic heating are derived from them. The state of the art on which parameters the plasmonic heating depends is explained in the last part of this chapter.

Irradiation at resonant wavelength of a single AuNR in dispersion results in heat dissipation to the matrix through a cascade of events, as illustrated in Figure 3- 1 A.[35, 36] Resonant irradiation induces a non-thermal electron distribution that thermalizes in ~500 fs via elastic electron-electron scattering to an equilibrium Fermi electron distribution that corresponds to a higher electron temperature. The Fermi distribution or "electron gas" cools by electron-phonon coupling with the gold lattice at a time scale of 2-5 ps. The electron-phonon relaxation is size and shape independent in the rods.[32] The lattice cools off by phonon-phonon interactions with the surrounding medium at timescales between 100 and 380 ps. Phonon-phonon interactions dissipate heat across a particle-matrix interface to an adjacent shell of matrix medium at a rate dependent on the matrix, particle size, and irradiation power as AuNRs return to their initial electron temperature.[35, 37]

The temperature field caused by the irradiating AuNRs can be expressed via the general heat transfer equation[3, 10, 38]

$$\rho c_{\mathrm{p}} \frac{\partial T(r)}{\partial t} = \nabla \cdot [\kappa \nabla T(r)] + Q \tag{3- 5}$$

where ρ and c_{p} are the density and specific heat capacity at constant pressure, respectively. κ is the thermal conductivity of the surrounding medium, $T(r)$ represents the absolute temperature of the system at a given distance r from the center of the AuNR, Q is the amount of generated heat by the AuNR, which originates from Joule heating. The equation describes the change in temperature with respect to time and space and is based on the principle of conservation of energy. The left-hand side of the equation represents the rate of change of temperature with time, while the right-hand side represents the sources and sinks of heat in the system. The equation is used to model the temperature profile of a nanostructure when it is irradiated with light and can be solved numerically to obtain the temperature distribution in the system.

The dissipated energy Q in a AuNR occurring due to the plasmonic heating is derived from Poynting´s theorem[3]

$$Q = \iiint \frac{1}{2}\mathrm{Re}(J \cdot E^*)\,\mathrm{d}V \tag{3- 6}$$

where the electric power loss density q within the nanostructure is defined as $q = ½\cdot\mathrm{Re}(J\cdot E^*)$ and J is the current density, which is a function of the electrical conductivity θ; $J = \theta\cdot E$.

To calculate the heat production with equation (3- 6), the electric field E in the nanostructure generated by the incident light must be known. This can be done by using finite element modeling (FEM) to numerically solve Maxwell´s equation[3]:

$$\nabla \times \mu_r^{-1}(\nabla \times E) - {k_0}^2\left(\varepsilon_r - i\frac{\theta}{\omega\varepsilon_0}\right)E = 0 \tag{3- 7}$$

This vector equation includes the electric field E, the sum of the incident and scattered fields. μ_r is the relative magnetic permeability of the medium, k_0 is the wave number, $\sigma / (\omega\varepsilon_0)$ incorporates dissipation losses to the medium with θ as the electrical conductivity of the material, ε_r as the relative permittivity of material and ω as the angular frequency.

The optical absorption cross section C_{abs} (see chapter 3.1, equation (3- 2) and (3- 3)) is a measure of the efficiency of a nanostructure in absorbing light and producing heat. The cross section can be obtained by dividing the rate of dissipated or absorbed energy Q in the nanostructure by the intensity I_0 of incident light which is a function of the incident electrical field E_{inc} from the incident light.

$$C_{abs} = \frac{Q}{I_0} = \frac{1}{c\varepsilon_0|E_{inc}|^2}\iiint \frac{1}{2}\mathrm{Re}(J \cdot E^*)\,\mathrm{d}V \tag{3- 8}$$

FEM is again used to numerically solve Maxwell´s equation and calculate C_{abs} for AuNRs, accounting for surrounding medium effects and non-uniform fields, unlike analytical methods (that are the basis for equation (3- 2) and (3- 4)) that assume idealized conditions.

By knowing the value C_{abs}, finally the temperature gradient $\Delta T(R_{eff})$, governed by equation (3- 5), around an irradiated AuNR can be determined.[3]

$$\Delta T(R_{eff}) = \frac{Q}{4\pi\kappa R_{eff}\beta} = \frac{C_{abs}\cdot I_0}{4\pi\kappa R_{eff}\cdot\beta} \tag{3- 9}$$

where R_{eff} is the effective radius of the gold nanorod, equal to the radius of a spherical particle with the same volume, β is the correction factor for the shape of particle, κ is the thermal

conductivity of the surrounding medium. β has been calculated for different shapes and for gold nanorods it has the value $\beta = 1 + 0.97 \ln^2(\mathrm{AR})$, where AR is the aspect ratio.[39]

Many reports are conducted to compute the heat generation on AuNRs depending on the abovementioned parameters. Baffou et al. computed the heat generation Q in AuNRs in aqueous medium at different irradiation wavelengths for different shapes with the same volume.[40] Increasing AR (1, 2, 3 and 4) caused a redshift of the LSPR and an increase of the generated heat power. The generated heat power in the nanoparticles was maximum at their LSPRs for all shapes (see Figure 3- 1 B). Figure 3- 1 B in the right depicts the heat power distribution along the rod with an AR = 4 at different incident wavelengths. At resonance, most of the heat originates from the center of the rod rather than from its edges due to the fact that electric current, which is responsible for the Joule heating, mostly flows from the center of the rod while the edges mainly accumulate charges.[40] Figure 3- 1 C shows simulations of the electric field magnitude at 800 nm in AuNRs with a constant AR = 4 with increasing volumes starting at dimension of 10 nm × 40 nm. The magnitude of the generated electric field after plasmonic stimulation in the AuNR decreased with increasing volumes at same AR. The smallest AuNR (10 nm × 40 nm) exhibits the highest heat generation. This is attributed to the decreasing absorption efficiency Q_{abs} (Figure 3- 1 D) with increasing volumes (see equation(3- 8) and (3- 9)). Q_{abs} decreases with increasing volume at same AR due to a red shift of the LSPR peak and additional damping effects, reducing absorption efficiency at 800 nm. Consequently, the most efficient morphology for photothermal applications at this irradiation wavelength is 10 nm × 40 nm with AR = 4.

The choice of the light source, whether a continuous wave (CW) laser or a pulsed laser, affects both the spatial temperature distribution around the AuNR and the maximum generated temperature on its surface. Under CW illumination, the radial temperature decay follows a $1 / R_{\mathrm{eff}}$ dependance, as described in equation (3- 9) and illustrated in Figure 3- 1 E. Using a pulsed laser with repetition rates below the timescale of phonon-phonon relaxation (Figure 3- 1 A), changes the heating profile. Under femtosecond-pulsed illumination the temperature increase is more confined in the vicinity of the AuNR, with a decay proportional to approximately $1 / R_{\mathrm{eff}}^3$ (Figure 3- 1 E).[5] Furthermore, the competitive lattice heating by electron-phonon interaction and the heat dissipation to the surrounding by phonon-phonon interaction can be controlled by the laser type resulting in different temperature increase on the AuNR. Petrova et al. applied femtosecond-pulsed laser on AuNR resulting in temperatures of 250 °C – 700 °C in the AuNR and within one hour surface melting occurred, transforming the AuNR into spheres.[41] Link et al. showed that using femtosecond-pulsed laser with high

energies (in the range of milli Joule) on AuNRs, particle ablation occurs. However, using a CW laser, the phonon-phonon relaxation dominates allowing heat dissipation to the surrounding of the AuNR resulting in temperature increase in the order of few tens of degrees.[32]

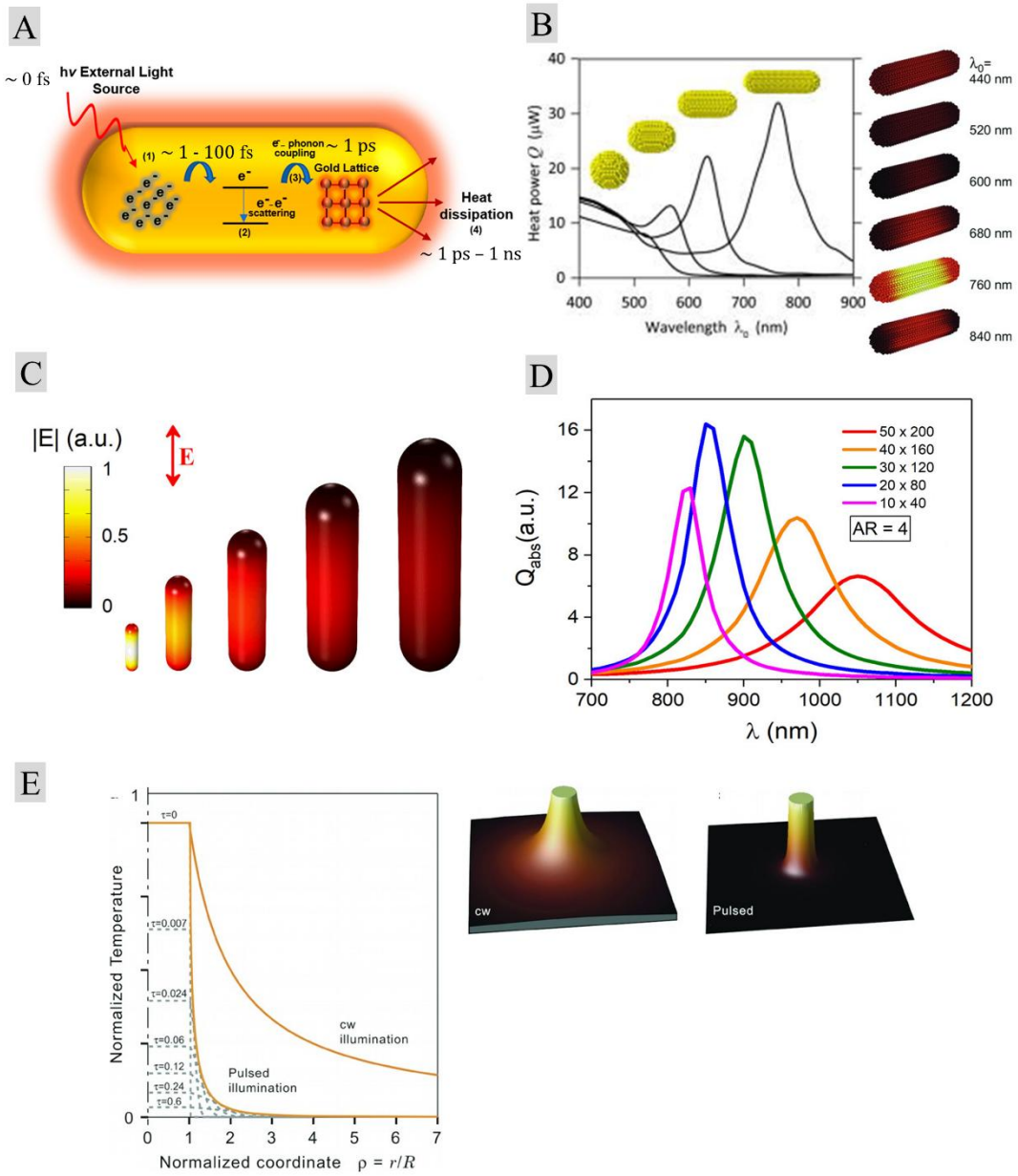

Figure 3- 1: Plasmonic properties of individual AuNRs described by Gans theory. A) Canonial picture of the photophysics of AuNR after absorbing light. Reprinted from permission from [36]. Copyright © 2019 American Chemical Society B) Calculated heat generation for gold nanosphere and AuNRs with different morphologies and same volume as a function of the irradiation wavelength. Reprinted from [40], with the permission of AIP Publishing. Used with permission from [5]. © 2012 by WILEY-VCH Verlag GmbH & Co. KGaA, Weinheim. C) Normalized electric field magnitude of AuNRs with a constant AR = 4 excited at λ = 800 nm. The smallest rod has dimensions of 10 nm × 40 (width and length), while the following rods maintain the same AR but have increasing volumes. Reprinted with permission from [3]. Copyright © 2019 American Chemical Society. D) Absorption cross section for the rods of C). Reprinted with permission from [3]. Copyright © 2019 American Chemical Society. E) Comparison of the spatial extension of the temperature profile in CW and pulsed illuminations: Left: Radial profiles of temperature in pulsed and CW illumination. The pulsed illumination curve provides additionally temperature profiles (dashed lines) with increasing pulsation rates along the y-axis. Right: Three-dimensional representation of the

temperature distribution around the nanoparticle under CW and pulsed irradiation. Used with permission from [5].

Computational models were used to estimate the temperature distribution of the surrounding of AuNRs when irradiated by femtosecond pulsed lasers. Ekici et al. investigated the temperature generation and distribution in and of the surrounding of AuNRs with dimension of 48 nm × 14 nm under pulsed irradiation with a fluence of 4.7 J/m^2 (Figure 3- 2 A-C).[42] Their results indicate a temperature generation of 1270 K in the AuNR´s surface during the electron-phonon interaction of 50 ps and a thermal equilibrium with the surrounding (phonon-phonon interaction) at 500 ps. At 70 ps, the temperature of the AuNR dropped to 1079 K and the surrounding water temperature was at 580 K at the AuNR/water interface (Figure 3- 2 A). The interface temperature decreased rapidly with increasing distance away from the particle. At a distance of 7 nm, the temperature dropped to ambient surrounding temperature of 300 K. Figure 3- 2 B shows the radial temperature profiles at 50 ps, 200 ps, and 500 ps. At 50 ps, the temperature at the gold-water interface reaches approximately 1200 K, with a steep thermal gradient extending radially to ~7 nm. At 200 ps, the temperature dropped to ~650 K, and the region over which temperature gradually decreases extends to ~15 nm. After 500 ps, the temperature at the interface significantly decreased to about 400 K, while the temperature profile extended further into the surrounding medium, reaching a depth of ~20 nm. Figure 3- 2 C illustrates the temporal evolution of electron, lattice, and water temperatures, with electron temperature peaking within 250 fs due to energy absorption, followed by lattice heating (~50 ps) via electron-phonon coupling and subsequent heat dissipation into water over ~500 ps. Figure 3- 2 C depicts the temporal evolution of AuNR and its surrounding water at the surface following femtosecond laser irradiation. The electron temperature during pulse duration of 250 fs reached values in the range of 10^5 K and thermal equilibrium between electron-phonon interaction was reached after about 50 ps. After about 500 ps thermal equilibrium between particles surface and surrounding was reached (Figure 3- 2 C).[42] Also, experimental studies on the temperature decay of the surrounding solid of AuNR after pulsed laser excitation was conducted. Maity et al. used perylene fluorescence molecules as optical thermometry for nanoscale range.[43] These experiments indicate an exponential decay of the temperature at AuNRs surface with increasing distance (Figure 3- 2 D).

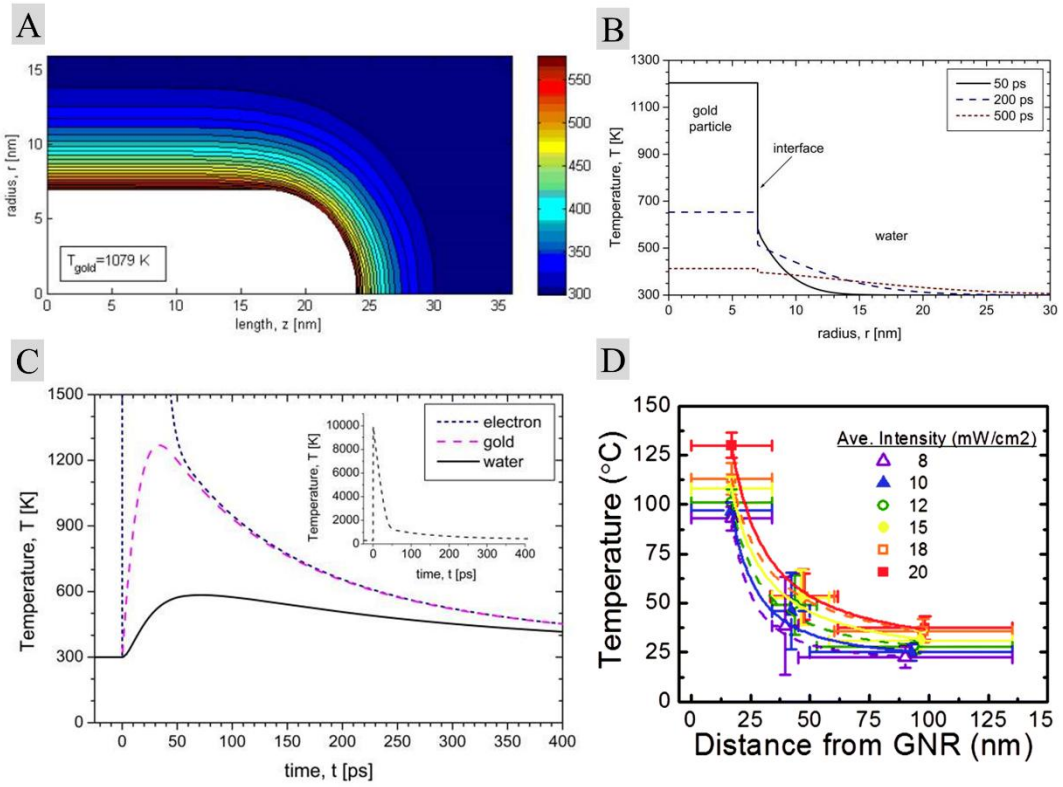

Figure 3- 2: Temporal and spatial temperature variations in both the gold nanorods and surrounding medium under femtosecond laser irradiation. A)–C) Computational modeling for the temperature generation in AuNRs (48 nm × 14 nm) and its surrounding water under application of femtosecond pulsed laser irradiation with a fluence of 4.7 J/m^2. Reproduced from [42], © IOP Publishing. Reproduced with permission. All rights reserved.
A) Temperature distribution of the AuNR surface and its decay in the surrounding water at 70 ps after irradiation. B) Temperature profiles at different times after laser exposure as a function of radial distance at length of $z = 0$. C) Temperatures of electron, lattice and surrounding water of AuNR in function of time after irradiation of single pulse laser. The inset shows the temperature of electron in function of time. D) Temperature distribution in function of distance from AuNR surface for varying average intensities of pulsed laser. Reproduced from Ref. [43]. © The Royal Society of Chemistry 2014.

3.3 Collective heating of dispersed gold nanorods

Chapter 3.1 and 3.2 introduced the temperature distribution T as a function of radial temperature decay R_{eff} of single AuNR during thermoplasmonic heating. Chapter 3.3 describes how the photothermal conversion efficiency (PCE) of collective AuNRs are calculated and determined. The PCE is an essential parameter in photothermal biomedical applications (see chapter 3.4) and describes the fraction of incident light converted into heat.

3.3.1 Parameters influencing heat generation

For therapeutical and biomedical applications, it is desirable to understand both the plasmonic heating of single AuNRs at the nanoscale (as described in chapter 3.2) as well the global temperature resulting from irradiating a known volume density of AuNRs with a CW laser.[3] Baffou et al. investigated the temperature gradients in suspensions with different densities of nanoparticles.[39, 44] They identified two distinct spatial and temporal regimes: a nanoscale regime, characterized by localized heating in the immediate vicinity of nanoparticles, and a global regime, representing heat diffusion over larger spatial scales ranging from 10^{-3} m to 10^{-2} m.[3, 39, 44] Baffou et al. and Keblinski et al. estimated the characteristic time $\tau = L^2 / D$ required to reach a steady state temperature distribution during plasmonic heating under CW laser illumination.[39, 44, 45] L is the typical length of the region of size and D is the thermal diffusivity (for water $D_{water} = 1.43 \cdot 10^{-8}$ m^2 s^{-1}). In the nanoscale regime ($L \leq 50$ nm), steady state is reached within approximately $\tau_{nano} \sim 100$ ns, whereas in the global regime ($L \sim 10$ mm) steady state requires several hundreds of seconds.[39] These time scales are plotted in Figure 3- 3 A which shows two plateaus originating from nanoscale heating and the effect from collective heating.[45] Keblinski et al. further estimated the steady state temperature rise $\Delta T_{global} \approx 10^1 - 10^2$ K for $L = 1$ mm for collective nanoparticles and $\Delta T_{nano} \approx 0.06$ K at individual nanoparticle's surface irradiated by CW laser (Figure 3- 3 A). The global temperature increase is orders of magnitude larger than the localized heating effects near individual nanoparticles when irradiated by CW laser. To achieve significant localized heating effects, high-power pulsed or modulated lasers with low duty cycles should be employed.

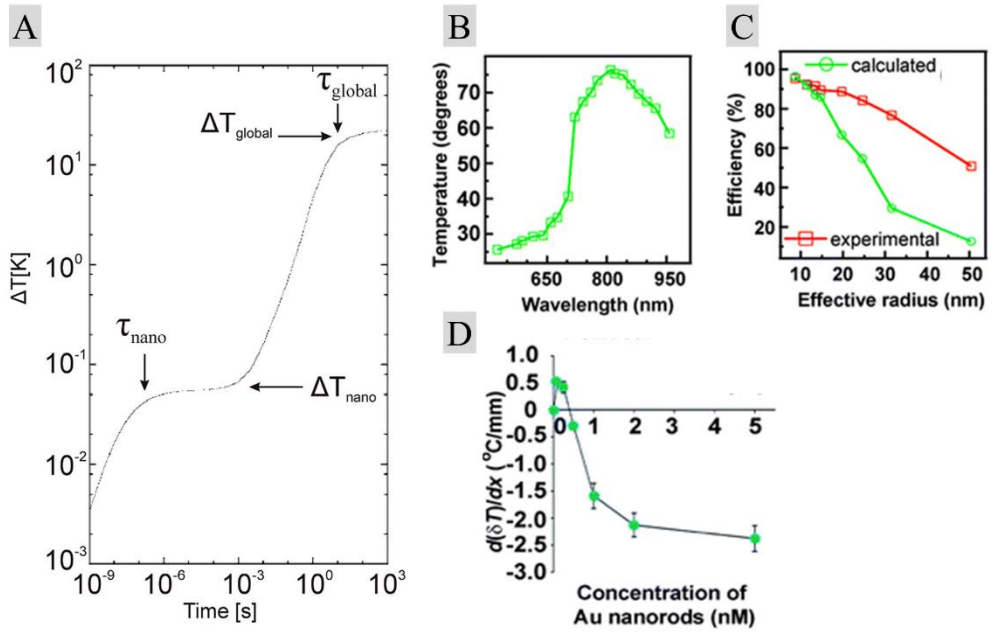

Figure 3- 3: Overview of the thermoplasmonic properties of AuNRs and their effects on local and global heating under laser irradiation. A) Time scales and temperature rise involved in single nanoparticle versus bulk heating. Temperature rise ΔT near the surface of a nanoparticle as a function of heating time. Characteristic time scales τ and ΔT at steady state are indicated for surrounding in nanometer and global scale. Reprinted from [45], with the permission of AIP Publishing. B) Temperature on the AuNR (AR = 4) in function of irradiation wavelength. C) Measured and calculated PCE of AuNRs in function of effective particle radius. D) Effect of AuNR concentration on the temperature gradient d(δT)/dx along the depth of the surrounding matrix during laser light irradiation of 2 W/cm^2 after 5 min. Used with permission from [46]. Copyright © 2011 WILEY-VCH Verlag GmbH & Co. KGaA, Weinheim.
B) - D) Reproduced from Ref. [10]. © The Royal Society of Chemistry 2013. B) – C) Used with permission from [47]. Copyright © 2010 WILEY-VCH Verlag GmbH & Co. KGaA, Weinheim

The temperature rise ΔT for dispersed AuNRs depends on their PCE and it is the most crucial factor for photothermal biomedical applications. The PCE of AuNRs have been found to strongly depend on the plasmon resonance wavelength, their volume and assembly state.[47] Chen et al. showed that that the PCE of AuNRs is highest with L-LSPR very close to the incident wavelength (Figure 3- 3 B).[47] In addition, the PCE decreases with larger AuNR volumes, even when LSPR wavelengths remain constant (Figure 3- 3 C).[47] This reduction in PCE is attributed to a lower radiative decay of the LSPR in smaller AuNR, where a greater fraction of absorbed light energy is efficiently converted into heat rather than being radiated as light.[10] Jang et al. investigated the effect of AuNR concentration on the temperature distribution caused by photothermal heating.[46] Their results show that temperature gradients develop and become larger as the concentration of AuNRs is increased (Figure 3- 3 D).

The temperature rise ΔT for plasmonic heating of colloidal AuNRs can be controlled experimentally by their concentration and the irradiant laser power density as given in equation (3- 24) derived in section 3.3.3. The collective heating from irradiated AuNRs can be measured using thermocouples (TC) or infrared camera (see section 3.3.4). Typical heating curves of collective AuNRs stimulated plasmonically by CW laser are shown in section 3.3.3 and 3.3.4.

3.3.2 Microscale heat transfer from thermoplasmonic gold nanoparticles

This section introduces the energy balance of irradiated AuNR dispersions. To quantify the photothermal conversion efficiency (PCE), an energy balance equation is required to describe the heat transfer processes occurring in the system (see section 3.3.3). The temperature change of an irradiated volume of AuNR dispersion can be described by equation (3- 10)[35, 48]

$$\sum_j Q_\mathrm{j} = \sum_i m_\mathrm{i} c_\mathrm{p,i} \frac{\mathrm{d}T}{\mathrm{d}t} \tag{3- 10}$$

where i terms $m_\mathrm{i}c_\mathrm{p,i}$ are products of mass and heat capacity for the system components (e.g. AuNR dispersion and cuvette), T is an aggregate system temperature, and t is time. The terms j include the thermoplasmonic term $Q_\mathrm{plasmonic}$, the baseline heat input Q_0 from the light source, the heat conduction Q_cond out of the system, and the radiation Q_rad.

$$\sum_j Q_\mathrm{j} = Q_\mathrm{plasmonic} + Q_0 - Q_\mathrm{cond} - Q_\mathrm{rad} \tag{3- 11}$$

$Q_\mathrm{plasmonic}$ represents the heat dissipation by the electron-phonon relaxation of plasmons with

$$Q_\mathrm{plasmonic} = I_0(1 - 10^{-A_\lambda})\eta \tag{3- 12}$$

where I_0 is the incident laser power, A_λ is the absorbance of the AuNR at specific wavelength λ, and η is the PCE. The PCE quantifies the proportion of absorbed light energy by AuNRs that is converted into thermal energy through plasmonic heating. Q_0 represents the baseline heat dissipation of the system in the absence of nanoparticles, which arises from thermal diffusion from the system and its surrounding medium. In this work, Q_0 is determined experimentally by measuring the temperature change of the cuvette filled with pure hydrogel or water under laser irradiation, without AuNRs. Q_0 is included to isolate the specific contribution of AuNRs to the overall heat generation in the system.

The heat conduction Q_cond is described by Fourier´s law, assuming a steady state condition for one-dimensional rectangular system[48]

$$Q_\mathrm{cond} = -kA \frac{(T - T_\mathrm{amb})}{L_\mathrm{cond}} \tag{3- 13}$$

where k is thermal conductivity, A is the area cross section perpendicular to conduction, L_cond is the distance over which heat conduction occurs between the system and its surroundings and T_amb is ambient temperature of surroundings.

Thermal radiation Q_{rad} is the heat exchange between two surfaces described by the Stefan-Boltzmann law:[35, 49]

$$Q_{rad=}\varepsilon\sigma_{SB}(T_{surface}^4 - T_{amb}^4) \quad (3\text{- }14)$$

The Stefan-Boltzmann constant ($\sigma_{SB} = 5.67\times10^{-8}$ W/m^2·K^4) relates the radiation power of a black body to its surface temperature $T_{surface}$. The emissivity ε is the surface material property that describes the ability of a real surface to emit radiation relative to a perfect black body. It ranges between ε = 0 (no radiative emission) and ε = 1 (black body).

For many applications, like the calculation of PCE in this work referred from publications[35, 49], it is convenient to express the radiation heat exchange in the linear form[48]

$$Q_{rad} = h_r A(T_{surface} - T_{amb}) \quad (3\text{- }15)$$

where, from equation (3- 14), the heat radiation heat transfer coefficient h_r is $h_r \equiv \varepsilon\sigma(T_{surface} + T_{amb})(T^2_{surface} + T^2_{amb})$. Radiative transport is modeled in a manner similar to convection.[48] This linearized radiation rate allows to linearize the heat equation rate used for calculating the PCE of colloidal nanoparticles, as described in chapter 3.3.3, making the experimental determination of heat transfer coefficient more convenient. Indeed, Roper et al. reported, that for temperature increases $\Delta T \leq 11$ K, Q_{rad} is constant to within 2.8% allowing a convenient linearization of the energy balance.[35] By expressing Q_{rad} in this linearized form, it becomes analogous to Q_{cond}, both representing heat dissipation to external environment as Q_{out} which is given by Newton´s law of cooling:[35, 49]

$$Q_{out} = hA(T_{surface} - T_{amb}) \quad (3\text{- }16)$$

The heat transfer coefficient h can be determined experimentally for specific conditions. In my work, I determined h as shown in chapter 3.3.3 using the method of Roper et al.[35] as an intermediate step to determine PCE. The energy balance in equation (3- 10) then simplifies to

$$Q_{plasmonic} + Q_0 - Q_{out} = \sum_i m_i c_{p,i} \frac{dT}{dt} \quad (3\text{- }17)$$

The next section 3.3.3 describes how the PCE can be determined by the basics of microscale heat transfer.

3.3.3 Derivation of the photothermal conversion efficiency

The PCE is the ratio of optical energy absorbed by plasmonic resonance to the thermal energy released by a collective of AuNRs – a crucial parameter in photothermal biomedical

applications.[47, 50]. Theoretical studies to quantify the PCE of plasmonic nanoparticles used discrete dipole approximation (DDA) simulations[51], along with other models of photothermal heating.[47, 52, 53] DDA simulations involve modeling nanoparticles as an array of polarizable points to calculate their optical properties such as absorption and scattering. The PCE is expressed as the ratio of the absorption cross section to the extinction cross section.[51] This ratio directly indicates the fraction of incident light energy that is absorbed and subsequently converted into thermal energy by the nanoparticles. Further, Mie theory has been employed to calculate the absorption-to-extinction ratios to derivate the PCE.[53] Other theoretical models analyze the heat generation in nanoparticles under light exposure by solving heat transfer equations, incorporating factors such as nanoparticle size, shape, and material properties.[47, 52]

Experimental studies include spectroscopic approaches such as the integrating sphere[54, 55] and double beam fluorescence thermometry.[56] Photocalorimetric methods determine the PCE [35, 49, 57, 58] by exploiting the conservation of energy and analyzing the temperature profile to determine the PCE (see equation (3- 10)). Roper´s model is often used to determine the PCE based on fitting the cooling profile of plasmonic stimulated colloidal particles.[35] Wang´s model is based on the analysis of the heating profile by defining internal and external light to heat conversion efficiencies.[9, 59]

The method of Roper et al. was used in this thesis.[35] Many reports exist on calculating the PCE of colloidal metal nanoparticles based on their method.[35, 47, 49, 60-63] The heat transfer energy balance of equation (3- 17) permits straightforward analytical determination of the PCE η, as shown in the following.[35, 49, 57]

By replacing the energy terms $Q_{\text{plasmonic}}$ and Q_{out} by equation (3- 12) and (3- 16) and defining $\Delta T(t) \equiv T(t) - T_{\text{amb}}$, equation (3- 17) can be expressed as

$$\frac{\mathrm{d}\Delta T}{\mathrm{d}t} = \frac{I_0(1-10^{-A_\lambda})\eta}{\sum_i m_{\mathrm{i}} c_{\mathrm{p,i}}} - \frac{\mathrm{h}A}{\sum_i m_{\mathrm{i}} c_{\mathrm{p,i}}}\Delta T + \frac{Q_0}{\sum_i m_{\mathrm{i}} c_{\mathrm{p,i}}} \tag{3- 18}$$

Defining $B = \sum_i hA/m_{\mathrm{i}}\, c_{\mathrm{p,i}}$ as the constant rate of heat dissipation from the sample to the environment and setting the boundary condition $T(t{=}0) = T_{\text{max}}$ leads to the change of temperature $T(t)$ after the light source is turned off ($Q_{\text{plasmonic}}{+}Q_0 = 0$):[49]

$$T(t) = T_{\text{amb}} + (T_{\text{max}} - T_{\text{amb}})e^{-Bt} \tag{3- 19}$$

This equation represents the cooling curve of the heated AuNR dispersion and allows us to determine B by fitting the curve with the known maximum temperature T_{max} when the laser is turned off, and the ambient temperature T_{amb}.

The heat transfer coefficient h can then be calculated as $B = \sum_i hA/m_i\, c_{p,i}$ using known surface area A of the nanocomposite hydrogel and the thermal mass $\sum_i m_i\, c_{p,i}$. At steady state, where Q_{out} equals to $Q_{plasmonic}$ and Q_0, the temperature increment will remain constant. Thus, equation (3- 18) can be rearranged to yield the PCE η by setting $Q_{plasmonic}+Q_0-Q_{out} = 0$, resulting in the equation[35]

$$\eta = \frac{hA(T_{max} - T_{amb}) - Q_0}{I_0(1 - 10^{-A_\lambda})} \tag{3- 20}$$

The heating profile of the AuNR dispersion when the laser is switched on is readily obtained by solving equation (3- 18) for $T(t)$ using $T(t=0) = T_{amb}$[49]:

$$T(t) = T_{amb}\frac{I_0(1 - 10^{-A_\lambda})\eta + Q_0}{\sum_i m_i c_{p,i}}(1 - e^{-Bt}) \tag{3- 21}$$

The system rate constant B depends on the experimental setup, while η is an intrinsic property of nanoparticles that depends on their shape and size[47, 64, 65]. The contribution of the scattering to the extinction increases with increasing nanoparticle sizes according to Mie theory. Hence, η decreases for larger nanoparticles with the same shape and composition.[47, 49]

It is also worth mentioning that the PCE is influenced by the type of irradiating laser. Continuous wave (CW) lasers induce less heating of nanoparticles because the nanoparticles have sufficient time to relax back to their initial state, dissipating energy as heat into the surrounding medium. On the other hand, using a modulated laser with pulse durations shorter than the relaxation time of the nanoparticles can enhance the PCE. This is because the phonon-phonon relaxation is inhibited during the pulse duration, allowing the nanoparticles to accumulate more thermal energy, which increases the overall heating. In this case, the energy remains in the system rather than being dissipated through relaxation processes, leading to a more significant temperature rise. Roper et al. increased PCE from 3.4% to 9.9% of colloidal gold nanospheres by modulating the incident continuous wave irradiation.

3.3.3.1 Roper´s method to determine the photothermal conversion efficiency

Roper et al[35] introduced a widely used approach for calculating the PCE η, which is followed in this section.[49, 62] In their publication, Roper et al. determined the PCE of gold nanoparticle suspensions by using incident resonant light to heat the nanoparticles, applying an energy

balance to calculate the microscale heat transfer time constant τ_s (which is the reciprocal value of *B* mentioned above) from the transient temperature profile. To facilitate this calculation, a dimensionless driving force temperature θ_T is introduced:[35]

$$\sigma_T = \frac{T_{amb} - T(t)}{T_{amb} - T_{max}} \tag{3- 22}$$

Equation (3- 17) can be solved for the $\theta_T(t)$ transient cooling profile by using the initial condition $\theta_T(t=0) = 1$ to give[35]

$$\sigma_T = e^{-\frac{t}{\tau_s}} \tag{3- 23}$$

The parameter τ_s is obtained experimentally by analyzing the cooling curve. Roper et al. determined τ_s by plotting $\ln(\theta_T)$ vs time *t*, which linearizes the equation (3- 23) (Figure 3- 4 A and B). The slope of this plot corresponds to $1/\tau_s$, allowing the heat transfer coefficient to be calculated. Substituting *h* into equation (3- 20), enables the determination of PCE.

Roper et al. used this method to measure a PCE of 3.4% for gold nanoparticles in water irradiated at a laser wavelength of λ = 514 nm. The temperature changes were measured in a vacuum chamber evacuated < 1 torr with a thermocouple (TC).

Jiang et al. used the same method but measured at ambient conditions.[49] They determined *B* by fitting equation (3- 19). The PCE η was determined by plotting the temperature increase as a function of laser power by rewriting equation (3- 20) as

$$\Delta T = \frac{I_0(1 - 10^{-A_\lambda})\eta}{\sum_i m_i c_{p,i}} \tag{3- 24}$$

The slope of this curve as a function of varying laser intensities corresponds to η (see Figure 3- 4 C). In this publication, the baseline energy input of the heated system without nanorods Q_0 was not considered.

Almada et al.[62] calculated the PCE η of AuNRs stabilized with different ligands in water using equation (3- 21) to determine τ_s and η from fitting the heating profile (Figure 3- 4 D) and considering $\Delta T(t) \equiv T(t) - T_{amb}$:

$$\Delta T(t) = \left[\frac{I_0(1 - 10^{-A_\lambda})\eta + Q_0}{\sum_i m_i c_{p,i}}\right]\left(1 - e^{-\frac{t}{\tau_s}}\right) \tag{3- 25}$$

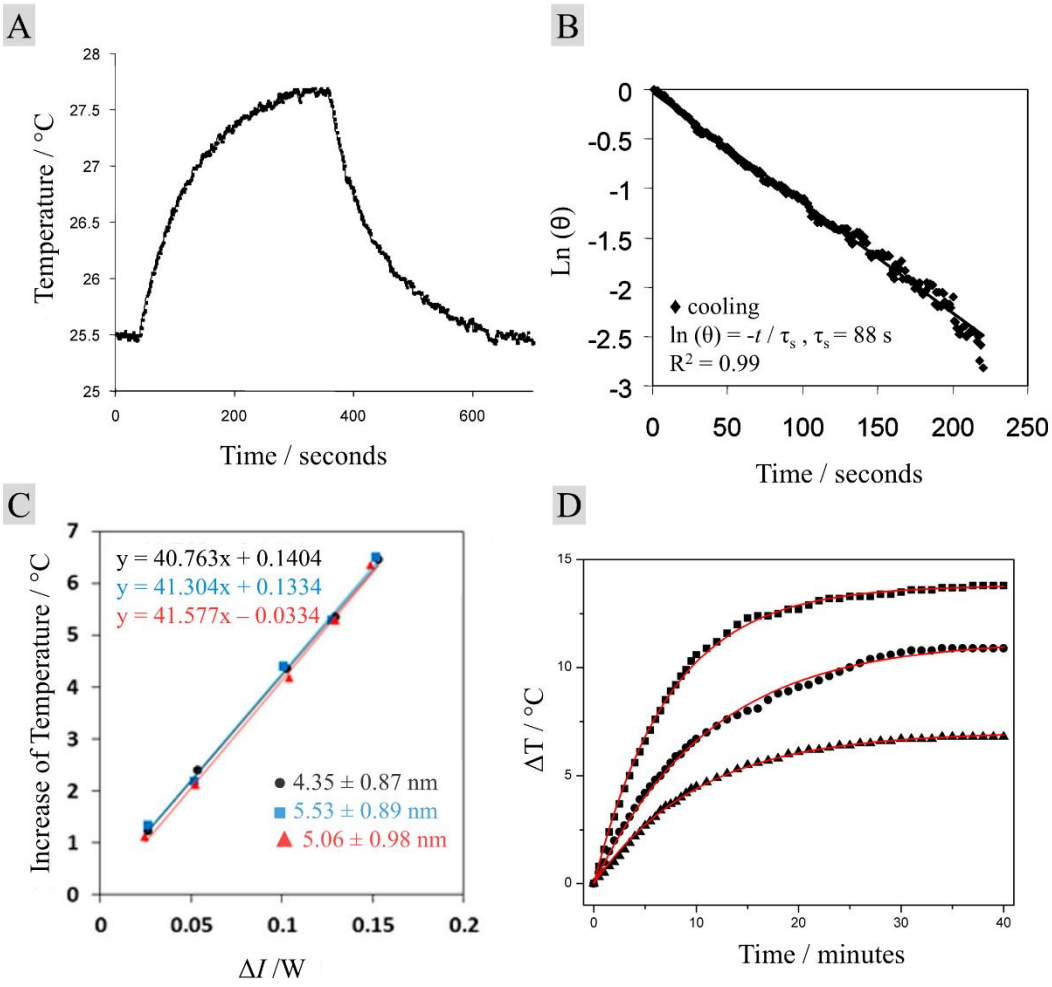

Figure 3- 4: Temperature profiles and analysis methods for determining the PCE of plasmonic nanoparticles. A) Temperature profile of plasmonically stimulated nanoparticles dispersed in water. The temperature increased from ambient to a maximal steady state during CW laser irradiation. After laser irradiation, the sample cooled to ambient temperature.[35] B) Linearization of the cooling profile from A) using equation (3- 22) and (3- 23) in function of time. The linear fit allows to determine the system time constant τ_s with equation (3- 23).[35] Copyright © 2007 American Chemical Society. C) Temperature increase of thermoplasmonic gold nanoparticles as a function of laser power intensity. The PCE was determined by fitting equation (3- 24).[49] Reprinted (adapted) with permission from J. Phys. Chem. C 2013, 117, 51, 27073–27080. Copyright © 2013 American Chemical Society. D) Heating profile of AuNRs in water. The red line correspond the data fit with equation (3- 25). Reprinted from [62] Copyright (2017), with permission from Elsevier.

Table 3- 1 summarizes the PCE of nanoparticles from selected publications which used CW laser and Roper´s method. It highlights the nanoparticle type, shape, and dispersing matrix. Ligands do not significantly affect the PCE if they are transparent to the excitation wavelength and thin enough to prevent scattering of the incident light.[62] For example, M.Almada et al. calculated the PCE of AuNR with three different ligands (chitosan, alginate and poly(vinylalcohol)) and concluded that the PCE of these three AuNRs do not change significantly.[62]

Table 3- 1: Determined PCE of colloidal nanoparticles from selected publications that used Roper´s method. Diameters and lengths are denoted by *d* and *L*, respectively. The dimensions represent the nanoparticle size without the ligands. λ_{ex} is the irradiation wavelength.

Nanoparticle	Dimensions	Dispersing matrix	λ_{ex} / nm	PCE / %	Ref.
Gold nanosphere	*d* = 20 nm	Water	514	3	[35]
	d = 5 nm	Water	532	80	[49]
	d = 20 nm	Water	532	74	[49]
	d = 50 nm	Water	532	65	[49]
Gold nanorod	*d* = 15 nm, *L* = 57 nm	Water	808	47-51	[62]
	d = 7 nm, *L* = 26 nm	Water	808	50	[66]
	d =13 nm, *L* = 44 nm	Water	815	55	[67]
	d = 10 nm, *L* = 41 nm	Hydrogel	808	47	[68]
	d = 14 nm, *L* = 57 nm	Water	795	70	[9]
Hollow Gold nanoshell	*d* = 38 nm	Hydrogel	808	12	[69]
Gold nanostar	Not given	Water	785	65-80	[9]
Copper nanoparticle	*d* = 88 nm	Hydrogel	660	22	[60]
Copper nanowire	*d* = 46 nm, *L* = 40 µm	Water	808	13	[70]
Graphene oxide nanocomplex	*d* = 100 nm–200 nm	Water	808	31	[71]
Ag_2S-Glutathione QD	*d* = 3 nm	Water	795	80	[72]
Ag_2S nanodot	d = 4-10 nm	Water	785	34-35	[73]

Publications that used Roper's method to measure PCE often report varying values for nanoparticles of the same material and dimensions. Sennaroglu et al. attributed these

discrepancies to factors such as heating of the unfilled portion of the cuvette, non-uniform laser beam intensity, evaporation of the dispersion media during heating, and different thermocouple placements within the cuvette.[74] Additionally, several studies[62] report plasmonically induced temperature increases exceeding $\Delta T = 11°C$, whereas Roper et al.[35] limited their analysis to $\Delta T \leq 11°C$ (see section 3.3.2). This is important because Roper's method assumes a linearized heat transfer model (see equation (3- 15)), which neglects radiative heat loss Q_{rad} in Q_{out}. At $\Delta T > 11°C$, however, Q_{rad} becomes a significant contribution, potentially affecting the accuracy of PCE calculations in studies that assume linear heat dissipation.

The PCE is a key factor in evaluating the biological applicability of thermoplasmonic nanoparticles (chapter 3.4). High PCEs minimize the risk of thermal damage to healthy tissue. Low PCEs would require excessive power levels to achieve the desired temperature increase.[74] A key goal of this work was to determine whether nanocomposites could achieve sufficient PCE for effective photothermal applications.

While section 3.3.3 discussed the theoretical framework for determining PCE using Roper's method, the next section 3.3.4 focuses on experimental techniques for measuring plasmonically induced temperature changes. Various methods, including infrared thermography, thermocouples, and luminescence-based nanothermometry, are introduced to assess temperature distributions in nanoparticle suspensions and nanocomposite hydrogels.

3.3.4 Temperature measurements in thermoplasmonic gold nanoparticles

Cells and most bacteria can live and grow only in certain temperature ranges.[75] Differences of just few degrees can lead to unwanted metabolic changes, thermal damage of surrounding tissue or post-treatment inflammatory responses in biomedical applications, e.g during photothermal therapy (see chapter 3.4).[75] Therefore, precise temperature monitoring and control are essential, particularly in thermoplasmonic stimulated engineered living materials, where thermal regulation governs bacterial activity and overall functionality. The thermoplasmonic properties can be deduced by temperature measurements. Infrared cameras[76, 77], thermocouples (TC)[49], fiber optic sensors,[78] ultrasound imaging[79], magnetic resonance imaging[80], and optical probes[81, 82] have been reported in literature for the analysis of thermoplasmonic AuNRs at different spatial resolution. This chapter covers all thermometry techniques used in this thesis, first macroscale thermometry such as infrared camera and thermocouples (TC), then nanoscale thermometry by optical probes.

3.3.4.1 Macroscale thermometry

Infrared cameras and thermocouples (TC) are commonly used to measure macroscopic temperatures with typical spatial resolutions of approximately 0.1–1 mm for infrared cameras and localized point measurements for thermocouples. Thermocouples vary in size, with fine-wire probes (50–200 µm) enabling precise small-scale measurements, while industrial versions range from 1–3 mm.[83] Wire lengths extend from centimeters to meters, depending on the application. These tools are ideal for monitoring heating and cooling profiles during collective plasmonic heating of nanoparticles (Figure 3- 5 A) under CW laser irradiation over several hundred seconds.[83] Infrared cameras provide non-invasive, real-time thermal mapping across large areas, while thermocouples offer precise, localized temperature readings. Together, they enable accurate tracking of temperature changes, essential for deriving the PCE as described in section 3.3.3.[3, 35, 47, 74]

TCs are based on the Seebeck effect, where temperature differences of two different metals or semiconductors (reference and measurement junction) generate electrical voltage, which is converted to the output temperature. TCs measure contact temperature but they are invasive and limited in spatial resolution in the range of 100 µm.[81, 84] In thermoplasmonic treatments involving AuNRs in both water and hydrogels, TCs are mainly used *in situ*[85] and *in vitro*.[85, 86] Jin et al. evaluated the photothermal properties of AuNRs in hydrogel with a TC by *in situ* recording the temperature changes triggered by CW laser (808 nm) irradiation (Figure 3- 5 B).[85] With increasing AuNR concentration between 0 µg/mL – 100 µg/mL in the hydrogel, the temperature change ΔT increases between 10 °C – 50 °C under laser power density of 1 W/cm^2 (Figure 3- 5 B top). Concentrations of 10 µg/mL of AuNRs in hydrogel resulted in ΔT between 16 °C – 27 °C under irradiation of laser power densities of 0.5 W/cm^2 – 1.5 W/cm^2 (Figure 3- 5 B bottom).

Infrared (IR) cameras capture IR radiation emitted by objects and convert it to a thermal image by exploiting Planck´s law. They can non-invasively monitor spatiotemporal temperature distributions at resolutions down to 10 µm[84], but infrared cameras are restricted on surface temperature. Infrared cameras have been used for monitoring thermoplasmonic processes involving AuNRs both in water and in hydrogels *in situ*[77, 87] (Figure 3- 5 C), *in vitro*[76, 88] and *in vivo*[76, 88-91] applications. *In vivo* measurements were mainly performed for photothermal therapy (PTT). Lee et al. measured the photothermal activation of AuNR composite hydrogels on tumor sites *in vitro* and *in vivo* by an infrared camera (Figure 3- 5 D and E).[76] The tumor temperature change profile measured by infrared camera helped them to

find the appropriate concentration of AuNRs and laser power density to heat at mild hyperthermia temperatures between 41 – 42 °C.

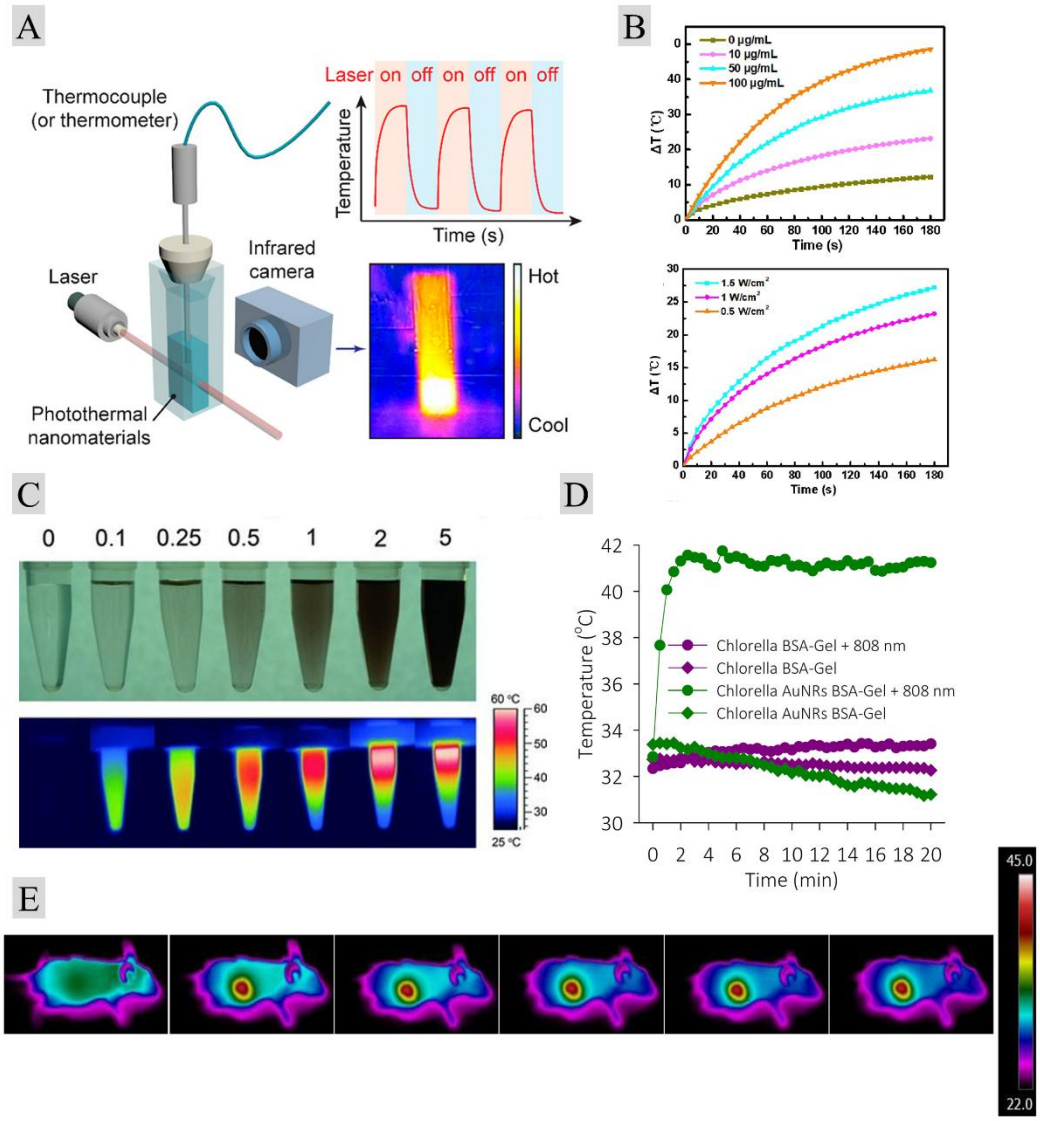

Figure 3- 5: Macroscopic temperature measurements on plasmonic heating of AuNRs in hydrogel and in water reveal temperature distributions and heating profiles. A) Schematic diagram of photothermal characterization of collective plasmonic heating of nanoparticles. Heating and cooling are controlled by switching the laser on and off and are monitored by a thermocouple or infrared camera. Infrared camera provides the surface temperature distribution.[83] Copyright © 2023 The Authors. Published by American Chemical Society. This publication is licensed under CC-BY 4.0. B) *In situ* temperature monitoring of a plasmonically stimulated AuNR composite hydrogel with a thermocouple. Typical heating curves at different concentrations (top) and at different laser power densities (bottom). Reprinted from [85], Copyright (2021), with permission from Elsevier. C) *In situ* temperature measurement by infrared camera of AuNRs in water with increasing concentration from left to right at same laser power density.[46]Copyright © 2011 WILEY-VCH Verlag GmbH & Co. KGaA, Weinheim. D) Heating curves obtained by *in vitro* photothermal imaging of AuNRs composite hydrogels in tumor cells with control measurements. E) Thermal images of *in vivo* photothermal stimulation of AuNRs in hydrogel injected on tumor site in a mouse. D) + E): Reprinted from [76]Copyright (2019), with permission from Elsevier.

3.3.4.2 Optical Nanothermometry

Luminescence nanothermometry provides the possibility of non-contact temperature measurement with outstanding spatial (< 1 µm) and good thermal resolution (0.5 °C).[78] It is based on the use of luminescent nanoparticles with temperature dependent intensity, peak

position, polarization anisotropy, fluorescence lifetime or band shape.[78, 92] Typically, the ratio of emission intensities from two thermally coupled energy levels, known as the fluorescence intensity ratio (FIR), is used to determine the temperature. This ratiometric approach provides high sensitivity and accuracy by minimizing the effects of external factors such as excitation power fluctuations or particle concentration.[78, 92] Rare earth based upconverting and downconverting particles[93], metallic nanoparticles[94, 95], and semiconductor quantum dots[96] have been used for thermometry.

A strategy for local temperature sensing involves UCNPs and thermoplasmonic-activated AuNRs at excitation wavelengths of 808 nm or 980 nm, where either the UCNPs or AuNRs are coated with SiO_2. The SiO_2 shell enables conjugation, provides a homogeneous dielectric spacer, and improves control over the distance between the UCNPs and AuNRs, ensuring accurate energy transfer and temperature measurements.[97-101] The use of UCNPs to monitor the local temperature is advantageous compared to traditional organic dyes due to their photo-stability, biological compatibility[102], resistance to higher temperatures and no photobleaching.[103, 104]

A crucial feature of UCNPs is their ability to undergo multiphoton excitation, leading to anti-Stokes emission.[105, 106] $BaYF_5$ and $NaYF_4$, with low phonon energies at approximately 350 cm^{-1} and 500 cm^{-1}, respectively, are effective host lattices due to their ability to accommodate high concentrations of lanthanide dopants, which enhance the luminescent properties for temperature sensing.[97, 107, 108] The low phonon energy is essential to reduce non-radiative relaxation from excited states increasing the quantum yield for emission. Nd^{3+} and Y^{3+} are dopants, called sensitizers, that activate the excitation in the NIR range of 808 nm and 980 nm.[99] The sensitizers non-radiatively transfer the absorbed excitation light energy to the activators. Activators such as Er^{3+} and Tm^{3+} facilitating emission of upconverted photons.[97, 99, 108] Er^{3+} has four characteristic emission bands centered at around 410 nm (blue, $^2H_{9/2} \rightarrow {}^4I_{15/2}$), 527 nm (green, $^2H_{11/2} \rightarrow {}^4I_{15/2}$), 545 nm (green, $^4S_{3/2} \rightarrow {}^4I_{15/2}$), and 660 nm (red, $^4F_{9/2} \rightarrow {}^4I_{15/2}$).[99] The emission bands of Er^{3+} are strongly sensitive to temperature. Usually, the fluorescence intensity ratios between the bands are used to convert it to temperature after calibration of these. The thermally coupled green bands show strong temperature dependence. This is due to the equilibrium in the population of the excited states, which follows a Boltzmann-type distribution, where the relative populations of the states vary with temperature.[109] UCNP nanothermometry can be used as biosensors[81], to monitor intracellular temperature changes[110], to monitor local temperatures of tissues[111] and to

measure temperature in living cells.[92] This approach provides valuable insights into temperature dynamics in biological systems.

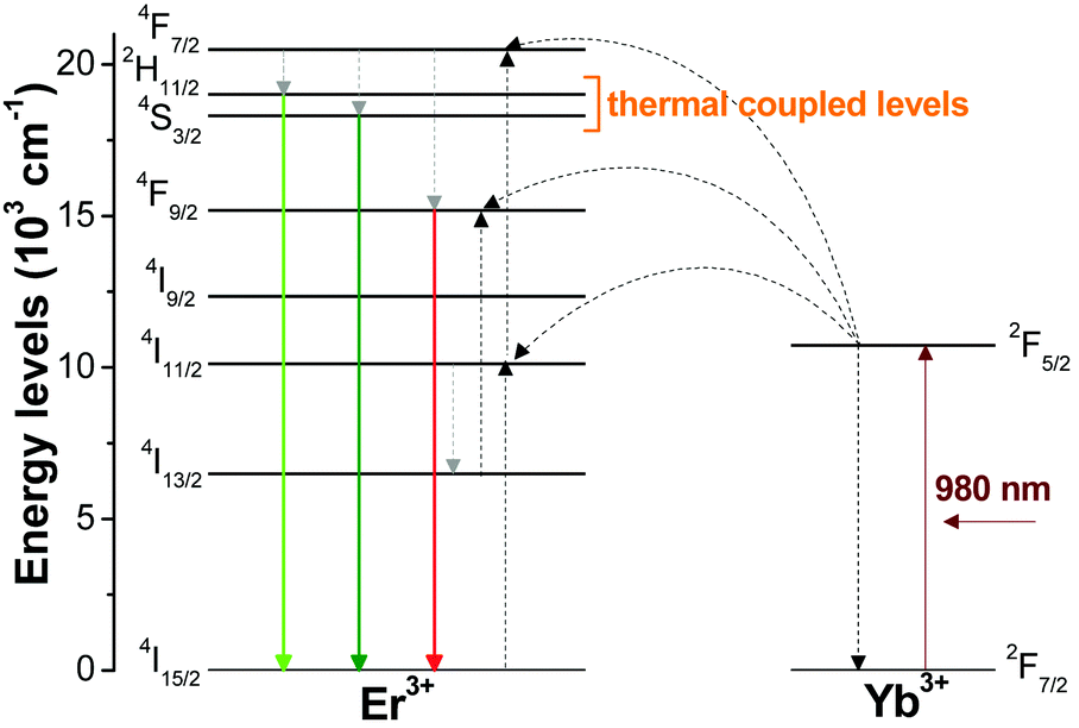

Figure 3- 6: Schematic energy level diagram of Yb^{3+} and Er^{3+} and the mechanism of upconversion emissions under 980 nm laser excitation.[109] Reproduced from Ref. [109] with permission from the Royal Society of Chemistry.

Building upon this, several reports have explored UCNP-AuNR conjugates, which combine the benefits of UCNP-based temperature sensing with the thermoplasmonic properties of AuNRs. These conjugates have been applied in local temperature sensing,[108] bioimaging,[108, 112, 113], bio sensors[114], PTT[108, 115] and PDT for cancer treatment.[101] Studies employing the thermoplasmonic effects of AuNRs for biomedical applications span *in situ*[75], *in vitro*[101] and *in vivo* contexts.[101] These findings suggest a high potential for UCNP-AuNP conjugates in ELMs, offering both safety for the living components and versatility for biomedical applications.

3.4 Thermoplasmonic gold nanoparticles in biomedical application

The thermoplasmonic properties of metallic nanoparticles make them suitable as nano-heaters for various biomedical purposes, including diagnosis[116], therapies and surgery.[117, 118] Various nanoparticle materials, including gold[9], silver[119], and platinum[120] have been explored for these applications. Among these, gold is the most widely used in biomedical applications due to its biocompatibility, physiochemical properties, ease of surface modification and optical properties (see chapters 3.1 and 3.2).[3, 121]. Thermoplasmonic gold nanoshells[122], gold nanospheres[32], gold nanocages[123], gold nanostars[124] and gold nanorods (AuNRs)[125] have been used as nanoheaters to achieve a reduction of tumor sizes in living animals.[88, 126-128] Beyond biomedical applications, gold nanoparticles are also used in photoacoustic imaging[129] and surface enhanced resonance spectroscopy.[130]

The localized surface plasmon resonance (LSPR) signal of rod-shaped AuNRs can be tuned to fit in the wavelength range of the biological transparency window of tissues to prevent light extinction by intrinsic chromophores in tissues and minimizing damage to healthy cells during photothermal applications (see section 3.4.1).[131] Due to their anisotropic shape, AuNRs exhibit a tunable LSPR in the NIR range, making them particularly effective for deep tissue applications. Their high photothermal conversion efficiency has been specifically leveraged in targeted therapies such as photothermal therapy (PTT)[10, 132, 133] (section 3.4.2), photothermal drug delivery (section 3.4.3), and wound healing (section 3.4.4), where controlled heating enhances therapeutic outcomes.

3.4.1 Extinction wavelength and intensity in biomedical thermoplasmonic applications

The absorption range of AuNRs can be tuned with changing aspect ratio (AR) (Figure 3- 7 A and B) to the biological transparency window (Figure 3- 7 C). For potential biomedical application of external triggering, it is important to know how light interacts with the tissue on host bodies. Light is attenuated as it passes through tissues mainly through absorption and scattering.[18] Scattering is wavelength dependent and becomes more prominent at lower wavelengths.[18] The absorption of light in tissues is determined by its content of melanin, hemoglobin and its oxygenation form, fat and water, and, to lesser extent, the yellow pigments bilirubin and β-carotene (Figure 3- 7 C).[3, 18, 134] NIR light in the range of 700 – 900 nm (referred as first biological window; NIR-I) is minimally absorbed by skin and tissue (Figure 3- 7 C) and can penetrate up to 10 cm into tissue (Figure 3- 7 D)[50, 70]. Other publications state that the maximum penetration depth L_e, defined as the depth at which irradiance declines

to 1/*e* (37%) of its initial value, ranges from approximately 3.5 to 5 mm in the NIR-I range.[18, 135] The difference (≈ magnitude 10^1 mm) in penetration depths are due to different definitions of maximal penetration depth, different tissue types, and different light sources. For example, NIR-I light from a microwatt laser has been shown to penetrate at least 10 cm through breast tissue, and 4 cm through brain/skull tissue before significant attenuation occurs.[136, 137] Higher power levels have been reported to increase the detectable penetration depth to 7 cm in muscle and neonatal skull/brain tissues, where the depth refers to the distance at which the light can still be detected.[136]

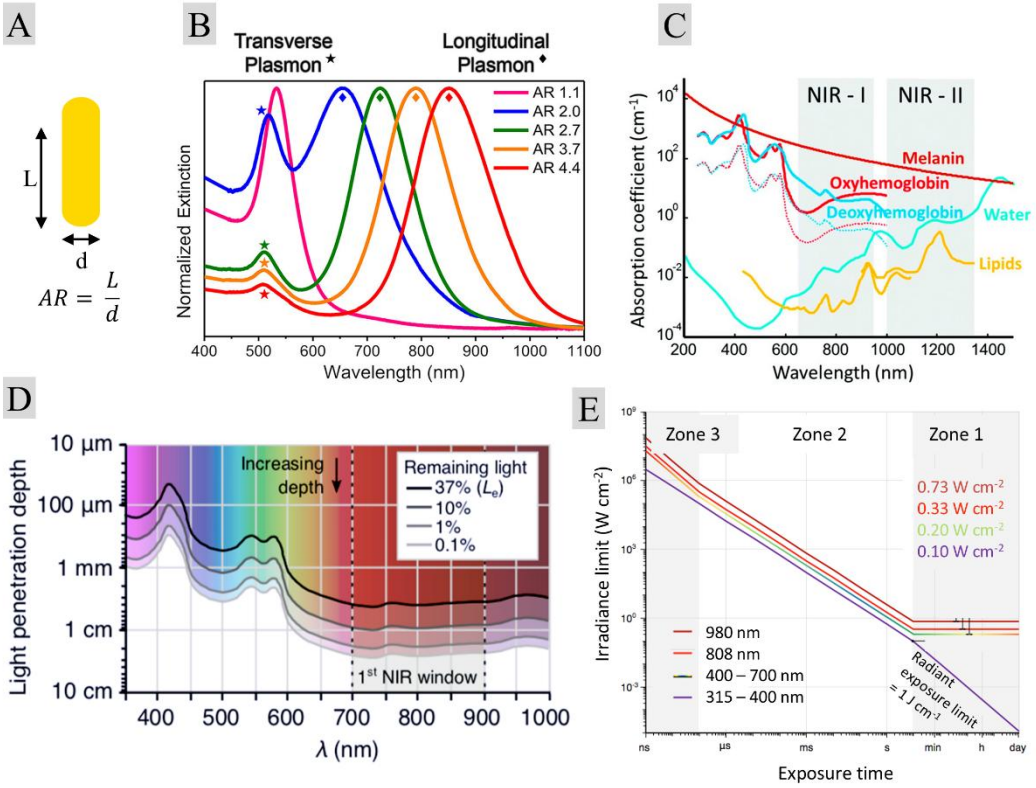

Figure 3- 7: Overview of the optical properties and biological relevance of gold nanorods in the context of biomedical applications. A) Aspect ratio (AR) of gold nanorods with length *L* and diameter *d*. B) Extinction spectrum of gold nanorods with increasing AR leading to a red shift of the LSPR. Reprinted (adapted) with permission from [8]. Copyright © 2016 American Chemical Society. Adapted with permission from [138]. Copyright 2014 American Chemical Society. C) Biological transparency windows NIR-I and NIR-II. Reproduced from Ref.[139] with permission from the Royal Society of Chemistry. D) Penetration depth L_e defines the depth at which the irradiance declines to 1/e ≈ 37% of its initial value. Lines are representing the depth at which light reaches 37 %, 10 %, 1 % and 0.1 % of incident light intensity.[18] © 2021 The Authors. Advanced Functional Materials published by Wiley-VCH GmbH. E) Maximum permissible exposure (MPE) for skin as a function of exposure time. Colored lines show the irradiance limits for human skin at wavelengths of 315 – 400 nm, 400 – 700 nm, 808 nm and 980 nm. [18, 140] © 2021 The Authors. Advanced Functional Materials published by Wiley-VCH GmbH.

The second and third biological window (1000 – 1800 nm) is favorable due to the lower scattering of tissues in that wavelength ranges.[135] The penetration depth of NIR light beyond 1000 nm is greater: For example, light at 808 nm diminishes over increasing penetration depth with complete signal loss at 5 mm in a phantom tissue, whereas light at 1525 nm could be detected through 10 mm of phantom tissue.[141]

Besides the penetration depth of wavelengths, the maximum permissible exposure (MPE) for light irradiation on tissues plays a critical role in biomedical applications. While increasing intensity may help overcome penetration limitations, it is constrained by the MPE, which defines the threshold at which photodamage, or heat-induced damage occurs. Thus, the light power must be balanced to prevent tissue damage while achieving adequate penetration.

The MPE of light on tissue is determined by the threshold at which photodamage or heat-induced damage occurs due to photon absorption. The MPE is dependent on both the exposure duration and the irradiance level, with the limits increasing as the wavelength increases. UV light generally has lower MPE values compared to visible (VIS) and near-infrared (NIR) wavelengths, as it is more likely to cause damage at lower exposure times and irradiances (Figure 3- 7 E).[18]

In this work, I used a CW laser light source at irradiance wavelength of 808 nm in NIR-I range. CW lasers are widely available and more cost-effective compared to pulsed lasers or lasers emitting beyond 1000 nm. The MPE for CW lasers at 808 nm is 0.33 W/cm^2 for exposures exceeding 1 min (Figure 3- 7 E) to skin tissue.[140] The use of 808 nm for the plasmonic heating of AuNRs during *in vivo* applications is well established.[76, 91, 142, 143]

3.4.2 Photothermal therapy

Photothermal therapy (PTT) using gold nanoparticles for cancer treatment has been widely studied and reported in the literature.[76, 142-144] Cancer was the second most common cause of premature death in the United States after heart diseases during 2015 – 2019 according to the reports of national center for health statistics.[144, 145] Nanoparticles are investigated to overcome the drawbacks of conventional cancer treatments, such as radiotherapy and chemotherapy, which include resistance of cancer cells and damage to healthy tissues.[144, 146] PTT is a non-invasive method using laser irradiation combined with plasmonic gold nanoparticles with high PCE for generating hyperthermia to kill cancer cells with high efficacy.[143, 147-149] Specially the use of AuNRs in PTT for cancer treatment are well reported[143, 149-151] and successfully employed in killing various types of cancer cells, such as prostate[152], breast[153] and gastric.[154] Figure 3- 8 A illustrates an example of the induction of PTT with thermoplasmonic AuNRs inside tumor cells. The surface of AuNRs can be modified with tumor-targeting units on PTT therapeutics allowing them to bioaccumulate in tumor cells and reduce damage to normal cells (see Figure 3- 8 A).[11, 132, 147, 149] An example for effective delivery systems to cancer cells with high specificity and affinity are

aptamers, such as single-stranded DNA or RNA sequences, that have been conjugated with AuNRs.[155, 156]

Zhang et al. reported that AuNR mediated PTT induced cell death in melanoma B16-BL6 cells.[13] They synthesized AuNRs with targeting adaptor folic acid (FA) to obtain AuNR-FA which showed a transfection rate of 96 % of melanoma cells (Figure 3- 8 A). They also showed the temperature dependent patterns of killing tumors in PTT; Photothermal heating of the AuNR-FA at 43 °C induced cell death due to apoptosis, necroptosis and necrosis, with respective percentual amounts of 10.2 %, 18.3 %, and 17.6 %. At 49 °C, necrosis was dominant with 49 %. At moderate temperatures of PTT treatment at 46 °C, necroptosis proportion was 35 % (Figure 3- 8 B). The authors used a NIR laser (808 nm, 15 min) with different laser powers at 0.9 W, 1.28 W and 1.59 W to reach the mentioned temperatures. Control of temperature is crucial since it is more favorable in PTT to induce apoptosis than necrosis.[157] Necrosis, a process where plasma membranes are destroyed and cytoplasmic components leak out, leads to inflammation and can induce metastasis and cancer growth.[158] Additionally, excessive heat exposure may damage surrounding healthy cells. On the other hand, apoptosis occurs through programmed cell death and does not cause inflammation at milder temperature ranges below 50 °C.[159] A potential drawback of PTT mediated apoptosis is the expression of heat shock promoters (HSPs) by the cancer cells[160, 161], which are known to help these cells resist PTT-induced apoptosis.[80, 162] Ali et al. found a new strategy targeting cancer cell apoptosis and avoiding necrosis by conjugating AuNRs with Quercetin to inhibit HSPs produced by cancer cells.[157]

In another study, Loo et al. reported simultaneous cancer imaging and PTT of breast cancer with gold-silica nanoshells conjugated with anti-Her2 antibodies as target molecule.[126]

Huang et al. conjugated AuNRs with monoclonal antibodies for targeting cancer cell lines. Antibody conjugated AuNRs bound preferentially to malignant cells and were irradiated by low power of 800 nm CW laser at 80 mW causing cell death.[149]

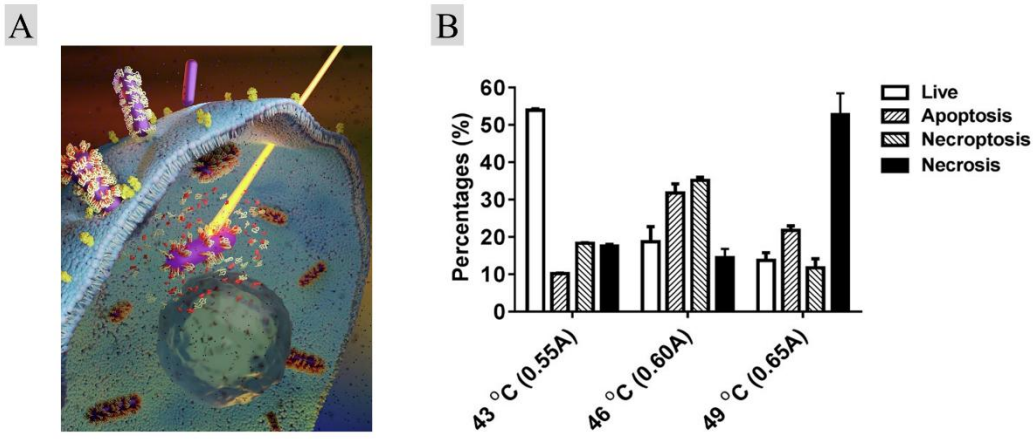

Figure 3- 8: A) Illustration of the induction of PTT inside the tumor cell. Reprinted from [144]. Copyright (2023), with permission from Elsevier B) Percentage of live, apoptotic, necroptotic, and necrotic cells at different temperature treatments after PTT with respective laser dogage. Reproduced from [13]. Licensed under CC BY 4.0.

In addition to thermoplasmonic approaches using NIR light, alternative methods for inducing hyperthermia in cancer treatment have been reported, including microwave and radiofrequency (without the use of nanoparticles)[163, 164], magnetic heating with magnetite nanoparticles[165] and ultrasound sources (without nanoparticles).[166] While these methods can achieve localized heating, thermoplasmonic approaches offer precise spatial control and tunable optical properties, making them particularly advantageous for targeted treatments.[167]

3.4.2.1 Local temperature rise in photothermal therapy

Huang et al. introduced a numerical method to predict the required laser intensity and optical density of gold nanoparticles required to reach a specific temperature for optimal hyperthermia treatment.[168] Fourier´s equation is adapted to describe the heat transfer of gold nanoparticles in the cellular environment:[168]

$$mc_{\mathrm{p}}\frac{\partial T(r,t)}{\partial t}=\frac{k}{r^2}\frac{\partial}{\partial r}\left(r^2\frac{\partial T(r,t)}{\partial r}\right)+Q_{\mathrm{plasmonic}} \tag{3-26}$$

T is the temperature (K), m is the cell mass (kg), c_{p} is the specific heat capacity of the cells (J/kg·K), k is the thermal conductivity of the cells and of their medium (W/m·K), t is the time (s), $Q_{\mathrm{plasmonic}}$ is the heat-source term (W) due to the nanoparticles heated by the continuous wave laser excitation and r is the radial distance (m) from the heated nanoparticles. The solution of (3- 26) is[168]

$$mc\frac{T_{\mathrm{i+2j}}}{\Delta t}=k\left(\frac{T_{\mathrm{ij+1}}+2T_{\mathrm{ij}}+T_{\mathrm{ij-1}}}{(\Delta r)^2}\right)+Q_{\mathrm{plasmonic}} \tag{3-27}$$

where Δt and Δr are the characteristic time and distance steps, and i and j represent the discrete spatial coordinates within the numerical model. The incident laser power required to reach cancer killing temperatures depends on the loading with photoabsorbers as shown in Figure 3-9. PTT mediated killing of cancer cells with gold nanoaparticles required about 19 W/cm^2[168], whereas with indocyanine dye required 104 W/cm^2.[169]

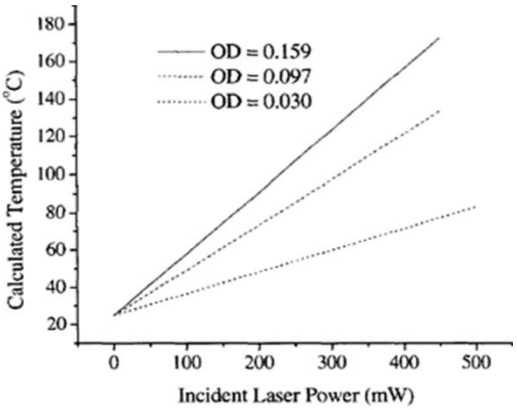

Figure 3- 9: Calculated temperature within the cells in the vicinity of gold nanoparticles in function of laser power with different optical densities of gold nanoparticles. Reproduced from [168]. Reproduced with permission from John Wiley & Sons, Inc. © The American Society of Photobiology.

3.4.3 Photothermal drug delivery

AuNRs are used as active carriers to deliver therapeutical agents. Their high surface area facilitates drug loading while also protecting the drugs from enzymatic degradation and premature clearance, thereby enhancing stability and therapeutic targeting to cancer cells.[133] Passive targeting relies on the enhanced high enhanced permeability and retention (EPR) of AuNRs in tumor tissues compared to normal tissues.[170] Active targeting uses moieties such as antibodies that are attached on the surface of AuNRs.[170] The PCE of AuNRs has been exploited to actively release drugs.[133] Thermoplasmonic-triggered drug release has been demonstrated for a variety of therapeutics, including nucleic acids in the form of DNA, plasmid DNA and RNA as well as small-molecule drugs such as doxorubicin and paclitaxel.[171-178].

Wijaya et al. loaded DNA molecules on the AuNR´s surface via thiol conjugation.[172] The release was induced by melting the AuNRs by pulsed NIR irradiation with release efficiencies of about 50–80% externally controllable by changing laser power densities.[172] The high temperatures at AuNRs surface generated by pulsed irradiation can degrade loaded drugs.[179] The use of CW lasers enables milder conditions, for example for AuNRs with thermo-sensitive shells of poly (N-isopropylacrylamide) hydrogels, in which drug molecules can be dispersed. Thermoplasmonic treatment induces a phase transition that results in drug release.[180] Zhong et al. encapsulated doxorubicin (DOX) within AuNRs coated with lipoylated poly(ethylene

glycol)-b-poly(ε-caprolactone) micelles.[181] At a CW laser power density of 0.2 W/cm^2, DOX was released due to the photothermal induced phase transition in the micellar shell, triggering the controlled release of DOX. The released DOX effectively inhibited the proliferation of breast cancer cells *in vitro*.[181]

Thermoplasmonic heating of AuNRs has been combined with chemotherapy to increase the efficacy of drug molecules due to the improved cell membrane permeability at higher temperatures.[133, 182] For example, Hauck et al. coupled cis-platin drugs with the generated hyperthermia of AuNRs and found an efficiency increase of 78%.[182]

3.4.4 Thermoplasmonic gold nanoparticles for wound healing

Wound healing is a regenerative process which needs coordinated regulation of various cell regeneration machineries.[183, 184] The major steps in wound healing are hemostasis, inflammation, tissue formation (proliferation) and tissue remodeling under the release of biological and cellular factors.[185-188] Recent advancements in thermoplasmonic gold nanoparticles have enabled external light-driven interventions that support wound healing processes through various mechanisms, including antimicrobial effects and the promotion of cellular regeneration.[189]

He et al. developed antimicrobial gold nanoparticles conjugated with polyhexamethylene biguanide for wound healing under NIR irradiation, leveraging synergistic photothermal and antibacterial effects.[190] The positively charged polymer coating enhanced bacterial adhesion, facilitating antimicrobial action. Upon NIR irradiation (808 nm, 2 W/cm^2, 5 min per treatment session for 7 days), the nanoparticles (9 µg/mL) generated localized heat (~54 °C) via thermoplasmonic effects, effectively disrupting bacterial membranes and inhibiting biofilm formation. *In vivo*, the treatment eradicated *Staphylococcus aureus*, a common wound pathogen, and promoted wound healing by inducing macrophage polarization from the pro-inflammatory M1 to the anti-inflammatory M2 phenotype, thereby enhancing angiogenesis and tissue regeneration.[190]

Xu et al. developed a photothermal therapy-assisted antibacterial system using polydopamine-coated hydroxyapatite with AuNRs to enhance wound healing *in vivo*.[191] The AuNRs catalyzed the generation of hydroxyl radicals from H_2O_2 solution, which was applied directly to the wound area, increasing oxidative damage to bacterial membranes and making them more susceptible to photothermal therapy at about 43 °C. Under NIR irradiation (808 nm, 1 W/cm^2, 10 min per session for 10 days), AuNRs (200 µg/mL) demonstrated effective antibacterial

activity against *E. coli* and *Staphylococcus aureus* compared to hydroxyl radicals or PTT alone. Additionally, this system promoted the expression of tissue repair-related genes such as basic fibroblast growth factor, facilitating granulation tissue formation, collagen synthesis, and overall wound regeneration.[191] Xu et al. functionalized AuNRs with an antimicrobial peptide (C-At5) and evaluated their photothermal and antibacterial effects for wound healing.[192] They treated *Staphylococcus aureus*-infected wounds in mice using AuNR@C-At5 (15 µg/mL AuNRs, 6.75 µg/mL peptide) combined with NIR laser irradiation (808 nm, 1 W/cm², 30 s), which significantly accelerated wound healing, reduced inflammation, and promoted tissue regeneration due to enhanced VEGF secretion of the endothelial cells in wounds *in vivo*.

Gold nanoparticles and AuNRs embedded in scaffolds[189], membrane[193] and hydrogels[194-196] (see section 3.4.7) were used to accelerate wound healing processes. Nanda et al. applied AuNRs incorporated in scaffold on wounds and showed that under NIR irradiation the generated mild temperature induced heat shock proteins expression of adjacent tissues enhancing more effectively cell proliferation compared to conventional wound dressings.[189]

3.4.5 Gold nanoparticles for photothermal induction of gene expression

Light-driven gene expression techniques have been developed using different wavelength ranges from UV, VIS or IR wavelengths to locally heat tissues and induce heat shock responses which triggers the gene expression of genes inserted downstream of heat shock promoters.[160] Heat generation can be made more efficient when bringing nanoparticles into the tissue, which allows the reduction of laser intensities and more efficient heating of deeper tissues *in vivo*. Gene expression by photothermal NIR-irradiation are reported for AuNRs[171, 197] and carbon nanohorns[160] induced by heat shock promoter (HSP)[160, 197] or DNA release[171].

Andersson et al. transfected *ex vivo* HeLa and B16 cancer cells with HSP-enhanced green fluorescent protein (EGFP) plasmid and polyethyleneimine (PEI)-conjugated AuNRs and then transplanted the cells in mice. Irradiation by 800 nm NIR-light from a clinical diode laser (50 W/cm^2–150 W/cm^2) for 6 hours and 24 hours induced the significant photothermal gene expression in the plasmid leading to the transcription of EGFP.[197] EGFP expression indicated the successful activation of gene expression by NIR light. Andersson et al. proposed a method for potential immunotherapy of cancer cells by this proof of concept. They suggest using plasmids to produce immunotherapeutics such as cytokines to activate immune response of healthy cells and to regress tumor growth.

Another interesting strategy for AuNR mediated gene expression was followed by Chen et al.[171] AuNRs were attached on EGFP-DNA genes and transfected into HeLa cells. NIR irradiation by 800 nm pulsed laser (~1 W/cm^2) induced shape transition of AuNRs leading to release of free EGFP-DNA activating the gene expression of GFPs in cells.

3.4.6 Thermoplasmonic waveguides

Waveguides are structures that direct electromagnetic waves, particularly light, along a defined path, using reflection or refraction to confine the wave.[198] They play an essential role in controlling light propagation, ensuring minimal loss and efficient transmission. Waveguides are commonly used in applications like telecommunications, sensors, and biomedical devices.[199]

Optical fibers, a specialized type of waveguide, are widely utilized in biomedical applications for their ability to transmit light with high precision and minimal signal loss. Composed of a core (where light propagates) and either a cladding layer or surrounding medium with a lower refractive index to ensure total internal reflection (TIR), they are essential for medical imaging techniques such as endoscopy, targeted laser delivery systems for therapies, and advanced optical sensing for diagnostics and monitoring.[199-202] While conventional fibers typically use materials such as silica or polymers,[203] hydrogel-based optical fibers have emerged as an innovative alternative, offering flexibility, biocompatibility, and the potential for functionalization.[204] Reported hydrogel-based optical fibers include materials such as PEG,[205] agarose[206], PMMA[207], N-isopropylacrylamide[207] and PluDA.[208]

Thermoplasmonic optical fibers combine the light-guiding efficiency of optical fibers with the heat-generating properties of plasmonic particles. By integrating plasmonic particles in, on or near the optical fibers, these hybrid systems leverage the photothermal effect to generate localized heat under light irradiation, particularly at NIR wavelengths. This localized heating capability has shown significant potential in biomedical applications such as photothermal therapy, neural stimulation, and controlled drug delivery.[209] These systems can provide precise, minimally invasive treatment options, even in deep tissue environments beyond the penetration range of pure NIR light (as discussed in section 3.4.1).[207]

Thermoplasmonic effects with integrated microparticles (1 µm to 1000 µm) were exploited in silica optical fibers for thermophoresis of bacteria to tumor sites for targeted drug delivery.[210, 211] Chen at al. injected Bi_2WO_6-x nanoparticles in tumor site in mice and explored interventional photothermal therapy by delivering NIR laser light (915 nm, 210 mW) through an optical fiber hydrogel.[207]

Gold nanoparticles (AuNPs) have been integrated into optical waveguides for biomedical applications. Hong et al. demonstrated the potential of thermoplasmonic optical fibers by coating AuNRs on the tip of glass/PMMA-based optical fibers for neural stimulation. NIR light illumination locally heated the AuNRs, modulating neural activity by activating temperature-sensitive ion channels or altering the capacitance of neuronal membranes.[209] Similarly, Kang et al. demonstrated the use of AuNR-coated glass optical fibers irradiated by a CW laser at 808 nm for *in vitro* neural activity modulation and simulated spatiotemporal temperature changes for potential *in vivo* applications.[212] They found a temperature increase at the optical fiber core tip *in vitro*, ranging from 5.38 °C to 11.03 °C for light powers between 24.4 mW and 50 mW. Kurochkin et al. demonstrated that the integration of gold nanoparticles onto photosensitive polymeric 3D microstructured films enables photothermal cargo release under NIR laser irradiation guided through a silica optical fiber.[213] This fabricated film can be coated onto implants and activated by light, serving as a drug delivery system for biomedical applications. Hydrogel-based optical fibers have also been investigated for plasmonic heating. Choi et al. embedded AuNPs into hydrogel-based optical fibers and demonstrated photothermal heating of it using a green CW laser (532 nm, 800 mW).[203] The fiber's temperature increased by ~16°C within 1 minute of light coupling, and it was inserted into the mouse intestine via the rectum, highlighting its potential for photothermal therapy (PTT).

Besides plasmonic heating, the LSPR absorption of gold nanoparticles in optical fibers is utilized for biosensing, bioimaging, and stimulation through genetic engineering applications.[214] These fibers exhibit high sensitivity to changes in the surrounding refractive index, a property that makes them suitable candidates for biosensing applications. By immobilizing AuNRs on the decladded surface of multimodal optical fibers, their LSPR shifts in response to variations in the refractive index, enabling precise detection of biochemical changes.[215] Chekkaramkodi et al. integrated gold nanoparticles into 3D-printed hydrogel-based optical fibers with a diameter of 5 mm and lengths ranging from 1 to 3 cm, illuminated using a green laser (532 nm).[216] They demonstrated that higher AuNP concentrations enhanced plasmonic absorption, reducing light transmission and reflection, and emphasized the potential of these fibers for biomedical applications.

3.4.7 Photothermally responsive nanocomposite hydrogels

Free dispersed AuNRs in *in vivo* biomedical applications have drawbacks such as cytotoxicity, biodistribution, rapid clearance and unspecific accumulations in organs.[14] While they can be reduced by modification of AuNRs for high loading yield, controlled release, prolonged

circulation and targeted delivery, room for improvement remains.[217] Implantable nanocomposite materials have emerged as therapeutic platforms that enable local treatment and targeted drug administration directly at the treatment site. These materials enhance the therapeutic effect by facilitating the prolonged retention of nanoparticles at the target site through the enhanced permeability and retention (EPR) effect. The EPR effect allows nanoparticles to accumulate more in tumor or inflamed tissues due to their leaky vasculature, while the materials themselves contribute to maintaining the localized presence of AuNRs near the treatment site, preventing their clearance into the circulation.[27]

Hydrogels are suitable as AuNR nanocomposite matrix. They have been extensively studied as bioscaffold materials for biomedical applications such as drug delivery, biosensors and wound healing due to their porous structure, controllable physiochemical properties, tunable degradation rates, long-term stability in host bodies, their biodegradability and excellent biocompatibility.[12, 14, 27, 218, 219] Hydrogels can mimic the extracellular matrix to reduce immune responses of host bodies in therapeutical applications.[220, 221] Hydrogels are a type of soft, biomimetic material composed of a crosslinked 3-D network structure of hydrophilic polymers (chapter 3.5.2). They can store large amounts of water, solvated biomolecules, and small drug molecules with sustained release kinetics.[12] However, challenges such as poor efficiency in encapsulating hydrophobic drugs, uncontrolled drug release, and limited responsiveness remain.[27] To overcome these limitations, the incorporation of nanostructures to form nanocomposite hydrogels has proven effective. For instance, encapsulated nanoparticles can act as stimuli-transducers, enabling the hydrogel's responsiveness to external stimuli.[27] These stimuli can be categorized into internal factors (e.g., glucose, redox, pH, and enzymes) and external triggers (e.g., temperature, magnetic fields, light, and ultrasound waves), which activate the nanocomposite’s properties for targeted therapeutic action.[14] Among these, light-responsive nanocomposite hydrogels are particularly attractive for non-invasive and remote biomedical applications, such as photothermal therapy (PTT) and wound healing, due to their ability to offer precise spatiotemporal control on demand.[27] Specifically, NIR light is advantageous for biomedical applications due to its ability to penetrate tissues effectively while minimizing damage to surrounding cells (see section 3.4.1).[24] However, pure hydrogels lack of ability to absorb and convert NIR light into heat, which is essential for PTT or other light-based treatments. This limitation can be addressed by incorporating nanoparticles, which act as photothermal transducers within the hydrogels (see chapter 3.2 and 3.3). These nanoparticles enhance the responsiveness of nanocomposite hydrogels to NIR light, enabling effective localized heating for various biomedical applications.

Metal-based nanoparticles, carbon-based nanomaterials and polydopamine nanoparticles have been used as photothermal transducers in hydrogels for biomedical application.[27] Metal-based nanoparticles such as gold, platin, palladium and iron oxide are widely used as effective photosensitizers in NIR-induced PTT due to their high PCE and easy synthesis and modification (see chapter 3.2 and 3.3).[27] The remainder of this section focused on gold nanoparticle composite hydrogels.

Sershen et al. encapsulated gold nanoshells in hydrogels. The composite absorbed NIR light and converted it to heat resulting in hydrogel collapse, leading to the release of the encapsulated model drugs, methylene blue and bovine serum albumin.[222] Moorcroft et al. combined AuNRs and liposome loaded hydrogels for the light-induced release of antimicrobial peptides, which were wrapped into liposomes.[223] NIR irradiation (860 nm, 1.8 W/cm^2 – 2.8 W/cm^2) for 10 minutes resulted in plasmonic heating of the hydrogel to about 50 °C – 65 °C, triggered the phase transition of liposomes, and induced the release of antimicrobial peptides against Gram-negative *Pseudonomas aeruginosa* and Gram-positive *Staphylococcus aureus*. Wang et al. designed DNA-based self-repairing hydrogels encapsulated with AuNRs (50 nM, OD ~ 1.2) and loaded with the drug doxorubicin.[224] NIR-light (808 nm, 80 mW) for 10 – 30 minutes resulted in photothermal heating of the AuNR composite hydrogel between 45 °C and 50 °C and induced the dehybridization of DNA duplexes resulting in decrease of the crosslinking degree of the hydrogel to release the drug. The amount of released doxorubicin was quantified by fluorescence. The cytotoxic effect of the drug release was monitored after a time interval of 3 days after irradiation. Irradiation time of 10 min, 20 min and 30 min resulted in cell viability of breast cancer cells of about 35 %, 17 %, and 8 %, respectively. Liu et al. injected nanocomposite hydrogels that combined paclitaxel-loaded AuNRs for enhanced localized photothermal chemo-therapy in breast tumor sites in mice.[91] Under NIR-irradiation (808 nm, 1.5 W/cm²) for 5 minutes, the nanocomposite hydrogel (AuNR concentration 100 µg/mL, drug concentration 6 mg/mL) reached 50.6 °C (measured by infrared camera). The induced heat increased the hydrogel erosion and the drug release rate. NIR-treatment of 5 minutes each day for 15 minutes resulted in *in vivo* inhibition of breast tumor growth in mice due to the chemo-photothermal effects of the nanocomposite hydrogel. Qu et al. introduced AuNR composite hydrogel loaded with doxorubicin. NIR-irradiation (808 nm, 1.5 W/cm²) for 5 minutes increased the hydrogel temperature to 47 °C – 50 °C triggering the release of the loaded drug (250 µg/mL) due to contraction of the gel, which reduced the breast tumor recurrence to 16.7 % in mice.[225]

Photothermally responsive gold nanoparticle composite hydrogels were also employed for wound healing processes. Qin et al. designed NIR-responsive AuNR composite hydrogels whose photothermal effect promoted healing of infected wounds *in vivo*.[226] Huang et al. integrated pro-angiogenic peptide functionalized AuNRs in hydrogel which release peptides under NIR-irradiation.[196] The thermoplasmonically generated heat induced hydrogel contraction resulting in AuNR release to promote angiogenesis, collagen deposition and bactericidal effects on wounds in rats.[196] Chen et al. developed an alginate-based hydrogel incorporating gold nanocages conjugated with 2,2′-azobis[2-(2-imidazolin-2-yl)propane] dihydrochloride and bromothymol blue.[227] This composite hydrogel enabled real-time infection diagnosis through visible color changes induced by the pH-sensitive bromothymol blue. The hydrogel was applied to infected wounds in mice and subjected to NIR irradiation (808 nm, 1.5 W/cm^2, 10 min per session over 11 days). The photothermal effect increased the temperature on wound site to approximately 47 °C and activated the ligand to generate toxic free radicals to form antibacterial therapy. The study demonstrated that the combination of photothermal treatment and free-radical generation significantly improved wound closure rates compared to controls.[227] Hyun et al. developed a thermoresponsive hydrogel composite by incorporating hollow gold nanoparticles into a poly(N-isopropylacrylamide) matrix for potential wound dressing applications.[228] Under NIR irradiation (808 nm, 3 W/cm², 1 min), the hydrogel reached temperatures up to 83.8 °C for 0.036-wt% nanoparticles, enabling photothermal sterilization. The hydrogel demonstrated wound contraction due to PNIPAM shrinkage above its lower critical solution temperature and effectively eradicated *E. coli* bacteria after multiple irradiation cycles, highlighting its potential as a multifunctional wound dressing material.[228]

3.4.7.1 Preparation of nanocomposite hydrogels

Nanocomposite hydrogels can be prepared through non-covalent interactions or covalent linkages either between the nanoparticles themselves or between the nanoparticles and the polymer network.[12] Several strategies have been developed to prepare nanocomposite hydrogels:[27] a) blending: Nanoparticles are incorporated as additives into the hydrogel network with minimal interaction between the nanoparticles and the polymers.[229] b) *in situ* synthesis: mixing the precursor of nanoparticles and polymers, and then initiating the formation of nanoparticles and hydrogels simultaneously.[230] c) grafting: surface-functionalized nanoparticles serve as the crosslinker for hydrogel formation.[231]

Moorcroft et al. dispersed liposomes (~ 400 nm in diameter) into a 4-arm-PEG-maleimide solution containing AuNRs. Through click conjugation between 4-arm-PEG-maleimide and PEG-dithiol, along with the well-dispersed hydrophilic AuNRs in the network, the photothermal-responsive hydrogel was synthesized.[223] Liu et al. loaded the hydrophobic chemotherapeutic drug paclitaxel into the hydrophobic cores of ligands conjugated to AuNRs. The AuNRs were then encapsulated within a poly(ethylene glycol)-based hydrogel, resulting in the sustained release of the embedded nanoparticles at a constant rate over two weeks under NIR radiation.[91] The AuNRs were precipitated as powder and were dispersed in the hydrogel precursor solution under the host-guest inclusion of α-cyclodextrin and during stirring at room temperature, the nanocomposite hydrogel was formed.[91]

Hydrogels based on polymers including polyacrylamide[24, 224, 225, 232], collagen[233], poly(ethylene glycol) (PEG)[234], Pluronic[195, 235] and PVA[236] have been used as matrices for gold nanoparticles to create composite hydrogels for the photothermal therapy of hypoxic tumors, and for drug or protein release *in vitro* and *in vivo*. AuNRs have also been introduced into polyelectrolytes[237, 238] and various polymer matrices[239] for the use as NIR-responsive materials in biomedical applications.

3.4.7.2 Colloidal stability of gold nanoparticles in hydrogel

The colloidal stability of gold nanoparticles (AuNPs) in hydrogels is a critical factor for their photothermal application. The PCE can decrease when particles agglomerate.[240] Different strategies have been explored to enhance the stability of AuNPs within hydrogels and their precursors. For example, amphiphilic copolymers with charged side chains have been used to coat AuNPs, enhancing their stability in aqueous solutions by preventing aggregation through electrostatic and steric stabilization. These coatings can be tailored by varying the charge and hydrophobic/hydrophilic balance of the copolymers, which affects the nanoparticles' interaction with their environment.[241] Embedding gold nanoparticles in hydrogels provide physical retention and stability even under conditions that typically cause aggregation in water.[242]

Factors influencing the colloidal stability in hydrogels include size and their surface´s interaction with the matrix polymer. Mahmoud et al. incorporated gold nanospheres and AuNRs with hydrophilic ligands that had positive, neutral and negative surface charges in Poloxamer 407 and hydroxypropyl methylcellulose (HMC) based hydrogels.[243] The gold nanoparticles were colloidally stable in hydrophilic Poloxamer 407, but showed poor stability in HMC due to its hydrophobic character that caused phase separation. The colloidal stability of gold nanoparticles in hydrogels also depends on pH, ionic strength and the presence of proteins.[244]

The density of ligands on gold nanoparticles influences their mobility within the hydrogel matrix. High grafting densities can lead to steric hindrance, limiting the mobility of the particles and their diffusion in the hydrogel. Conversely, lower grafting densities allow for greater particle mobility, improving the dispersion of particles within the hydrogel during mixing.[245] Ishikawa et al. found, that higher crosslinking densities in hydrogels reduced the diameters of of nanoparticles formed *in situ* and improved dispersion due to increased surface area for electrostatic interaction between particle and matrix.[246]

The colloidal stability of gold nanoparticles in hydrogels can be assessed using UV-VIS spectroscopy, zeta potential measurements, and transmission electron microscopy (TEM).[243] Zeta potential measurements assess the electrostatic potential at the surface of nanoparticles, with high absolute zeta potential values indicating strong colloidal stability (> 20 mV).[243, 247, 248] In contrast, low absolute zeta potential values suggest weak repulsive forces and a propensity for aggregation. UV-VIS spectroscopy is commonly used to monitor aggregation by analyzing the localized surface plasmon resonance (LSPR) peak. Aggregated nanoparticles show a redshift of the LSPR peak and an increase in its full width at half maximum (FWHM) due to plasmon coupling, whereas well-dispersed particles exhibit a sharp and symmetric LSPR peak.[243] TEM provides direct visualization of the nanoparticle distribution within the hydrogel matrix. The degree of aggregation is assessed by analyzing interparticle distances and identifying clustered versus dispersed particles.

3.5 Stimuli-responsive engineered living materials

Engineered Living Materials (ELMs) are composite materials that have arisen from the combination of synthetic biology and material science.[1, 22] ELMs encapsulate living microorganisms, e.g. bacteria, yeast and algae, in inanimate materials such as polymers, ceramics, and hydrogels e.g. for biosensing[249], drug delivery[15], self-healing adhesives[250], biofilters to trap metals and viruses[251, 252], and soft robots.[253] Often, living microorganisms are tuned for functionality through genetic engineering, whereas the material acts as supportive scaffold. Living cells are highly efficient metabolic machines capable of adapting to their environment and can be genetically engineered.[2] This thesis reports on ELM with engineered bacterial strains derived from *ClearColi* or probiotic *E.coli* Nissle 1917. *ClearColi* is a genetically modified strain of *E. coli* that lacks endotoxic lipopolysaccharides in its outer membrane, making it suitable for applications requiring reduced immunogenicity.[254] Due to the relevance of bacterial engineering in this work, the state of the art in this chapter focuses on the role of bacteria in ELMs.

Stimuli-responsive ELMs enable programmable, on-demand activation by incorporating bacteria to control their functional states.[255] External triggers such as biochemicals, electrical fields, physiological biomarkers, and light, activate bacteria enabling ELMs to function as biosensors or drug delivery devices.[2] Among these stimuli, light is particularly attractive due to its low cost, non-invasiveness, availability, and application at different intensities and wavelengths with spatiotemporal control. Light is used for patterning[21], actuation[256] and drug release[15] in ELMs.

The following sections provide a structured overview of key aspects related to the development and application of ELMs. Section 3.5.1 describes the preparation of stimuli-responsive ELMs, focusing on how synthetic biology enables bacterial responsiveness to external triggers. Section 3.5.2 discusses hydrogels as the primary matrix for ELMs, emphasizing their role in providing a supportive environment for encapsulated bacteria. Finally, section 3.5.3 explores the application of ELMs in wound healing, a particularly relevant aspect of this thesis, as the developed ELMs were designed with potential therapeutic applications for wound treatment.

3.5.1 Design of stimuli-responsive engineered living materials

The fabrication of stimuli-responsive materials requires the design of a matrix that ensures control, stability, and survival of the living components. Several strategies for incorporating bacteria in material have been conducted, such as adsorption on surfaces, emulsification,

extrusion, spray drying, 3-D printing, electrospinning, and molding.[2] Synthetic hydrogels are often used as scaffolds because they provide a protective environment for living cells, allow the exchange of nutrients and waste with the surrounding media and, can be made bioinert and non-degradable to prevent release of the encapsulated genetically modified organisms.[257] Encapsulating engineered bacteria which are tailored to activated by external stimulus in material enables the stimuli-responsiveness of ELMs.

3.5.1.1 Engineering bacteria for stimuli-responsive engineered living materials

Engineered bacteria can enable stimulus-responsive ELMs.[2] A common route to create an ELM is to modify the embedded bacteria to express reporter genes that encode for proteins that produce e.g. fluorescent or calorimetric signals in response to target stimuli like chemicals, temperature or light.[258] Fluorescent reporters like red fluorescent mCherry derived from the coral *Discosoma sp.*, can be employed to identify bacteria, track bacterial localization, and monitor transcriptional activity.[259, 260] Other commonly used reporters include β-galactosidase, encoded by lacZ gene.[261]

Among these stimuli, thermoresponsiveness offers a distinct advantage. It enables precise and non-invasive control of bacterial gene expression via heat, which can be applied uniformly and remotely. Several thermal bioswitches such as microbial heat shock factors, membrane-associated proteins, RNA thermometers, and transcriptional repressors are available to control gene expression in engineered bacteria. Temperature-dependent transcriptional repressors like TlpA are favourable due to their sharp thermal transition, orthogonality and large change in activity.[28] They provide switch-like control of bacterial gene expression at thresholds spanning the biomedically relevant range of 32 °C – 46 °C.[28] Remotely controlled induction of gene expression by heat generated by laser lights[262] and focused ultrasound[263] for living cells has been reported. For example, Piraner et al. developed several thermal biological circuits using the TlpA bioswitch for microbial therapeutical applications.[28] TlpA originates from *Salmonella typhimirium*, and acts as a thermoresponsive repressor along with its ptlpA promoter. In its native organism, TlpA regulates the expression of genes involved in plasmid maintenance by repressing transcription at lower temperatures and derepressing it when temperatures rise above 37 °C. The genetic sequence encoding TlpA was adapted for use in *E. coli*, enabling precise temperature-controlled gene expression in engineered microbial systems. TlpA undergoes sharp, temperature dependent uncoiling at temperatures between 30 °C and 45 °C. Piraner et al. further evolved TlpA to achieve sharp switching from off and on when heated by only 2 °C, from 37 °C to 39 °C. The uncoiling changes the dimeric state to

the monomeric state of the protein and detaches on the DNA surface enabling the transcription of the TlpA operator-promoter at higher temperatures which induces the gene expression.[264] Plasmids encoding the TlpA gene along with its ptlpA promoter are transformed in *E. coli* to engineer thermoresponsive strains. Piraner et al. used focused ultrasonic at about 1 kHz to generate local heat for activating the engineered bacteria.[28]

The use of engineered bacteria in therapeutic applications can be challenging due to concerns such as infection or immune response, transfer of genetically engineered elements to surrounding cells, nonspecific colonization, or uncontrolled growth on treatment sites when they are freely circulating in the host body.[15, 16] A practical solution is the encapsulation of the bacteria in scaffolds e.g. like hydrogels (see section 3.5.1.2) to form engineered living materials. This approach helps mitigate the risks associated with free-floating microorganisms. For example, Yanamandra et al. discovered that the immunogenicity and cytotoxicity of *E. coli* bacteria is reduced when encapsulated in Pluronic F127 based hydrogels.[265] The next section (3.5.1.2) explores the methods for incorporating these engineered bacteria into matrices to design stimuli-responsive ELMs.

3.5.1.2 Fabrication strategies for engineered living materials

To encapsulate bacteria in synthetic hydrogels, the bacteria cells can be first dispersed in the hydrogel precursor solution, which is then crosslinked during fabrication.[22, 23] Molding, emulsion processing, light-mediated patterning, electrospinning and 3-D printing have been used to structure synthetic hydrogels that encapsulate bacteria.[23, 266] An alternative encapsulation strategy employs the introduction of bacterial cells into pores or channels of the hydrogel after crosslinking.[267]

Mostly, 3-D-printed ELMs have been prepared using extrusion-based techniques.[2] The bacteria are contained in a soft pre-gel matrix with shear-thinning properties. This matrix behaves as a fluid under shear stress during extrusion, allowing it to be precisely deposited. Once the shear force is removed, the material rapidly recovers its viscosity, enabling it to retain its printed shape prior to crosslinking. For example, Liu et al. 3-D-printed an ELM in two steps. PluDA hydrogel inks with embedded engineered *E. coli* strains were written directly and UV-cured with Irgacure 2595 as photoinitiator. This yielded gel constructs that were 3 cm in length at a high spatial resolution of 30 µm. The ELMs were stimulated with isopropyl β-d-1-thiogalactopyranoside (IPTG) to respond in GFP expression, enabling their use for the detection of chemicals on human skins when patched as a tattoo.[266]

Electrospinning utilizes electrostatic forces to form micro/nanometer scale polymeric fibers and yields fiber mats with high porosity and surface area.[2] A variety of polymers including pluronic derivates and PVA have been used to encapsulate bacteria.[22] For example, *E. coli* was mixed in Pluronic F-127 dimethacrylate solutions in its liquid state at 4 °C. The electrospinning was conducted at room temperature followed by chemical crosslinking resulting in hydrogel fibers.[268]

ELMs can be structured by molding, a scalable and widely available process. Polymer precursor solutions with homogenized bacteria are injected in pre-shaped geometries, templates or molds. After crosslinking, the ELM has the desired shape. In this dissertation, I used commercial well plates as molds to shape ELMs in cylindrical shapes (see chapter 5.1 and 5.2). Several studies have utilized molding for ELM construction. Liu et al. designed magnetic living hydrogels in cylindrical molds with radius and thickness of 1 mm. They mixed engineered *E. coli* Nissle 1917 strain and magnetic microparticles in a PVA solution and poured into a mold. At -20 °C, phase separation of the polymer in water resulted in hydrogel formation through crosslinking of PVA nanocrystalline domains. The molded ELM showed magnetic properties in the abdominal skin and was able to detect gastrointestinal bleeding.[269] Tang et al. molded ELMs with core-shell hydrogel structures in parafilm. A premix of engineered *E. coli* in alginate was loaded into a syringe and then disposed onto parafilm molds. Crosslinking with calcium ions resulted in the core structure. The core was then coated with a tougher alginate based hydrogel enabling robust physical containment of the bacteria in the core. The ELM was stimulated by heavy metals like cadmium and responded in GFP expression making it a potential candidate as robust biosensor.[270] Dhakane et al. used polydimethylsiloxane (PDMS) molds to shape core-shell ELMs. PDMS was made in desired geometries for core and shell structures. Optogenetically modified *ClearColi* was mixed in liquid PluDA precursor at temperatures of 4°C, the dispersion was injected via a pipette in PDMS molds and then crosslinked by UV light. The cylindrical core diameter was 6 mm with a height of 0.8 mm. The protective PluDA shell layer was prepared in same manner without bacteria in PDMS molds with diameter of 10 mm and height of 1.2 mm. The resulting ELM secreted a VEGF-mimetic peptide under stimulation of blue LED light at 450 nm.[271]

3.5.2 Hydrogels as materials for engineered living materials

Various materials have been explored in literature as scaffolds for ELMs such as polymer based nanofibers[272, 273], silk fibroins[274] and curli nanofibers.[22] Among these, hydrogels stand out as particularly promising candidates due to their biocompatibility for therapeutical

applications and their ideal ability to support 3-D cell growth.[221, 275] Hydrogels protect encapsulated bacteria from immune system attack and prevents leaking out the bacteria to the surrounding treatment site avoiding potential threats.[276] Furthermore, hydrogels provide good environment for nutrient transfer, cell growth, sensing and create chemical gradients.[23, 276]

Hydrogels consist of polymer networks infiltrated with water with high content (70 – 99 vol%).[23] Hydrogels can be either produced by living cells or synthesized from naturally occurring polymers (like agar, agarose, alginate, cellulose and gelatin) or synthetic polymers (like polyacrylamide, polyvinyl alcohol, polyethylene glycol and Pluronics).[23] The following section 3.5.2.1 focuses on polyvinyl alcohol (PVA) and Pluronic (Plu) based hydrogels.

3.5.2.1 Polyvinyl alcohol and Pluronic F127 based hydrogels

The ELMs in this thesis are based on hydrogels with polyvinyl alcohol (PVA) and Pluronic® F- 127. PVA and Pluronic-based hydrogels are known for their long-term physical and chemical stability, which is crucial for preserving bacteria over extended periods. This stability arises from their molecular structure, with C-C and C-O-C linkages physically crosslinked within a 3-D matrix, providing a durable framework for long-term preservation.[23] The physical crosslinks are due to hydrogen bonding and hydrophobic interactions.[277] Additionally, their functionalizing capability gives opportunities for additional chemical crosslinking providing even more robust matrices.

Pluronics are triblock amphiphilic copolymers composed of a central hydrophobic chain of polypropylene oxide (PPO) and hydrophilic chains of polyethylene oxide (PEO) arranged in a PEO-PPO-PEO configuration with thermoresponsive properties. Below critical micelle temperature (CMT), Pluronic copolymers are dissolved in water as monomers. Above CMT, Pluronic polymers start forming micelles with the hydrophobic PPO cores surrounded by hydrophilic PEO coronas and the solution becomes more viscous, but remains a liquid.[277, 278] Above lower critical gelation temperature (LCGT), the micelles aggregate due to the increasing hydrophobicity of PEO and form a 3-D structure. This networks traps water, leading to the formation of hydrogel.

Pluronic exists with different PPO and PEO chain lengths. This thesis reports on Pluronic® F- 127 with PEO_{106}-PPO_{70}-PEO_{106},[279] where “F” stands for flake, and “127” refers to an average PPO molecular weight of 12600 Da, with 70 wt% of PEO.[280] The

viscosity of the neat polymer solution is 3.1 Pas and the critical micellar concentration is 0.725 wt% at 25 °C.[279] The LCGT is 14 °C at concentrations above 0.5 wt%.[279] The diameter of the PPO core of the micelles were reported to be 5-7 nm[281], the hydrodynamic diameter of micelles was determined as 22 nm[282], the micelle diameter was recorded as 17.6 nm[283] and the intermicellar distance was recorded as 20 nm at specific concentrations above 19 wt% and at room temperature.[284]

The mechanical and structural stability of Pluronic® F- 127 based hydrogels can be enhanced through chemical crosslinking between the micelles. Their terminal hydroxyl group can be modified with covalently crosslinkable functional groups like folic acid, dimethacyrlate, and diacrylate undergoing chemical crosslinking under presence of chemicals or light.[285] In my work, I used diacrylate functionalized Pluronic® F- 127 (PluDA). In the presence of a photoinitiator like Irgacure 2959 (2-Hydroxy-4′-(2-hydroxyethoxy)-2-methylpropiophenon) in the PluDA hydrogel, the diacrylate groups can be crosslinked by UV light at 395 nm.[279, 286] The shear storage modulus of PluDA at 0.1% strain amplitude increased from 15.3 ± 1.8 kPa to 47.5 ± 2.9 kPa as the PluDA content increased from 0 to 100 % at room temperature.[287]

Bhusari et al. encapsulated optogenetically engineered *E. coli* in PluDA thin film hydrogels and analyzed the bacterial growth in the gel at different DA fractions, labeled as X. They found that *E. coli* in PluDA hydrogels with X>50 grew in spherical colonies and did not leak out of the hydrogel for at least two weeks.[288]

PVA is a biocompatible hydrogel and has been used for the encapsulation of bacteria in many reports.[289, 290] Its hydroxyl groups can be crosslinked by physical method like freeze thawing process or by a chemical method with crosslinking agents such as glutaraldehyde or hexamethylene diisocyanate.[291] Photocrosslinking of PVA based hydrogels is also possible. For example, Puertas-Bartolomé et al. functionalized PVA with vinyl sulfone (VS) groups to form a stable network under irradiation with blue light (402 nm) after the addition of the photoinitiator lithium-phenyl-2,4,6-trimethylbenzoylphosphinat (LAP). The shear storage modulus of the 10% w/v PVA-VS hydrogel after photocrosslinking had a shear modulus (G') of 17.9 ± 0.1 kPa at room temperature.[290]

PVA hydrogels have been used for stimulus-responsive ELM. For example, Schulz-Schönhagen et al. encapsulated engineered *Bacillus subtilis* in PVA hydrogels. The ELM generated a fluorescence signal in response to the chemical isopropyl-β-d-thiogalactopyranoside. Such ELMs have the potential to quantify chemicals like toxins, antibiotics and carbohydrates in correlation with the induced fluorescence intensity.[249]

3.5.3 Engineered living materials for wound healing

The skin plays a crucial role in preventing the body from water loss and blocking the invasion of harmful substances and pathogenic microorganisms from the surroundings.[292] Traditional wound treatments kill the pathogenic bacteria, but also suppress healthy wound cells and the growth of useful bacteria, thus destroying the balance of the microbial ecosystem on the wound.[276] ELMs are an interesting alternative for future wound healing strategies. Therapeutic biofilms, drug-delivering skin patches, living bacterial cellulose[293] and living hydrogels[294, 295] were developed for wound healing.[22, 276, 296]

Ming et al. developed ELM for wound healing that combats infection, reduces inflammation, and promotes wound closure and new tissue growth.[276] The ELM contained a probiotic *Lactobacillus reuteri* encapsulated in hydrogel, which secrets reuterin, an antimicrobial substance tested *in vivo* on mice skin wounds.[276] Another study engineered *E. coli* Nissle 1917 strain to produce tissue adhesive curli fibres in a biofilm to restore epithelial functions and to recover wound tissues.[297] González et al embedded engineered *B. subtilis* spores in agarose-hydrogel based bioinks and printed these on wounds.[295] The ELM was used to seal wounds and additionally was able to produce anti-microbial agents secreted by *B. subtilis* to kill the wound infectious bacteria *Staphylococcus aureus*. Lu et al. encapsulated the bacteria *Lactococcus* in a heparin-poloxamer based thermoresponsive hydrogel.[296] The ELM produced VEGF and secreted lactic acid and patched on wounds to increase proliferation, migration, network formation of endothelial cells with an additionally anti-inflammatory effect resulting in accelerating angiogenesis in wounds.[296]

A controllable drug release for wound healing with regulated concentrations of the released drug over time is advantageous. For example, a high release on growth factors like VEGF can cause overstimulation and or off-site differentiation of cells leading to necrosis or tumorigenesis.[271, 298] ELMs can be designed to produce and release drugs on demand by external stimuli such as light. Liu et al. synthesized a light-controlled bactericidal wound dressing by encapsulating *Komagataeibacter sucrofermentans* in cellulose.[293] The metabolized product of *K. sucrofermentans* has an efficient ROS production upon light irradiation responsible for the antibacterial effect on wounds.[293] Dhakane et al. reported ELMs containing optogenetically engineered *ClearColi* to release a pro-angiogenic protein upon 450 nm radiation and showed wound healing effects *in vitro*.[271]

Bibliography

[1] P.Q. Nguyen, N.D. Courchesne, A. Duraj-Thatte, P. Praveschotinunt, N.S. Joshi, Engineered Living Materials: Prospects and Challenges for Using Biological Systems to Direct the Assembly of Smart Materials, Adv Mater 30 (2018) e1704847.
[2] L.K. Rivera-Tarazona, Z.T. Campbell, T.H. Ware, Stimuli-responsive engineered living materials, Soft Matter 17 (2021) 785-809.
[3] L. Jauffred, A. Samadi, H. Klingberg, P.M. Bendix, L.B. Oddershede, Plasmonic Heating of Nanostructures, Chemical Reviews 119 (2019) 8087-8130.
[4] A. Lalisse, G. Tessier, J. Plain, G. Baffou, Quantifying the Efficiency of Plasmonic Materials for Near-Field Enhancement and Photothermal Conversion, The Journal of Physical Chemistry C 119 (2015) 25518-25528.
[5] G. Baffou, R. Quidant, Thermo-plasmonics: using metallic nanostructures as nano-sources of heat, Laser & Photonics Reviews 7 (2013) 171-187.
[6] A.O. Govorov, H.H. Richardson, Generating heat with metal nanoparticles, Nano Today 2 (2007) 30-38.
[7] C.M. Cobley, J. Chen, E.C. Cho, L.V. Wang, Y. Xia, Gold nanostructures: a class of multifunctional materials for biomedical applications, Chemical Society Reviews 40 (2011) 44-56.
[8] N.D. Burrows, W. Lin, J.G. Hinman, J.M. Dennison, A.M. Vartanian, N.S. Abadeer, E.M. Grzincic, L.M. Jacob, J. Li, C.J. Murphy, Surface Chemistry of Gold Nanorods, Langmuir 32 (2016) 9905-9921.
[9] X. Wang, G. Li, Y. Ding, S. Sun, Understanding the photothermal effect of gold nanostars and nanorods for biomedical applications, RSC Advances 4 (2014) 30375-30383.
[10] H. Chen, L. Shao, Q. Li, J. Wang, Gold nanorods and their plasmonic properties, Chem Soc Rev 42 (2013) 2679-2724.
[11] X. Huang, P.K. Jain, I.H. El-Sayed, M.A. El-Sayed, Plasmonic photothermal therapy (PPTT) using gold nanoparticles, Lasers in Medical Science 23 (2008) 217-228.
[12] S. Huang, X. Hong, M. Zhao, N. Liu, H. Liu, J. Zhao, L. Shao, W. Xue, H. Zhang, P. Zhu, R. Guo, Nanocomposite hydrogels for biomedical applications, Bioengineering & Translational Medicine 7 (2022) e10315.
[13] Y. Zhang, X. Zhan, J. Xiong, S. Peng, W. Huang, R. Joshi, Y. Cai, Y. Liu, R. Li, K. Yuan, N. Zhou, W. Min, Temperature-dependent cell death patterns induced by functionalized gold nanoparticle photothermal therapy in melanoma cells, Scientific Reports 8 (2018) 8720.
[14] P. Lavrador, M.R. Esteves, V.M. Gaspar, J.F. Mano, Stimuli-Responsive Nanocomposite Hydrogels for Biomedical Applications, Advanced Functional Materials 31 (2021) 2005941.
[15] S. Sankaran, J. Becker, C. Wittmann, A. Del Campo, Optoregulated drug release from an engineered living material: self-replenishing drug depots for long-term, light-regulated delivery, Small 15 (2019) 1804717.
[16] S. Sankaran, A. del Campo, Optoregulated Protein Release from an Engineered Living Material, Advanced Biosystems 3 (2019) 1800312.
[17] E. Ruggiero, S. Alonso-de Castro, A. Habtemariam, L. Salassa, Upconverting nanoparticles for the near infrared photoactivation of transition metal complexes: new opportunities and challenges in medicinal inorganic photochemistry, Dalton Transactions 45 (2016) 13012-13020.
[18] S. Pearson, J. Feng, A. del Campo, Lighting the Path: Light Delivery Strategies to Activate Photoresponsive Biomaterials In Vivo, Advanced Functional Materials 31 (2021) 2105989.

[19] H. Pan, L. Li, G. Pang, C. Han, B. Liu, Y. Zhang, Y. Shen, T. Sun, J. Liu, J. Chang, H. Wang, Engineered NIR light-responsive bacteria as anti-tumor agent for targeted and precise cancer therapy, Chemical Engineering Journal 426 (2021) 130842.
[20] C. Wu, M. Cui, L. Cai, C. Chen, X. Zhu, Y. Wu, J. Liu, H. Wang, Y. Zhang, NIR-Responsive Photodynamic Nanosystem Combined with Antitumor Immune Optogenetics Bacteria for Precise Synergetic Therapy, ACS Applied Materials & Interfaces 14 (2022) 13094-13106.
[21] F. Moser, E. Tham, L.M. González, T.K. Lu, C.A. Voigt, Light-controlled, high-resolution patterning of living engineered bacteria onto textiles, ceramics, and plastic, Advanced Functional Materials 29 (2019) 1901788.
[22] A. Rodrigo-Navarro, S. Sankaran, M.J. Dalby, A. del Campo, M. Salmeron-Sanchez, Engineered living biomaterials, Nature Reviews Materials 6 (2021) 1175-1190.
[23] X. Liu, M.E. Inda, Y. Lai, T.K. Lu, X. Zhao, Engineered Living Hydrogels, Advanced Materials 34 (2022) 2201326.
[24] X. Sun, D. Liu, X. Xu, Y. Shen, Y. Huang, Z. Zeng, M. Xia, C. Zhao, NIR-triggered thermo-responsive biodegradable hydrogel with combination of photothermal and thermodynamic therapy for hypoxic tumor, Asian Journal of Pharmaceutical Sciences 15 (2020) 713-727.
[25] J.-H. Kim, T. Randall Lee, Discrete thermally responsive hydrogel-coated gold nanoparticles for use as drug-delivery vehicles, Drug Development Research 67 (2006) 61-69.
[26] L. Petrini, F. Migliavacca, Biomedical Applications of Shape Memory Alloys, Journal of Metallurgy 2011 (2011) 501483.
[27] K.-H. Shen, C.-H. Lu, C.-Y. Kuo, B.-Y. Li, Y.-C. Yeh, Smart near infrared-responsive nanocomposite hydrogels for therapeutics and diagnostics, Journal of Materials Chemistry B 9 (2021) 7100-7116.
[28] D.I. Piraner, M.H. Abedi, B.A. Moser, A. Lee-Gosselin, M.G. Shapiro, Tunable thermal bioswitches for in vivo control of microbial therapeutics, Nature Chemical Biology 13 (2017) 75-80.
[29] S. Dey, C.E. Seyfert, C. Fink-Straube, A.M. Kany, R. Müller, S. Sankaran, Thermo-amplifier circuit in probiotic E. coli for stringently temperature-controlled release of a novel antibiotic, Journal of Biological Engineering 18 (2024) 66.
[30] T.A. Tabish, P. Dey, S. Mosca, M. Salimi, F. Palombo, P. Matousek, N. Stone, Smart Gold Nanostructures for Light Mediated Cancer Theranostics: Combining Optical Diagnostics with Photothermal Therapy, Advanced Science 7 (2020) 1903441.
[31] Q. Fu, Z. Li, F. Fu, X. Chen, J. Song, H. Yang, Stimuli-Responsive Plasmonic Assemblies and Their Biomedical Applications, Nano Today 36 (2021) 101014.
[32] X. Huang, M.A. El-Sayed, Gold nanoparticles: Optical properties and implementations in cancer diagnosis and photothermal therapy, Journal of Advanced Research 1 (2010) 13-28.
[33] C.J. Orendorff, C.J. Murphy, Quantitation of Metal Content in the Silver-Assisted Growth of Gold Nanorods, The Journal of Physical Chemistry B 110 (2006) 3990-3994.
[34] C.F.B.a.D.R. Huffman, Absorption and Scattering of Light by Small Particles, John Wiley & Sons (1983).
[35] D.K. Roper, W. Ahn, M. Hoepfner, Microscale Heat Transfer Transduced by Surface Plasmon Resonant Gold Nanoparticles, The Journal of Physical Chemistry C 111 (2007) 3636-3641.
[36] C.J. Murphy, H.-H. Chang, P. Falagan-Lotsch, M.T. Gole, D.M. Hofmann, K.N.L. Hoang, S.M. McClain, S.M. Meyer, J.G. Turner, M. Unnikrishnan, M. Wu, X. Zhang, Y. Zhang, Virus-Sized Gold Nanorods: Plasmonic Particles for Biology, Accounts of Chemical Research 52 (2019) 2124-2135.
[37] T.S. Ahmadi, S.L. Logunov, M.A. El-Sayed, Picosecond Dynamics of Colloidal Gold Nanoparticles, The Journal of Physical Chemistry 100 (1996) 8053-8056.

[38] L.D.L. Landau, E. M., Fluid Mechanics, Pergamom Press: Oxford, U.K. 2nd ed. (1987).
[39] G. Baffou, R. Quidant, F.J. García de Abajo, Nanoscale Control of Optical Heating in Complex Plasmonic Systems, ACS Nano 4 (2010) 709-716.
[40] G. Baffou, R. Quidant, C. Girard, Heat generation in plasmonic nanostructures: Influence of morphology, Applied Physics Letters 94 (2009).
[41] H. Petrova, J. Perez Juste, I. Pastoriza-Santos, G.V. Hartland, L.M. Liz-Marzán, P. Mulvaney, On the temperature stability of gold nanorods: comparison between thermal and ultrafast laser-induced heating, Physical Chemistry Chemical Physics 8 (2006) 814-821.
[42] O. Ekici, R.K. Harrison, N.J. Durr, D.S. Eversole, M. Lee, A. Ben-Yakar, Thermal Analysis of Gold Nanorods Heated with Femtosecond Laser Pulses, J Phys D Appl Phys 41 (2008) 185501.
[43] S. Maity, W.-C. Wu, C. Xu, J.B. Tracy, K. Gundogdu, J.R. Bochinski, L.I. Clarke, Spatial temperature mapping within polymer nanocomposites undergoing ultrafast photothermal heating via gold nanorods, Nanoscale 6 (2014) 15236-15247.
[44] G. Baffou, P. Berto, E. Bermúdez Ureña, R. Quidant, S. Monneret, J. Polleux, H. Rigneault, Photoinduced Heating of Nanoparticle Arrays, ACS Nano 7 (2013) 6478-6488.
[45] P. Keblinski, D.G. Cahill, A. Bodapati, C.R. Sullivan, T.A. Taton, Limits of localized heating by electromagnetically excited nanoparticles, Journal of Applied Physics 100 (2006).
[46] B. Jang, Y.S. Kim, Y. Choi, Effects of gold nanorod concentration on the depth-related temperature increase during hyperthermic ablation, Small 7 (2011) 265-270.
[47] H. Chen, L. Shao, T. Ming, Z. Sun, C. Zhao, B. Yang, J. Wang, Understanding the Photothermal Conversion Efficiency of Gold Nanocrystals, Small 6 (2010) 2272-2280.
[48] F.P. Incropera, Fundamentals of Heat and Mass Transfer, John Wiley & Sons, Inc.2006.
[49] K. Jiang, D.A. Smith, A. Pinchuk, Size-Dependent Photothermal Conversion Efficiencies of Plasmonically Heated Gold Nanoparticles, The Journal of Physical Chemistry C 117 (2013) 27073-27080.
[50] Z. Zhang, J. Wang, C. Chen, Near-Infrared Light-Mediated Nanoplatforms for Cancer Thermo-Chemotherapy and Optical Imaging, Advanced Materials 25 (2013) 3869-3880.
[51] Z. Qin, Y. Wang, J. Randrianalisoa, V. Raeesi, W.C.W. Chan, W. Lipiński, J.C. Bischof, Quantitative Comparison of Photothermal Heat Generation between Gold Nanospheres and Nanorods, Scientific Reports 6 (2016) 29836.
[52] H. Breitenborn, J. Dong, R. Piccoli, A. Bruhacs, L.V. Besteiro, A. Skripka, Z.M. Wang, A.O. Govorov, L. Razzari, F. Vetrone, R. Naccache, R. Morandotti, Quantifying the photothermal conversion efficiency of plasmonic nanoparticles by means of terahertz radiation, APL Photonics 4 (2019).
[53] J. Mesicek, K. Kuca, Summary of numerical analyses for therapeutic uses of laser-activated gold nanoparticles, International Journal of Hyperthermia 34 (2018) 1255-1264.
[54] O.A. Savchuk, J.J. Carvajal, J. Massons, M. Aguiló, F. Díaz, Determination of photothermal conversion efficiency of graphene and graphene oxide through an integrating sphere method, Carbon 103 (2016) 134-141.
[55] A. Nexha, J.J. Carvajal, M.C. Pujol, F. Díaz, M. Aguiló, Synthesis of monoclinic Ho,Tm:KLu(WO4)2 microrods with high photothermal conversion efficiency via a thermal decomposition-assisted method, Journal of Materials Chemistry C 9 (2021) 2024-2036.
[56] L.M. Maestro, P. Haro-González, A. Sánchez-Iglesias, L.M. Liz-Marzán, J. García Solé, D. Jaque, Quantum Dot Thermometry Evaluation of Geometry Dependent Heating Efficiency in Gold Nanoparticles, Langmuir 30 (2014) 1650-1658.
[57] H.H. Richardson, M.T. Carlson, P.J. Tandler, P. Hernandez, A.O. Govorov, Experimental and Theoretical Studies of Light-to-Heat Conversion and Collective Heating Effects in Metal Nanoparticle Solutions, Nano Letters 9 (2009) 1139-1146.

[58] D.K. Kim, M.S. Amin, S. Elborai, S.-H. Lee, Y. Koseoglu, M. Zahn, M. Muhammed, Energy absorption of superparamagnetic iron oxide nanoparticles by microwave irradiation, Journal of Applied Physics 97 (2005).
[59] A. Paściak, R. Marin, L. Abiven, A. Pilch-Wróbel, M. Misiak, W. Xu, K. Prorok, O. Bezkrovnyi, Ł. Marciniak, C. Chanéac, F. Gazeau, R. Bazzi, S. Roux, B. Viana, V.-P. Lehto, D. Jaque, A. Bednarkiewicz, Quantitative Comparison of the Light-to-Heat Conversion Efficiency in Nanomaterials Suitable for Photothermal Therapy, ACS Applied Materials & Interfaces 14 (2022) 33555-33566.
[60] S. Chen, F. Tang, L. Tang, L. Li, Synthesis of Cu-Nanoparticle Hydrogel with Self-Healing and Photothermal Properties, ACS Applied Materials & Interfaces 9 (2017) 20895-20903.
[61] Vikas, R. Kumar, S. Soni, Concentration-dependent photothermal conversion efficiency of gold nanoparticles under near-infrared laser and broadband irradiation, Beilstein Journal of Nanotechnology 14 (2023) 205-217.
[62] M. Almada, B.H. Leal-Martínez, N. Hassan, M.J. Kogan, M.G. Burboa, A. Topete, M.A. Valdez, J. Juárez, Photothermal conversion efficiency and cytotoxic effect of gold nanorods stabilized with chitosan, alginate and poly(vinyl alcohol), Materials Science and Engineering: C 77 (2017) 583-593.
[63] W. Yang, B. Xia, L. Wang, S. Ma, H. Liang, D. Wang, J. Huang, Shape effects of gold nanoparticles in photothermal cancer therapy, Materials Today Sustainability 13 (2021) 100078.
[64] P.K. Jain, K.S. Lee, I.H. El-Sayed, M.A. El-Sayed, Calculated Absorption and Scattering Properties of Gold Nanoparticles of Different Size, Shape, and Composition: Applications in Biological Imaging and Biomedicine, The Journal of Physical Chemistry B 110 (2006) 7238-7248.
[65] M.A. Mackey, M.R.K. Ali, L.A. Austin, R.D. Near, M.A. El-Sayed, The Most Effective Gold Nanorod Size for Plasmonic Photothermal Therapy: Theory and In Vitro Experiments, The Journal of Physical Chemistry B 118 (2014) 1319-1326.
[66] V.P. Pattani, J.W. Tunnell, Nanoparticle-mediated photothermal therapy: A comparative study of heating for different particle types, Lasers in Surgery and Medicine 44 (2012) 675-684.
[67] J.R. Cole, N.A. Mirin, M.W. Knight, G.P. Goodrich, N.J. Halas, Photothermal Efficiencies of Nanoshells and Nanorods for Clinical Therapeutic Applications, The Journal of Physical Chemistry C 113 (2009) 12090-12094.
[68] S. Basaran, S. Dey, S. Bhusari, S. Sankaran, T. Kraus, Plasmonic stimulation of gold nanorods for the photothermal control of engineered living materials, Biomaterials Advances 147 (2023) 213332.
[69] R. Jin, J. Yang, D. Zhao, X. Hou, C. Li, W. Chen, Y. Zhao, Z. Yin, B. Liu, Hollow gold nanoshells-incorporated injectable genetically engineered hydrogel for sustained chemo-photothermal therapy of tumor, Journal of Nanobiotechnology 17 (2019) 99.
[70] K.-C. Li, H.-C. Chu, Y. Lin, H.-Y. Tuan, Y.-C. Hu, PEGylated Copper Nanowires as a Novel Photothermal Therapy Agent, ACS Applied Materials & Interfaces 8 (2016) 12082-12090.
[71] J. Liang, B. Chen, J. Hu, Q. Huang, D. Zhang, J. Wan, Z. Hu, B. Wang, pH and Thermal Dual-Responsive Graphene Oxide Nanocomplexes for Targeted Drug Delivery and Photothermal-Chemo/Photodynamic Synergetic Therapy, ACS Applied Bio Materials 2 (2019) 5859-5871.
[72] M. Hashemkhani, K. Bilici, A. Muti, A. Sennaroglu, H.Y. Acar, Ag2S-Glutathione quantum dots for NIR image guided photothermal therapy, New Journal of Chemistry 44 (2020) 5419-5427.

[73] T. Yang, Y.a. Tang, L. Liu, X. Lv, Q. Wang, H. Ke, Y. Deng, H. Yang, X. Yang, G. Liu, Y. Zhao, H. Chen, Size-Dependent Ag2S Nanodots for Second Near-Infrared Fluorescence/Photoacoustics Imaging and Simultaneous Photothermal Therapy, ACS Nano 11 (2017) 1848-1857.
[74] A. Sennaroglu, M. Khan, M. Hashemkhani, H. Yağci Acar, Determination of the Wavelength-Dependent Photothermal Conversion Efficiency of Photosensitizers for Photothermal Therapy: Application to Ag2S-Glutathione Quantum Dots, The Journal of Physical Chemistry B 125 (2021) 11650-11659.
[75] M. Quintanilla, I. García, I. de Lázaro, R. García-Alvarez, M. Henriksen-Lacey, S. Vranic, K. Kostarelos, L.M. Liz-Marzán, Thermal monitoring during photothermia: hybrid probes for simultaneous plasmonic heating and near-infrared optical nanothermometry, Theranostics 9 (2019) 7298-7312.
[76] C. Lee, K. Lim, S.S. Kim, L.X. Thien, E.S. Lee, K.T. Oh, H.-G. Choi, Y.S. Youn, Chlorella-gold nanorods hydrogels generating photosynthesis-derived oxygen and mild heat for the treatment of hypoxic breast cancer, Journal of Controlled Release 294 (2019) 77-90.
[77] C. Bermúdez-Jiménez, N. Niño-Martínez, N. Patiño-Marín, F. Martínez-Gutiérrez, F. Ruiz, H. Bach, G. Martínez-Castañón, Effective control of biofilms by photothermal therapy using a gold nanorod hydrogel, Journal of Biomedical Materials Research Part B: Applied Biomaterials 108 (2020) 333-342.
[78] B. del Rosal, E. Ximendes, U. Rocha, D. Jaque, In Vivo Luminescence Nanothermometry: from Materials to Applications, Advanced Optical Materials 5 (2017) 1600508.
[79] J. Shah, S.R. Aglyamov, K. Sokolov, T.E. Milner, S.Y. Emelianov, Ultrasound imaging to monitor photothermal therapy–Feasibility study, Optics Express 16 (2008) 3776-3785.
[80] M.N. Rylander, R.J. Stafford, J. Hazle, J. Whitney, K.R. Diller, Heat shock protein expression and temperature distribution in prostate tumours treated with laser irradiation and nanoshells, International Journal of Hyperthermia 27 (2011) 791-801.
[81] C. Wang, L. Ling, Y. Yao, Q. Song, One-step synthesis of fluorescent smart thermo-responsive copper clusters: A potential nanothermometer in living cells, Nano Research 8 (2015) 1975-1986.
[82] A. Nexha, J.J. Carvajal, M.C. Pujol, F. Díaz, M. Aguiló, Lanthanide doped luminescence nanothermometers in the biological windows: strategies and applications, Nanoscale 13 (2021) 7913-7987.
[83] X. Cui, Q. Ruan, X. Zhuo, X. Xia, J. Hu, R. Fu, Y. Li, J. Wang, H. Xu, Photothermal Nanomaterials: A Powerful Light-to-Heat Converter, Chemical Reviews 123 (2023) 6891-6952.
[84] C.D. Brites, P.P. Lima, N.J. Silva, A. Millán, V.S. Amaral, F. Palacio, L.D. Carlos, Thermometry at the nanoscale, Nanoscale 4 (2012) 4799-4829.
[85] X. Jin, S. Yao, F. Qiu, Z. Mao, B. Wang, A multifunctional hydrogel containing gold nanorods and methylene blue for synergistic cancer phototherapy, Colloids and Surfaces A: Physicochemical and Engineering Aspects 614 (2021) 126154.
[86] J. Zhang, J. Li, N. Kawazoe, G. Chen, Composite scaffolds of gelatin and gold nanoparticles with tunable size and shape for photothermal cancer therapy, Journal of materials chemistry B 5 (2017) 245-253.
[87] S. Jiang, K. Wang, Y. Dai, X. Zhang, F. Xia, Near-Infrared Light-Triggered Dual Drug Release Using Gold Nanorod-Embedded Thermosensitive Nanogel-Crosslinked Hydrogels, Macromolecular Materials and Engineering 304 (2019) 1900087.
[88] J.T. Jørgensen, K. Norregaard, P. Tian, P.M. Bendix, A. Kjaer, L.B. Oddershede, Single Particle and PET-based Platform for Identifying Optimal Plasmonic Nano-Heaters for Photothermal Cancer Therapy, Scientific Reports 6 (2016) 30076.

[89] X. Zhu, W. Feng, J. Chang, Y.-W. Tan, J. Li, M. Chen, Y. Sun, F. Li, Temperature-feedback upconversion nanocomposite for accurate photothermal therapy at facile temperature, Nature Communications 7 (2016) 10437.
[90] N. Alifu, A. Zebibula, J. Qi, H. Zhang, C. Sun, X. Yu, D. Xue, J.W.Y. Lam, G. Li, J. Qian, B.Z. Tang, Single-Molecular Near-Infrared-II Theranostic Systems: Ultrastable Aggregation-Induced Emission Nanoparticles for Long-Term Tracing and Efficient Photothermal Therapy, ACS Nano 12 (2018) 11282-11293.
[91] M. Liu, P. Huang, W. Wang, Z. Feng, J. Zhang, L. Deng, A. Dong, An injectable nanocomposite hydrogel co-constructed with gold nanorods and paclitaxel-loaded nanoparticles for local chemo-photothermal synergetic cancer therapy, Journal of Materials Chemistry B 7 (2019) 2667-2677.
[92] D. Jaque, F. Vetrone, Luminescence nanothermometry, Nanoscale 4 (2012) 4301-4326.
[93] E.J. McLaurin, L.R. Bradshaw, D.R. Gamelin, Dual-Emitting Nanoscale Temperature Sensors, Chemistry of Materials 25 (2013) 1283-1292.
[94] L. Shang, F. Stockmar, N. Azadfar, G.U. Nienhaus, Intracellular thermometry by using fluorescent gold nanoclusters, Angew. Chem., Int. Ed 52 (2013) 11154-11157.
[95] Y. Cui, F. Zhu, B. Chen, G. Qian, Metal–organic frameworks for luminescence thermometry, Chemical communications 51 (2015) 7420-7431.
[96] P. Haro-González, W.T. Ramsay, L.M. Maestro, B. del Rosal, K. Santacruz-Gomez, M. del Carmen Iglesias-de la Cruz, F. Sanz-Rodríguez, J.Y. Chooi, P.R. Sevilla, M. Bettinelli, D. Choudhury, A.K. Kar, J.G. Solé, D. Jaque, L. Paterson, Quantum Dot-Based Thermal Spectroscopy and Imaging of Optically Trapped Microspheres and Single Cells, Small 9 (2013) 2162-2170.
[97] S. Rohani, M. Quintanilla, S. Tuccio, F. De Angelis, E. Cantelar, A.O. Govorov, L. Razzari, F. Vetrone, Enhanced Luminescence, Collective Heating, and Nanothermometry in an Ensemble System Composed of Lanthanide-Doped Upconverting Nanoparticles and Gold Nanorods, Advanced Optical Materials 3 (2015) 1606-1613.
[98] D. Wawrzynczyk, A. Bednarkiewicz, M. Nyk, M. Gordel, W. Strek, M. Samoc, Modulation of up-conversion luminescence of lanthanide (III) ion co-doped NaYF4 nanoparticles using gold nanorods, Optical Materials 34 (2012) 1708-1712.
[99] F. Kang, J. He, T. Sun, Z.Y. Bao, F. Wang, D.Y. Lei, Plasmonic Dual-Enhancement and Precise Color Tuning of Gold Nanorod@SiO2 Coupled Core–Shell–Shell Upconversion Nanocrystals, Advanced Functional Materials 27 (2017) 1701842.
[100] M.-H. Chan, S.-P. Chen, C.-W. Chen, Y.-C. Chan, R.J. Lin, D.P. Tsai, M. Hsiao, R.-J. Chung, X. Chen, R.-S. Liu, Single 808 nm laser treatment comprising photothermal and photodynamic therapies by using gold nanorods hybrid upconversion particles, The Journal of Physical Chemistry C 122 (2018) 2402-2412.
[101] C.-W. Chen, Y.-C. Chan, M. Hsiao, R.-S. Liu, Plasmon-Enhanced Photodynamic Cancer Therapy by Upconversion Nanoparticles Conjugated with Au Nanorods, ACS Applied Materials & Interfaces 8 (2016) 32108-32119.
[102] M. Runowski, S. Goderski, J. Paczesny, M. Ksiezopolska-Gocalska, A. Ekner-Grzyb, T. Grzyb, J.D. Rybka, M. Giersig, S. Lis, Preparation of biocompatible, luminescent-plasmonic core/shell nanomaterials based on lanthanide and gold nanoparticles exhibiting SERS effects, The Journal of Physical Chemistry C 120 (2016) 23788-23798.
[103] M. Haase, H. Schäfer, Upconverting Nanoparticles, Angewandte Chemie International Edition 50 (2011) 5808-5829.
[104] C. Chen, C. Li, Z. Shi, Current Advances in Lanthanide-Doped Upconversion Nanostructures for Detection and Bioapplication, Advanced Science 3 (2016) 1600029.
[105] F. Auzel, Upconversion and Anti-Stokes Processes with f and d Ions in Solids, Chemical Reviews 104 (2004) 139-174.

[106] H. Dong, L.-D. Sun, C.-H. Yan, Basic understanding of the lanthanide related upconversion emissions, Nanoscale 5 (2013) 5703-5714.
[107] S.L. Maurizio, G. Tessitore, K.W. Krämer, J.A. Capobianco, BaYF5:Yb3+,Tm3+ Upconverting Nanoparticles with Improved Population of the Visible and Near-Infrared Emitting States: Implications for Bioimaging, ACS Applied Nano Materials 4 (2021) 5301-5308.
[108] D.T. Vu, T.T. Vu-Le, V.N. Nguyen, Q.M. Le, C.-R.C. Wang, L.-K. Chau, T.-S. Yang, M.W.Y. Chan, C.-I. Lee, C.-C. Ting, J.-Y. Lin, H.-C. Kan, C.C. Hsu, Gold nanorods conjugated upconversion nanoparticles nanocomposites for simultaneous bioimaging, local temperature sensing and photothermal therapy of OML-1 oral cancer cells, International Journal of Smart and Nano Materials 12 (2021) 49-71.
[109] K. Nigoghossian, S. Ouellet, J. Plain, Y. Messaddeq, D. Boudreau, S.J. Ribeiro, Upconversion nanoparticle-decorated gold nanoshells for near-infrared induced heating and thermometry, Journal of materials chemistry B 5 (2017) 7109-7117.
[110] N. Wu, Y. Sun, M. Kong, X. Lin, C. Cao, Z. Li, W. Feng, F. Li, Er-Based Luminescent Nanothermometer to Explore the Real-Time Temperature of Cells under External Stimuli, Small 18 (2022) 2107963.
[111] I.Y. Yanina, E. Volkova, A. Zaharevich, J. Konyukhova, V. Kochubey, V. Tuchin, Temperature sensing of adipose tissue heating with the luminescent upconversion nanoparticles as nanothermometer: in vitro study, Dynamics and Fluctuations in Biomedical Photonics XIV, SPIE, 2017, pp. 153-162.
[112] C. Wang, C. Xu, L. Xu, C. Sun, D. Yang, J. Xu, F. He, S. Gai, P. Yang, A novel core–shell structured upconversion nanorod as a multimodal bioimaging and photothermal ablation agent for cancer theranostics, Journal of Materials Chemistry B 6 (2018) 2597-2607.
[113] M. Sun, L. Xu, W. Ma, X. Wu, H. Kuang, L. Wang, C. Xu, Hierarchical Plasmonic Nanorods and Upconversion Core-Satellite Nanoassemblies for Multimodal Imaging-Guided Combination Phototherapy, Advanced materials (Deerfield Beach, Fla.) 28 (2016) 898-904.
[114] S. Zhang, J. Wang, W. Xu, B. Chen, W. Yu, L. Xu, H. Song, Fluorescence resonance energy transfer between NaYF4:Yb,Tm upconversion nanoparticles and gold nanorods: Near-infrared responsive biosensor for streptavidin, Journal of Luminescence 147 (2014) 278-283.
[115] C.-W. Chen, P.-H. Lee, Y.-C. Chan, M. Hsiao, C.-H. Chen, P.C. Wu, P.R. Wu, D.P. Tsai, D. Tu, X. Chen, Plasmon-induced hyperthermia: hybrid upconversion NaYF 4: Yb/Er and gold nanomaterials for oral cancer photothermal therapy, Journal of Materials Chemistry B 3 (2015) 8293-8302.
[116] Y. Liu, F. Mo, J. Hu, Q. Jiang, X. Wang, Z. Zou, X.-Z. Zhang, D.-W. Pang, X. Liu, Precision photothermal therapy and photoacoustic imaging by in situ activatable thermoplasmonics, Chemical Science 12 (2021) 10097-10105.
[117] S.H. Yun, S.J.J. Kwok, Light in diagnosis, therapy and surgery, Nature Biomedical Engineering 1 (2017) 0008.
[118] X. Zhao, Y. Shi, T. Pan, D. Lu, J. Xiong, B. Li, H. Xin, In Situ Single-Cell Surgery and Intracellular Organelle Manipulation Via Thermoplasmonics Combined Optical Trapping, Nano Letters 22 (2022) 402-410.
[119] V. Ramalingam, Chapter 10 - Silver nanoparticles for biomedical applications, in: P. Kesharwani, K.K. Singh (Eds.), Nanoparticle Therapeutics, Academic Press2022, pp. 359-375.
[120] A. Samadi, H. Klingberg, L. Jauffred, A. Kjær, P.M. Bendix, L.B. Oddershede, Platinum nanoparticles: a non-toxic, effective and thermally stable alternative plasmonic material for cancer therapy and bioengineering, Nanoscale 10 (2018) 9097-9107.
[121] S. Wang, X. Zhao, S. Wang, J. Qian, S. He, Biologically Inspired Polydopamine Capped Gold Nanorods for Drug Delivery and Light-Mediated Cancer Therapy, ACS Applied Materials & Interfaces 8 (2016) 24368-24384.

[122] M.P. Melancon, W. Lu, Z. Yang, R. Zhang, Z. Cheng, A.M. Elliot, J. Stafford, T. Olson, J.Z. Zhang, C. Li, In vitro and in vivo targeting of hollow gold nanoshells directed at epidermal growth factor receptor for photothermal ablation therapy, Mol Cancer Ther 7 (2008) 1730-1739.
[123] J. Chen, D. Wang, J. Xi, L. Au, A. Siekkinen, A. Warsen, Z.-Y. Li, H. Zhang, Y. Xia, X. Li, Immuno Gold Nanocages with Tailored Optical Properties for Targeted Photothermal Destruction of Cancer Cells, Nano Letters 7 (2007) 1318-1322.
[124] H. Yuan, C.G. Khoury, C.M. Wilson, G.A. Grant, A.J. Bennett, T. Vo-Dinh, In vivo particle tracking and photothermal ablation using plasmon-resonant gold nanostars, Nanomedicine 8 (2012) 1355-1363.
[125] Y.-T. Liao, C.-H. Liu, Y. Chin, S.-Y. Chen, S.H. Liu, Y.-C. Hsu, K.C.W. Wu, Biocompatible and multifunctional gold nanorods for effective photothermal therapy of oral squamous cell carcinoma, Journal of Materials Chemistry B 7 (2019) 4451-4460.
[126] C. Loo, A. Lowery, N. Halas, J. West, R. Drezek, Immunotargeted Nanoshells for Integrated Cancer Imaging and Therapy, Nano Letters 5 (2005) 709-711.
[127] R. Bardhan, W. Chen, C. Perez-Torres, M. Bartels, R.M. Huschka, L.L. Zhao, E. Morosan, R.G. Pautler, A. Joshi, N.J. Halas, Nanoshells with Targeted Simultaneous Enhancement of Magnetic and Optical Imaging and Photothermal Therapeutic Response, Advanced Functional Materials 19 (2009) 3901-3909.
[128] W.I. Choi, A. Sahu, Y.H. Kim, G. Tae, Photothermal Cancer Therapy and Imaging Based on Gold Nanorods, Annals of Biomedical Engineering 40 (2012) 534-546.
[129] W. Li, X. Chen, Gold nanoparticles for photoacoustic imaging, Nanomedicine 10 (2015) 299-320.
[130] X. Huang, I.H. El-Sayed, W. Qian, M.A. El-Sayed, Cancer Cells Assemble and Align Gold Nanorods Conjugated to Antibodies to Produce Highly Enhanced, Sharp, and Polarized Surface Raman Spectra: A Potential Cancer Diagnostic Marker, Nano Letters 7 (2007) 1591-1597.
[131] D. Pissuwan, S.M. Valenzuela, M.B. Cortie, Prospects for Gold Nanorod Particles in Diagnostic and Therapeutic Applications, Biotechnology and Genetic Engineering Reviews 25 (2008) 93-112.
[132] H.N. Green, D.V. Martyshkin, C.M. Rodenburg, E.L. Rosenthal, S.B. Mirov, Gold Nanorod Bioconjugates for Active Tumor Targeting and Photothermal Therapy, Journal of Nanotechnology 2011 (2011) 631753.
[133] A.M. Alkilany, L.B. Thompson, S.P. Boulos, P.N. Sisco, C.J. Murphy, Gold nanorods: Their potential for photothermal therapeutics and drug delivery, tempered by the complexity of their biological interactions, Advanced Drug Delivery Reviews 64 (2012) 190-199.
[134] S.L. Jacques, Optical properties of biological tissues: a review, Physics in Medicine & Biology 58 (2013) R37.
[135] S. He, J. Song, J. Qu, Z. Cheng, Crucial breakthrough of second near-infrared biological window fluorophores: design and synthesis toward multimodal imaging and theranostics, Chemical Society Reviews 47 (2018) 4258-4278.
[136] R. Weissleder, A clearer vision for in vivo imaging, Nature Biotechnology 19 (2001) 316-317.
[137] V. Ntziachristos, A. Yodh, M. Schnall, B. Chance, Concurrent MRI and diffuse optical tomography of breast after indocyanine green enhancement, Proceedings of the National Academy of Sciences 97 (2000) 2767-2772.
[138] N.S. Abadeer, M.R. Brennan, W.L. Wilson, C.J. Murphy, Distance and Plasmon Wavelength Dependent Fluorescence of Molecules Bound to Silica-Coated Gold Nanorods, ACS Nano 8 (2014) 8392-8406.

[139] X.L. Deán-Ben, S. Gottschalk, B. Mc Larney, S. Shoham, D. Razansky, Advanced optoacoustic methods for multiscale imaging of in vivo dynamics, Chemical Society Reviews 46 (2017) 2158-2198.
[140] P. International Commission on Non-Ionizing Radiation, ICNIRP Guidelines on Limits of Exposure to Laser Radiation of Wavelengths between 180 nm and 1,000 μm, Health Physics 105 (2013).
[141] D.J. Naczynski, M.C. Tan, M. Zevon, B. Wall, J. Kohl, A. Kulesa, S. Chen, C.M. Roth, R.E. Riman, P.V. Moghe, Rare-earth-doped biological composites as in vivo shortwave infrared reporters, Nature Communications 4 (2013) 2199.
[142] G.S. Terentyuk, G.N. Maslyakova, L.V. Suleymanova, N.G. Khlebtsov, B.N. Khlebtsov, G.G. Akchurin, I.L. Maksimova, V.V. Tuchin, Laser-induced tissue hyperthermia mediated by gold nanoparticles: toward cancer phototherapy, J Biomed Opt 14 (2009) 021016.
[143] E.B. Dickerson, E.C. Dreaden, X. Huang, I.H. El-Sayed, H. Chu, S. Pushpanketh, J.F. McDonald, M.A. El-Sayed, Gold nanorod assisted near-infrared plasmonic photothermal therapy (PPTT) of squamous cell carcinoma in mice, Cancer Letters 269 (2008) 57-66.
[144] M. Nejabat, A. Samie, M. Ramezani, M. Alibolandi, K. Abnous, S.M. Taghdisi, An Overview on Gold Nanorods as Versatile Nanoparticles in Cancer Therapy, Journal of Controlled Release 354 (2023) 221-242.
[145] F.B. Ahmad, R.N. Anderson, The Leading Causes of Death in the US for 2020, JAMA 325 (2021) 1829-1830.
[146] E. Bidram, Y. Esmaeili, H. Ranji-Burachaloo, N. Al-Zaubai, A. Zarrabi, A. Stewart, D.E. Dunstan, A concise review on cancer treatment methods and delivery systems, Journal of Drug Delivery Science and Technology 54 (2019) 101350.
[147] I.H. El-Sayed, X. Huang, M.A. El-Sayed, Selective laser photo-thermal therapy of epithelial carcinoma using anti-EGFR antibody conjugated gold nanoparticles, Cancer Letters 239 (2006) 129-135.
[148] J. Kim, S. Park, J.E. Lee, S.M. Jin, J.H. Lee, I.S. Lee, I. Yang, J.-S. Kim, S.K. Kim, M.-H. Cho, T. Hyeon, Designed Fabrication of Multifunctional Magnetic Gold Nanoshells and Their Application to Magnetic Resonance Imaging and Photothermal Therapy, Angewandte Chemie International Edition 45 (2006) 7754-7758.
[149] X. Huang, I.H. El-Sayed, W. Qian, M.A. El-Sayed, Cancer Cell Imaging and Photothermal Therapy in the Near-Infrared Region by Using Gold Nanorods, J Am Chem Soc 128 (2006) 2115-2120.
[150] W.-q. Li, C.-y. Sun, F. Wang, Y.-c. Wang, Y.-w. Zhai, M. Liang, W.-j. Liu, Z.-m. Liu, J. Wang, F. Sun, Achieving a New Controllable Male Contraception by the Photothermal Effect of Gold Nanorods, Nano Letters 13 (2013) 2477-2484.
[151] A.F. Bagley, S. Hill, G.S. Rogers, S.N. Bhatia, Plasmonic Photothermal Heating of Intraperitoneal Tumors through the Use of an Implanted Near-Infrared Source, ACS Nano 7 (2013) 8089-8097.
[152] K.H. Min, Y.H. Kim, Z. Wang, J. Kim, J.S. Kim, S.H. Kim, K. Kim, I.C. Kwon, D.O. Kiesewetter, X. Chen, Engineered Zn(II)-Dipicolylamine-Gold Nanorod Provides Effective Prostate Cancer Treatment by Combining siRNA Delivery and Photothermal Therapy, Theranostics 7 (2017) 4240-4254.
[153] X. Kang, X. Guo, X. Niu, W. An, S. Li, Z. Liu, Y. Yang, N. Wang, Q. Jiang, C. Yan, H. Wang, Q. Zhang, Photothermal therapeutic application of gold nanorods-porphyrin-trastuzumab complexes in HER2-positive breast cancer, Scientific Reports 7 (2017) 42069.
[154] Y. Yang, J. Zhang, F. Xia, C. Zhang, Q. Qian, X. Zhi, C. Yue, R. Sun, S. Cheng, S. Fang, W. Jin, Y. Yang, D. Cui, Human CIK Cells Loaded with Au Nanorods as a Theranostic Platform for Targeted Photoacoustic Imaging and Enhanced Immunotherapy and Photothermal Therapy, Nanoscale Research Letters 11 (2016) 285.

[155] R. Chandrasekaran, A.S.W. Lee, L.W. Yap, D.A. Jans, K.M. Wagstaff, W. Cheng, Tumor cell-specific photothermal killing by SELEX-derived DNA aptamer-targeted gold nanorods, Nanoscale 8 (2016) 187-196.
[156] Y. Noh, M.-J. Kim, H. Mun, E.-J. Jo, H. Lee, M.-G. Kim, Aptamer-based selective KB cell killing by the photothermal effect of gold nanorods, Journal of Nanoparticle Research 21 (2019) 112.
[157] M.R.K. Ali, H.R. Ali, C.R. Rankin, M.A. El-Sayed, Targeting heat shock protein 70 using gold nanorods enhances cancer cell apoptosis in low dose plasmonic photothermal therapy, Biomaterials 102 (2016) 1-8.
[158] P. Orosz, B. Echtenacher, W. Falk, J. Rüschoff, D. Weber, D.N. Männel, Enhancement of experimental metastasis by tumor necrosis factor, Journal of Experimental Medicine 177 (1993) 1391-1398.
[159] P. Davidovich, C.J. Kearney, S.J. Martin, Inflammatory outcomes of apoptosis, necrosis and necroptosis, Biological Chemistry 395 (2014) 1163-1171.
[160] E. Miyako, T. Deguchi, Y. Nakajima, M. Yudasaka, Y. Hagihara, M. Horie, M. Shichiri, Y. Higuchi, F. Yamashita, M. Hashida, Photothermic regulation of gene expression triggered by laser-induced carbon nanohorns, Proceedings of the National Academy of Sciences 109 (2012) 7523-7528.
[161] A. Burke, X. Ding, R. Singh, R.A. Kraft, N. Levi-Polyachenko, M.N. Rylander, C. Szot, C. Buchanan, J. Whitney, J. Fisher, Long-term survival following a single treatment of kidney tumors with multiwalled carbon nanotubes and near-infrared radiation, Proceedings of the National Academy of Sciences 106 (2009) 12897-12902.
[162] N. Larson, A. Gormley, N. Frazier, H. Ghandehari, Synergistic enhancement of cancer therapy using a combination of heat shock protein targeted HPMA copolymer–drug conjugates and gold nanorod induced hyperthermia, Journal of Controlled Release 170 (2013) 41-50.
[163] T. Seki, M. Wakabayashi, T. Nakagawa, M. Imamura, T. Tamai, A. Nishimura, N. Yamashiki, A. Okamura, K. Inoue, Percutaneous microwave coagulation therapy for patients with small hepatocellular carcinoma, Cancer 85 (1999) 1694-1702.
[164] G.S. Gazelle, S.N. Goldberg, L. Solbiati, T. Livraghi, Tumor Ablation with Radio-frequency Energy, Radiology 217 (2000) 633-646.
[165] I. Hilger, R. Hiergeist, R. Hergt, K. Winnefeld, H. Schubert, W.A. Kaiser, Thermal Ablation of Tumors Using Magnetic Nanoparticles: An In Vivo Feasibility Study, Investigative Radiology 37 (2002).
[166] F.A. Jolesz, K. Hynynen, Magnetic resonance image-guided focused ultrasound surgery, Cancer J 8 Suppl 1 (2002) S100-112.
[167] A. Guglielmelli, F. Pierini, N. Tabiryan, C. Umeton, T.J. Bunning, L. De Sio, Thermoplasmonics with Gold Nanoparticles: A New Weapon in Modern Optics and Biomedicine, Advanced Photonics Research 2 (2021) 2000198.
[168] X. Huang, P.K. Jain, I.H. El-Sayed, M.A. El-Sayed, Determination of the Minimum Temperature Required for Selective Photothermal Destruction of Cancer Cells with the Use of Immunotargeted Gold Nanoparticles, Photochemistry and Photobiology 82 (2006) 412-417.
[169] W.R. Chen, R.L. Adams, A.K. Higgins, K.E. Bartels, R.E. Nordquist, Photothermal effects on murine mammary tumors using indocyanine green and an 808-nm diode laser: an in vivo efficacy study, Cancer Letters 98 (1996) 169-173.
[170] M. Ferrari, Cancer nanotechnology: opportunities and challenges, Nature Reviews Cancer 5 (2005) 161-171.
[171] C.-C. Chen, Y.-P. Lin, C.-W. Wang, H.-C. Tzeng, C.-H. Wu, Y.-C. Chen, C.-P. Chen, L.-C. Chen, Y.-C. Wu, DNA−Gold Nanorod Conjugates for Remote Control of Localized Gene Expression by near Infrared Irradiation, J Am Chem Soc 128 (2006) 3709-3715.

[172] A. Wijaya, S.B. Schaffer, I.G. Pallares, K. Hamad-Schifferli, Selective Release of Multiple DNA Oligonucleotides from Gold Nanorods, ACS Nano 3 (2009) 80-86.
[173] H. Takahashi, Y. Niidome, S. Yamada, Controlled release of plasmid DNA from gold nanorods induced by pulsed near-infrared light, Chemical communications (2005) 2247-2249.
[174] S.E. Lee, D.Y. Sasaki, T.D. Perroud, D. Yoo, K.D. Patel, L.P. Lee, Biologically Functional Cationic Phospholipid−Gold Nanoplasmonic Carriers of RNA, J Am Chem Soc 131 (2009) 14066-14074.
[175] R. Huschka, J. Zuloaga, M.W. Knight, L.V. Brown, P. Nordlander, N.J. Halas, Light-induced release of DNA from gold nanoparticles: nanoshells and nanorods, J Am Chem Soc 133 (2011) 12247-12255.
[176] J. Liao, W. Li, J. Peng, Q. Yang, H. Li, Y. Wei, X. Zhang, Z. Qian, Combined cancer photothermal-chemotherapy based on doxorubicin/gold nanorod-loaded polymersomes, Theranostics 5 (2015) 345-356.
[177] F. Ren, S. Bhana, D.D. Norman, J. Johnson, L. Xu, D.L. Baker, A.L. Parrill, X. Huang, Gold Nanorods Carrying Paclitaxel for Photothermal-Chemotherapy of Cancer, Bioconjugate Chemistry 24 (2013) 376-386.
[178] D.V. Peralta, Z. Heidari, S. Dash, M.A. Tarr, Hybrid Paclitaxel and Gold Nanorod-Loaded Human Serum Albumin Nanoparticles for Simultaneous Chemotherapeutic and Photothermal Therapy on 4T1 Breast Cancer Cells, ACS Applied Materials & Interfaces 7 (2015) 7101-7111.
[179] J. Huang, K.S. Jackson, C.J. Murphy, Polyelectrolyte Wrapping Layers Control Rates of Photothermal Molecular Release from Gold Nanorods, Nano Letters 12 (2012) 2982-2987.
[180] T. Kawano, Y. Niidome, T. Mori, Y. Katayama, T. Niidome, PNIPAM Gel-Coated Gold Nanorods for Targeted Delivery Responding to a Near-Infrared Laser, Bioconjugate Chemistry 20 (2009) 209-212.
[181] Y. Zhong, C. Wang, L. Cheng, F. Meng, Z. Zhong, Z. Liu, Gold Nanorod-Cored Biodegradable Micelles as a Robust and Remotely Controllable Doxorubicin Release System for Potent Inhibition of Drug-Sensitive and -Resistant Cancer Cells, Biomacromolecules 14 (2013) 2411-2419.
[182] T.S. Hauck, T.L. Jennings, T. Yatsenko, J.C. Kumaradas, W.C.W. Chan, Enhancing the Toxicity of Cancer Chemotherapeutics with Gold Nanorod Hyperthermia, Advanced Materials 20 (2008) 3832-3838.
[183] M.S. Khan, M.L. Bhaisare, J. Gopal, H.-F. Wu, Highly efficient gold nanorods assisted laser phototherapy for rapid treatment on mice wound infected by pathogenic bacteria, Journal of Industrial and Engineering Chemistry 36 (2016) 49-58.
[184] R.F. Diegelmann, M.C. Evans, Wound healing: an overview of acute, fibrotic and delayed healing, Front biosci 9 (2004) 283-289.
[185] M.C. Robson, T.A. Mustoe, T.K. Hunt, The future of recombinant growth factors in wound healing, The American journal of surgery 176 (1998) 80S-82S.
[186] A.J. Makowski, J.M. Davidson, A. Mahadevan-Jansen, E.D. Jansen, In vivo analysis of laser preconditioning in incisional wound healing of wild-type and HSP70 knockout mice with Raman spectroscopy, Lasers in surgery and medicine 44 (2012) 233-244.
[187] A.R. Medrado, L.S. Pugliese, S.R.A. Reis, Z.A. Andrade, Influence of low level laser therapy on wound healing and its biological action upon myofibroblasts, Lasers in surgery and medicine 32 (2003) 239-244.
[188] C.L. Baum, C.J. Arpey, Normal cutaneous wound healing: clinical correlation with cellular and molecular events, Dermatologic surgery 31 (2005) 674-686.
[189] S.S. Nanda, T. Wang, M.I. Hossain, H.Y. Yoon, S.T. Selvan, K. Kim, D.K. Yi, Gold-nanorod-based scaffolds for wound-healing applications, ACS Applied Nano Materials 5 (2022) 8640-8648.

[190] X. He, L. Dai, L. Ye, X. Sun, O. Enoch, R. Hu, X. Zan, F. Lin, J. Shen, A Vehicle-Free Antimicrobial Polymer Hybrid Gold Nanoparticle as Synergistically Therapeutic Platforms for Staphylococcus aureus Infected Wound Healing, Advanced Science 9 (2022) 2105223.
[191] X. Xu, X. Liu, L. Tan, Z. Cui, X. Yang, S. Zhu, Z. Li, X. Yuan, Y. Zheng, K.W.K. Yeung, P.K. Chu, S. Wu, Controlled-temperature photothermal and oxidative bacteria killing and acceleration of wound healing by polydopamine-assisted Au-hydroxyapatite nanorods, Acta Biomaterialia 77 (2018) 352-364.
[192] X. Xu, Y. Ding, R. Hadianamrei, S. Lv, R. You, F. Pan, P. Zhang, N. Wang, X. Zhao, Antimicrobial peptide functionalized gold nanorods combining near-infrared photothermal therapy for effective wound healing, Colloids and Surfaces B: Biointerfaces 220 (2022) 112887.
[193] J.E. Kim, J. Lee, M. Jang, M.H. Kwak, J. Go, E.K. Kho, S.H. Song, J.E. Sung, J. Lee, D.Y. Hwang, Accelerated healing of cutaneous wounds using phytochemically stabilized gold nanoparticle deposited hydrocolloid membranes, Biomaterials science 3 (2015) 509-519.
[194] N.N. Mahmoud, S. Hikmat, D.A. Ghith, M. Hajeer, L. Hamadneh, D. Qattan, E.A. Khalil, Gold nanoparticles loaded into polymeric hydrogel for wound healing in rats: Effect of nanoparticles' shape and surface modification, International journal of pharmaceutics 565 (2019) 174-186.
[195] M.G. Arafa, R.F. El-Kased, M.M. Elmazar, Thermoresponsive gels containing gold nanoparticles as smart antibacterial and wound healing agents, Scientific reports 8 (2018) 13674.
[196] X. Huang, L. Xu, X. Yu, Y. Li, Z. Huang, R. Xu, W. Zeng, Z. Zhang, W. Li, F. Deng, Near-infrared light-responsive multifunctional hydrogel releasing peptide-functionalized gold nanorods sequentially for diabetic wound healing, Journal of Colloid and Interface Science 639 (2023) 369-384.
[197] H.A. Andersson, Y.-S. Kim, B.E. O'Neill, Z.-Z. Shi, R.E. Serda, HSP70 promoter-driven activation of gene expression for immunotherapy using gold nanorods and near infrared light, Vaccines 2 (2014) 216-227.
[198] M.S.B. Sadeque, H.K. Chowdhury, M. Rafique, M.A. Durmuş, M.K. Ahmed, M.M. Hasan, A. Erbaş, İ. Sarpkaya, F. Inci, M. Ordu, Hydrogel-integrated optical fiber sensors and their applications: a comprehensive review, Journal of Materials Chemistry C 11 (2023) 9383-9424.
[199] H. Mukundan, A.S. Anderson, W.K. Grace, K.M. Grace, N. Hartman, J.S. Martinez, B.I. Swanson, Waveguide-Based Biosensors for Pathogen Detection, Sensors 9 (2009) 5783-5809.
[200] Y. Choi, C. Yoon, M. Kim, T.D. Yang, C. Fang-Yen, R.R. Dasari, K.J. Lee, W. Choi, Scanner-Free and Wide-Field Endoscopic Imaging by Using a Single Multimode Optical Fiber, Physical Review Letters 109 (2012) 203901.
[201] Y. Zhang, J. Zheng, F. Jin, J. Xiao, N. Lan, Z. Xu, X. Yue, Z. Li, C. Li, D. Cao, Y. Wang, W. Zhong, Y. Ran, B.-O. Guan, Fiber-optic drug delivery strategy for synergistic cancer photothermal-chemotherapy, Light: Science & Applications 13 (2024) 228.
[202] P.Y.M. Yew, P.L. Chee, Q. Lin, C. Owh, J. Li, Q.Q. Dou, X.J. Loh, D. Kai, Y. Zhang, Hydrogel for light delivery in biomedical applications, Bioactive Materials 37 (2024) 407-423.
[203] M. Choi, M. Humar, S. Kim, S.H. Yun, Step-Index Optical Fiber Made of Biocompatible Hydrogels, Adv Mater 27 (2015) 4081-4086.
[204] C.F. Guimarães, R. Ahmed, A.P. Marques, R.L. Reis, U. Demirci, Engineering Hydrogel-Based Biomedical Photonics: Design, Fabrication, and Applications, Advanced Materials 33 (2021) 2006582.

[205] M. Choi, J.W. Choi, S. Kim, S. Nizamoglu, S.K. Hahn, S.H. Yun, Light-guiding hydrogels for cell-based sensing and optogenetic synthesis in vivo, Nature Photonics 7 (2013) 987-994.
[206] A. Jain, A.H.J. Yang, D. Erickson, Gel-based optical waveguides with live cell encapsulation and integrated microfluidics, Opt. Lett. 37 (2012) 1472-1474.
[207] G. Chen, K. Hou, N. Yu, P. Wei, T. Chen, C. Zhang, S. Wang, H. Liu, R. Cao, L. Zhu, B.S. Hsiao, M. Zhu, Temperature-adaptive hydrogel optical waveguide with soft tissue-affinity for thermal regulated interventional photomedicine, Nature Communications 13 (2022) 7789.
[208] Z. Kafrashian, S. Brück, P. Rogin, M. Khamdan, H.S.U.B. Farrukh, S. Pearson, A. del Campo, Segmented, Side-Emitting Hydrogel Optical Fibers for Multimaterial Extrusion Printing, Advanced Materials n/a (2024) 2309166.
[209] W. Hong, J. Lee, D. Kim, Y. Hwang, H.-J. Kwon, J.E. Jang, H. Kang, Computational Thermal Analysis of the Photothermal Effect of Thermoplasmonic Optical Fiber for Localized Neural Stimulation In Vivo, Electronics 10 (2021) 118.
[210] J.A. Kim, Y. Hou, M. Keshavarz, E.M. Yeatman, A.J. Thompson, Characterization of bacteria swarming effect under plasmonic optical fiber illumination, Journal of Biomedical Optics 28 (2023) 075003.
[211] J.A. Kim, E.M. Yeatman, A.J. Thompson, Plasmonic optical fiber for bacteria manipulation—characterization and visualization of accumulation behavior under plasmo-thermal trapping, Biomed. Opt. Express 12 (2021) 3917-3933.
[212] H. Kang, W. Hong, Y. An, S. Yoo, H.-J. Kwon, Y. Nam, Thermoplasmonic Optical Fiber for Localized Neural Stimulation, ACS Nano 14 (2020) 11406-11419.
[213] M.A. Kurochkin, O.A. Sindeeva, E.P. Brodovskaya, M. Gai, J. Frueh, L. Su, A. Sapelkin, V.V. Tuchin, G.B. Sukhorukov, Laser-triggered drug release from polymeric 3-D micro-structured films via optical fibers, Materials Science and Engineering: C 110 (2020) 110664.
[214] X. Yu, S. Zhang, M. Olivo, N. Li, Micro- and nano-fiber probes for optical sensing, imaging, and stimulation in biomedical applications, Photon. Res. 8 (2020) 1703-1724.
[215] J. Cao, T. Sun, K.T.V. Grattan, Gold nanorod-based localized surface plasmon resonance biosensors: A review, Sensors and Actuators B: Chemical 195 (2014) 332-351.
[216] D. Chekkaramkodi, S.E. Turk, M. Ali, H. Butt, In-situ synthesis and integration of gold nanoparticles into 3D printed optical fiber probes, Scientific Reports 14 (2024) 29736.
[217] W. Gao, Y. Zhang, Q. Zhang, L. Zhang, Nanoparticle-Hydrogel: A Hybrid Biomaterial System for Localized Drug Delivery, Annals of Biomedical Engineering 44 (2016) 2049-2061.
[218] B.P. Purcell, D. Lobb, M.B. Charati, S.M. Dorsey, R.J. Wade, K.N. Zellars, H. Doviak, S. Pettaway, C.B. Logdon, J.A. Shuman, Injectable and bioresponsive hydrogels for on-demand matrix metalloproteinase inhibition, Nature materials 13 (2014) 653-661.
[219] N.A. Peppas, P. Bures, W. Leobandung, H. Ichikawa, Hydrogels in pharmaceutical formulations, European journal of pharmaceutics and biopharmaceutics 50 (2000) 27-46.
[220] B. Davaji, J.E. Richie, C.H. Lee, Microscale direct measurement of localized photothermal heating in tissue-mimetic hydrogels, Scientific Reports 9 (2019) 6546.
[221] M.W. Tibbitt, K.S. Anseth, Hydrogels as extracellular matrix mimics for 3D cell culture, Biotechnology and Bioengineering 103 (2009) 655-663.
[222] S.R. Sershen, S.L. Westcott, N.J. Halas, J.L. West, Temperature-sensitive polymer–nanoshell composites for photothermally modulated drug delivery, Journal of Biomedical Materials Research 51 (2000) 293-298.
[223] S.C.T. Moorcroft, L. Roach, D.G. Jayne, Z.Y. Ong, S.D. Evans, Nanoparticle-Loaded Hydrogel for the Light-Activated Release and Photothermal Enhancement of Antimicrobial Peptides, ACS Appl Mater Interfaces 12 (2020) 24544-24554.

[224] C. Wang, X. Liu, V. Wulf, M. Vázquez-González, M. Fadeev, I. Willner, DNA-Based Hydrogels Loaded with Au Nanoparticles or Au Nanorods: Thermoresponsive Plasmonic Matrices for Shape-Memory, Self-Healing, Controlled Release, and Mechanical Applications, ACS Nano 13 (2019) 3424-3433.
[225] Y. Qu, B.Y. Chu, J.R. Peng, J.F. Liao, T.T. Qi, K. Shi, X.N. Zhang, Y.Q. Wei, Z.Y. Qian, A biodegradable thermo-responsive hybrid hydrogel: therapeutic applications in preventing the post-operative recurrence of breast cancer, NPG Asia Materials 7 (2015) e207-e207.
[226] M. Qin, Y. Guo, F. Su, X. Huang, Q. Qian, Y. Zhou, J. Pan, High-strength, fatigue-resistant, and fast self-healing antibacterial nanocomposite hydrogels for wound healing, Chemical Engineering Journal 455 (2023) 140854.
[227] Y. Chen, X. Hao, Z. Lu, D. Wang, Near-IR-Regulated Composite Hydrogel with Real-Time Infection Monitoring and a Combined Antibacterial Effect for Efficient Wound Management, ACS Applied Materials & Interfaces 15 (2023) 40255-40266.
[228] M. Hyun, C. Choi, Y. Kim, Thermoresponsive polymer-hollow gold nanoparticle composites for effective photothermal sterilization as a potential wound dressing film, Colloids and Surfaces A: Physicochemical and Engineering Aspects 704 (2025) 135520.
[229] Z. Cao, D. Wang, Y. Li, W. Xie, X. Wang, L. Tao, Y. Wei, X. Wang, L. Zhao, Effect of nanoheat stimulation mediated by magnetic nanocomposite hydrogel on the osteogenic differentiation of mesenchymal stem cells, Sci China Life Sci 61 (2018) 448-456.
[230] S. Agnihotri, S. Mukherji, S. Mukherji, Antimicrobial chitosan–PVA hydrogel as a nanoreactor and immobilizing matrix for silver nanoparticles, Applied Nanoscience 2 (2012) 179-188.
[231] Y.Y. Liang, L.M. Zhang, W. Jiang, W. Li, Embedding magnetic nanoparticles into polysaccharide-based hydrogels for magnetically assisted bioseparation, Chemphyschem 8 (2007) 2367-2372.
[232] M. Bikram, A.M. Gobin, R.E. Whitmire, J.L. West, Temperature-sensitive hydrogels with SiO2–Au nanoshells for controlled drug delivery, Journal of Controlled Release 123 (2007) 219-227.
[233] R. Xing, K. Liu, T. Jiao, N. Zhang, K. Ma, R. Zhang, Q. Zou, G. Ma, X. Yan, An Injectable Self-Assembling Collagen–Gold Hybrid Hydrogel for Combinatorial Antitumor Photothermal/Photodynamic Therapy, Advanced Materials 28 (2016) 3669-3676.
[234] C.W. Peak, S. Nagar, R.D. Watts, G. Schmidt, Robust and Degradable Hydrogels from Poly(ethylene glycol) and Semi-Interpenetrating Collagen, Macromolecules 47 (2014) 6408-6417.
[235] T. Li, M. Zhang, J. Wang, T. Wang, Y. Yao, X. Zhang, C. Zhang, N. Zhang, Thermosensitive Hydrogel Co-loaded with Gold Nanoparticles and Doxorubicin for Effective Chemoradiotherapy, The AAPS Journal 18 (2016) 146-155.
[236] M. Fargharazi, M.M. Bagheri-Mohagheghi, Enhanced photothermal performance and water purification via silver and gold plasmonic nanoparticles in polyvinyl alcohol: glutaraldehyde/activated carbon hydrogel, Optical and Quantum Electronics 56 (2024) 1102.
[237] T.-R. Kuo, V.A. Hovhannisyan, Y.-C. Chao, S.-L. Chao, S.-J. Chiang, S.-J. Lin, C.-Y. Dong, C.-C. Chen, Multiple Release Kinetics of Targeted Drug from Gold Nanorod Embedded Polyelectrolyte Conjugates Induced by Near-Infrared Laser Irradiation, J Am Chem Soc 132 (2010) 14163-14171.
[238] A.G. Skirtach, C. Dejugnat, D. Braun, A.S. Susha, A.L. Rogach, W.J. Parak, H. Möhwald, G.B. Sukhorukov, The Role of Metal Nanoparticles in Remote Release of Encapsulated Materials, Nano Letters 5 (2005) 1371-1377.
[239] K.C. Hribar, M.H. Lee, D. Lee, J.A. Burdick, Enhanced Release of Small Molecules from Near-Infrared Light Responsive Polymer−Nanorod Composites, ACS Nano 5 (2011) 2948-2956.

[240] Y.-C. Chuang, H.-L. Lee, J.-F. Chiou, L.-W. Lo, Recent Advances in Gold Nanomaterials for Photothermal Therapy, Journal of Nanotheranostics 3 (2022) 117-131.
[241] D. Valdeperez, N. Wutke, L.-M. Ackermann, W.J. Parak, M. Klapper, B. Pelaz, Colloidal stability of polymer coated zwitterionic Au nanoparticles in biological media, Inorganica Chimica Acta 534 (2022) 120820.
[242] B. Miranda, R. Moretta, S. De Martino, P. Dardano, I. Rea, C. Forestiere, L. De Stefano, A PEGDA hydrogel nanocomposite to improve gold nanoparticles stability for novel plasmonic sensing platforms, Journal of Applied Physics 129 (2021).
[243] N.N. Mahmoud, R. Hamed, E.A. Khalil, Colloidal stability and rheological properties of gold nanoparticle–loaded polymeric hydrogels: impact of nanoparticle's shape, surface modification, and concentration, Colloid and Polymer Science 298 (2020) 989-999.
[244] F.L. Heredia, P.J. Resto, E.I. Parés-Matos, Fast Adhesion of Gold Nanoparticles (AuNPs) to a Surface Using Starch Hydrogels for Characterization of Biomolecules in Biosensor Applications, Biosensors 10 (2020) 99.
[245] P.J. Moncure, J.E. Millstone, J.E. Laaser, Role of Ligand Shell Density in the Diffusive Behavior of Nanoparticles in Hydrogels, The Journal of Physical Chemistry B 127 (2023) 9366-9377.
[246] D. Ishikawa, K. Maruyama, M. Hara, DNA Motifs Hydrogel Microparticles as Gold Nanocatalyst Support Material, Particle & Particle Systems Characterization n/a 2400060.
[247] J. Rodriguez-Loya, M. Lerma, J.L. Gardea-Torresdey, Dynamic Light Scattering and Its Application to Control Nanoparticle Aggregation in Colloidal Systems: A Review, Micromachines 15 (2024) 24.
[248] K. Rahme, M.T. Nolan, T. Doody, G.P. McGlacken, M.A. Morris, C. O'Driscoll, J.D. Holmes, Highly stable PEGylated gold nanoparticles in water: applications in biology and catalysis, RSC Advances 3 (2013) 21016-21024.
[249] K. Schulz-Schönhagen, N. Lobsiger, W.J. Stark, Continuous Production of a Shelf-Stable Living Material as a Biosensor Platform, Advanced materials technologies 4 (2019) 1900266.
[250] C. Zhang, J. Huang, J. Zhang, S. Liu, M. Cui, B. An, X. Wang, J. Pu, T. Zhao, C. Fan, Engineered Bacillus subtilis biofilms as living glues, Materials Today 28 (2019) 40-48.
[251] J. Pu, Y. Liu, J. Zhang, B. An, Y. Li, X. Wang, K. Din, C. Qin, K. Li, M. Cui, Virus disinfection from environmental water sources using living engineered biofilm materials, Advanced Science 7 (2020) 1903558.
[252] C. Knierim, M. Enzeroth, P. Kaiser, C. Dams, D. Nette, A. Seubert, A. Klingl, C.L. Greenblatt, V. Jérôme, S. Agarwal, Living composites of bacteria and polymers as biomimetic films for metal sequestration and bioremediation, Macromolecular Bioscience 15 (2015) 1052-1059.
[253] S. Wang, L.K. Rivera-Tarazona, M.K. Abdelrahman, T.H. Ware, Digitally Programmable Manufacturing of Living Materials Grown from Biowaste, ACS Applied Materials & Interfaces 14 (2022) 20062-20072.
[254] U. Mamat, R.W. Woodard, K. Wilke, C. Souvignier, D. Mead, E. Steinmetz, K. Terry, C. Kovacich, A. Zegers, C. Knox, Endotoxin-free protein production—ClearColi™ technology, Nature Methods 10 (2013) 916-916.
[255] X. Zhu, S. Chen, X. Hu, L. Zhao, Y. Wang, J. Huang, J. Chen, Y. Qiu, X. Zhang, M. Wang, X. Yang, Y. Zhang, Y. Zhu, Near-Infrared Nano-Optogenetic Activation of Cancer Immunotherapy via Engineered Bacteria, Advanced Materials 35 (2023) 2207198.
[256] S.-J. Park, M. Gazzola, K.S. Park, S. Park, V. Di Santo, E.L. Blevins, J.U. Lind, P.H. Campbell, S. Dauth, A.K. Capulli, Phototactic guidance of a tissue-engineered soft-robotic ray, Science 353 (2016) 158-162.

[257] J. Condi Mainardi, K. Rezwan, M. Maas, Embedding live bacteria in porous hydrogel/ceramic nanocomposites for bioprocessing applications, Bioprocess and Biosystems Engineering 42 (2019) 1215-1224.
[258] A.K. Struss, P. Pasini, S. Daunert, Biosensing Systems Based on Genetically Engineered Whole Cells, in: M. Zourob (Ed.), Recognition Receptors in Biosensors, Springer New York, New York, NY, 2010, pp. 565-598.
[259] E.L. Lagendijk, S. Validov, G.E.M. Lamers, S. De Weert, G.V. Bloemberg, Genetic tools for tagging Gram-negative bacteria with mCherry for visualization in vitro and in natural habitats, biofilm and pathogenicity studies, FEMS Microbiology Letters 305 (2010) 81-90.
[260] N.C. Shaner, R.E. Campbell, P.A. Steinbach, B.N.G. Giepmans, A.E. Palmer, R.Y. Tsien, Improved monomeric red, orange and yellow fluorescent proteins derived from Discosoma sp. red fluorescent protein, Nature Biotechnology 22 (2004) 1567-1572.
[261] A.J.M. Walhout, M. Vidal, High-Throughput Yeast Two-Hybrid Assays for Large-Scale Protein Interaction Mapping, Methods 24 (2001) 297-306.
[262] F. Zeng, M. Du, Y. Yang, J. Fang, Y. Wang, M. Goh, Y. Lin, H. Wang, F. Yan, Z. Chen, Enhancing photothermal therapy of tumors with image-guided thermal control of gene-expressing bacteria, Theranostics 14 (2024) 5945-5964.
[263] A. Moncion, J.N. Harmon, Y. Li, S. Natla, E.C. Farrell, O.D. Kripfgans, J.P. Stegemann, F.M. Martín-Saavedra, N. Vilaboa, R.T. Franceschi, M.L. Fabiilli, Spatiotemporally-controlled transgene expression in hydroxyapatite-fibrin composite scaffolds using high intensity focused ultrasound, Biomaterials 194 (2019) 14-24.
[264] R. Hurme, K.D. Berndt, E. Namork, M. Rhen, DNA Binding Exerted by a Bacterial Gene Regulator with an Extensive Coiled-coil Domain (∗), Journal of Biological Chemistry 271 (1996) 12626-12631.
[265] A.K. Yanamandra, S. Bhusari, A. del Campo, S. Sankaran, B. Qu, In vitro evaluation of immune responses to bacterial hydrogels for the development of living therapeutic materials, Biomaterials Advances 153 (2023) 213554.
[266] X. Liu, H. Yuk, S. Lin, G.A. Parada, T.-C. Tang, E. Tham, C. de la Fuente-Nunez, T.K. Lu, X. Zhao, 3D Printing of Living Responsive Materials and Devices, Advanced Materials 30 (2018) 1704821.
[267] T. Bhattacharjee, S.S. Datta, Bacterial hopping and trapping in porous media, Nature Communications 10 (2019) 2075.
[268] Y. Liu, M.H. Rafailovich, R. Malal, D. Cohn, D. Chidambaram, Engineering of bio-hybrid materials by electrospinning polymer-microbe fibers, Proceedings of the National Academy of Sciences 106 (2009) 14201-14206.
[269] X. Liu, Y. Yang, M.E. Inda, S. Lin, J. Wu, Y. Kim, X. Chen, D. Ma, T.K. Lu, X. Zhao, Magnetic Living Hydrogels for Intestinal Localization, Retention, and Diagnosis, Advanced Functional Materials 31 (2021) 2010918.
[270] T.-C. Tang, E. Tham, X. Liu, K. Yehl, A.J. Rovner, H. Yuk, C. de la Fuente-Nunez, F.J. Isaacs, X. Zhao, T.K. Lu, Hydrogel-based biocontainment of bacteria for continuous sensing and computation, Nature Chemical Biology 17 (2021) 724-731.
[271] P. Dhakane, V.S. Tadimarri, S. Sankaran, Light-Regulated Pro-Angiogenic Engineered Living Materials, Advanced Functional Materials 33 (2023) 2212695.
[272] M.G. de Morais, C. Stillings, R. Dersch, M. Rudisile, P. Pranke, J.A.V. Costa, J. Wendorff, Preparation of nanofibers containing the microalga Spirulina (Arthrospira), Bioresource Technology 101 (2010) 2872-2876.
[273] S.H. Kim, C. Shin, S.K. Min, S.-M. Jung, H.S. Shin, In vitro evaluation of the effects of electrospun PCL nanofiber mats containing the microalgae Spirulina (Arthrospira) extract on primary astrocytes, Colloids and Surfaces B: Biointerfaces 90 (2012) 113-118.

[274] B.G. Cha, H.W. Kwak, A.R. Park, S.H. Kim, S.Y. Park, H.J. Kim, I.S. Kim, K.H. Lee, Y.H. Park, Structural characteristics and biological performance of silk fibroin nanofiber containing microalgae spirulina extract, Biopolymers 101 (2014) 307-318.
[275] X. Zhang, M.R. Battig, N. Chen, E.R. Gaddes, K.L. Duncan, Y. Wang, Chimeric Aptamer–Gelatin Hydrogels as an Extracellular Matrix Mimic for Loading Cells and Growth Factors, Biomacromolecules 17 (2016) 778-787.
[276] Z. Ming, L. Han, M. Bao, H. Zhu, S. Qiang, S. Xue, W. Liu, Living Bacterial Hydrogels for Accelerated Infected Wound Healing, Advanced Science 8 (2021) 2102545.
[277] R. Basak, R. Bandyopadhyay, Encapsulation of Hydrophobic Drugs in Pluronic F127 Micelles: Effects of Drug Hydrophobicity, Solution Temperature, and pH, Langmuir 29 (2013) 4350-4356.
[278] E. Kushan, E. Senses, Thermoresponsive and Injectable Composite Hydrogels of Cellulose Nanocrystals and Pluronic F127, ACS Applied Bio Materials 4 (2021) 3507-3517.
[279] S. Bhusari, S. Sankaran, A. del Campo, Regulating Bacterial Behavior within Hydrogels of Tunable Viscoelasticity, Advanced Science 9 (2022) 2106026.
[280] E. Russo, C. Villa, Poloxamer Hydrogels for Biomedical Applications, Pharmaceutics 11 (2019) 671.
[281] K. Mortensen, Y. Talmon, Cryo-TEM and SANS microstructural study of pluronic polymer solutions, Macromolecules 28 (1995) 8829-8834.
[282] R.K. Prud'homme, G. Wu, D.K. Schneider, Structure and rheology studies of poly (oxyethylene− oxypropylene− oxyethylene) aqueous solution, Langmuir 12 (1996) 4651-4659.
[283] J. Li, C. Marmorat, G. Vasilyev, J. Jiang, N. Koifman, Y. Guo, I. Talmon, E. Zussman, D. Gersappe, R. Davis, Flow induced stability of pluronic hydrogels: injectable and unencapsulated nucleus pulposus replacement, Acta Biomaterialia 96 (2019) 295-302.
[284] N. Gjerde, K. Zhu, K.D. Knudsen, B. Nyström, Influence of poly (ε-caprolactone) end-groups on the temperature-induced macroscopic gelation of Pluronic in aqueous media, European Polymer Journal 112 (2019) 493-503.
[285] A. Saha, T.G. Johnston, R.T. Shafranek, C.J. Goodman, J.G. Zalatan, D.W. Storti, M.A. Ganter, A. Nelson, Additive Manufacturing of Catalytically Active Living Materials, ACS Applied Materials & Interfaces 10 (2018) 13373-13380.
[286] C.R. López-Barrón, R. Chen, N.J. Wagner, P.J. Beltramo, Self-assembly of Pluronic F127 diacrylate in ethylammonium nitrate: structure, rheology, and ionic conductivity before and after photo-cross-linking, Macromolecules 49 (2016) 5179-5189.
[287] S. Bhusari, M. Hoffmann, P. Herbeck-Engel, S. Sankaran, M. Wilhelm, A. del Campo, Rheological behavior of Pluronic/Pluronic diacrylate hydrogels used for bacteria encapsulation in engineered living materials, Soft Matter 20 (2024) 1320-1332.
[288] S. Bhusari, J. Kim, K. Polizzi, S. Sankaran, A. del Campo, Encapsulation of bacteria in bilayer Pluronic thin film hydrogels: A safe format for engineered living materials, Biomaterials Advances 145 (2023) 213240.
[289] Y. Zhu, Z. Wang, L. Bai, J. Deng, Q. Zhou, Biomaterial-based encapsulated probiotics for biomedical applications: Current status and future perspectives, Materials & Design 210 (2021) 110018.
[290] M. Puertas-Bartolomé, I. Gutiérrez-Urrutia, L.L. Teruel-Enrico, C.N. Duong, K. Desai, S. Trujillo, C. Wittmann, A. del Campo, Self-Lubricating, Living Contact Lenses, Advanced Materials 36 (2024) 2313848.
[291] S. Bonakdar, S.H. Emami, M.A. Shokrgozar, A. Farhadi, S.A.H. Ahmadi, A. Amanzadeh, Preparation and characterization of polyvinyl alcohol hydrogels crosslinked by biodegradable polyurethane for tissue engineering of cartilage, Materials Science and Engineering: C 30 (2010) 636-643.

[292] J. Oh, A.L. Byrd, M. Park, H.H. Kong, J.A. Segre, Temporal stability of the human skin microbiome, Cell 165 (2016) 854-866.
[293] X. Liu, M. Wu, M. Wang, Q. Hu, J. Liu, Y. Duan, B. Liu, Direct Synthesis of Photosensitizable Bacterial Cellulose as Engineered Living Material for Skin Wound Repair, Advanced Materials 34 (2022) 2109010.
[294] L. Li, C. Yang, B. Ma, S. Lu, J. Liu, Y. Pan, X. Wang, Y. Zhang, H. Wang, T. Sun, D. Liu, Hydrogel-Encapsulated Engineered Microbial Consortium as a Photoautotrophic "Living Material" for Promoting Skin Wound Healing, ACS Applied Materials & Interfaces 15 (2023) 6536-6547.
[295] L.M. González, N. Mukhitov, C.A. Voigt, Resilient living materials built by printing bacterial spores, Nature chemical biology 16 (2020) 126-133.
[296] Y. Lu, H. Li, J. Wang, M. Yao, Y. Peng, T. Liu, Z. Li, G. Luo, J. Deng, Engineering Bacteria-Activated Multifunctionalized Hydrogel for Promoting Diabetic Wound Healing, Advanced Functional Materials 31 (2021) 2105749.
[297] P. Praveschotinunt, A.M. Duraj-Thatte, I. Gelfat, F. Bahl, D.B. Chou, N.S. Joshi, Engineered E. coli Nissle 1917 for the delivery of matrix-tethered therapeutic domains to the gut, Nature communications 10 (2019) 5580.
[298] H.M. Verheul, H.M. Pinedo, The role of vascular endothelial growth factor (VEGF) in tumor angiogenesis and early clinical development of VEGFReceptor kinase inhibitors, Clinical Breast Cancer 1 (2000) S80-S84.

4 Statement of Contributions and Publication Report

Chapter 5.1: The contents of Chapter 5.1 were published in a peer reviewed journal:

Basaran, S.; Dey, S.; Bhusari, S.; Sankaran, S.; Kraus, T., Plasmonic stimulation of gold nanorods for the photothermal control of engineered living materials. Biomaterials Advances 2023, 147, 213332.

The contribution of each co-author is described below within the taxonomy CRediT (Contributor Roles Taxonomy):

- Selim Basaran: Formal analysis, Investigation, Methodology, Writing – original draft.
- Sourik Dey: Investigation, Resources.
- Shardul Bhusari: Methodology, Resources
- Shrikrishnan Sankaran: Conceptualization, Validation, Writing – original draft, Writing – review & editing, Supervision
- Tobias Kraus: Conceptualization, Validation, Writing – original draft, Writing – review & editing, Supervision.

Chapter 5.2:

This project was done in collaboration with Anwesha Chatterjee, a PhD student of the Bioprogrammable Materials group at the INM – Leibniz Institute for New Materials. She provided the engineered *E. coli* Nissle 1917 (see section 5.2.2.4). Further, she made measurements with Luciferase to detect the amount of PCQ produced by the ELM (as described in 5.2.2.8). The calibration curve used to convert the luminescence of expressed PCQ proteins to their concentration was constructed by Anwesha Chatterjee, who also prepared the collagen gel. Lara Luana Enrico Teruel from Dynamic Biomaterials group at INM provided the PVA-VS hydrogel precursor. All other work, particularly the preparation and characterization of nano- and bacterial composite hydrogels, the photothermal experiments and their analysis, and laser and LED setup construction, was done by me.

Chapter 5.3:

This project was done in collaboration with Zahra Kafrashian, a PhD student of the Dynamic Biomaterials group at INM – Leibniz Institute for New Materials. She prepared the waveguides from PluDA hydrogels by 3-D printing and conducted photothermal experiments. The laser setup for focusing laser light into the waveguides was made by Peter Rogin from Optical Materials group at INM. I extended the setup by integrating the infrared camera and the laser in this setup. I analyzed thermal images.

5 Results

5.1 Publication: Plasmonic stimulation of gold nanorods for the photothermal control of engineered living materials

Basaran, S.; Dey, S.; Bhusari, S.; Sankaran, S.; Kraus, T., Plasmonic stimulation of gold nanorods for the photothermal control of engineered living materials. Biomaterials Advances 2023, 147, 213332.

147 (2023) 213332

Contents lists available at ScienceDirect

Biomaterials Advances

journal homepage: www.journals.elsevier.com/materials-science-and-engineering-c

Plasmonic stimulation of gold nanorods for the photothermal control of engineered living materials

Selim Basaran [a], Sourik Dey [a], Shardul Bhusari [a,b], Shrikrishnan Sankaran [a,*], Tobias Kraus [a,c]

[a] INM – Leibniz Institute for New Materials, Saarbrücken, Germany
[b] Chemistry Department, Saarland University, 66123 Saarbrücken, Germany
[c] Colloids and Interface Chemistry, Saarland University, Saarbrücken, Germany

ARTICLE INFO

Keywords:
Engineered living materials
Near infrared stimulation
Surface plasmon resonance
Photothermal nanocomposite
Thermogenetics

ABSTRACT

Engineered living materials (ELMs) encapsulate microorganisms within polymeric matrices for biosensing, drug delivery, capturing viruses, and bioremediation. It is often desirable to control their function remotely and in real time and so the microorganisms are often genetically engineered to respond to external stimuli. Here, we combine thermogenetically engineered microorganisms with inorganic nanostructures to sensitize an ELM to near infrared light. For this, we use plasmonic gold nanorods (AuNR) that have a strong absorption maximum at 808 nm, a wavelength where human tissue is relatively transparent. These are combined with Pluronic-based hydrogel to generate a nanocomposite gel that can convert incident near infrared light into heat locally. We perform transient temperature measurements and find a photothermal conversion efficiency of 47 %. Steady-state temperature profiles from local photothermal heating are quantified using infrared photothermal imaging and correlated with measurements inside the gel to reconstruct spatial temperature profiles. Bilayer geometries are used to combine AuNR and bacteria-containing gel layers to mimic core-shell ELMs. The thermoplasmonic heating of an AuNR-containing hydrogel layer that is exposed to infrared light diffuses to the separate but connected hydrogel layer with bacteria and stimulates them to produce a fluorescent protein. By tuning the intensity of the incident light, it is possible to activate either the entire bacterial population or only a localized region.

1. Introduction

Engineered living materials (ELMs) are a rapidly developing class of composite materials born from the combination of synthetic biology and materials science [1,2]. In ELMs, living microorganisms (bacteria, yeast, algae etc.) are combined with inanimate materials to yield advanced constructs applicable as biosensors [3], self-healing adhesives [4], biofilters to trap metals and viruses [5,6], smart drug delivery devices [7], soft robots [8], and other devices. In most of these cases, the functionalities are realized through genetic engineering of the microorganisms while the material component acts as a supportive scaffold.

Light is an attractive stimulus for ELMs that can be applied at different intensities, wavelengths, and spatial dimensions at low cost. Light has been used for patterning [9,10], actuation [11], and drug release [7] in ELMs. Existing systems typically use blue light with short wavelengths that act on optogenetic systems in bacteria [7,10]. Blue light, however, exhibits low penetration depths in vivo, limiting e.g. translational potential for implanted ELMs [12]. Green-, red- and near-infrared (NIR)-responsive optogenetic circuits [9] have been reported but require co-factors that are not naturally present in most bacteria and therefore need to be externally supplied or produced by the bacteria themselves through engineered complex enzyme cascades.

Here, we follow an alternative strategy that combines an inanimate functional material which acts as an optical absorber with heat-responsive genetic circuits in bacteria. The combination retains the advantages of long-wavelength light (spatiotemporal control with relatively high penetration depth in skin) without requiring light-responsive genetic circuits. The optical absorber is based on gold nanorods (AuNR) that are well-accepted in biomedical applications due to their biocompatibility [13,14], unique absorption properties in the visible and NIR regions arising from conduction electron-light interactions [15,16], localized surface plasmon resonance (LSPR) that can be tuned by changing the geometry [17], and high photothermal efficiency [18]. Nanorods have thus been used in cancer therapy [19–21], drug delivery

* Corresponding author.
E-mail addresses: shrikrishnan.sankaran@leibniz-inm.de (S. Sankaran), tobias.kraus@leibniz-inm.de (T. Kraus).

https://doi.org/10.1016/j.bioadv.2023.213332
Received 31 October 2022; Received in revised form 3 February 2023; Accepted 7 February 2023
Available online 14 February 2023

[20,22–24], and photothermal therapy (PTT) [18]. They can trigger hyperthermia in tissues [25,26] and induce cell death via necrosis and apoptosis at temperatures above 45 °C [27]. Gold nanorods of suitable geometry can efficiently absorb NIR light in the range of the tissue transparency window of 650–1350 nm [28,29]. Stimulation at such wavelengths can be safe to tissues, cells, and bacteria with the ability of deep tissue penetration [12,30,31]. The absorption of NIR light causes a plasmon oscillation of the conduction electrons that is dampened by lattice collision resulting in thermalization, which heats the surrounding matrix [32].

It is challenging to use free, dispersed AuNR in the body. Challenges include insufficient retention [30] and the need for specific surface functionalization for targeting [26,28] and to prevent cytotoxicity [33–35]. Here, we avoid such problems by embedding the AuNR in hydrogels, resulting in gold nanorod nanocomposite hydrogels (AuNR gels) that retain the AuNR and enable spatiotemporal control of stimulation by local illumination [36]. Such composites have been applied for PTT by local heating [34], for drug delivery by shrinking or decomposing the gel through the generated heat [30,36–39], and photodynamic treatments with dyes that generate radical oxygen species [26,28]. Comparable AuNR gels have been formulated to mimic the mechanical properties of human tissues and minimize immune reactions [40]. They can be injected locally and retain the AuNR at the treatment site [41]. Local heating by several 10 °C is possible with AuNR gels [42]. A temperature increase to 45 °C or above has been demonstrated and used to kill cancer cells [43].

Combining AuNRs with ELMs will expand their applicability to achieve a wide range of targeted therapies while requiring only moderate heating (~40 °C). Accordingly, in this study, we demonstrate the activation of thermogenetically engineered bacteria by NIR light in an ELM using AuNR capable of photothermal energy conversion. We created ELM constructs in which heat-responsive bacteria and AuNR are encapsulated in adjacent hydrogel layers, mimicking the structure of core-shell ELMs [44]. This allowed us to separately study the properties of AuNR and bacteria-laden gels and demonstrate the thermal coupling of both. We quantify and control the thermoplasmonic conversion to reach temperature levels that are harmless for the surrounding tissue and optimal for the activation of the bacteria and show that a moderate plasmonically induced temperature increase (to ~40 °C) is sufficient to activate bacteria in the adjacent layer. Activation is then quantified via fluorescence microscopy using bacteria that express the fluorescent protein mCherry.

2. Materials and methods

2.1. Materials

Gold nanorods (length: 41 nm, diameter: 10 nm) capped with CTAB in water were purchased from Nanopartz Inc. (Canada). The hydrogel precursor, Pluronic diacrylate (PLUDA), was synthesized by reacting Pluronic F127 (Plu, MW ≈ 12,600 g/mol, Sigma-Aldrich) with acryloyl chloride in the presence of triethylamine according to a reported protocol [46]. 30 % (w/v) solutions were prepared in milliQ water ($PLUDA_{MQ}$) and LB medium ($PLUDA_{LB}$) containing Irgacure 2959 as photoinitiator at 0.2 % w/v.

Microscopy slides with 15 wells (type "μ-slide Angiogenesis") with uncoated bottoms were obtained from ibidi (Gräfelfing, Germany). Silicone oil (350 cSt, Sigma Aldrich) was used to cover the ELM and prevent it from drying.

2.2. Creation of thermoresponsive mCherry ClearColi Strain

The mCherry double-stranded gene insert was procured from Integrated DNA Technologies (Coralville, USA) and assembled into the pTlpA39-Wasabi vector (Addgene #86116) [47] using the NEBuilder HiFi DNA Assembly Cloning Kit (New England Biolabs, GmbH). The mCherry gene was inserted downstream of the PtlpA promoter by replacing the mWasabi reporter gene. The recombinant plasmid construct was sequence verified (Eurofins GmbH, Germany) and subsequently transformed in the ClearColi BL21(DE3) strain (BioCat GmbH, Germany) and maintained in LB Miller medium (Carl Roth GmbH, Germany) supplemented with 100 μg/mL Ampicillin.

2.3. Preparation and characterization of AuNR gel

The CTAB stabilized gold nanorods were centrifuged at 12,500 rpm for 8 min at room temperature and the surfactant was removed by pipetting. Then the suspension was diluted with the $PLUDA_{MQ}$ to the desired concentrations at 4 °C. The mixture was incubated at room temperature for 5 min to allow gelation. The AuNR gel was exposed to a UV lamp (365 nm, 6 mW/cm^2) inside Alpha Innotech FluorChem Q system (Biozym, Oldendorf, Germany) for 2 min to crosslink the diacrylate groups. The AuNR gel was characterized by UV-VIS-NIR spectrometer. The absorbance was measured in a 10 mm disposal cuvette. The baseline was pure hydrogel in cuvette.

The distribution of the gold nanorods was observed by cryo-TEM. A small amount of the AuNR gel was placed on a holey carbon grid (Plano, Wetzlar, Germany, type S1474-4), blotted for 2 s, and plunged into liquid ethane using a Gatan (Pleasanton, CA, United States) CP3 cryo plunger operating at $T = -165$ °C. The vitrified sample was transferred to a Gatan model 914 cryo-TEM sample holder and investigated by bright field TEM (JEOL, Akishima, Japan, JEM-2100 LaB6) imaging at 200 kV accelerating voltage and $T = -170$ °C under low-dose conditions. A Gatan Orius SC1000 CCD camera was used for image acquisition (2 s exposure time).

2.4. Preparation of bilayer hydrogel structures

The hydrogel precursor for non-bacterial experiments contained 30 % (w/v) of a diacrylated Pluronic F127 (PLUDA) in Milli-Q water, and 0.2 % of the photoinitiator Irgacure (2-benzyl-2-(dimethylamino)-1-[4-(morpholinyl) phenyl)]-1-butanone). A dispersion of gold nanorods (AuNR@CTAB) with an Optical Density (OD) of $OD_{808nm} = 40$ was obtained by centrifugation of a dilute suspension at 12,500 rpm for 8 min at room temperature. It was immediately mixed with $PLUDA_{MQ}$ (180 μL) at 4 °C to dilute to the desired $OD_{808nm} = 4$. The mixture was immediately used to prepare AuNR gels. The hydrogel precursor for the bacterial hydrogels contained 30 % (w/v) of PLUDA in lysogeny broth (LB) medium, and 0.2 % of the photoinitiator Irgacure. This mixture is denoted as $PLUDA_{LB}$ in the following.

The thermoresponsive mCherry producing ClearColi BL21(DE3) strain was inoculated in LB Miller – 2 % NaCl medium supplemented with 100 μg/mL ampicillin and incubated at 37 °C, 250 rpm shaking conditions for 18 h. The bacterial culture reached the late logarithmic phase and the bacterial cell density was adjusted to $OD_{600nm} = 2$ by centrifugation (9600 rpm, 4 °C, 3 min). Determination of the cell density was done by a NanoDrop Microvolume UV–Vis 175 spectrophotometer (ThermoFisher Scientific GmbH, Germany) and resuspension in fresh medium was done by vortexing for <1 min. A volume of 10 μL was dispersed in $PLUDA_{LB}$ (90 μL) at 4 °C and homogenized to a resulting $OD_{600nm} = 0.2$. The mixture was immediately used to prepare the bacterial hydrogel layers.

The bilayer hydrogel structures were prepared in patterned polymer microscopy slides with 5 × 3 microwells and uncoated bottoms (Fig. 1). Each microwell had an inner well (10 μL, diameter 4 mm) that was used to form the bacterial hydrogel layer and an upper well (50 μL, diameter 5 mm) that was used to hold the AuNR gel layer. 10 μL of the bacterial hydrogel precursor solution were pipetted at 4 °C in the lower well and then incubated for 5 min at room temperature for gelation. The physically assembled gel was photopolymerized at a wavelength of 395 nm and a power density of 6 mW/cm^2 for 2 min using a FluorChemQ light source (Alpha Innotech). The AuNR gel precursor (20 μL) was injected in

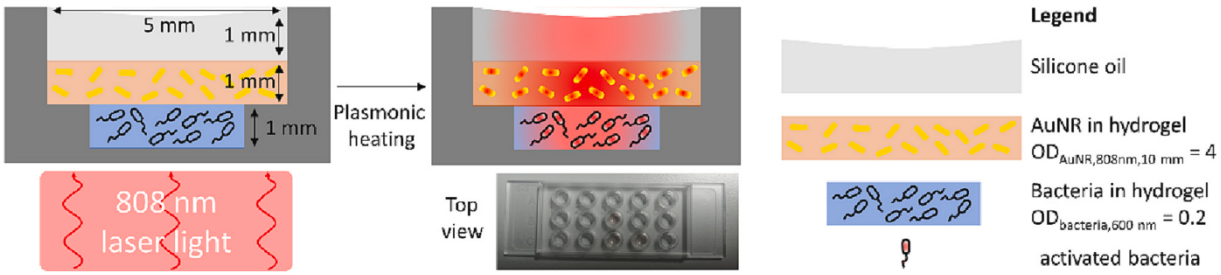

Fig. 1. Schematic depiction of the bilayer hydrogel construct in a polymer well plate. The top layer contained the plasmonically absorbing gold nanorods that convert irradiation at 808 nm into heat. This increased the temperature of the bottom layer, which contained bacteria genetically modified to produce mCherry at temperatures above 39 °C.

the upper well, incubated for 5 min at room temperature for physical gelation, and UV cured in the same way as the lower gel. The obtained bilayer hydrogel structure was topped with 20 μL silicone oil to prevent drying. The result was a cylindrical shaped bacterial hydrogel with a diameter of 4 mm and a height 1 mm and a cylindrical AuNR gel with a diameter of 5 mm and a height of 1 mm. A 1 mm thick silicone layer covered it to prevent drying.

2.5. Laser setup

The laser setup for the photothermal excitation of the bilayer hydrogel is schematically depicted in Fig. S1. A continuous wave (CW) infrared laser (CNI, China) emitted light at 808 nm with adjustable power from 1 to 6 W. The laser light was coupled into a SMA 905 multimode fiber (400 μm core diameter, CNI, China) connected to a collimator (FOC-01, CNI, China) that parallelized the outcoming light to a 5 mm diameter spot. We used neutral density (ND) filters (NE10A-B, Thorlabs, Germany) between collimator and photodiode to reduce outcoming laser power to the range of 100 mW when using laser power of 1 W. A mechanical shutter with an integrated Si photodiode (FDS10X10, Thorlabs, Germany, behind an ND filter from Thorlabs) was used to monitor the laser power.

A dielectric right angle prism mirror (MRA20-E03, Thorlabs, Germany) guided the light to the sample that was at a distance of 10 cm from the collimator inside the patterned microscopy slide (see above). The lateral position of the beam spot on the sample was adjusted with the aid of a monochromic camera (DMK 23U445, The Imaging Source, Germany). An infrared camera (VarioCam@HD 980 S, Infratech, Germany) was mounted 10 cm above the sample to measure the temperature distribution.

2.6. Photothermal conversion efficiency (PCE)

The photothermal conversion efficiency (PCE) of AuNR gels was quantified using published methods [48,49]. Hydrogels with and without nanorods were exposed to light, the temperature changes were measured and interpreted by balancing the photothermal heat produced by the gold nanorods (Q_{in}), transient heating of quartz cuvette-hydrogel system (Q_0), and heat dissipation to the external environment (Q_{out}) [48]:

$$\sum_i m_i c_{p,i} \frac{dT}{dt} = Q_{in} + Q_0 - Q_{out} \quad (1)$$

with m_i and $c_{p,i}$ the mass and specific heat capacity of component i, and T the temperature of all components (assumed to be uniform) at time t. Both m_i and $c_{p,i}$ can be determined experimentally. The photothermal conversion efficiency η at steady-state is

$$\eta = \frac{hA(T_{max} - T_{amb}) - Q_0}{I_0\left(1 - 10^{-A_{808nm}}\right)} \quad (2)$$

with h the heat transfer coefficient, A the area of the interface between AuNR gel and the external environment, T_{amb} the measured ambient temperature, T_{max} the measured maximal temperature reached under illumination at steady-state, I_0 the incident laser power, and $A_{808\ nm}$ the absorbance of the AuNR gel at the laser wavelength (808 nm).

To calculate hA, we analyzed transient temperature changes. The parameter $B \equiv hA/m_i c_{p,i}$ quantifies the heat dissipation from the AuNR gel to the external environment; we assume that it is time-invariant. It can be calculated using an exponential fit of the cooling curve as the laser is turned off [49]:

$$T(t) = T_{amb} + (T_{max} - T_{amb}) \cdot e^{-Bt} \quad (3)$$

The Supporting Information provides further details on the fit and the PCE calculation.

2.7. Temperature measurements for PCE quantification and stability testing

A thermocouple (K-Type, 1.4541 stainless steel) was inserted in AuNR gel ($OD_{AuNR,2mm}$ = 0.67, 100 μL) in a glass cuvette (Hellma, Germany) with a beam path length of 2 mm and a glass thickness of 0.5 mm. An infrared diode laser (808 nm, 89 mW) with beam diameter of 10 mm (collimator FOC-01, CNI, China) was used to illuminate the nanorod-containing gel and a reference gel without rods. The temperature change was recorded at 5 s intervals using a 4-channel data logger (TC direct, Germany) via the *SE521* software. The laser was switched off after 10 min and the cooling curve was recorded during the subsequent 10 min. The ambient temperature was measured with an additional TC.

The steady-state temperature profiles in hydrogel bilayers were quantified in the wells of the patterned polymer slide. The photothermal stability of the AuNR gel during prolonged and cyclical excitation was evaluated, too. The bilayers were prepared as explained in Fig. 1, but without bacteria in the bottom layer. Top layers with an $OD_{AuNR,808nm}$ = 4 were illuminated with laser power densities of 0.4 W/cm^2, 0.5 W/cm^2, 0.6 W/cm^2, 0.7 W/cm^2 and 0.8 W/cm^2; top layers with $OD_{AuNR,808nm}$ = 0, 1, 2, 3, 4, 5 were illuminated with laser power density of 0.8 W/cm^2 to provide systematic data. Local temperatures at the (oil-air) interface were obtained through infrared thermography using an infrared camera (Infratec, Germany).

2.8. Photothermally triggered protein expression

Bilayered ELMs were prepared as explained in Section 2.4 and Fig. 1 with a top layer AuNR concentration equivalent to $OD_{AuNR,808\ nm}$ = 4. They were irradiated at laser power densities of 0.5–0.7 W/cm^2 to reach different maximal steady-state temperatures during 0 h, 1 h, 2 h, 3 h, and 4 h.

The constructs were then observed under a Keyence BZ-X800 fluorescence microscope with an 4× objective. The magnification was chosen to depict the entire microslide well in one image. We used the

filter cubes BZ-X Filter OP-87764 with an excitation of 545 nm (25 nm bandpass) and an emission of 605 nm (70 nm bandpass) at an integration time of 1.5 s of the digital camera. The fluorescence intensities of the acquired images were evaluated via *ImageJ*. A rectangular selection with length 4 mm and height 0.17 mm was chosen to plot profiles for all the fluorescence images. The rectangular selection was rotated by 34.6 °C to evaluate the diagonal of the fluorescence images, thus covering the entire diameter of the well (see Fig. S2). Only the lateral positions between 0.2 and 3.8 mm were considered to avoid optical scattering effects of the well border.

The lateral temperature distribution during the experiment was quantified by IR thermography and the images were analyzed using the software *IRBIS 3.1*. Steady-state temperature distributions obtained at t = 60–595 s were converted to TIFF raw data. A rectangular area with a length of 4 mm, a height of 0.17 mm, and a rotation angle of 34.6° that coincided with that used in fluorescence analysis was analyzed using *ImageJ* to obtain averaged linear profiles.

Each experiment was repeated 3 times and the mean local fluorescence intensities and mean lateral steady-state temperatures with their standard deviation were plotted.

2.8.1. Statistical analysis

All values reported in this work are given as arithmetic means of multiple measurements ± standard deviations (SD). Data processing, normalization and fitting to equations were carried out using *Microsoft Excel* and *Origin Pro 9.1*. The sample numbers (denoted n in the following) and repetitions of each experiment (denoted N) are provided in the captions of the corresponding figures.

3. Results and discussion

3.1. Preparation and characterization of AuNR gels

The Photothermal Conversion Efficiency (PCE) and the uniformity of the AuNR gels depends on the agglomeration state of the nanorods. We used commercial, CTAB-stabilized gold nanorods (41 nm long, 10 nm diameter) in aqueous suspension (AuNR@CTAB). They were adjusted to the desired concentrations by centrifugation, mixed with $PLUDA_{MQ}$ at 4 °C below the lower critical solution temperature (LCST) of 15 °C [46], incubated to initiate gelation at room temperature, and cross-linked with UV light. The overall process entails several risks of agglomeration: the concentration of the ligand, CTAB, is lowered by a factor 40 to 0.125 mM during centrifugation due to surfactant removal, possible causing desorption of the weakly bound molecule from the rod. Tebbe et al. and Reiser et al. reported that gold nanorods are stable at CTAB concentrations of 0.1 mM and 0.08 mM for a short time [33,50]. On the other hand, AuNR concentration is increased to approximately $OD_{AuNR,\ 808\ nm}$ = 40 during centrifugation. The combination of high AuNR concentration and low concentrations of CTAB increases the agglomeration risks.

We prevented agglomeration by minimizing the time between concentration increase and gelation of the hydrogel, which prevents diffusion [46], and used optical spectroscopy to assess the agglomeration state in the gels. Pure hydrogels (without AuNR) had an OD of below 0.13 between 400 and 900 nm, with an OD = 0.09 at 808 nm (see Fig. S3), the wavelength that we used for the photothermal heating in this work. The UV-VIS spectrum of an AuNR-containing hydrogel in Fig. 2(a) shows the localized surface plasmon resonance (LSPR) of an aqueous AuNR dispersion with the transversal (T-LSPR) resonance at 510 nm and the longitudinal resonance (L-LSPR) at about 808 nm. The

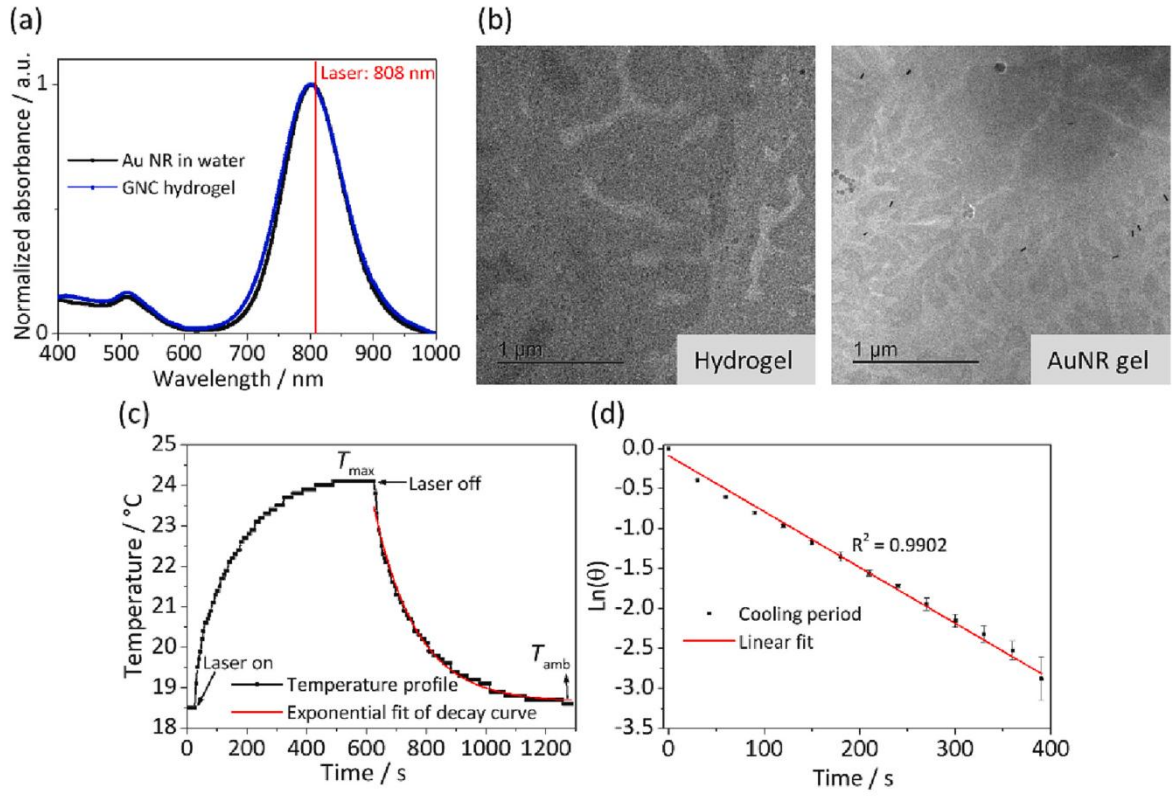

Fig. 2. Agglomeration state of the AuNR in the AuNR gel. (a) Normalized UV-VIS absorbance spectra of an aqueous dispersion of AuNR@CTAB and the AuNR gel. (b) Cryo-TEM of the pure hydrogel (top) and the AuNR gel (bottom). (c) Typical heating and cooling profile of a laser illuminated AuNR gel. The red line represents the exponential decay fit of Eq. (3). (d) Linear fit of ln(θ) as a function of time after laser was turned off (N = 3). R^2 is the coefficient of determination of the fit.

L-LSPR peak shifted from 805 nm to 803 nm in the gel, as expected due to the 30 wt-% of PLUDA polymer that increases the refractive index of the rods' environment. Note that the L-SPR is more sensitive to the environment than the T-SPR due to the larger longitudinal polarizability [16,51], as visible in the plot. The full width half at maximum (FWHM) of the L-LSPR changed from 111.3 ± 0.4 nm for AuNR@CTAB to 118.6 nm ± 0.4 nm in the gel, indicating no or very limited agglomeration [52,53]. This is consistent with cryo-TEMs (Fig. 2(b)) that show mainly well-distributed rods. Fig. S3(b) shows additional cryo-TEM images of other regions in the AuNR gel. Most of the AuNR appear well-dispersed in the micrographs. Note that cryo-TEM of hydrogels is prone to preparation artefacts that can lead to sample deformations that bring the rods closer together than they are in the original bulk.

Nanorods with a L-LSPR at 808 nm were chosen to match the transmissive window of tissues and ensure the availability of excitation lasers. In the following, we analyze whether the photothermal conversion efficiency of the AuNR gels is comparable to those reported for AuNR gel dispersions using an established measurement technique reported by Roper et al. [48]. A high PCE is critical to avoid exceeding the irradiation limit of 0.3 W/cm^2 for 808 nm lasers on human tissue [54]. Typical mammalian tissues attenuate 808 nm light to 10 % of the incoming intensity in 1 cm [55].

Fig. 2(c) shows a typical heating curve of an illuminated AuNR gel with a maximal temperature increase of 5.7 ± 0.11 °C at a laser power of 0.09 W and an $OD_{2mm,808nm} = 0.67$. The steady state was reached after approximately 600 s. Cooling after laser deactivation was exponential and reached $T_{amb} = 18.6$ °C after 600 s. It was used for the quantification of the PCE [48,49,56] by fitting Eq. (3) that indicated a heat dissipation rate $B = 0.00693 \pm 8 \bullet 10^{-5}\ s^{-1}$ and thus, a PCE of $\eta = 47 \pm 0.01$ % ($N = 3$) from Eq. (2). This is the first reported value of a PCE of gold nanorods in a gel to the best of our knowledge. The value, an intrinsic property that depends on the shape and size of AuNRs [56,57], is comparable to that from previous reports on AuNR in water of 50 % and 55 % [58,59].

Fig. 2(d) shows a linear fit of ln(θ) as a function of time after turning the laser off after 600 s of heating, where $\theta = [(T(t) - T_0) / (T_{max} - T_{amb})]$ (derived from Eq. (3), see SI for detailed description). The slope of the fit is consistent with $B = 0.00699 \pm 2 \cdot 10^{-4}\ s^{-1}$, consistent with the analysis above.

3.2. Photothermal activity and stability of the bilayer hydrogel

We prepared bilayers in microwells with pure hydrogel as bottom and AuNR gel as top layer. The bottom layer will be loaded with encapsulated bacteria in later experiments; we assume that they do not significantly affect the photothermal properties of the gel because their volume fraction is low (<8 % v/v according to literature [46]) and their heat capacity close to that of the gel. The bilayers were formed by adding the liquid gel precursors at 4 °C. They gelled at room temperature and were stabilized by photochemical UV cross linking.

Illumination of the bilayer hydrogel with 808 nm light resulted in heating. The gold nanorods in the top layer absorbed the light and converted it into heat. Fig. S4 shows the relevant heat flows: heat is thermoplasmonically generated at a rate Q_{gen} in the top layer. It diffuses to the surroundings, heating the lower layer by heat conduction $Q_{cond,1}$ and the silicon oil by conduction Q_{cond} and convection Q_{conv}. Some heat is lost by diffusion through the polymer microwells, $Q_{cond,2}$. Convection $Q_{air,conv}$ to the surrounding air finally removes heat from the system. In steady state, heat is constantly dissipated to the environment, and a constant temperature distribution in the bilayer hydrogel emerges. We measured the temperature at the silicone-air surface using an infrared camera. Fig. S5 shows representative IR image of the construct.

We quantified the photothermal excitation of the bilayer construct by analyzing the temperature at a defined point of the silicon oil (marked in Fig. S5) as a function of time. When irradiated with 808 nm light, this temperature increased and reached a plateau after approximately 6 min (Fig. 3(c) and (d)). The thermal stability of the construct

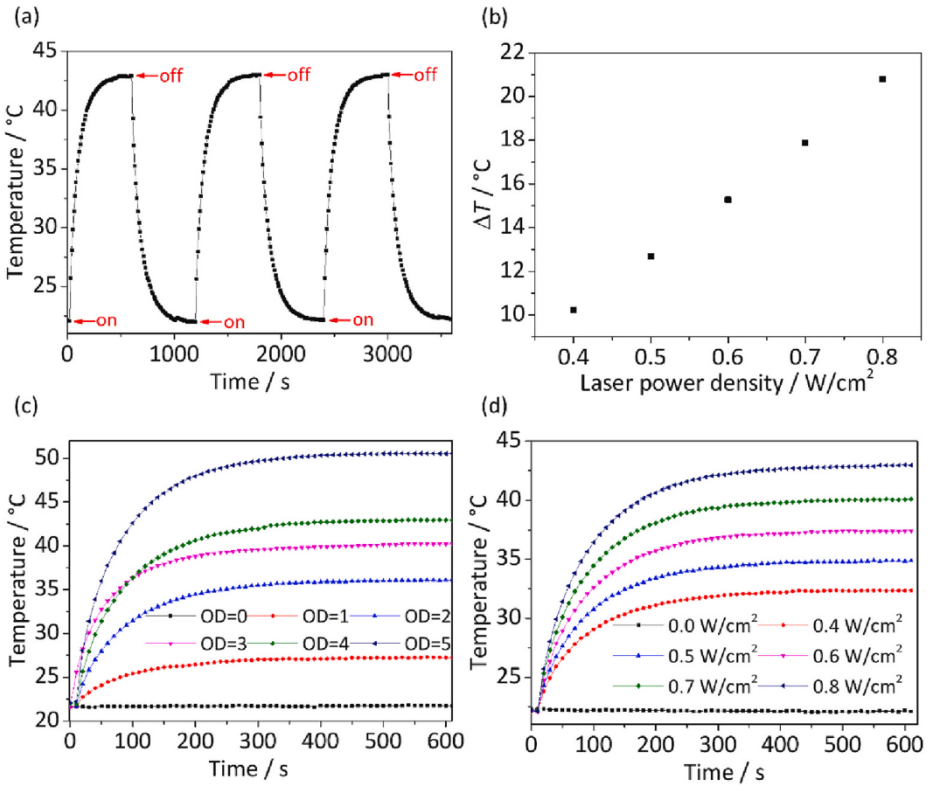

Fig. 3. Photothermal heating of bilayer structures. (a) Stability test by intermittent illumination of a AuNR gel with $OD_{AuNR,808nm} = 4$ at a laser power density of 0.8 W/cm^2. (b) Plateau temperature differences of the AuNR NC as a function of laser power density. The differences between the initial temperatures of the hydrogels and the maximal steady state temperatures are shown. (c) Heating of illuminated hydrogel bilayers at 0.8 W/cm^2 for different AuNR gel OD. (d) Heating of illuminated hydrogel bilayers at a AuNR gel $OD_{AuNR,808nm} = 4$ and different laser power densities.

was tested by repeated illumination (laser power density 0.8 W/cm^2 and $OD_{AuNR,\ 808nm} = 4$) and cooling (by turning the laser off) (Fig. 3(a)) in three cycles. Heating and cooling curves followed the expected exponential kinetics. These results confirm stable and efficient photothermal heating of the hydrogel bilayer.

In steady-state, Q_{gen} equals the dissipating heat output $Q_{cond,i}$ and $Q_{conv.}$ At a laser power density of 0.8 W/cm^2 and AuNR concentration $OD_{AuNR,808nm}$ of 4, a steady-state difference to the environmental temperature of $\Delta T \approx 22$ °C had stabilized after 6 min. We varied the incident laser power density from 0.4 W/cm^2 to 0.8 W/cm^2 at an AuNR concentration of $OD_{AuNR,\ 808nm}$ of 4 and found ΔT between 10 °C and 21 °C in accordance with Eq. (2) (Fig. 3(b)). Increasing AuNR concentrations $OD_{AuNR,\ 808nm}$ from 1 to 5 at a laser power of 0.8 W/cm^2 led to ΔT between 5 °C and nearly 29 °C (Fig. 3(c)).

3.3. Temperatures inside the bottom layer of the bilayer hydrogel

Infrared thermometry provided the temperature at the silicone oil surface. We were interested in the temperatures inside the bulk gel and embedded a thermocouple (TC) within the bottom hydrogel layer. Fig. 4 (b) shows a representative surface temperature profile at 0.6 W/cm^2 from the IR camera and a plot of the surface temperature T_{IR} at position P1 (Fig. 4(c)). The same plot shows the temperature concurrently measured inside the gel with a TC (T_{TC}) directly below P1 at a depth of 3 mm.

The temperatures inside the gel were always above the surface temperature. We measured steady state temperatures for laser powers ranging from 0.6 W/cm^2 to 1.0 W/cm^2 at an $OD_{AuNR,808nm}$ of 4 and found a linear correlation between T_{TC} and T_{IR}. This enables a simple conversion of the IR observation into bulk temperature for point P1:

$$T_{TC} = -2.89°C + 1.15 \times T_{IR}°C \quad (4)$$

Note that while the precision of the measurement is good, its accuracy is limited by the positioning of the TC and the reproducibility of the hydrogel layer geometry. We estimate errors for 2 mm of spatial uncertainty (see Fig. S7) for the positioning of the TC. This corresponds to uncertainties of the measured temperature on the order of 0.4–0.7 °C for laser power densities of 0.57–1.0 W/cm^2. Note also that there exist both lateral and normal temperature gradients in the gel such that bacteria experience different temperatures depending on their exact position. We tuned laser power in all subsequent experiments such that the bottom hydrogel was in a range of 39–50 °C and report the surface temperatures of the IR camera that can be converted into bulk temperatures using Eq. (4).

The temperatures inside the gel always exceeded those at its surface, providing an additional safeguard that protects the surrounding tissue from thermal damage. This is an inherent property of the system, because heat generation in bulk will always lead to larger temperatures inside the body if the thermal conductivity does not drop in the surroundings. Embedding the AuNR in ELM thus protects the tissue from

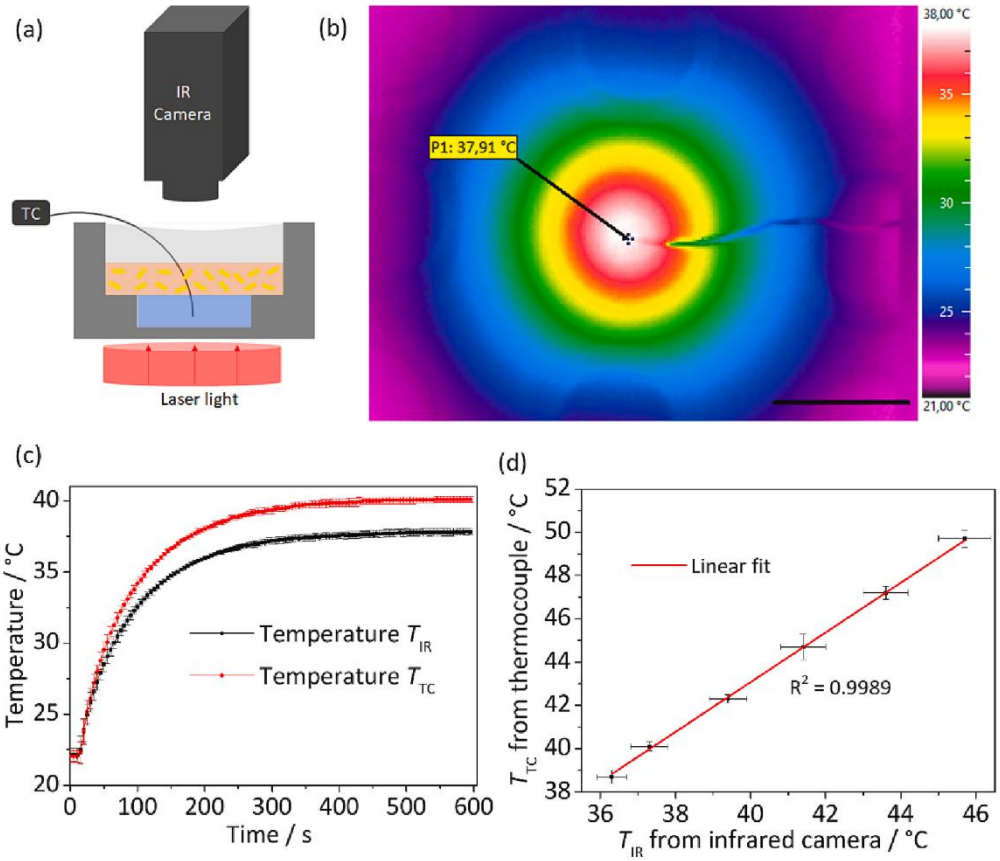

Fig. 4. Comparison of surface and bulk temperatures. (a) Cross section of one well of the microslide depicting the TC and IR camera position. (b) Steady-state temperature profile from IR thermometry at a laser power density of 0.6 W/cm^2 and OD = 4. P1 denotes the position used for comparing IR measurements with the reading from an embedded thermocouple (TC). The scale bar is 5 mm. (c) Temperatures T_{IR} measured at P1 by IR and T_{TC} measures below P1 by TC during transient heating at 0.6 W/cm^2 ($N = 3$, mean ± SD) (d) Relation of T_{TC} and T_{IR} for steady-state temperatures. The steady state temperatures at $t = 595$ s were averaged, and their standard deviation calculated at laser power densities of 0.57 W/cm^2, 0.62 W/cm^2, 0.70 W/cm^2, 0.77 W/cm^2, 0.85 W/cm^2 and 0.93 W/cm^2 ($N = 3$). R^2 is the coefficient of determination of the linear fit.

potentially large temperature in the direct vicinity of the nanostructures. It remains important, of course, to limit the laser power density. We found that laser power densities between 0.5 and 0.7 W/cm^2 did not lead to temperatures above 39–45 °C anywhere in the construct.

3.4. Thermoplasmonic NIR stimulation of mCherry producing thermoresponsive bacteria

We then tested the ability of the AuNR gels to activate ClearColi bacteria that were genetically engineered to thermo-responsively express a red fluorescent protein (mCherry). The bacteria were engineered with a TlpA regulator [47] that had a sharp switch-like transition from keeping gene expression OFF at 37 °C to switching it ON above 39 °C (see Fig. S8). The bacteria were encapsulated in the bottom layer and covered by a AuNR gel layer (Fig. 1). The temperature of the surface layer (silicon oil) was determined from IR thermography. Power densities of 0.5–0.7 W/cm^2 of the 808 nm laser were set to achieve surface temperatures between 35 °C and 41.5 °C. The bottom layer temperature can be estimated from this temperature using Eq. (4); it is always above the surface temperature and was sufficient to activate the bacteria.

Activation of the thermo-responsive bacterial switch was indicated by the expression of mCherry, whose fluorescent signal across the entire bacterial hydrogel was detected using fluorescence microscopy initially and after each hour four maximal 4 h of photothermal stimulation. Such microscopy imaging allowed spatial quantification of fluorescence intensities with a spatial resolution down to 2 μm in the XY plane (Fig. 5 (a)–(b)). During the experimental duration of 4 h, an increase of fluorescence intensity with photothermal stimulation was observed over time (Fig. S9(a)–(b)). A uniform expression of mCherry was observed after photothermal heating at 0.7 W/cm^2 laser power density, equivalent to a temperature range of 38–41.5 °C on the silicon oil surface depending on the lateral position and a higher temperature in the bulk gel (Fig. 5(d)). We conclude that this level of heating created an ideal steady-state temperature range to achieve the highest rate of gene expression while keeping the bacteria viable. Heating with 0.5–0.6 W/cm^2 led to a surface temperature profile in a range of 35–37.5 °C, leading to maximum mCherry expression in the center that dropped to low levels at the periphery as visible Fig. 5(a) and (c). This indicates the possibility to achieve locally confined activation of ELM functions using this system. Thus, by tuning the laser power at same AuNR gel concentrations, it is possible to influence the spatial profile in which the ELMs can be activated.

The stability of the steady-state temperature profiles was excellent, with deviations below 1 K over several hours at each of the individual positions. Variations between different samples were due to uncertainties in the exact AuNR concentration of the AuNR gel and the geometry of the casted gels. Pipetting identical Pluronic precursor solutions at low volumes is difficult since they quickly form physical gels above 10 °C and form menisci at the walls. This explains deviations that we found e.g. between the three different samples shown in the error bars of Fig. 5(c)–(d). Such uncertainties can be reduced by improved processing when larger amounts of ELM are prepared. This is, to our

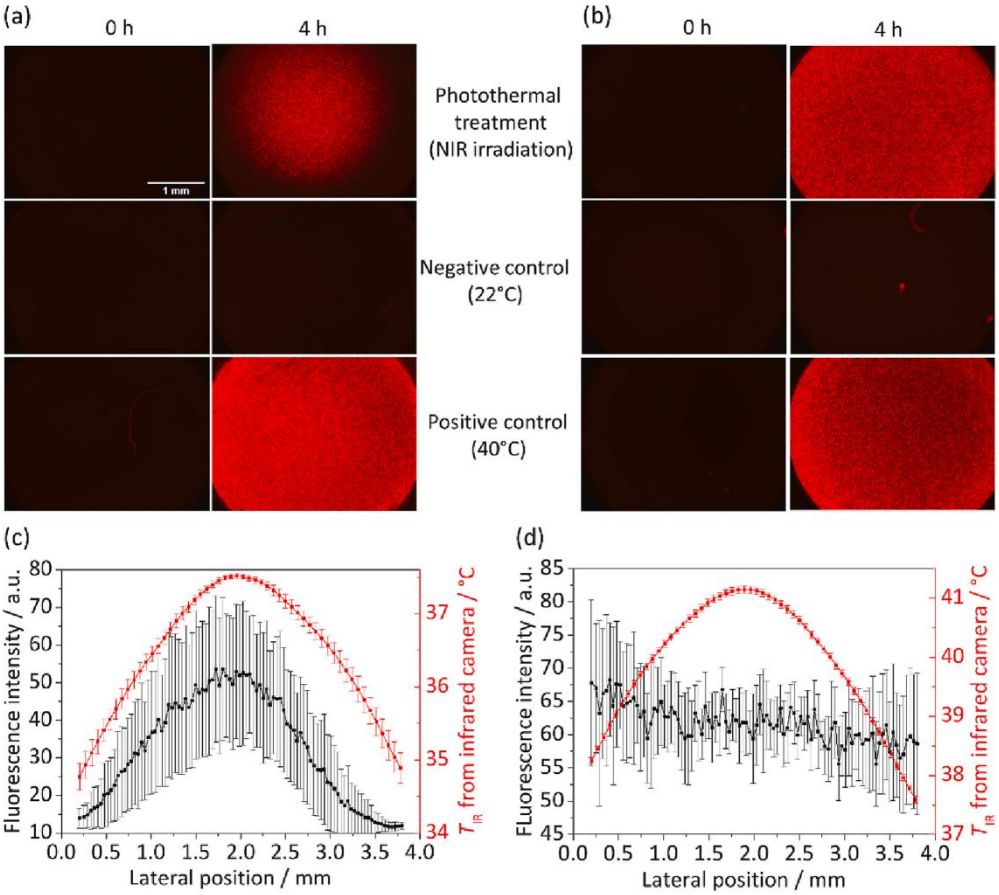

Fig. 5. Expression of fluorescent mCherry in thermoplasmonically stimulated ELMs. Fluorescence micrographs of ELM before and after 4 h stimulation at 0.5 W/cm^2(a) and (b) 0.7 W/cm^2. The temperatures reached in (a) were sufficient to activate bacteria in the center, but not at the border. The temperatures reached in (b) were sufficient for uniform activation, leading to uniform fluorescence. (c) Mean ± SD fluorescence and surface temperature profiles for laser power densities of 0.5–0.6 W/cm ($N = 3$). (d) Profiles for a laser power density of 0.7 W/cm^2 ($N = 3$).

knowledge, the first report on spatiotemporally controlled temperature distributions to activate bacterial gene expression in ELMs.

4. Conclusion

We designed an ELM with a bilayer hydrogel structure containing AuNRs and thermoresponsive bacteria and demonstrated the use of NIR light for the activation of the bacteria through photothermal conversion. This provides new options for the on-demand activation of ELM activity for therapeutic applications.

We demonstrated that the colloidal stability of AuNR@CTAB in hydrogel is sufficient to prepare NIR absorber gels with high efficiency. Agglomeration was not observed, and reproducible photothermal heating was achieved with the AuNR gel. The PCE of the AuNR gel was around 47 %, comparable with literature reports on pure nanorods, sufficient for the application, and stable over multiple cycles. Illumination with a collimated laser spot of 5 mm diameter at 808 nm and a power density of 0.7 W/cm^2 heated a cylindrical bilayered hydrogel in air from an initial 22 °C to a steady-state temperature of 41 °C in 300 s. Infrared thermometry indicated a lateral surface temperature gradient from center to border with a maximum temperature difference of 4.7 °C.

It is possible to complement the IR and thermocouple measurements and provide temperature data from inside the bulk. Luminescence nanothermometry can, for example, measure the temperature of hydrogels in vivo [60]. Suitable lanthanides or Ag_2S quantum dots can be embedded in the hydrogel layer, where they provide spatially resolvable, temperature-dependent photoluminescence [61,62].

The irradiation limit on human tissue (maximum permissible exposure, MPE) equals 0.3 W/cm^2 for 808 nm lasers [54]. Light at 808 nm penetrating mammalian tissues was attenuated to 10–20 % at 1 cm [55]. Assuming a linear relation between generated temperature difference and laser power density [48], and the data reported above, we would expect a temperature increase on the order of 1 K for the temperature increase of a Living Material embedded in tissue at 1 cm depth at a laser power density of 0.3 W/cm^2. The true value will be considerably larger because the convective cooling in our experiments is more efficient than the thermal diffusion that will remove heat from the implanted ELM. We are currently working on experimental setups to better emulate this situation. In addition, it will be possible to increase the temperature at lower laser power densities of 0.3 W/cm^2 by increasing the concentration of gold nanorods; one order of magnitude in concentration is probably attainable with suitable ligands that prevent agglomeration. An additional route to larger temperatures is a switch of laser wavelength to 1275 nm with an MPE of 1 W/cm^2 and higher penetration depths in tissue [63], at the cost of more expensive laser sources and optics.

We quantified bacterial activity in a AuNR gel-sensitized ELM as a function of laser power, time, and position via ex situ fluorescence microscopy. The fluorescence intensity correlated with the temperature distribution. Protein production at 0.5–0.6 W/m^2 was maximal at the center of the illuminated area and declined at its borders, where temperature dropped. Increasing laser power first led to an increase of fluorescence intensity at the borders. A uniform fluorescence intensity was reached across the illuminated area at 0.7 W/m^2. Protein expression continued for at least 4 h, with a linear increase of fluorescence that indicated sustained expression activity of the bacteria.

In summary, we demonstrated the NIR stimulation of an ELM and its efficacy using a model bacterium. This concept can be expanded to include additional stimuli such as magnetic fields or ultrasound in order to create multi-stimulus ELMs [64,65].

CRediT authorship contribution statement

Selim Basaran: Formal analysis, Investigation, Methodology, Writing – original draft. **Sourik Dey:** Investigation, Resources. **Shardul Bhusari:** Methodology, Resources. **Shrikrishnan Sankaran:** Conceptualization, Validation, Writing – original draft, Writing – review & editing, Supervision. **Tobias Kraus:** Conceptualization, Validation, Writing – original draft, Writing – review & editing, Supervision.

Declaration of competing interest

The authors declare that they have no known competing financial interests or personal relationships that could have appeared to influence the work reported in this paper.

Data availability

Data will be made available on request.

Acknowledgement

Funding from the Leibniz Science Campus “Living Therapeutic Materials” (LifeMat) is gratefully acknowledged. The authors thank Marcus Koch for his support in cryo-TEM imaging of the AuNR gel and Peter Rogin and Robert Strahl for fruitful discussions about the laser setup. The pTlpA39-Wasabi vector was a gift from Prof. Mikhail Shapiro, Addgene #86116.

Appendix A. Supplementary data

Supplementary data to this article can be found online at https://doi.org/10.1016/j.bioadv.2023.213332.

References

[1] P.Q. Nguyen, N.D. Courchesne, A. Duraj-Thatte, P. Praveschotinunt, N.S. Joshi, Engineered living materials: prospects and challenges for using biological systems to direct the assembly of smart materials, Adv. Mater. 30 (2018), e1704847.
[2] A. Rodrigo-Navarro, S. Sankaran, M.J. Dalby, A. del Campo, M. Salmeron-Sanchez, Engineered living biomaterials, Nat. Rev. Mater. 6 (2021) 1175–1190.
[3] K. Schulz-Schönhagen, N. Lobsiger, W.J. Stark, Continuous production of a shelf-stable living material as a biosensor platform, Adv. Mater. Technol. 4 (2019), 1900266.
[4] C. Zhang, J. Huang, J. Zhang, S. Liu, M. Cui, B. An, X. Wang, J. Pu, T. Zhao, C. Fan, T.K. Lu, C. Zhong, Engineered Bacillus subtilis biofilms as living glues, Mater. Today 28 (2019) 40–48.
[5] J. Pu, Y. Liu, J. Zhang, B. An, Y. Li, X. Wang, K. Din, C. Qin, K. Li, M. Cui, S. Liu, Y. Huang, Y. Wang, Y. Lv, J. Huang, Z. Cui, S. Zhao, C. Zhong, Virus disinfection: virus disinfection from environmental water sources using living engineered biofilm materials (Adv. Sci. 14/2020), Adv. Sci. 7 (2020), 2070076.
[6] C. Knierim, M. Enzeroth, P. Kaiser, C. Dams, D. Nette, A. Seubert, A. Klingl, C. L. Greenblatt, V. Jérôme, S. Agarwal, R. Freitag, A. Greiner, Living composites of bacteria and polymers as biomimetic films for metal sequestration and bioremediation, Macromol. Biosci. 15 (2015) 1052–1059.
[7] S. Sankaran, J. Becker, C. Wittmann, A. del Campo, Optoregulated drug release from an engineered living material: self-replenishing drug depots for long-term, light-regulated delivery, Small 15 (2019), 1804717.
[8] S. Wang, L.K. Rivera-Tarazona, M.K. Abdelrahman, T.H. Ware, Digitally programmable manufacturing of living materials grown from biowaste, ACS Appl. Mater. Interfaces 14 (2022) 20062–20072.
[9] F. Moser, E. Tham, L.M. González, T.K. Lu, C.A. Voigt, Light-controlled, high-resolution patterning of living engineered bacteria onto textiles, ceramics, and plastic, Adv. Funct. Mater. 29 (2019), 1901788.
[10] S. Sankaran, A. del Campo, Optoregulated protein release from an engineered living material, Adv. Biosyst. 3 (2019), 1800312.
[11] S.-J. Park, M. Gazzola, K.S. Park, S. Park, V. Di Santo, E.L. Blevins, J.U. Lind, P. H. Campbell, S. Dauth, A.K. Capulli, F.S. Pasqualini, S. Ahn, A. Cho, H. Yuan, B. M. Maoz, R. Vijaykumar, J.-W. Choi, K. Deisseroth, G.V. Lauder, L. Mahadevan, K. K. Parker, Phototactic guidance of a tissue-engineered soft-robotic ray, Science 353 (2016) 158–162.
[12] E. Ruggiero, S. Alonso-de Castro, A. Habtemariam, L. Salassa, Upconverting nanoparticles for the near infrared photoactivation of transition metal complexes: new opportunities and challenges in medicinal inorganic photochemistry, Dalton Trans. 45 (2016) 13012–13020.
[13] R. Shukla, V. Bansal, M. Chaudhary, A. Basu, R.R. Bhonde, M. Sastry, Biocompatibility of gold nanoparticles and their endocytotic fate inside the cellular compartment: a microscopic overview, Langmuir 21 (2005) 10644–10654.
[14] Y. Pan, S. Neuss, A. Leifert, M. Fischler, F. Wen, U. Simon, G. Schmid, W. Brandau, W. Jahnen-Dechent, Size-dependent cytotoxicity of gold nanoparticles, Small 3 (2007) 1941–1949.
[15] G.V. Hartland, Optical studies of dynamics in Noble metal nanostructures, Chem. Rev. 111 (2011) 3858–3887.

[16] H. Chen, L. Shao, Q. Li, J. Wang, Gold nanorods and their plasmonic properties, Chem. Soc. Rev. 42 (2013) 2679–2724.
[17] B. Nikoobakht, M.A. El-Sayed, Preparation and growth mechanism of gold nanorods (NRs) using seed-mediated growth method, Chem. Mater. 15 (2003) 1957–1962.
[18] S. Liao, W. Yue, S. Cai, Q. Tang, W. Lu, L. Huang, T. Qi, J. Liao, Improvement of gold nanorods in photothermal therapy: recent progress and perspective, Front. Pharmacol. 12 (2021).
[19] L. Wu, B. Lin, H. Yang, J. Chen, Z. Mao, W. Wang, C. Gao, Enzyme-responsive multifunctional peptide coating of gold nanorods improves tumor targeting and photothermal therapy efficacy, Acta Biomater. 86 (2019) 363–372.
[20] Z. Zhang, L. Wang, J. Wang, X. Jiang, X. Li, Z. Hu, Y. Ji, X. Wu, C. Chen, Mesoporous silica-coated gold nanorods as a light-mediated multifunctional theranostic platform for cancer treatment, Adv. Mater. 24 (2012) 1418–1423.
[21] H. Zhu, Y. Chen, F.-J. Yan, J. Chen, X.-F. Tao, J. Ling, B. Yang, Q.-J. He, Z.-W. Mao, Polysarcosine brush stabilized gold nanorods for in vivo near-infrared photothermal tumor therapy, Acta Biomater. 50 (2017) 534–545.
[22] Y. Li, D. He, J. Tu, R. Wang, C. Zu, Y. Chen, W. Yang, D. Shi, T.J. Webster, Y. Shen, The comparative effect of wrapping solid gold nanoparticles and hollow gold nanoparticles with doxorubicin-loaded thermosensitive liposomes for cancer thermo-chemotherapy, Nanoscale 10 (2018) 8628–8641.
[23] X. Jin, S. Yao, F. Qiu, Z. Mao, B. Wang, A multifunctional hydrogel containing gold nanorods and methylene blue for synergistic cancer phototherapy, Colloids Surf. A Physicochem. Eng. Asp. 614 (2021).
[24] X. Xu, Z. Huang, Z. Huang, X. Zhang, S. He, X. Sun, Y. Shen, M. Yan, C. Zhao, Injectable, NIR/pH-responsive nanocomposite hydrogel as long-acting implant for chemophotothermal synergistic cancer therapy, ACS Appl. Mater. Interfaces 9 (2017) 20361–20375.
[25] X. Huang, P.K. Jain, I.H. El-Sayed, M.A. El-Sayed, Plasmonic photothermal therapy (PPTT) using gold nanoparticles, Lasers Med. Sci. 23 (2008) 217–228.
[26] R.S. Riley, E.S. Day, Gold nanoparticle-mediated photothermal therapy: applications and opportunities for multimodal cancer treatment, Wiley Interdiscip. Rev. Nanomed. Nanobiotechnol. 9 (2017).
[27] R.K. Kannadorai, G.G.Y. Chiew, K.Q. Luo, Q. Liu, Dual functions of gold nanorods as photothermal agent and autofluorescence enhancer to track cell death during plasmonic photothermal therapy, Cancer Lett. 357 (2015) 152–159.
[28] S.M. M, S. Veeranarayanan, T. Maekawa, External stimulus responsive inorganic nanomaterials for cancer theranostics, Adv. Drug Deliv. Rev. 138 (2019) 18–40.
[29] R. Weissleder, A clearer vision for in vivo imaging, Nat. Biotechnol. 19 (2001) 316–317.
[30] L.E. Strong, J.L. West, Hydrogel-coated near infrared absorbing nanoshells as light-responsive drug delivery vehicles, ACS Biomater Sci. Eng. 1 (2015) 685–692.
[31] E.S. Day, J.G. Morton, J.L. West, Nanoparticles for thermal cancer therapy, J. Biomech. Eng. 131 (2009).
[32] L. Jauffred, A. Samadi, H. Klingberg, P.M. Bendix, L.B. Oddershede, Plasmonic heating of nanostructures, Chem. Rev. 119 (2019) 8087–8130.
[33] M. Tebbe, C. Kuttner, M. Mannel, A. Fery, M. Chanana, Colloidally stable and surfactant-free protein-coated gold nanorods in biological media, ACS Appl. Mater. Interfaces 7 (2015) 5984–5991.
[34] Y.-T. Liao, C.-H. Liu, Y. Chin, S.-Y. Chen, S.H. Liu, Y.-C. Hsu, K.C.W. Wu, Biocompatible and multifunctional gold nanorods for effective photothermal therapy of oral squamous cell carcinoma, J. Mater. Chem. B 7 (2019) 4451–4460.
[35] M.R.L. Zanetti, A.M. Percebom, T.A. Ribeiro, M.L. Dias, A.P. Oliveira, E.R. Júnior, A.L. Rossi, C.A.G. Soares, P.H.S. Picciani, Improving in vitro biocompatibility of gold nanorods with thiol-terminated triblock copolymer, Colloid Polym. Sci. 297 (2019) 1477–1487.
[36] H. Zhang, S. Guo, S. Fu, Y. Zhao, A near-infrared light-responsive hybrid hydrogel based on UCST triblock copolymer and gold nanorods, Polymers (Basel) 9 (2017).
[37] X. Dong, C. Wei, J. Liang, T. Liu, D. Kong, F. Lv, Thermosensitive hydrogel loaded with chitosan-carbon nanotubes for near infrared light triggered drug delivery, Colloids Surf. B: Biointerfaces 154 (2017) 253–262.
[38] A.G. Skirtach, C. Dejugnat, D. Braun, A.S. Susha, A.L. Rogach, W.J. Parak, H. Möhwald, G.B. Sukhorukov, The role of metal nanoparticles in remote release of encapsulated materials, Nano Lett. 5 (2005) 1371–1377.
[39] A. Shiotani, T. Mori, T. Niidome, Y. Niidome, Y. Katayama, Stable incorporation of gold nanorods into N-isopropylacrylamide hydrogels and their rapid shrinkage induced by near-infrared laser irradiation, Langmuir 23 (2007) 4012–4018.
[40] S. Malekmohammadi, N.Sedghi Aminabad, A. Sabzi, A. Zarebkohan, M. Razavi, M. Vosough, M. Bodaghi, H. Maleki, Smart and biomimetic 3D and 4D printed composite hydrogels: opportunities for different biomedical applications, Biomedicines 9 (2021) 1537.
[41] S. Tong, Q. Li, Q. Liu, B. Song, J. Wu, Recent advances of the nanocomposite hydrogel as a local drug delivery for diabetic ulcers, Front. Bioeng. Biotechnol. 10 (2022).
[42] J. Liao, K. Shi, Y. Jia, Y. Wu, Z. Qian, Gold nanorods and nanohydroxyapatite hybrid hydrogel for preventing bone tumor recurrence via postoperative photothermal therapy and bone regeneration promotion, Bioact. Mater. 6 (2021) 2221–2230.
[43] B. Leber, U. Mayrhauser, B. Leopold, S. Koestenbauer, K. Tscheliessnigg, V. Stadlbauer, P. Stiegler, Impact of temperature on cell death in a cell-culture model of hepatocellular carcinoma, Anticancer Res. 32 (2012) 915–921.
[44] S. Bhusari, J. Kim, K. Polizzi, S. Sankaran, A. del Campo, Encapsulation of bacteria in bilayer pluronic thin film hydrogels: a safe format for engineered living materials, Biomater. Adv. 145 (2023), 213240.
[46] S. Bhusari, S. Sankaran, A. Del Campo, Regulating bacterial behavior within hydrogels of tunable viscoelasticity, Adv. Sci. (Weinheim, Ger.) 9 (2022), e2106026.
[47] D.I. Piraner, M.H. Abedi, B.A. Moser, A. Lee-Gosselin, M.G. Shapiro, Tunable thermal bioswitches for in vivo control of microbial therapeutics, Nat. Chem. Biol. 13 (2017) 75–80.
[48] D.K. Roper, W. Ahn, M. Hoepfner, Microscale heat transfer transduced by surface plasmon resonant gold nanoparticles, J. Phys. Chem. C 111 (2007) 3636–3641.
[49] K. Jiang, D.A. Smith, A. Pinchuk, Size-dependent photothermal conversion efficiencies of plasmonically heated gold nanoparticles, J. Phys. Chem. C 117 (2013) 27073–27080.
[50] B. Reiser, L. González-García, I. Kanelidis, J.H.M. Maurer, T. Kraus, Gold nanorods with conjugated polymer ligands: sintering-free conductive inks for printed electronics, Chem. Sci. 7 (2016) 4190–4196.
[51] S. Jayabal, A. Pandikumar, H.N. Lim, R. Ramaraj, T. Sun, N.M. Huang, A gold nanorod-based localized surface plasmon resonance platform for the detection of environmentally toxic metal ions, Analyst 140 (2015) 2540–2555.
[52] R. Kanjanawarut, B. Yuan, S. XiaoDi, UV-vis spectroscopy and dynamic light scattering study of gold nanorods aggregation, Nucleic Acid Ther. 23 (2013) 273–280.
[53] Y. Wang, Z. Gao, Z. Han, Y. Liu, H. Yang, T. Akkin, C.J. Hogan, J.C. Bischof, Aggregation affects optical properties and photothermal heating of gold nanospheres, Sci. Rep. 11 (2021) 898.
[54] ICNIRP guidelines on limits of exposure to laser radiation of wavelengths between 180 nm and 1,000 μm, Health Phys. 105 (2013) 271–295.
[55] C.E. Tedford, S. DeLapp, S. Jacques, J. Anders, Quantitative analysis of transcranial and intraparenchymal light penetration in human cadaver brain tissue, Lasers Surg. Med. 47 (2015) 312–322.
[56] M. Almada, B.H. Leal-Martínez, N. Hassan, M.J. Kogan, M.G. Burboa, A. Topete, M. A. Valdez, J. Juárez, Photothermal conversion efficiency and cytotoxic effect of gold nanorods stabilized with chitosan, alginate and poly(vinyl alcohol), Mater. Sci. Eng. C 77 (2017) 583–593.
[57] P.K. Jain, K.S. Lee, I.H. El-Sayed, M.A. El-Sayed, Calculated absorption and scattering properties of gold nanoparticles of different size, shape, and composition: applications in biological imaging and biomedicine, J. Phys. Chem. B 110 (2006) 7238–7248.
[58] V.P. Pattani, J.W. Tunnell, Nanoparticle-mediated photothermal therapy: a comparative study of heating for different particle types, Lasers Surg. Med. 44 (2012) 675–684.
[59] J.R. Cole, N.A. Mirin, M.W. Knight, G.P. Goodrich, N.J. Halas, Photothermal efficiencies of nanoshells and nanorods for clinical therapeutic applications, J. Phys. Chem. C 113 (2009) 12090–12094.
[60] Y. Qi, J. Ye, S. Ren, G. Wang, J. Lv, S. Zhang, Y. Che, Y. Li, B. Chen, G. Ning, Temperature feedback-controlled photothermal/photodynamic/chemodynamic combination cancer therapy based on NaGdF4:er, Yb@NaGdF4:Nd@Cu-BIF nanoassemblies, Adv. Healthc. Mater. 9 (2020), 2001205.
[61] B. del Rosal, D. Ruiz, I. Chaves-Coira, B.H. Juárez, L. Monge, G. Hong, N. Fernández, D. Jaque, In vivo contactless brain nanothermometry, Adv. Funct. Mater. 28 (2018), 1806088.
[62] B. del Rosal, E. Ximendes, U. Rocha, D. Jaque, In vivo luminescence nanothermometry: from materials to applications, Adv. Opt. Mater. 5 (2017).
[63] X. Wu, Y. Suo, H. Shi, R. Liu, F. Wu, T. Wang, L. Ma, H. Liu, Z. Cheng, Deep-tissue photothermal therapy using laser illumination at NIR-IIa window, Nano-Micro Lett. 12 (2020) 38.
[64] B. Gambin, E. Kruglenko, R. Tymkiewicz, J. Litniewski, Ultrasound assessment of the conversion of sound energy into heat in tissue phantoms enriched with magnetic micro- and nanoparticles, Med. Phys. 46 (2019) 4361–4370.
[65] K. Kaczmarek, T. Hornowski, I. Antal, M. Timko, A. Józefczak, Magneto-ultrasonic heating with nanoparticles, J. Magn. Magn. Mater. 474 (2019) 400–405.

Supporting Information

Plasmonic Stimulation of Gold Nanorods for the Photothermal Control of Engineered Living Materials

Selim Basaran[1], Sourik Dey[1], Shardul Bhusari[1,2], Shrikrishnan Sankaran[1*], Tobias Kraus[1,3*]

[1] INM – Leibniz Institute for New Materials, Saarbrücken, Germany
[2] Chemistry Department, Saarland University, 66123 Saarbrücken, Germany
[3] Colloids and Interface Chemistry, Saarland University, Saarbrücken, Germany
*Corresponding authors: tobias.kraus@leibniz-inm.de, shrikrishnan.sankaran@leibniz-inm.de

Laser setup

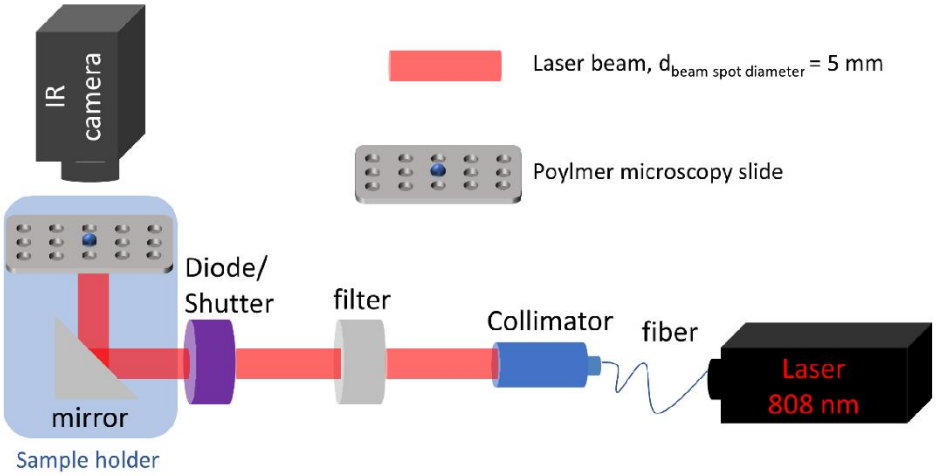

Figure S 1: Laser setup used for laser excitation at 808 nm with concurrent observation of surface temperature with an IR camera.

Fluorescence intensity analysis in micrographs

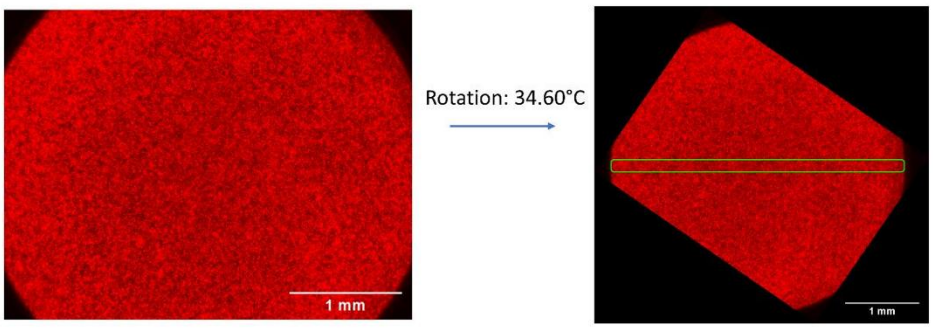

Figure S 2: Quantification of fluorescence intensity via image analysis. The fluorescence micrograph was analyzed using Image J by rotating the image by 33.6° and inscribing a rectangle with 0.17 mm height and 4 mm length. The pixel values were then averaged along the height and the mean value used as a line profile.

UV–VIS absorbance spectra from hydrogel

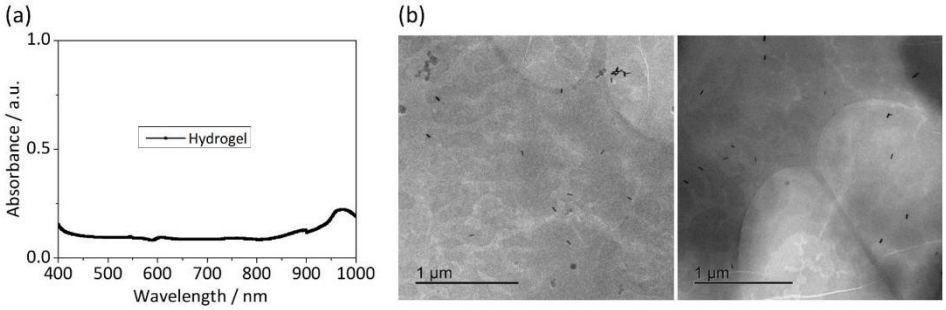

Figure S 3: (a) UV–VIS absorbance spectra from hydrogel without embedded AuNR. (b) cryo-TEM of AuNR embedded in a hydrogel.

Heat transfer in hydrogel bilayer in a microwell

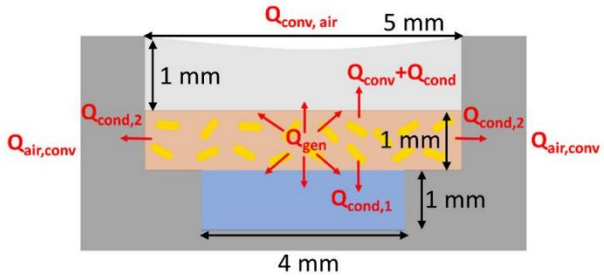

Figure S 4: Schematic structure of the hydrogel bilayer in a microwell. Schematic structure of the hydrogel bilayer in a microwell. Thermal transport dissipated the heat generated photothermally at a rate Q_{gen} through thermal diffusion and convection to the environment. The result was a steady-state temperature distribution at the surface that we quantified.

Position P1 for evaluation of photothermal activity and stability

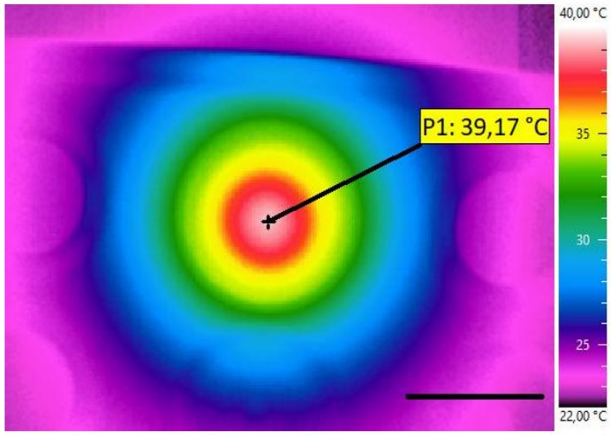

Figure S 5: Infrared thermography image with the marked position P1 that we used for the photothermal stability measurements in section 3.2. Representative steady state temperature shown here. Scale bar indicates 5 mm.

Setup for determing Photothermal Conversion Efficiency (PCE)

The PCE of the gold nanorod composite (GNC) hydrogel was determined in a glass cuvette. A thermocouple was embedded in the GNC hydyrogel to follow the temperature changes induced by thermoplasmonic heating upon 808 nm laser irradiation.

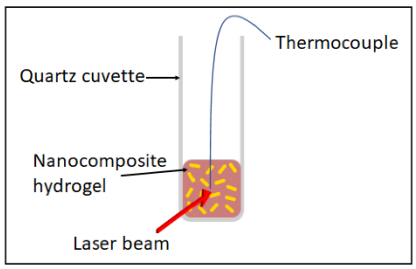

Figure S 6: Setup for the determination of the PCE of a gold nanorod composite (GNC) hydrogel in a glass cuvette. The thermocouple was used to quantify the temperature change upon illumination.

Calculation of the Photothermal Conversion Efficiency

The photothermal conversion efficiency was calculated following literature.[1-4] The total energy balance of the system is described as:

$$\sum_i m_i c_{p,i} \frac{dT}{dt} = Q_{in} + Q_0 - Q_{out} \quad (1)$$

where m_i and $c_{p,i}$ are the mass and heat capacity of GNC hydrogel and glass cuvette in the system, T is the system temperature, and t is time.
Q_{in} is the photothermal energy emitted by the illuminated AuNRs under laser light illumination:

$$Q_{in} = I_0(1 - 10^{-A_{808nm}})\eta \quad (2)$$

where I_0 is the incident laser power (89 mW), A_{808nm} is the absorbance of GNC hydrogel in cuvette at 808 nm which was measured to be $OD_{AuNR,2mm,808nm}$ = 0.67, and η is the photothermal conversion efficiency. Q_0 is the energy input contributed to adsorption by the pure hydrogel and the cuvette and was determined to be 0.35 mW.
The heat dissipated to the external environment is given by Q_{out}:

$$Q_{out} = hS(T(t) - T_{amb}) \quad (3)$$

where h is the heat transfer coefficient, S is the surface are of the quartz cuvette, $T(t)$ is the temperature of the GNC hydrogel at time t, and T_{amb} is the ambient temperature of the surroundings. By defining $\Delta T \equiv T(t) - T_{amb}$, equation 1 can be expressed as:

$$\frac{d\Delta T}{dt} = \frac{I_0(1 - 10^{-A_{808nm}})\eta}{\sum_i m_i c_{p,i}} - \frac{hS}{\sum_i m_i c_{p,i}} \Delta T + Q_0 \quad (4)$$

A time constant of the overall system is defined as $B \equiv hS / \sum m_i c_{p,i}$. It is determined experimentally by measuring the decreasing temperature profile after the laser is turned off, setting $Q_{in} = 0$ in equation 4, and setting $T(t = 0\ s) = T_{max}$, resulting in the cooling temperature profile:

$$T(t) = T_{amb} + (T_{max} - T_{amb})e^{-Bt} \quad (5)$$

where T_{max} is the maximum temperature at which the laser is turned off.

The cooling curve was fitted with Eq. 5 to determine the constant *B*. We use it to calculate *hS*, making it possible to determine the PCE η:

$$\eta = \frac{hA(T_{\max} - T_{\text{amb}}) - Q_0}{I_0(1 - 10^{-A_{808\text{nm}}})} \quad (6)$$

Another method to determine the heat dissipation rate *B* is to determine the slope of temperature profile after laser is turned off by using Eq. (5).[4] Eq. (5) is linearized by plotting the natural log of θ as a function of time after turning laser off at time interval of 30 s. θ is defined as $[(T(t) - T_{amb}) / (T_{max} - T_{amb})]$. *B* is calculated by determining the slope.

IR image for determing the lateral uncertainty of section 3.3

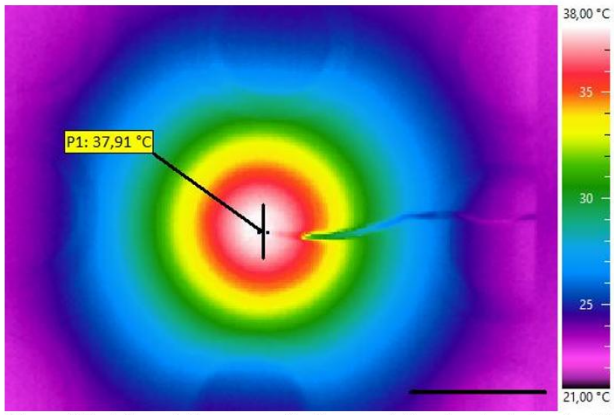

Figure S 7: Infrared thermography image of the steady state of a illuminated, bilayered hydrogel. The inset at the center (length: 2 mm) indicates the temperature gradient that we used to calculate the lateral uncertainty in temperature. Scale bar indicates 5 mm.

Temperature range for the bacterial activity

Bacterial cultures were incubated overnight in 5 mL of LB-NaCl media (supplemented with 100 µg/mL ampicillin) at 30°C with continuous shaking (250 rpm). The following day, cultures were diluted to 0.1 OD_{600} in 3 mL of antibiotic-supplemented fresh media and regrown at 30°C, 250 rpm. At OD_{600} = 0.3, the cultures were dispensed into Fisherbrand™ 0.2mL PCR Tube Strips with Flat Caps (Thermo Electron LED GmbH, Germany) and placed in the Biometra Thermocycler (Analytik Jena. GmbH, Germany). The thermal assay was set at a temperature gradient from 31◦C to 43◦C with regular increment of 2◦C. The lid temperature was set at 50◦C to prevent the evaporation of the liquid and maintain a homogeneous temperature in the spatially allocated PCR tubes. After a time interval of 18 h, the PCR strips were centrifuged in a tabletop minicentrifuge (Biozym GmbH, Germany) to pellet down the cells and discard the supernatant. The cells were then resuspended in 200 µL of 1X PBS and added to the clear bottom 96-well microtiter plate (Corning® 96 well clear bottom black plate, USA). The samples were then analyzed in the Microplate Reader Infinite 200 Pro (Tecan Deutschland GmbH, Germany) and both the absorbance (600 nm wavelength) and mCherry fluorescence intensity (Ex_λ / Em_λ = 587 nm/625 nm) were measured. The z-position and gain settings for recording the mCherry fluorescent intensity were set to 19442 µm and 136 respectively. Fluorescence values were normalized with the optical density of the bacterial cells to calculate the Relative Fluorescence Units (RFU) using the formula RFU = Fluorescence/OD_{600}.

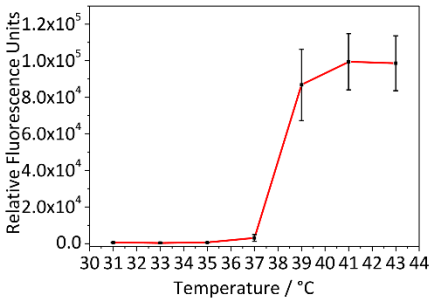

Figure S 8: Fluoresence intensity of mCherry produced by the Clearcoli bacteria expressed in relative fluorescence units as a function of temperature. Symbols represent means and whiskers represent standard deviation from three individual experiments.

Thermoplasmonic NIR stimulation of mCherry producing bacteria

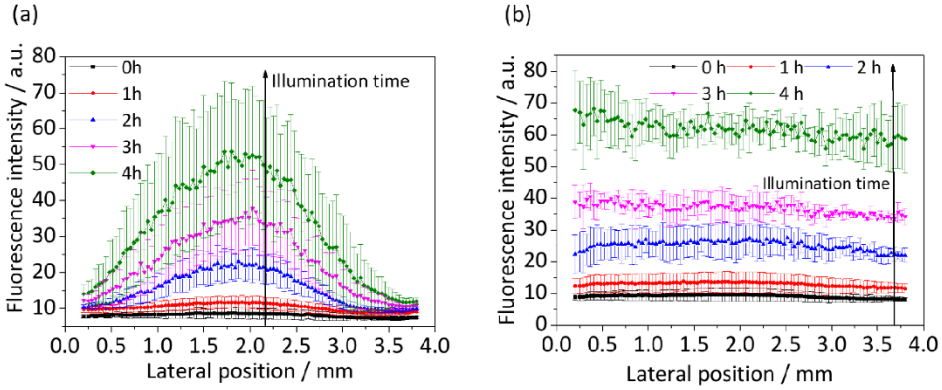

Figure S 9: Expression of fluorescent mCherry in thermoplasmonically stimulated ELMs at illumination times 0 h, 1 h, 2 h, 3 h and 4 h. (a) Mean fluorescence and surface temperature profiles for laser power densities of 0.5–0.6 W/cm (N = 3, mean ± standard deviation). (b) Profiles for a laser power density of 0.7 W/cm² (N = 3, mean ± standard deviation).

Positive and negative controls for photothermally simulated ELM

The expression of the mCherry protein upon photothermal stimulation was compared to positive and negative controls. As a positive control, the bilayered hydrogel was incubated at 40 °C in an oven for 0 h, 1 h, 2 h, 3 h, and 4 h. Uniform bacterial activity was observed. As a negative control, the sample was kept at 22 °C. No bacterial activity was observed.

As an additional negative control, non-engineered bacteria ("wild type") were encapsulated in a gel, exposed to NIR Irradiation, and incubated at 40°C. No mCherry production was detected.

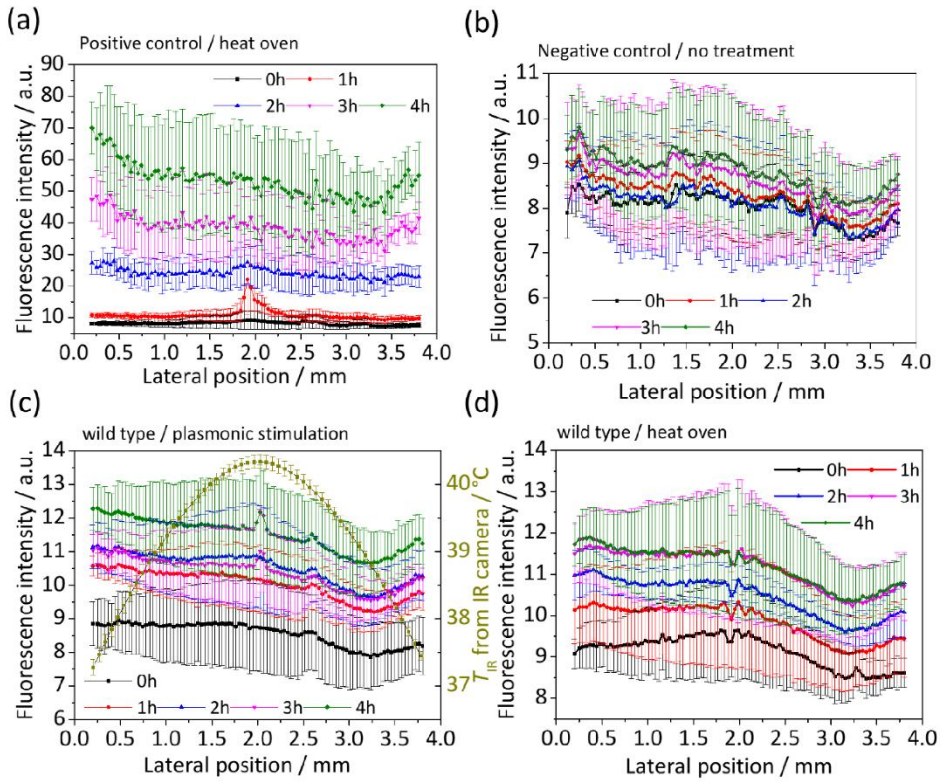

Figure S 10: (a) The engineered bilayer hydrogel ELM was incubated in an oven at 40°C as positive control. A continuous increase of mCherry production with time was observed (N = 3, mean ± standard deviation). (b) Negative control of mCherry production of the engineered bilayer hydrogel (N = 3, mean ± standard deviation). The hydrogel was incubated at room temperature at 22°C without any stimulation. No significant mCherry production was observed. (c)+(d) Negative control with wild type bacteria encapsulated in the bilayer structure. (c) Plasmonic stimulation. The spatial mCherry production was quantified via fluorescence intensity at different plasmonic stimulation durations (N = 3, mean ± standard deviation). No significant mCherry production was detected. (d) Incubation at 40°C (N = 3, mean ± standard deviation). No significant mCherry production was observed.

Literature

[1] K.C. Li, H.C. Chu, Y. Lin, H.Y. Tuan, Y.C. Hu, PEGylated Copper Nanowires as a Novel Photothermal Therapy Agent, ACS Appl Mater Interfaces 8 (2016) 12082-12090.
[2] S. Chen, F. Tang, L. Tang, L. Li, Synthesis of Cu-Nanoparticle Hydrogel with Self-Healing and Photothermal Properties, ACS Appl Mater Interfaces 9 (2017) 20895-20903.
[3] D.K. Roper, W. Ahn, M. Hoepfner, Microscale Heat Transfer Transduced by Surface Plasmon Resonant Gold Nanoparticles, The Journal of Physical Chemistry C 111 (2007) 3636-3641.
[4] K. Jiang, D.A. Smith, A. Pinchuk, Size-Dependent Photothermal Conversion Efficiencies of Plasmonically Heated Gold Nanoparticles, The Journal of Physical Chemistry C 117 (2013) 27073-27080.

5.2 Thermoplasmonic stimulation of PCQ producing engineered living materials

The publication in chapter 5.1 introduced a strategy for activating Engineered Living Materials (ELMs) using near-infrared (NIR) light at 808 nm. We leveraged the thermoplasmonic properties of gold nanorods (AuNRs). The proof-of-concept utilized a thermoresponsive *ClearColi* strain producing mCherry as a model protein. This section extends the concept to NIR-responsive ELMs designed for therapeutic applications, specifically wound healing.

Single-layer ELMs were developed, that contain both bacteria and AuNRs in the same hydrogel layer. The ELM had a cylindrical shape with a diameter of 4 mm and a volume of 10 µL. This design eliminates the need for bilayer structures, where heat conduction across layers was required, as described in chapter 5.1. The close proximity of AuNR and the bacteria reduces the laser power densities required to reach bacterial activation temperature and avoids exceeding the Maximum Permissible Exposure (MPE) limits (see section 3.4.1).

5.2.1 Introduction

In this work, cytotoxic AuNR@CTAB particles used in chapter 5.1 were replaced by biocompatible, non-cytotoxic bovine serum albumin-stabilized gold nanorods (AuNR@BSA). [1, 2] The bacterial strain was changed to the well-characterized probiotic *E. coli* Nissle 1917[3], which was genetically engineered to exhibit thermoresponsive behavior. A polyvinyl alcohol-vinyl sulfone (PVA-VS) hydrogel was used for encapsulation, because it has been reported as a safe matrix for *E. coli* Nissle by Riedel et al.[4] The engineered *E. coli* Nissle strain produces QK peptide (KLTWQELYQLKYKGI), a synthetic analog of vascular endothelial growth factor (VEGF), upon heat exposure between 38 °C and 44 °C. VEGF is a key mediator in promoting proliferation and angiogenesis for wound healing.

AuNRs have been explored for wound healing as free dispersions (see section 3.4.4) and as nanocomposites (see Section 3.4.7). Current approaches rely on uncontrolled VEGF expression by wound tissue stimulated by thermoplasmonic AuNRs, which typically require 5–15 days for enhanced wound healing.[5] This VEGF expression is induced by heat-mediated activation of heat shock proteins and other cellular stress responses, which upregulate angiogenic factors, including VEGF, to promote tissue regeneration and vascularization. To achieve more controlled angiogenesis, alternative strategies involve the surface modification of AuNRs[6], such as functionalization with pro-angiogenic peptides[7, 8] or antimicrobial peptides[8], as well as the incorporation of antioxidant agents[9, 10] into AuNR-based formulations, often within complex dermatological scaffolds.[5, 11] These approaches are limited by complex

fabrication, and finite drug release. In contrast, the approach presented here utilizes thermally triggered ELMs for controlled, on-demand VEGF-mimetic peptide expression. This targeted strategy avoids side effects and the challenges of modifying nanoparticles, offering a more straightforward and potentially faster wound healing process.

ELMs have already been used for wound healing (see section 3.5.3). Dhakane et al. designed core-shell ELMs where an optogenetically modified *ClearColi* strain was embedded in PluDA with a core volume of about 23 µL and an initial bacterial density of $OD_{600\,nm}$ = 0.1.[12] The ELM was activated by blue light (450 nm, 100 – 200 µW/cm^{-2}) to secrete a QK-bearing fusion protein (YCQ) that diffused into the surrounding media and promoted wound healing. In this work, *E. coli* Nissle 1917 was engineered with a TlpA repressor integrated thermal circuit[13], which stimulated the bacteria to express QK peptide-bearing PCQ protein between 38°C and 44°C.[14] To the best of my knowledge, this is the first report on the combination of AuNRs and engineered bacteria in a single-layer ELM for wound healing. The AuNRs enable NIR light-triggered activation in deep tissues (see section 3.4.1). The localized heating via NIR light minimizes unintended thermal damage to surrounding tissues while maintaining bacterial activity during treatment.

In this study, the photothermal conversion efficiency (PCE) of AuNR@BSA was evaluated in various matrices, including water, LB media, hydrogels, and in bacterial hydrogels (ELMs). It was found that bacterial growth after 20 h influenced the PCE in LB media and bacterial hydrogels, while the colloidal stability of AuNR@BSA remained largely unaffected within the hydrogel matrix. This is the first report on the impact of bacterial growth on PCE.

The PCQ protein production from the ELM during thermoplasmonic stimulation was evaluated. NIR laser irradiation (808 nm, 0.3 W/cm²) for 30 min triggered gene expression, demonstrating bacterial survival during plasmonic heating. The previously used laser was replaced by a more skin-friendly LED lamp (0.02 W/cm²) to stimulate PCQ expression for 60 min in a tissue model, achieving VEGF release under moderate light intensities.

The ELM introduced here has the potential to overcome limitations of traditional growth factor engineering, such as poor stability, and complex delivery requirements, offering a localized treatment strategy for vascularization in wound healing applications. By integrating AuNRs as NIR-sensitive nanoheaters, these ELMs hold potential for advanced biomedical applications, providing controlled, on-demand therapeutic molecule release.

5.2.2 Materials and methods

This section outlines the materials and experimental methods employed in this work. It details the preparation and characterization of AuNR@BSA hydrogels and ELMs, as well as the setup and execution of photothermal experiments. Additionally, the biological circuit of the engineered *E. coli* Nissle 1917 and the quantification method for the produced therapeutic QK peptide-bearing PCQ proteins are described.

5.2.2.1 Materials

Gold nanorods (length: 41 nm, diameter: 10 nm) capped with BSA (AuNR@BSA) in water were purchased from Nanopartz Inc. (Canada). An optical density of $OD_{808\ nm} = 1$ corresponds to a concentration of 35 µg/mL. The bacterial growth medium used was LB Miller (Carl Roth GmbH, Germany). The hydrogel precursor, polyvinyl alcohol vinyl sulfone (PVA-VS) aqueous solution, was provided by INM´s Dynamic Biomaterials group. A PVA-VS aqueous solution was further treated by adding 1.25%wt of photocrosslinker lithium-phenyl-2,4,6-trimethylbenzoylphosphinate (LAP, Sigma-Aldrich, Germany) and LB media at a volume ratio of 1:0.8. This hydrogel precursor is denoted as PVA-VS_{LB}. Microscopy slides with 15 wells (type "µ-slide Angiogenesis") with uncoated bottoms were obtained from Ibidi (Gräfelfing, Germany). A thermoresponsive *E .coli* Nissle 1917 strain was provided by INM´s Bioprogrammable Materials group. A collagen gel was provided by INM´s Bioprogrammable Materials group.

5.2.2.2 Preparation and characterization of AuNR@BSA nanocomposite gel

The AuNR@BSA ($OD_{808\ nm} = 1$) in water was centrifuged at 12,500 rpm for 8 min at room temperature to obtain desired concentration of $OD_{808\ nm} = 60$. 5 %v/v AuNR gels were prepared by mixing the PVA-VS_{LB} precursor with AuNR@BSA suspension to a final concentration of $OD_{808\ nm} = 3$. The AuNR gel was exposed to blue light (402 nm, 6 mW/cm^2) in a radiation chamber (Opsytec Dr. Göbel, Germany) to crosslink the vinyl sulfone groups.

The resulting nanocomposite gel was characterized by UV-VIS-NIR spectrometer (Cary 5000 UV-VIS-NIR spectrophotometer, Germany) in a disposable cuvette.

5.2.2.3 Setup for photothermal stimulation by laser

A laser setup for the photothermal excitation of AuNRs was constructed. A continuous wave (CW) laser (CNI, China) provided excitation light at 808 nm (NIR-I biology window) with an

adjustable power between 100 mW and 6 W. The laser light was coupled into a SMA 905 multimode fiber (400 µm core diameter, CNI, China) and connected to a collimator (FOC-01, CNI, China). The collimated laser beam spot diameter was 10 mm. A mechanical shutter with an integrated Si photodiode (FDS10X10, Thorlabs, Germany, behind a ND filter from Thorlabs) was used to control the irradiation on/off states and to measure the incoming laser power. A dielectric right angle prism mirror (MRA20-E03, Thorlabs, Germany) reflected the laser light to a single well of the well plate (µ-slide Angiogenesis, ibidi, Germany on the sample holder. It was aligned with the help of a monochromatic camera (DMK 23U445, The Imaging Source, Germany). The distance between the well plate and collimator was 10 cm. An infrared camera (VarioCam@HD 980 S, Infratech, Germany) was mounted 10 cm above the sample to measure the temperature distribution. Optionally, a thermocouple (K-Type, 1.4541 stainless steel) was inserted in the well with the gel inside as a supplementary thermometry.

5.2.2.4 Biological circuit of engineered *E. coli* Nissle 1917

E. coli Nissle 1917 was engineered by Anwesha Chatterjee of INM´s Bioprogrammable Materials to express and secrete a QK-bearing fusion protein (PCQ) at temperatures between 38 °C and 44 °C.

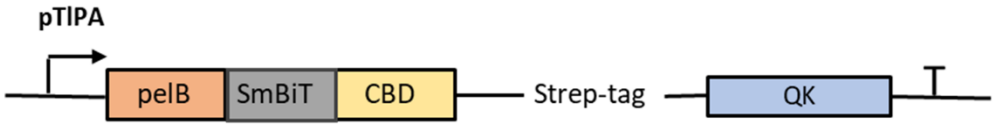

Figure 5- 1: The biological circuit of the engineered *E. coli* Nissle strain. This scheme was done by Anwesha Chatterjee and is used by her permission.

The biological circuit (Figure 5- 1), which encodes the PCQ fusion protein, consists of multiple functional domains: the pelB leader sequence, which directs the protein to the periplasm in *E. coli*; the SmBiT tag, enabling quantification via the Split Luciferase Assay; a collagen-binding domain (CBD) for immobilization within the extracellular matrix; a Strep-TagII peptide for purification and staining; and the QK peptide, which promotes angiogenesis. The PCQ protein was cloned into a *E. coli* Nissle 1917 strain. A TlpA promoter that drives expression (see section 3.5.1.1) was used to make it thermoresponsive.

5.2.2.5 Preparation and photothermal stimulation of ELM

E. coli Nissle 1917 was inoculated in LB media from glycerol stock and grown at 35°C until it reached its log phase ($OD_{600\,nm}$ = 0.7–0.8) of expansion. The bacterial suspension was then centrifuged at 9,600 rpm for 3 min at room temperature to reach an $OD_{600\,nm}$ = 8. The aqueous

dispersion of AuNR@BSA ($OD_{808\ nm}$ = 1) was centrifuged at 12,500 rpm for 8 min at room temperature to $OD_{808\ nm}$ = 60.

To prepare the mixture, 10% v/v of bacteria ($OD_{600\ nm}$ = 8) and AuNRs (OD808 nm = 60) were combined in a 1:1 volume ratio with the PVA-VS_{LB} precursor. The mixed dispersion of bacteria, AuNR@BSA, and polymer (10 µL) was injected into wells (µ-slide Angiogenesis) and then photopolymerized at 402 nm (2 min, 6 mW/cm^2) using a radiation chamber (Opsytec Dr.Göbel, Germany).The final concentrations of bacteria and AuNR in the PVA-VS gel were $OD_{600\ nm}$ = 0.4 and $OD_{808\ nm}$ = 3, respectively. The final product ("ELM" in the following) was covered with LB media (40 µL). The ELM volumes had cylindrical shapes with a diameter of 4 mm and a height of 1 mm covered by liquid LB media (40 µL) which filled a volume of a diameter of 5 mm and a height of 2 mm.

The well plate with the ELMs was placed in a plastic box where wet tissues generated high humidity to minimize evaporation of the LB medium. The plastic box was placed in an incubator (New Brunswick Innova® 44/44R, Eppendorf, Canada) at 35 °C for 20 h for letting the bacteria grow over night in the gel. On the following day, the supernatant was replaced with fresh LB medium to ensure sufficient nutrients for bacterial activity before initiating the photothermal experiments. The samples were then subjected to NIR irradiation and corresponding control conditions for 30 minutes. NIR-radiation (808 nm, CW laser) was performed at a power density of 0.2–0.3 W/cm². The temperature evolution during irradiation was monitored using an infrared camera (VarioCam@HD 980 S, Infratech, Germany) to assess the photothermal response of the samples.

For the positive control, samples were incubated at 40 °C in a humid plastic box inside an incubator (New Brunswick Innova® 44/44R, Eppendorf, Canada) to mimic thermal activation without NIR irradiation. The negative control was conducted under identical conditions at 35 °C to represent baseline bacterial activity without thermoplasmonic stimulation. Blank samples of pure PVA-VS gels and PVA-VS gels with AuNRs ($OD_{808\ nm}$ = 3) without bacteria were conducted and treated in same way as plasmonic treatment.

The LB media of all treated wells was pipetted from the well, weighted on a balance and diluted with fresh LB media to the initial 40 µL of volume to compensate for evaporation. The concentration of the secreted PCQ in the medium is determined as described in section 5.2.2.8.

The concentration of PCQ peptides in the hydrogels were measured by transferring them into white, flat-bottomed 96-well plates with the help of tweezers. The determination of PCQ

concentration in supernatant and in gel was done by a microplate reader (Tecan Infinite M Plex) (see section 5.2.2.8).

5.2.2.6 Photothermal conversion efficiency

The PCEs of AuNR@BSA in water, LB medium, PVA-VS hydrogel, and in ELM were determined in glass cuvettes. An infrared camera monitored the temperature changes induced by thermoplasmonic heating upon 808 nm laser irradiation with a beam diameter of 10 mm. The maximum temperature of the sample was recorded for PCE calculations. The temperature gradient detected by the infrared camera within the system was ≤ 0.6 °C, and only the highest recorded temperature within the distribution was used for analysis.

All PCEs were determined as described in section 3.3.3. The energy balance of the system is described in equation (3- 17), where $m_i c_{p,i}$ are the products of the mass and heat capacities of the AuNR@BSA in their respective matrix and the quartz cuvette, T is the system temperature, and t is time. Here, m_i was determined experimentally, while $c_{p,i}$ was assumed to be 4.2 (J/g·K) for all aqueous matrices and 0.84 J/(g·K) for the quartz cuvette.

The photothermal energy $Q_{plasmonic}$ that is emitted by the illuminated AuNRs is given by equation (3- 12), where I_0 is the incident laser power (134 mW), A_{808nm} is the absorbance of AuNRs in their respective matrices in cuvette at 808 nm which was measured to be 0.2 – 0.3 for all systems, and η is the PCE. The energy contribution from the pure matrices and the cuvette, Q_0, was determined by measuring the temperature increase in cuvettes containing only the matrix material (water, LB medium, hydrogel, or ELM) without AuNRs. Temperature changes were recorded using the IR camera. No significant temperature increase was observed, allowing Q_0 to be considered negligible.

The heat dissipation Q_{out} to the external environment is given by equation (3- 16), where h is the heat transfer coefficient, A is the surface are of the quartz cuvette, $T_{surface}$ is the temperature of the system at time t, and T_{amb} is the ambient temperature of the surroundings. The ambient temperature was measured separately for each experimental assay using a TC placed near the system to measure the temperature of the surrounding air.

The system´s overall time constant, $B = \sum_i hA/m_i\, c_{p,i}$, was determined experimentally by measuring the cooling temperature profile after the laser is turned off. The data were fitted by equation (3- 19), where T_{max} is the maximum temperature at which the laser is turned off. The obtained B values were used to calculate hA, enabling the determination of PCE η with equation (3- 20).

The dimensionless driving force temperature θ_T is given by equation (3- 22). The cooling curve can then be described by equation (3- 23). To further analyze heat dissipation, *B* was also determined by plotting $\ln(\theta_T)$ vs time *t*, which linearizes the equation (3- 23). The slope of this plot corresponds to *B*, providing an alternative method for determining . This linearization validates that cooling follows a first-order decay (see section 3.3.3). Additionally, it allows for direct comparison of heat dissipation dynamics between different matrices, clarifying how the surrounding environment influences nanoparticle-mediated thermal transport.

5.2.2.7 Analysis of temperature distribution using thermal imaging

Thermal images were recorded using an infrared camera (VarioCam@HD 980 S, Infratech, Germany) and analyzed with *IRBIS 3.1* software. The infrared camera, positioned 10 cm above the sample, captured the entire template area, including all wells (Figure 5- 2 A and B). Images were taken at 30-second intervals, including initial conditions with the laser turned off (Figure 5- 2 A and C), and during steady-state heating (Figure 5- 2 B and D).

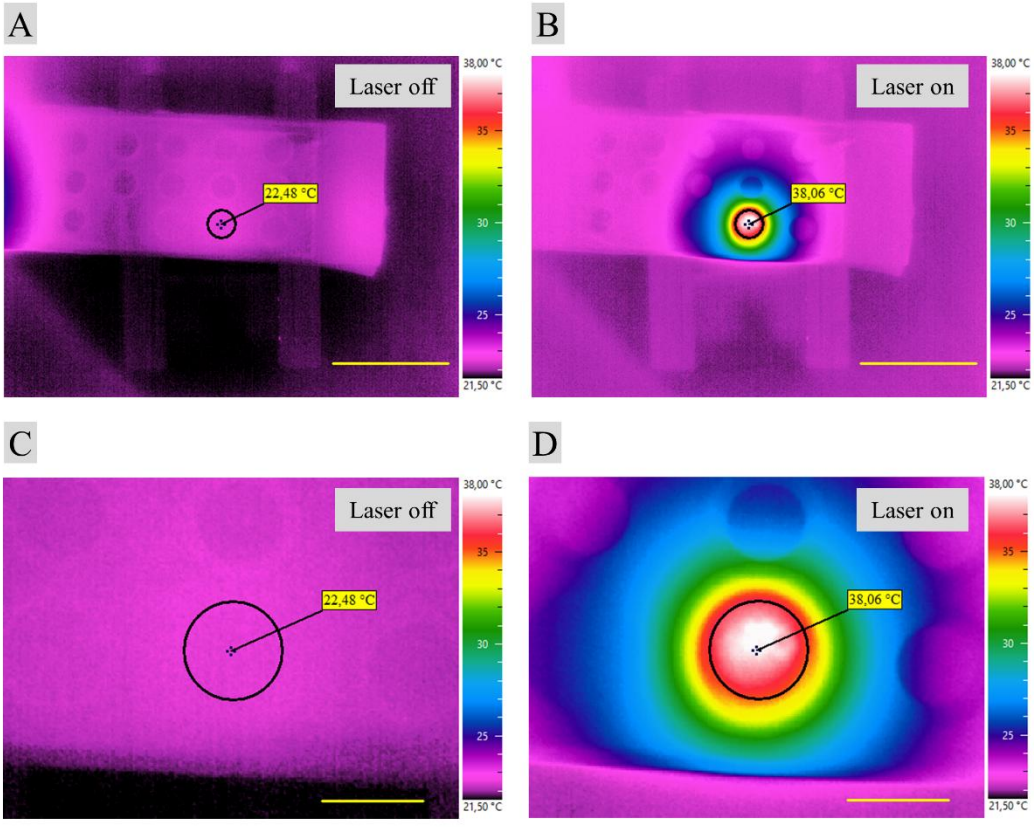

Figure 5- 2: A) + B): Infrared image of the template containing the ELM in one of the wells. Inset circle with diameter of 5 mm indicating the position of ELM in the template. Scale bars right bottom: 20 mm. C) + D): Magnified thermal image. The inset circle has a diameter of 5 mm indicating position of heated ELM in well .Scale bars: 5 mm

Spatial calibration was done using the known well plate dimensions to analyze the temperature distribution within the wells. The software calculated minimum, average, and maximum

temperatures within the defined circle of a 5 mm diameter. The center of the well was selected as a representative point to monitor approximately the maximum generated temperature during photothermal treatment. The infrared image was zoomed in the area of interest, focusing on the relevant well (Figure 5- 2 C and D).

5.2.2.8 Principle of quantification of PCQ production

The PCQ peptide concentration was determined by using the NanoBiT® assay (Promega Corporation, NanoBiT® Luciferase Assay System) based on Nanoluciferase in white, 96-well flat-bottomed microplates and a luminescence microplate reader (Tecan Infinite M Plex). All measurements were performed in duplicates with continuous shaking during 60 s and integration time of 1000 ms for each luminescence measurements. The supernatant (25 µL) was added to a buffer solution (75 µL) containing large BiT (LgBiT), small BiT (SmBiT), and Furimazine. SmBiT, conjugated to the PCQ protein, binds with LgBiT on the secreted QK peptides to form a functional Nanobit, producing luminescence. The hydrogel (10 µL) was added to LB medium (15 µL) and buffer solution (75 µL). The luminescence intensity was measured using a microplate reader.

The strength of luminescence of Nanobit signal directly correlates to the amount of secreted PCQ protein. A calibration curve was measured and used to calculate the concentrations with function of different PCQ concentrations. The calibration curve accounts for the dilution factors introduced during sample preparation, such as the mixing of the buffer solution.

5.2.2.9 Setup for photothermal stimulation by LED

A LED lamp (M810L5, Thorlabs, Germany) was equipped with a lens tube (SM1L10 - SM1, Thorlabs, Germany) and a collimator (COP5-A, Thorlabs, Germany) to ensure a uniform and directed light beam. The power of the LED was regulated using a LED driver (LEDD1B - T-Cube, Thorlabs, Germany), and the output power was measured with a power meter (FieldMaster, Coherent, Germany). The well plate was aligned with the 20 mm LED beam spot using a monochromatic camera (DMK 23U445, The Imaging Source, Germany). The distance between the collimator and the well plate was set to 10 cm, with the LED positioned directly above the sample. The entire setup was placed inside an incubator (New Brunswick Innova®44, Eppendorf, Germany) maintained at a temperature of 35 °C.

5.2.2.10 In vitro NIR stimulation of ELM

Single layer ELMs were prepared as explained in section 5.2.2.5 with bacterial concentrations of OD_{600nm} = 0.4 and AuNR@BSA concentration of OD_{808nm} = 3. The ELM was placed on top of a collagen gel in a 96 well plate (Greiner, Germany). A thermocouple (K-Type, 1.4541 stainless steel) was inserted in the gel to evaluate the temperature increase under LED irradiation. The surface of collagen gel and ELM was covered by a transparent film (Tegaderm™Roll) to prevent drying out. The amount of produced PCQ protein by LED stimulation in the system model was quantified as explained in section 5.2.2.8.

5.2.3 Results and discussion

The following section discusses the preparation and characterization of AuNR@BSA in water, hydrogel, and bacterial hydrogel, focusing on their colloidal stability and photothermal properties. The thermoplasmonic activation of bacteria within the ELM was analyzed, and the resulting production and release of the PCQ protein were quantified. *In vitro* model experiments were conducted to test the use of LED stimulation of the ELM to simulate therapeutic applications.

5.2.3.1 Preparation and characterization of AuNR@BSA in different matrices

I used AuNRs stabilized with bovines serum albumin (BSA) (AuNR@BSA), a globular protein with a hydrodynamic diameter of 7 nm in its native form.[15, 16] These AuNRs are biocompatible and non-cytotoxic due to their surface modification.[1, 2] This is particularly important as the AuNRs are mixed with the bacterial suspension during hydrogel precursor preparation, which means they can come into contact with *E. coli* Nissle 1917 during mixing and within the formed hydrogel network. The AuNRs were commercially available and used as received. Length and diameter are 41 nm and 10 nm, respectively, as specified by the manufacturer. These dimensions result in lower scattering compared to larger nanorods, thereby enhancing plasmonic absorption and increasing local heat generation upon light irradiation (see chapter 3.1 and 3.2).[17] BSA has a molecular weight of about 66 kDa, and both hydrophobic and hydrophilic components, but its hydrophilicity is predominant.[18] The colloidal stability of AuNR@BSA in water is governed by the charged functional groups of BSA, which impart overall electrostatic repulsion above its isoelectric point at pH values above 4.7.[1, 2] BSA is a multivalent ligand and its adsorption on AuNRs surface is due to hydrophobic and van der Waals interactions.[1, 2]

The commercial suspension of AuNR@BSA was centrifuged, mixed with PVA-VS precursor solution containing the crosslinking agent lithium-phenyl-2,4,6-trimethylbenzoylphosphinate and then crosslinked by blue light at 402 nm. During this process, changes in the nanorod environment and mixing procedure can influence AuNR´s colloidal stability, which directly affects their plasmonic heating efficiency. Agglomerates scatter the incident light resulting in less effective plasmonic heating. The L-LSPR of the chosen AuNR@BSA lies within the biological window, around 808 nm, which corresponds to the light sources used in this work to plasmonically heat the AuNR@BSA dispersion. The matching of L-LSPR to the thermoplasmonic excitation is crucial for an efficient response to laser or LED irradiation.

Tebbe et al. reported that AuNR@BSA is colloidal stable in water and in biological medium like phosphate buffer saline and Dulbecco's Modified Eagle's Medium at very high concentrations (20 mg/mL) and at a wide pH range between 2 – 11.[2] The colloidal stability of AuNR@BSA in LB media and in PVA based hydrogels solutions has not been reported yet; it is evaluated in the following. The colloidal stability can be investigated by UV-VIS-NIR spectroscopy of the particles´ L-LSPR, which is sensitive to agglomeration. Agglomeration is usually indicated through high red shift and broadening of the L-LSPR along with a significantly decrease of its intensity.[19]

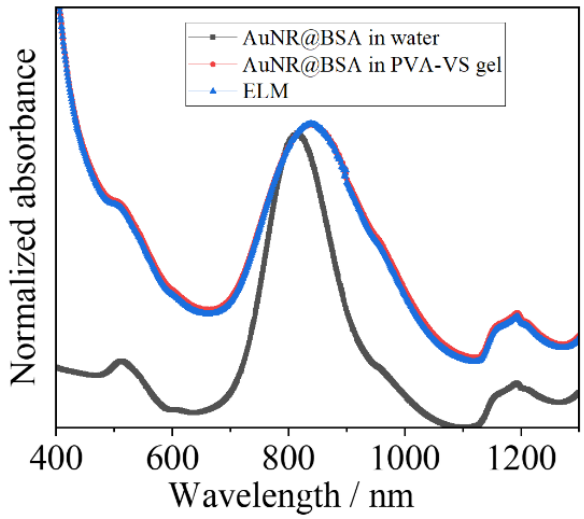

Figure 5- 3: Normalized absorbance of AuNR@BSA in water and in PVA-VS hydrogel and also of ELM obtained by UV-VIS-NIR spectra.

The UV-VIS-NIR spectra in Figure 5- 3 show the plasmonic bands of AuNR@BSA in water and in PVA-VS hydrogel. The T-LSPR was at about 511 nm for both dispersion media. This observation is expected, since the transversal plasmonic band is not sensitive to changes to the surrounding matrix. The L-LSPR of AuNR@BSA in water and in hydrogel was at 820 nm and

at 845 nm, respectively. The absorption bands at about 1200 nm are attributed to vibrational transitions of water associated with its bending and stretching of H-O-H bond.

The L-LSPR band of AuNR@BSA in PVA-VS hydrogel shows a red shift of ca. 25 nm compared to the AuNR@BSA in water. This is likely due to the changes of the local refractive index in the vicinity of the AuNR@BSA and due to slight agglomeration of the particles. The broadening of the fullwidth at half maximum (FWHM) to approximately 80 nm by 40 % suggests partial agglomeration of AuNR@BSA in the hydrogel. The colloidal stability of AuNRs is determined by the intrinsic properties of their surface ligands and the interaction of the ligand with the surrounding matrix. BSA is miscible in PVA solutions because both have hydrophilic character. Agglomeration of AuNR@BSA in the PVA-VS hydrogel may be attributed to multiple factors. Both BSA and PVA exhibit hydrophobic regions within their molecular structures, which can interact and lead to reduced miscibility of the nanorods in the hydrogel matrix. Although BSA is predominantly hydrophilic, certain hydrophobic domains may facilitate interactions with hydrophobic segments of PVA, promoting partial aggregation of the nanoparticles. Additionally, ligand-polymer interactions between the BSA coating on AuNRs and PVA chains through van der Waals forces and hydrogen bonding could further induce clustering, particularly if BSA adsorbs onto the PVA chains, altering the local colloidal stability.

Another factor influencing agglomeration is the mixing process, in which a small volume (10 µL) of highly concentrated AuNR@BSA suspension (OD = 60) is added to a much larger volume (190 µL) of the highly viscous PVA-VS precursor (see chapter 3.5.2.1). The precursor's high viscosity limits nanoparticle mobility, making homogenization challenging. This can result in temporary local concentration gradients, which increase the tendency for agglomeration before crosslinking.

I investigated whether the incorporation of engineered *E. coli* Nissle 1917 affects the plasmonic activity of the nanorods in the hydrogel. The bacterial suspension was centrifuged and mixed in the nanorod containing precursor gel (see section 5.2.2.5). The UV-VIS-NIR spectrum (Figure 5- 3) of ELM shows a T-LSPR and L-LSPR of 511 nm and 845 nm. The FWHM is 92 nm. These results indicate that the incorporation of bacteria in hydrogel does not change the colloidal stability of the nanorod dispersion compared to the AuNR@BSA in gel without bacteria.

The bacteria in the ELM had initial concentrations of $OD_{600\ nm} = 0.5$, correlating to 5×10^8 colony-forming units per milliliter.[20] *E. coli* Nissle 1917 has the shape of a rounded cylinder

with a diameter of about 0.5 µm and a length of about 2 µm.[21] The bacteria were cultured within the gel at 35 °C for 20 h to increase the bacterial concentration and achieve more peptide production. The bacteria grow from single cells to spherical colonies with a diameter of about 10 µm, as reported in literature for Pluronic-based hydrogels.[22] Let us assume similar colony sizes, as the use of PVA hydrogel is expected to provide comparable conditions for bacterial growth.[22] I evaluated whether bacterial growth over the 20 h period influenced the optical properties of the ELM (Figure 5- 4). Furthermore, the time dependent colloidal stability of AuNR@BSA in different matrix like in LB media, in hydrogel and of ELM was investigated (Figure 5- 4). UV-VIS spectra were measured at initial material preparation at t = 0 h and after the duration for bacterial growth incubation at t = 20 h. The change of L-LSPR and the FWHM of AuNR@BSA in the UV-VIS-NIR spectra were compared and the change of optical properties for the therapeutical applications were evaluated. All matrices were prepared to maintain a consistent LB medium to water ratio across all samples. Bacterial growth depends on factors such as nutrient availability, temperature fluctuations, and metabolic variability, which cannot be controlled precisely and lead to deviations in growth behavior. Therefore, the experiments were repeated in triplicate to account for these variations and ensure reliable results. The following spectra (Figure 5- 4) were measured without a baseline to adapt to real measurements.

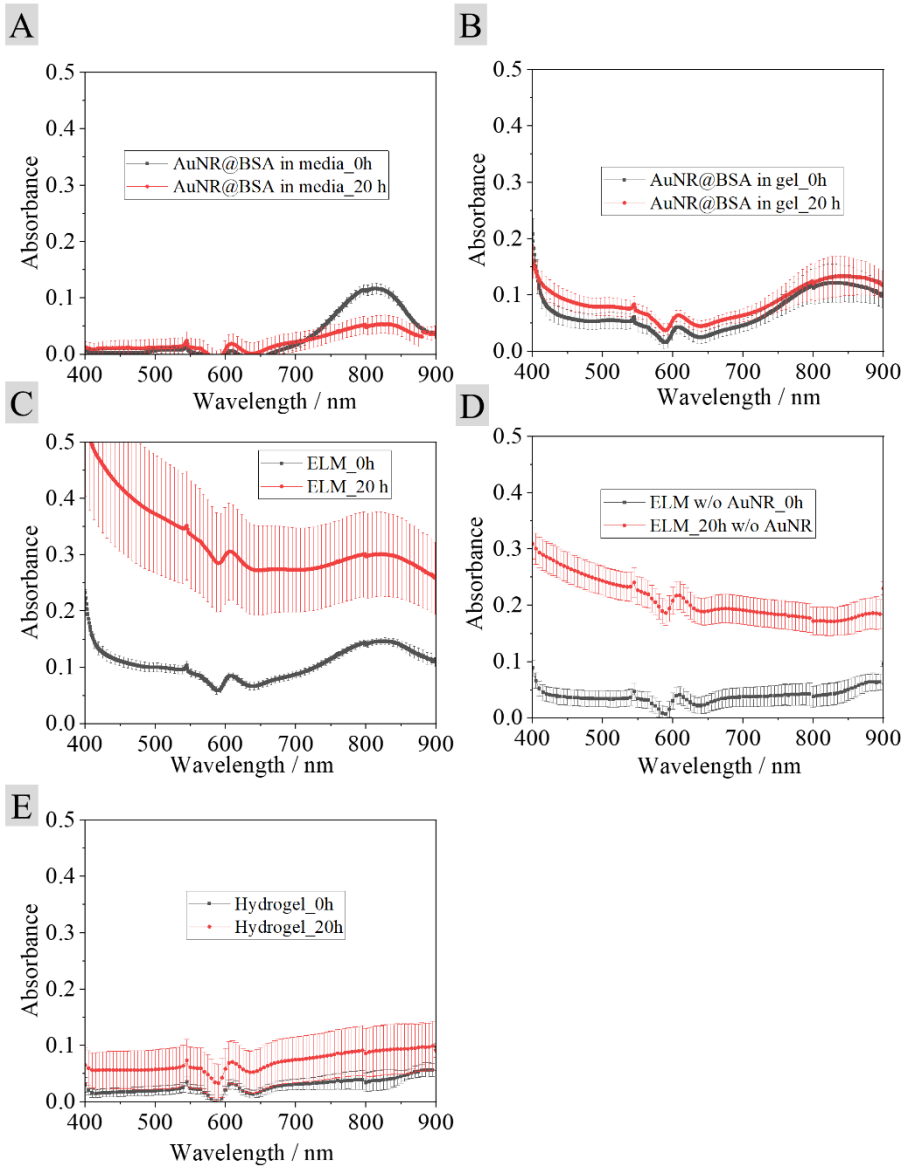

Figure 5- 4: UV-VIS-NIR spectra illustrating the colloidal stability of AuNR@BSA in various matrices, including LB media, PVA-VS hydrogel, ELM with and without AuNR@BSA, and pure PVA-VS hydrogel, at initial measurement directly after gelation (t = 0 h, black) and after 20 hours of incubation (t = 20 h, red). A) Absorbance spectra of AuNR@BSA in LB media at t = 0 h (black) and t = 20 h (red). The decrease and broadening of the LSPR peak at t = 20 h indicate colloidal instability. B) Absorbance spectra of AuNR@BSA in PVA-VS hydrogel at t = 0 h (black) and t = 20 h (red). The minimal change in LSPR peak suggests colloidal stability within the hydrogel matrix. C) Absorbance spectra of AuNR@BSA in the bacterial hydrogel (denoted as ELM) at t = 0 h (black) and t = 20 h (red). The red spectrum shows an offset due to scattering caused by bacterial colony growth.D) Absorbance spectra of ELM without AuNR@BSA at t = 0 h (black) and t = 20 h (red). The absence of an LSPR peak confirms the lack of nanoparticles in the hydrogel. E) Absorbance spectra of pure PVA-VS hydrogel at t = 0 h (black) and t = 20 h (red). No significant changes are observed, indicating the hydrogel's stability over the incubation period.

The change of the colloidal stability of AuNR@BSA in LB medium and in PVA-VA hydrogel without bacteria at t = 0 h and at t = 20 h was evaluated first (Figure 5- 4 A and B). The LB medium is necessary for the survival and growth of bacteria. The L-LSPR absorption at 808 nm for AuNR@BSA in LB medium decreased by 36 % and the FWHM broadened by 40 % from t = 0 h and t = 20 h, whereas no significant optical changes for the nanorods were observed in hydrogel. The results show that the nanorods are not colloidal stable in LB media but remain stable in hydrogel. The LB medium contains NaCl and K_2HPO_4 with a pI of 6–8 which reduces

the Debye screening length to 1-2 nm, reducing stability. Attractive van der Waals forces become dominant and the particles start agglomerating. The incorporation of AuNR@BSA in a hydrogel hinders their diffusion, thus preventing agglomeration. Hydrophilic interaction between PVA chains of the hydrogel and the BSA might further stabilize the nanorods. The UV-VIS spectra of AuNR@BSA in pure hydrogel (Figure 5- 4 B) shows no significant optical changes from $t = 0$ h and $t = 20$ h.

The effect of bacterial growth on the optical properties of the ELM with and without AuNRs (Figure 5- 4 C and D) was evaluated. As the bacteria proliferated within the hydrogel matrix, changes in the L-LSPR absorption were observed. The L-LSPR absorption of the ELM increased by 114 % and the FWHM broadened by 20 % from $t = 0$ h to $t = 20$ h (Figure 5- 4C). The growth of bacteria changed the optical properties of the ELM. The higher offset at $t = 20$ h of the L-LSPR indicates that the formation of spherical colonies after 20 hours of incubation increased optical scattering compared to single bacteria. The spherical colonies have a diameter of about 10 µm, far above the UV-VIS-NIR wavelengths and cause Mie scattering. Comparing the spectra of AuNR@BSA in pure hydrogel (Figure 5- 4 B) with the ELM (Figure 5- 4 C) at $t = 0$ h, it is evident that single bacteria distributed within the hydrogel matrix do not significantly affect the material's optical properties.

The absorption peak at 808 nm of the ELM after 20 h incubation is a sum of absorption and Mie scattering (Figure 5- 4 C) but only absorption by the AuNR contributes to plasmonic heating. To accurately determine the true absorption of AuNR@BSA at 808 nm within the ELM, the contribution of scattering from bacterial growth must be accounted for. This was achieved by measuring the absorbance of ELMs without nanorods as a baseline (Figure 5- 4 D). The baseline spectra revealed that the absorbance at 808 nm increased from 0.04 ± 0.02 at $t = 0$ h to 0.17 ± 0.02 at $t = 20$ h, confirming that bacterial growth significantly contributed to light scattering over time. The absorbance at 808 nm of the ELM containing AuNR@BSA was initially 0.143 ± 0.00 and increased to 0.30 ± 0.08 after 20 hours. However, after subtracting the baseline spectrum of the ELM without nanorods, the corrected absorbance at 808 nm was 0.10 ± 0.02 at $t = 0$ h and 0.13 ± 0.08 at $t = 20$ h, which is comparable to that of AuNR@BSA in pure hydrogel ($t = 0$ h: 0.12 ± 0.03, $t = 20$ h: 0.13 ± 0.03). This indicates that bacterial growth did not significantly alter the plasmonic absorption. Although bacterial colonies increase the overall scattering within the material, they do not significantly hinder the intrinsic absorption of AuNR@BSA. This suggests that while some of the incident light is scattered by bacterial colonies, the effective photon flux available for plasmonic excitation of the AuNRs remains largely constant. However, the subtraction of absorbances used to isolate the contribution of

AuNR@BSA absorption in the ELM has limitations, as it does not differentiate between potential interaction effects between scattered photons and AuNR absorption. In highly scattering media, such secondary interactions could lead to over- or underestimation of the corrected absorbance. Therefore, while subtracting the baseline of the ELM without nanorods accounts for scattering by bacteria, it cannot fully decouple all scattering-related effects. To improve the accuracy of the absorbance measurement in such complex systems, future studies could employ techniques such as integrating sphere spectroscopy or angular-dependent scattering measurements to better separate absorption and scattering contributions.

The error margins in the ELM with AuNR@BSA at t = 20 h were substantially larger (166% increase compared to t = 0 h), whereas the baseline-corrected AuNR@BSA absorbance in hydrogel remained relatively stable. This suggests that the presence of nanorods influenced bacterial growth, leading to less reproducible colony formation within the hydrogel matrix. Additionally, a spectrum of pure PVA-VS hydrogel was recorded to assess its contribution to light absorption and scattering at 808 nm (Figure 5- 4 E). The absorbance at 808 nm showed a minor increase after 20 h, but the overall absorbance remained negligible, confirming that the hydrogel itself does not contribute significantly to the scattering of the ELM under NIR irradiation.

In summary AuNR@BSA in media and in hydrogel retained plasmonic absorption at 808 nm at initial preparation. Incubation overnight did not change the plasmonic properties of the AuNR themselves, except for particles in LB media, where a significant reduction of L-LSPR was observed due to the colloidal instability of the particles in this medium. To analyze further the effects of the single containments to the materials´ properties, the photothermal activity and efficiency was evaluated. The photothermal activity of the nanorods is the crucial point in this work which is an indicator for the activation efficiency for engineered living materials.

5.2.3.2 Photothermal activation of AuNR@BSA in bacterial hydrogel

I prepared PVA-VS hydrogel based ELMs containing AuNR@BSA and *E. coli* in microwells. 10 µL of the liquid hydrogel precursors were pipetted into the wells and crosslinked using blue light to create cylindrical gel plugs in the wells. They were overlayed with LB media to prevent drying of the gel. The wells were covered by Parafilm to prevent water evaporation of LB media. As Parafilm (a mixture of polyethylene and paraffin) is partially transmissive to infrared light, the IR camera can effectively capture temperature readouts through it.

The photothermal excitation in function of time was quantified in these wells after incubation time of $t = 20$ h. The optical density of the rods and the laser power density was varied to find values that were suitable to sufficiently heat the ELM for peptide production.

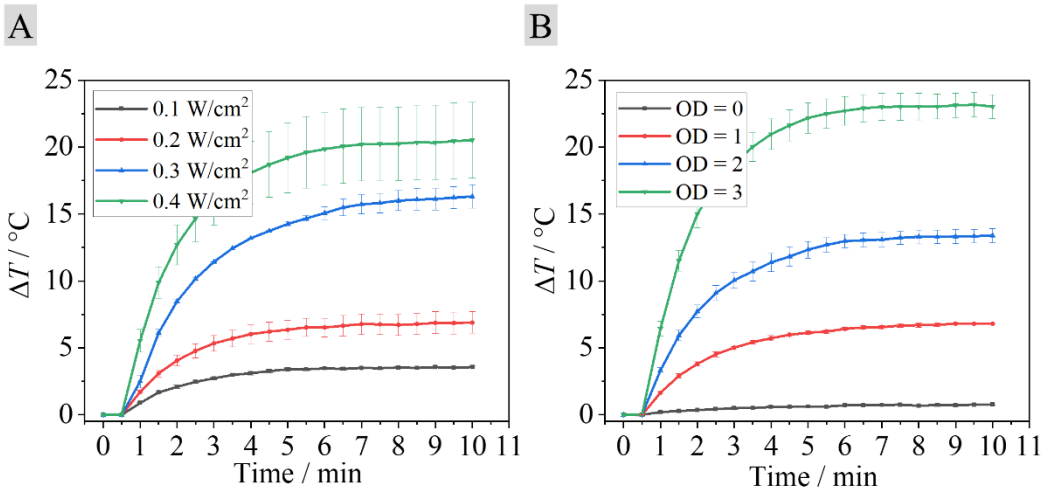

Figure 5- 5: Photothermal heating of ELM. A) Heating of laser illuminated ELMs at $OD_{808nm} = 3$ and laser power densities between 0.1 W/cm² – 0.4 W/cm². (N = 3, mean ± standard deviation) B) Heating of laser illuminated ELMs at 0.5 W/cm² for $OD_{808\ nm}$ between 0 – 3 (N = 3, mean ± standard deviation).

Irradiation with a CW laser at a wavelength of 808 nm resulted in plasmonic heating of the gels (Figure 5- 5 A and B). The temperature gel was detected with the infrared camera at a defined point (see 5.2.2.7). Steady state temperature was reached after an irradiation time of about 7 minutes. Irradiation at a power density of 0.5 W/cm² of the AuNR@BSA composite PVA-VS hydrogel with nanorod concentrations of OD = 0, 1, 2 and 3 resulted in steady state temperature differences to initial temperatures of $\Delta T = 0.8$ °C ± 0.1 °C, 6.8 °C ± 0.2 °C, 13.4 °C ± 0.5 °C, and 23.0 ± 0.9 after 10 minutes, respectively (Figure 5- 4 B). Laser power densities of 0.1 W/cm², 0.2 W/cm², 0.3 W/cm² and 0.4 W/cm² at $OD_{808\ nm} = 3$ resulted in $\Delta T = 3{,}6$ °C ± 0.1 °C, $\Delta T = 6.9$ °C ± 0.8 °C, $\Delta T = 16.3$ °C ± 0.9 °C, and $\Delta T = 20.5$ °C ± 2.8 °C, respectively (Figure 5- 5 A) (n = 1, N = 3).

5.2.3.3 Photothermal conversion efficiencies of AuNR@BSA in different matrices

Knowledge of the photothermal conversion efficiencies (PCE) of AuNR@BSA in different matrices enables targeted material design for applications that require precise thermal control, such as thermoresponsive ELMs and biomedical therapies. I established PCEs in water, LB media and hydrogel (Figure 5- 6 A and B and Table 5- 1) and evaluated whether the bacteria and their growth affects the PCE of the overall ELM.

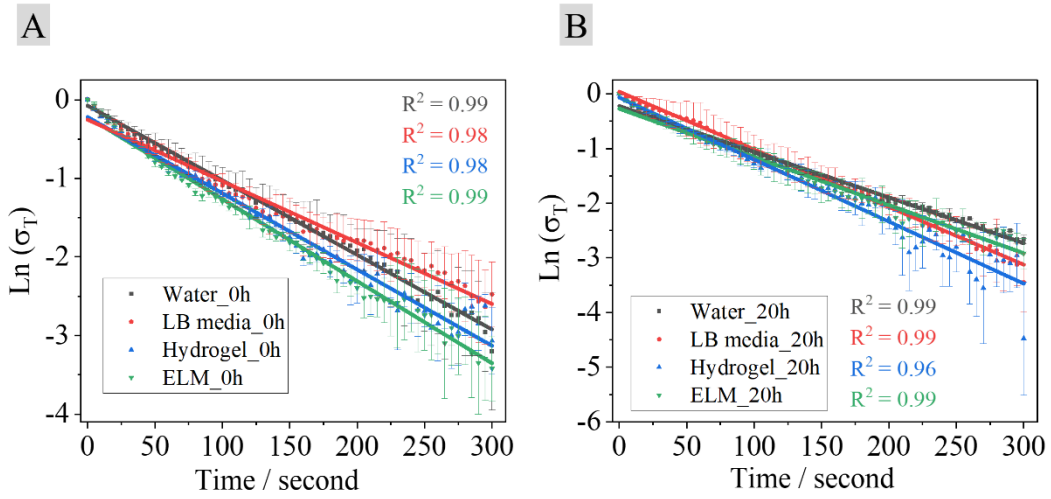

Figure 5- 6: Thermal relaxation behavior of AuNR@BSA in different matrices by analyzing the dimensionless driving force temperature, $\ln(\theta_T)$, after laser irradiation was turned off. A) Linear fit of $\ln(\theta_T)$ as a function of time after laser was turned off (N = 3, n = 2) for AuNR@BSA in water, in LB media, in hydrogel and of ELM at t = 0 h. B) Linear fit of $\ln(\theta_T)$ as a function of time after laser was turned off (N = 3, N = 2) for AuNR@BSA in water, in LB media, in hydrogel and of ELM at t = 20 h. R^2 is the coefficient of determination of the fit.

The photothermal conversion properties were determined using Roper´s model as described in section 3.3.3.[23] Roper et al. introduced a dimensionless driving force temperature θ_T (see equation (3- 23)) and a system time constant B from a heat transfer model to calculate the PCE (see section 3.3.3).[23] The characteristic B depends on the experimental setup, while the PCE is an intrinsic property of the nanoparticles and depends on their shape and size.[24] The effective PCE of the ELM differs from the theoretical PCE of isolated AuNRs because its components, such as the surrounding matrix and bacterial content, influence heat dissipation and light absorption. The system time constant B accounts for heat losses within the experimental setup. A lower value of B indicates a slower rate of heat dissipation, meaning the system retains heat longer. Conversely, a higher B value signifies a faster heat loss to the environment.

The absorption and scattering of light by growing bacterial colonies (as observed in section 5.2.3.1) in the material can diminishe the apparent efficiency of photothermal conversion of the AuNR. The colloidal stability of AuNR in LB medium was discussed in section 5.2.3.1. and their agglomeration affects the PCE (see section 3.4.7.2). These effects can be quantified by comparing the system time constants B and the apparent PCEs of AuNR@BSA in different matrices. I measured B and PCE in water, LB media, pure hydrogel, and bacteria-containing hydrogel (ELM) immediately after mixing at time t = 0 (Figure 5- 6 A) and after incubation at t = 20 h (Figure 5- 6 B). An incubation time of t = 20 h was chosen because it is sufficient to allow the formation of bacterial colonies from single bacteria in the hydrogel. Experimental cooling curves were obtained by fitting the cooling curves of the nanocomposite (see section

3.3.3.1) and analyzed with equations (3- 19) and (3- 23) (Figure 5- 6). The laser power of 134 mW and the concentration of AuNR@BSA ($OD_{808\,nm} = 3$) were kept constant for all measurements.

The determined system time constants *B* varied from 0.0102 – 0.0134 s^{-1} and the PCE varied from 41 % – 63 %. All PCEs were in range of those previously reported (Table 3- 1 in section 3.3.3).

The system time constants *B* for AuNR@BSA in water were 0.0104 ± 0.0010 and 0.0102 ± 0.0002 for $t = 0$ h and $t = 20$ h, respectively. The PCEs were 63 ± 6 % and 57 ± 2 % for $t = 0$ h and $t = 20$ h, respectively. Neither *B* nor PCE changed significantly after incubation, indicating colloidal stability of AuNR@BSA in water.

AuNR@BSA in LB medium exhibited values of $B = 0.0107 \pm 0.0011$ at $t = 0$ h and $B = 0.0121 \pm 0.0010$ at $t = 20$ h and a PCE of 58 ± 8 % at $t = 0$ h and 41 ± 3 % at $t = 20$ h. The observed increase in the system time constant *B* and the decrease in PCE of AuNR@BSA in LB medium after 20 h of incubation suggest nanoparticle agglomeration. This aggregation enhances heat dissipation due to increased local thermal conductivity,[25, 26] leading to higher *B* values. Additionally, agglomeration diminishes L-LSPR absorption (see Figure 5- 4 A), reduces the effective surface area, and increases light scattering, collectively resulting in a lower PCE. These findings align with previous studies indicating that nanoparticle aggregation can enhance thermal conductivity[25, 26] and reduce PCE.[27]

The values *B* and PCE of AuNR@BSA in water and in LB media at $t = 0$ h did not significantly differ from each other, indicating colloidal stability in both environments initially. However, at $t = 20$ h, a significant increase in *B* and decrease in PCE in LB medium suggest nanoparticle agglomeration, whereas no such changes are observed in water. This confirms that agglomeration occurs within the 20 h incubation period in LB medium.

AuNR@BSA particles in hydrogel remain colloidal stable after 20 h of incubation time, as *B* and PCE do not change significantly, which also correlate with the UV-VIS-NIR spectra shown in Figure 5- 4. Comparing AuNR@BSA in hydrogel to those in water, it is observable that value *B* is higher in the gel at both $t = 0$ h and $t = 20$ h. This is due to slight agglomeration of the particles when mixed in hydrogel (see Figure 5- 4 in section 5.2.3.1) resulting in lower PCE compared to the colloidal stable particles in water.

AuNR@BSA in bacterial hydrogel is noted as ELM. Its *B* were measured as 0.0132 ± 0.0008 at $t = 0$ h and as 0.0134 ± 0.0020 at $t = 20$ h, while the PCEs were 59 ± 3 % at $t = 0$ h and 54 ± 14 % at $t = 20$ h. The constant values suggest unchanged nano- and microscale structures.

Compared to other matrices, the ELM has the highest B at t = 0 h and t = 20 h, suggesting that the bacterial content increases the heat dissipation rate in the gel.

Table 5- 1: Photothermal conversion efficiencies of AuNR@BSA ($OD_{808nm,10mm}$ = 3) in water, in LB media, in hydrogel and in ELM directly after mixing (t = 0h) and after an incubation time of t = 20 h (n=1, N=3).

AuNR@BSA	B (0 h) / s^{-1}	B (20 h) / / s^{-1}	PCE / % (0 h)	PCE / % (20 h)
Water	0.0104 ± 0.0010	0.0102 ± 0.0002	63 ± 6	57 ± 2
LB media	0.0107 ± 0.0011	0.0121 ± 0.0010	58 ± 8	41 ± 3
Hydrogel	0.0116 ± 0.0005	0.0121 ± 0.0013	53 ± 3	50 ± 5
ELM	0.0132 ± 0.0008	0.0134 ± 0.0020	59 ± 3	54 ± 14

A high PCE is critical to avoid exceeding the irradiation limit of 0.33 W/cm^2 for 808 nm lasers on human tissue for therapeutical applications (see chapter 3.4.1). The results show high PCE for the nanorods in all matrices. I demonstrated that the bacterial content does not significantly affect the PCE; however, the reproducibility of PCE was limited due to the non-reproducible bacterial growth in the hydrogels, as evidenced by the high standard deviations. To the best of my knowledge, this work is the first to discuss the effect of bacterial growth on the PCE of AuNRs in hydrogel matrices.

5.2.3.4 Photothermal adjustment of AuNR@BSA in PVA-VS hydrogel

Above results show that the PCEs of AuNR@BSA are potentially sufficient for therapeutic ELMs. The thermoplasmonically generated steady state temperature can be controlled by laser power density and by the concentration of AuNR@BSA. Note that the results above were obtained by monitoring temperatures with an infrared camera, a non-invasive method, that does not disrupt ELM structure and avoids bacterial leakage. It is limited to the surface temperatures of the LB media overlaying the ELM. The thermoplasmonically generated heat dissipates to the surroundings and the recorded temperature is due to heat transfer from ELM to LB media and air. Thus, the temperature inside the ELM is above that reported in the previous sections. The control of temperature inside the ELM is crucial due to the bacterial activity range of 38 °C – 44 °C, beyond which bacteria stop expressing substances or even die.

Thermocouples (TC) and infrared camera imaging can be combined to infer internal ELM temperatures. In the following, I recorded a temperature T_{TC} using a TC inside AuNR@BSA hydrogel and correlated it with the surface temperature T_{IRcam} recorded by the infrared camera simultaneously during laser light irradiation of AuNR@BSA in hydrogel (Figure 5- 7 A). The

TC is injected in the center of the ELM directly below P1 in a depth of 3 mm (Figure 5- 7 B). To account for uncertainties in TC positioning, a line with a length of 2 mm was defined in the infrared image (Figure 5- 7 B), and the average temperature along this line was used for $T_{IR\ cam}$.

The concentration of AuNR@BSA was chosen as OD = 3 and the laser power density as 0.3 W/cm^2, as these parameters generate the required temperature range for bacterial activation (Figure 5- 5). Figure 5- 7 C shows the temperature values measured by infrared camera and TC. The temperature difference $\Delta T = T_{TC} - T_{IRcam}$ is shown as a function of time in Figure 5- 7 D. The irradiation duration was 30 min, sufficient to induce peptide production (see section 5.2.3.5). The cooling curve was recorded after switching off the laser.

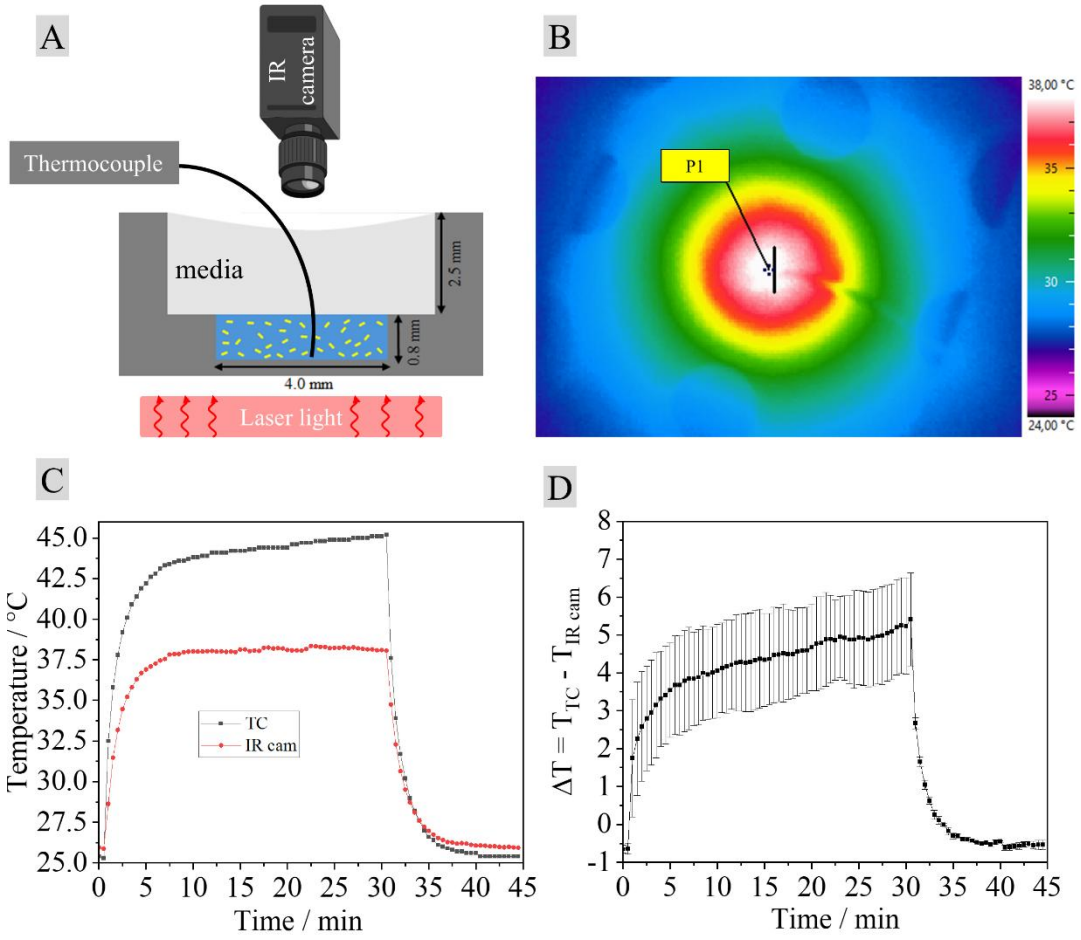

Figure 5- 7: Comparison of surface and bulk temperatures. A) Cross section of one well of the microslide depicting the TC and infrared camera position. B) Infrared thermography image of the well from top position during steady state during laser light illumination. The inset line at the center (length: 2 mm) indicates the temperature gradient that I used to calculate the lateral uncertainty for TC positioning. C) Average temperature T_{IRcam} acquired from the line by infrared camera from B) and temperature T_{TC} measured in the ELM by TC during plasmonic heating at 0.3 W/cm^2. D) The temperature difference $\Delta T = T_{TC} - T_{IRcam}$ in function of time (N = 3, mean ± SD).

The results indicate ΔT of 4.6 ± 1.2 °C during steady state (7 mins – 30 mins). This adjustment enables temperature control in the ELM using the non-invasive infrared camera. In the next section, infrared camera measurements are adjusted by adding 4.6 ± 1.2 °C to estimate the

internal ELM temperature at steady state. This correction is assumed to be valid across the entire ELM due to its small size (4 mm diameter), which minimizes significant thermal gradients.

It is worth mentioning, that the measurement´s accuracy is limited by the positioning of the TC and the reproducibility of the hydrogel layer geometry. I estimate errors for 2 mm of spatial uncertainty (see Figure 5- 7 B) for the positioning of the TC. This corresponds to uncertainties of the measured temperature on the order of 0.64 °C ± 0.25 °C (N = 3, mean ± SD) for laser power density of 0.3 W/cm^2. Note also that there exist both lateral and axial temperature gradients in the gel such that bacteria experience different temperatures depending on their exact position.

5.2.3.5 Photothermal stimulation of PCQ producing ELM

The ELM was prepared in µ-slide Angiogenesis templates as described in section 5.2.2.5. The ELM system contained genetically engineered *E. coli* Nissle 1917, designed to express the QK peptide-bearing PCQ protein, a VEGF peptidomimetic that promotes angiogenesis, between temperatures of 38 °C – 44 °C.[13] AuNR@BSA and bacteria were mixed with the PVA-VS hydrogel precursor and injected in the cylindrical wells and then crosslinked with blue light. LB media as supernatant was added on top of the ELM in a 4:1 volume ratio to the ELM. The LB media prevents dehydration and provides additional nutrients for bacterial growth. After incubation at 35 °C for 20 h, the LB media was replaced to replenish nutrients, assuming significant consumption by bacterial growth overnight. During heat exposure, the bacteria express the PCQ protein and secret it to the surrounding matrix. First, the temperature evaluation via thermoplasmonic stimulation is discussed, followed by the analysis of the amount of PCQ produced.

Thermoplasmonic stimulation was conducted at a AuNR@BSA concentration of $OD_{808\ nm} = 3$ and a laser power density of 0.2 – 0.3 W/cm^2 based on the results of section 5.2.3.2. These parameters ensured that the LB media's maximal surface temperature reached approximately 38°C, corresponding to an internal ELM temperature in the range of 42°C (see section 5.2.3.4), which is optimal for activating the engineered *E. coli* Nissle 1917 strain. Temperature distributions on the ELM surface were monitored via infrared camera imaging (Figure 5- 8 A + B). The steady state surface temperatures measured via infrared imaging were adjusted by adding ΔT = 4.6 ± 1.2 °C, as determined in section 5.2.3.4, to estimate the internal ELM temperatures. Temperature distribution analysis is essential to ensure that the bacterial activation range (38 – 44°C) is achieved throughout the gel during thermoplasmonic

stimulation, which is critical for effective and reliable PCQ protein production. Thermal gradients within the hydrogel arise due to heat transfer mechanisms such as conduction and convection. As described in chapter 5.1, the center of the hydrogel exhibits higher temperatures than the edges.

A circular region of interest with a diameter of 5 mm was selected to assess the ELM system´s surface temperature in the well (see materials and methods 5.2.2.7). This region enabled the extraction of minimum, average, and maximum surface temperatures, providing a quantitative representation of the temperature distribution. The minimum and maximum temperatures correspond to the edge and center of the ELM, respectively, reflecting the temperature gradient across its surface.

The heating profile of the whole well defined by the above-mentioned circle of several samples (n=3, N=3) is monitored in Figure 5- 8 D. At t = 0.5 min, upon switching on the laser, the ELM system exhibited an exponential temperature increase from ambient conditions. Steady state temperature was reached after approximately 7 minutes of irradiation, and the laser was maintained for an additional 23 minutes, providing a total heating duration of 30 minutes (Figure 5- 8 C). The minimum temperature, average temperature and the maximum temperature during steady state (t = 7 min – 30 min) through the ELM´s surface measured by infrared camera is 35.1 °C ± 0.2 °C, 36.8 °C ± 0.5 °C and 38.5 °C ± 0.5 °C respectively, reflecting the temperature distribution across the ELM system.

To account for the difference between infrared camera measurements and inside ELM temperatures, the adjusted ΔT = 4.6 °C ± 1.2 °C obtained from section 5.2.3.4 is applied, resulting in adjusted ELM temperatures of 39.7 °C ± 1.2 °C, 41.4 °C ± 1.3 °C and 43.1 °C ± 1.3 °C for the minimum, average, and maximum values, respectively. These temperatures fall within the activation range for the bacteria across the entire ELM, ensuring effective stimulation.

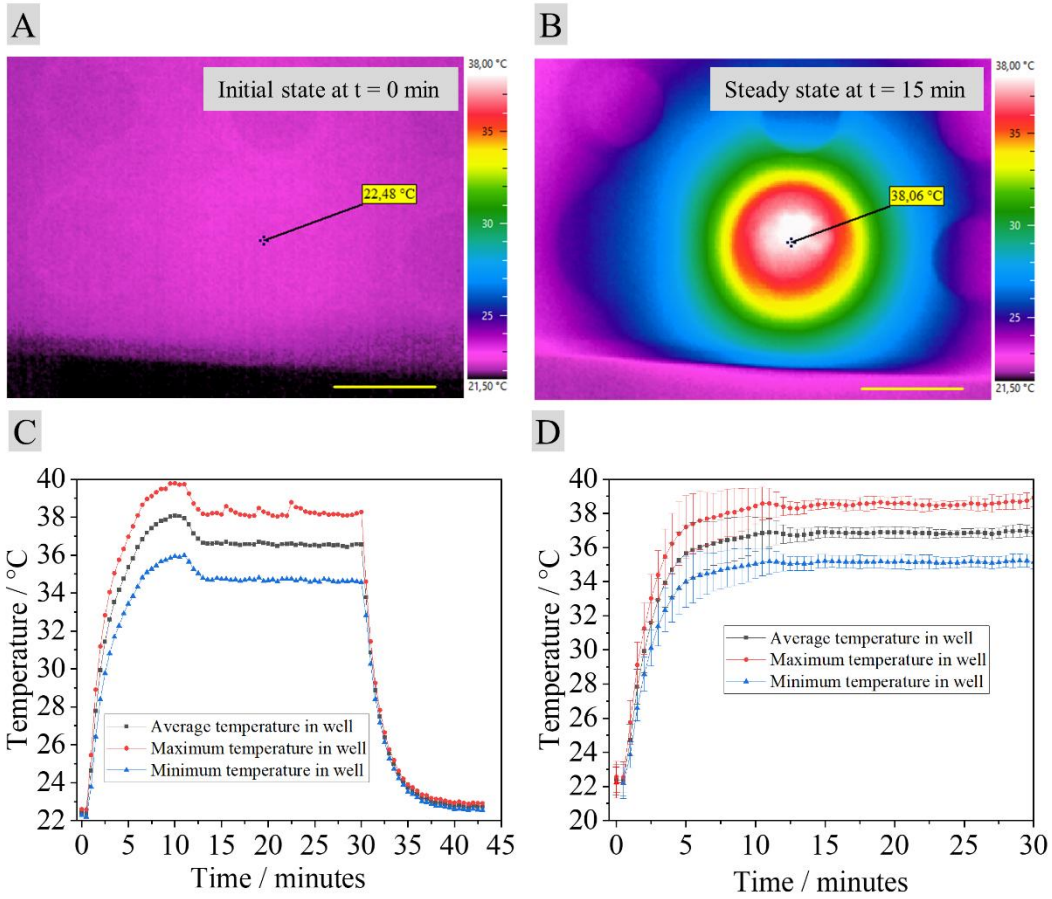

Figure 5- 8: Thermal images and temperature profiles of thermoplasmonic ELMs. A): Thermal image of ELM in well at initial state at $t = 0$ min when laser is turned off. B): Thermal image of ELM in well at steady state at $t = 15$ min during laser irradiation. C) Heating and cooling profile of an ELM in well at laser power density of 0.2 W – 0.3 W/cm2. The average, maximum and minimum temperature in the well is plotted. D) Heating profile of ELMs at power density between 0.2 W – 0.3 W/cm^2. The average, maximum and minimum temperature is plotted (n = 3, N = 3). A + B: Inset scale bar on right bottom is 5 mm.

After thermoplasmonic treatment, the ELM was incubated for 30 min at 35 °C to allow diffusion of PCQ protein into the supernatant. This resulted in a total treatment duration of 60 min. To quantify the amount secreted PCQ proteins, the supernatant was immersed to a buffer solution containing large BiT (LgBiT), small BiT (SmBiT), and Furimazine. SmBiT, conjugated to the PCQ protein, binds with LgBiT on the secreted QK peptides to form a functional Nanobit, producing luminescence (see section 5.2.2.4 and 5.2.2.8). The luminescence intensity was measured using a microplate reader, with a calibration curve translating luminescence to PCQ concentrations.

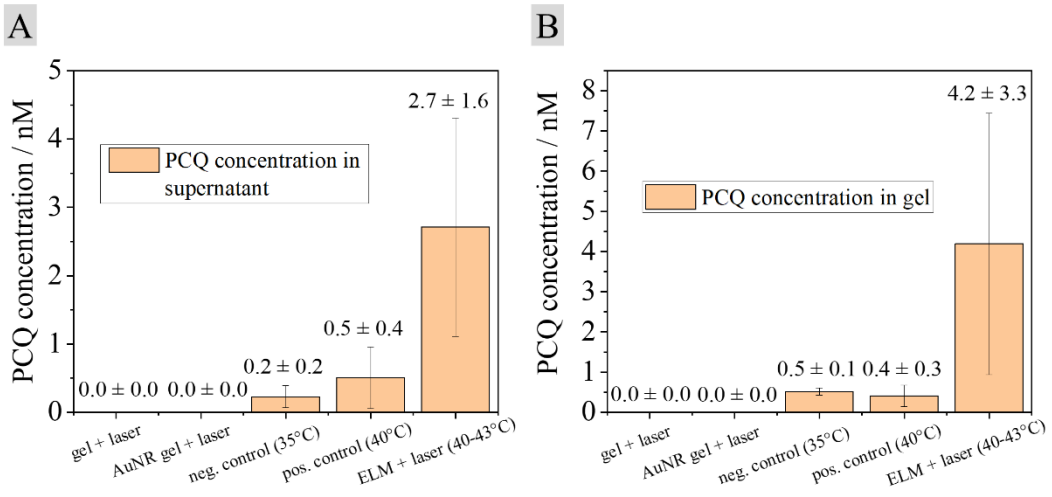

Figure 5- 9: Concentrations of PCQ protein in supernatants and in hydrogels (N = 3, n = 3, mean ± SD). A) Concentration of the diffused PCQ protein in the supernatant. B) Concentration of the non-diffused PCQ remaining in the ELM gel.

The concentration of secreted PCQ was analyzed both in the supernatant (Figure 5- 9 A) and in the hydrogel (Figure 5- 9 B). Luminescence measurements indicated a PCQ concentration of 2.7 nM ± 1.6 nM in the supernatant and 4.2 nM ± 3.3 nM in the hydrogel. The total expressed PCQ concentration was 6.9 nM ± 3.7 nM with high variability attributed to batch-dependant differences in bacterial growth and temperature distribution in the well (see Figure 5- 8 D). For comparison, oven-based positive controls at 40 °C produced significantly lower total PCQ concentrations of 0.9 nM ± 0.5 nM, despite falling within the bacterial activation range. This difference was likely due to faster heating achieved by plasmonic stimulation. Negative controls at 35 °C yielded negligible PCQ expression (0.7 nM ± 0.5 nM), consistent with the thermal activation threshold of the bacteria. Control experiments with pure hydrogel and AuNR@BSA composite hydrogel showed no PCQ expression under laser irradiation, confirming that PCQ production was exclusively bacterial. The experiments show that thermoplasmonic stimulation of ELM for therapeutical protein release was successful.

The observed PCQ concentrations (6.9 nM ± 3.7 nM) approach the therapeutic range (5 – 20 nM) reported by Dhakane et al. for wound healing.[12] Notably, the concentration measured in the supernatant, 2.7 nM ± 1.6 nM, holds particular therapeutic relevance as it represents the fraction of proteins that diffused out of the gel matrix and is accessible for promoting angiogenesis in wound tissues. While the supernatant concentration is crucial for immediate therapeutic efficacy, the total PCQ production in the ELM is higher. The remaining proteins within the ELM likely persist due to the limited diffusion period of 30 min. With a longer diffusion period, more proteins would gradually migrate out of the hydrogel, increasing their availability for therapeutic application without requiring additional stimulation. Puertas Batolomé et al. determined that the pores in the PVA-VS hydrogel network are larger than

160 kDa, allowing proteins smaller than 25 kDa to diffuse through the hydrogel within 4 h, as observed via electrophoresis.[28] Given that PCQ has a molecular weight of 9 kDa, it is significantly smaller than the hydrogel pores and is expected to diffuse freely. Based on these findings, the remaining PCQ in the ELM should gradually diffuse out within 4. Over extended diffusion times, the fraction of PCQ retained in the ELM would decrease as diffusion progresses, potentially leading to near complete release over time. However, diffusion is driven by the concentration gradient between the hydrogel and the surrounding medium, meaning that as PCQ accumulates in the supernatant, the driving force for further release diminishes, potentially leading to incomplete release, unless the surrounding medium is refreshed.

The total treatment duration in this study (60 min) is substantially shorter than the 9-day protocol employed by Dhakane et al.[12] The thermoplasmonic approach demonstrated here allows for a significantly faster induction of peptide secretion compared to previous methods.[12] This accelerated activation is attributed to deeper heat penetration and uniform bacterial activation across the ELM compared to optogenetic systems, which rely on limited light penetration. The TlpA-based heat-responsive circuit in *E. coli* Nissle 1917 also provides superior productivity due to precise temperature control.

These findings validate the potential of thermoplasmonic ELMs for efficient therapeutic protein production, positioning them as promising candidates for localized wound healing applications

5.2.3.6 *In vitro* LED stimulation of ELMs on skin mimicking collagen gels

To simulate *in vitro* conditions for therapeutic PCQ production, ELMs were placed on a collagen gel that mimics skin tissue, providing a relevant model for wound-related experiments. In contrast to section 5.2.3.5, where activation was achieved using laser light, an 808 nm LED was used in this section. LEDs offer advantages over lasers, including broader light distribution, reduced risk of localized overheating on skin, and improved compatibility with biomedical applications due to their lower cost and ease of integration into wearable or portable systems.[29]. The collagen gel used in this setup was composed of rat tail collagen, phosphate-buffered saline (PBS), and agarose. This composition mimics key properties of skin tissue, providing a biologically relevant environment. Collagen is the primary structural protein in the extracellular matrix of the skin, while PBS maintains physiological pH and ionic strength, and agarose contributes to the mechanical stability of the gel, resembling the viscoelastic nature of soft tissues.

The ELMs were prepared in templates with an initial bacterial concentration of $OD_{600nm} = 0.4$ and incubated at 35 °C to allow bacterial growth as described in section 5.2.2.5. After incubation, ELMs were transferred onto collagen gels (100 µL) within wells of 7 mm diameter. The samples were then incubated in an oven to reach thermal equilibrium at 35 °C representing physiological host body temperature. The samples were then irradiated by LED at 0.02 W/cm^2 for 60 min in the oven (see section 5.2.2.9).

To assess the role of thermoplasmonic heating in bacterial activation, three samples were compared. One sample was ELM with AuNR@BSA irradiated by LED to evaluate thermoplasmonic heating induced PCQ protein expression. The second sample was an ELM without AuNR@BSA irradiated by LED to determine whether LED irradiation alone was sufficient to induce bacterial activation. The third sample served as a positive control, where ELM was incubated in an oven at 40 °C for 60 minutes to verify that bacterial activation occurs at this temperature in the absence of optical stimulation. The amount of produced PCQ protein in the *in vitro* samples (collagen gel + ELM) was quantified as described in section 5.2.2.8.

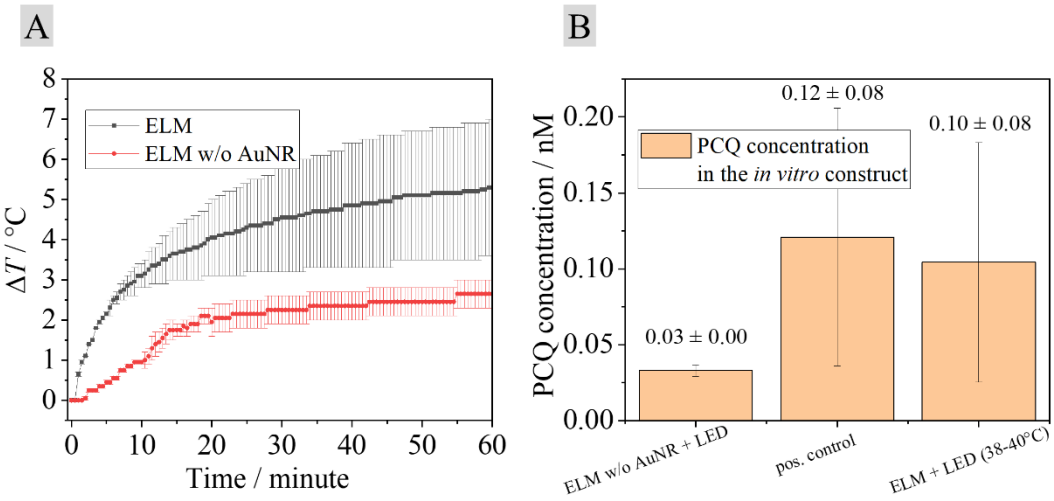

Figure 5- 10: Expressed PCQ protein by LED illuminated ELMs (N=2, mean ± SD) A) Temperature increase Δ*T* of ELM (black) and ELM without AuNRs (red) under LED irradiation at 0.02 W/cm^2 for 60 min with concentration of AuNR@BSA OD = 3 – 4. B) Concentration of PCQ expressed from ELM under LED irradiation.

ELM with AuNR@BSA at $OD_{808\ nm}$ = 3 reached bacterial activation temperatures between 38 °C and 42 °C under LED irradiation, starting from an initial temperature of 35 °C. (Figure 5- 10 A). In contrast, ELMs without AuNR@BSA did not exceed 38 °C, indicating that thermoplasmonic heating is essential for achieving the required activation temperature.

PCQ protein expression was observed in both ELMs with and without AuNR@BSA when irradiated by LED, with concentrations of 0.03 nM ± 0.00 nM and 0.10 nM ± 0.08 nM, respectively ((Figure 5- 10 B). The lower PCQ concentration in ELM without AuNR@BSA

confirms that the lack of thermoplasmonic particles resulted in insufficient heating for optimal gene expression. The positive control yielded a PCQ concentration of 0.12 nM ± 0.08 nM, demonstrating that PCQ production derives from thermal activation.

Compared to laser irradiation (section 5.2.3.5), LED-based heating required longer exposure times (60 min vs. 30 min) but still resulted in lower peptide concentrations. This discrepancy is attributed to differences in experimental conditions. In plasmonic laser treatment, peptides were dissolved in 50 µL of matrix, while the LED treatment involved a total volume of 110 µL, diluting the peptide concentration. In the LED treatment, no supernatant was present in the collagen gel constructs, restricting protein diffusion and potentially limiting overall expression.

Despite these limitations, this experiment successfully demonstrates thermoplasmonic bacterial activation using LED light, highlighting its potential for photothermal based therapeutic applications.

5.2.4 Conclusion and Outlook

I prepared therapeutic ELMs based on PVA-VS hydrogel containing bacteria and AuNR@BSA, that enabled thermoplasmonic stimulation. The living component was and engineered *E. coli* Nissle 1917 with a thermocircuit inducing gene expression during heat exposure at temperatures between 38 °C – 44 °C. This system was designed to explore thermoplasmonic activation as a strategy for on demand therapeutic VEGF mimicking peptide production, particularly for potential applications in wound healing.

I first analyzed the colloidal stability of AuNR@BSA in water, PVA-VS hydrogel and ELM by UV-VIS-NIR spectroscopy. The particles were stable in water as reported in literature, but slight agglomeration occurs when mixed in PVA-VS hydrogel. Adding *E. coli* did not further change colloidal stability in the gel.

I also compared the colloidal state after $t = 20$ h of incubation time at 35 °C in water, LB medium, PVA-VS hydrogel and ELM to the initial results at $t = 0$ h. AuNR@BSA in water, in hydrogel and ELM did not change. AuNR@BSA in LB media agglomerated. These results indicate the important role of the hydrogel in trapping the AuNRs and maintaining their arrangement over time, which is relevant for therapeutic applications in wound healing.

The PCEs of AuNR@BSA in water, in LB media, in hydrogel and in ELM were measured and found to be 63 % ± 6 %, 58 % ± 8 %, 53 % ± 3 % and 59 % ± 3 % directly after preparing the mixtures ($t = 0$ h). The PCEs after $t = 20$ h in water, LB medium, hydrogel and in ELM were 57 % ± 2 %, 41 % ± 3 %, 50 % ± 5 % and 54 % ± 14 %, respectively. The larger error bar for

the PCE of ELM is related to variations in bacterial growth that cause optical scattering. The PCEs were sufficient for the thermoplasmonic activation of ELMs.

I used the results to introduce an efficient strategy for thermoplasmonic stimulation of therapeutic ELMs, potentially advancing wound healing applications by enabling rapid, controlled, and localized protein production. The gene expression of the genetically programmed *E. coli* in the ELM induced by thermoplasmonic treatment with NIR laser light for 30 min resulted in an expressed total PCQ concentration of 6.9 nM ± 3.7 nM. This study presents the first reported protocol for NIR-light activation of ELMs to achieve controlled therapeutic protein release.

In vitro measurements were performed by placing the ELMs onto cylindrical collagen gels (diameter 7 mm, 100 µL) designed to mimic skin tissue. The ELMs (diameter 4 mm, 10 µL) were positioned on top of collagen gels to simulate a localized treatment scenario. Collagen gels serve as a skin tissue model due to their structural and biochemical similarity to the extracellular matrix, providing a relevant environment for assessing LED-induced thermoplasmonic activation under physiologically relevant conditions. LED irradiation with therapeutical dosage of 0.02 W/cm^2 on the ELM for 60 minutes resulted in expression of PCQ concentrations of 0.10 nM ± 0.08 nM.

This study shows the potential application of ELMs for therapeutical release with tissue-harmless LED powers for the on-demand supplication of proteins for chronic wound treatments. LED light sources provide reduced equipment costs and enhance safety profiles compared to traditional laser systems. This strategy aligns with the goal of developing more accessible and user-friendly therapeutic interventions.

Bibliography

[1] P. Khullar, V. Singh, A. Mahal, P.N. Dave, S. Thakur, G. Kaur, J. Singh, S. Singh Kamboj, M. Singh Bakshi, Bovine Serum Albumin Bioconjugated Gold Nanoparticles: Synthesis, Hemolysis, and Cytotoxicity toward Cancer Cell Lines, The Journal of Physical Chemistry C 116 (2012) 8834-8843.
[2] M. Tebbe, C. Kuttner, M. Männel, A. Fery, M. Chanana, Colloidally Stable and Surfactant-Free Protein-Coated Gold Nanorods in Biological Media, ACS Applied Materials & Interfaces 7 (2015) 5984-5991.
[3] A. Rodrigo-Navarro, S. Sankaran, M.J. Dalby, A. del Campo, M. Salmeron-Sanchez, Engineered living biomaterials, Nature Reviews Materials 6 (2021) 1175-1190.
[4] F. Riedel, M.P. Bartolomé, L.L.T. Enrico, C. Fink-Straube, C.N. Duong, F. Gherlone, Y. Huang, V. Valiante, A. Del Campo, S. Sankaran, Engineered living materials for the conversion of a low-cost food-grade precursor to a high-value flavonoid, Frontiers in Bioengineering and Biotechnology 11 (2023).

[5] J.E. Kim, J. Lee, M. Jang, M.H. Kwak, J. Go, E.K. Kho, S.H. Song, J.E. Sung, J. Lee, D.Y. Hwang, Accelerated healing of cutaneous wounds using phytochemically stabilized gold nanoparticle deposited hydrocolloid membranes, Biomaterials science 3 (2015) 509-519.
[6] S.-h. Hsu, Y.-B. Chang, C.-L. Tsai, K.-Y. Fu, S.-H. Wang, H.-J. Tseng, Characterization and biocompatibility of chitosan nanocomposites, Colloids and surfaces B: Biointerfaces 85 (2011) 198-206.
[7] X. Huang, L. Xu, X. Yu, Y. Li, Z. Huang, R. Xu, W. Zeng, Z. Zhang, W. Li, F. Deng, Near-infrared light-responsive multifunctional hydrogel releasing peptide-functionalized gold nanorods sequentially for diabetic wound healing, Journal of Colloid and Interface Science 639 (2023) 369-384.
[8] X. Xu, Y. Ding, R. Hadianamrei, S. Lv, R. You, F. Pan, P. Zhang, N. Wang, X. Zhao, Antimicrobial peptide functionalized gold nanorods combining near-infrared photothermal therapy for effective wound healing, Colloids and Surfaces B: Biointerfaces 220 (2022) 112887.
[9] J.-G. Leu, S.-A. Chen, H.-M. Chen, W.-M. Wu, C.-F. Hung, Y.-D. Yao, C.-S. Tu, Y.-J. Liang, The effects of gold nanoparticles in wound healing with antioxidant epigallocatechin gallate and α-lipoic acid, Nanomedicine: Nanotechnology, Biology and Medicine 8 (2012) 767-775.
[10] S.-A. Chen, H.-M. Chen, Y.-D. Yao, C.-F. Hung, C.-S. Tu, Y.-J. Liang, Topical treatment with anti-oxidants and Au nanoparticles promote healing of diabetic wound through receptor for advance glycation end-products, European Journal of Pharmaceutical Sciences 47 (2012) 875-883.
[11] S.S. Nanda, T. Wang, M.I. Hossain, H.Y. Yoon, S.T. Selvan, K. Kim, D.K. Yi, Gold-nanorod-based scaffolds for wound-healing applications, ACS Applied Nano Materials 5 (2022) 8640-8648.
[12] P. Dhakane, V.S. Tadimarri, S. Sankaran, Light-Regulated Pro-Angiogenic Engineered Living Materials, Advanced Functional Materials 33 (2023) 2212695.
[13] D.I. Piraner, M.H. Abedi, B.A. Moser, A. Lee-Gosselin, M.G. Shapiro, Tunable thermal bioswitches for in vivo control of microbial therapeutics, Nature chemical biology 13 (2017) 75-80.
[14] G. Santulli, M. Ciccarelli, G. Palumbo, A. Campanile, G. Galasso, B. Ziaco, G.G. Altobelli, V. Cimini, F. Piscione, L.D. D'Andrea, C. Pedone, B. Trimarco, G. Iaccarino, In vivo properties of the proangiogenic peptide QK, J Transl Med 7 (2009) 41.
[15] D.C. Carter, J.X. Ho, Structure of Serum Albumin, in: C.B. Anfinsen, J.T. Edsall, F.M. Richards, D.S. Eisenberg (Eds.), Advances in Protein Chemistry, Academic Press1994, pp. 153-203.
[16] G. Shouren, K. Kojio, A. Takahara, T. Kajiyama, Bovine serum albumin adsorption onto immobilized organotrichlorosilane surface: Influence of the phase separation on protein adsorption patterns, Journal of Biomaterials Science, Polymer Edition 9 (1998) 131-150.
[17] P.K. Jain, K.S. Lee, I.H. El-Sayed, M.A. El-Sayed, Calculated Absorption and Scattering Properties of Gold Nanoparticles of Different Size, Shape, and Composition: Applications in Biological Imaging and Biomedicine, The Journal of Physical Chemistry B 110 (2006) 7238-7248.
[18] B.A. Russell, K. Kubiak-Ossowska, P.A. Mulheran, D.J.S. Birch, Y. Chen, Locating the nucleation sites for protein encapsulated gold nanoclusters: a molecular dynamics and fluorescence study, Physical Chemistry Chemical Physics 17 (2015) 21935-21941.
[19] T.R. Ray, B. Lettiere, J. de Rutte, S. Pennathur, Quantitative Characterization of the Colloidal Stability of Metallic Nanoparticles Using UV–vis Absorbance Spectroscopy, Langmuir 31 (2015) 3577-3586.
[20] A.L. Koch, Turbidity measurements of bacterial cultures in some available commercial instruments, Analytical Biochemistry 38 (1970) 252-259.

[21] U. Sonnenborn, Escherichia coli strain Nissle 1917—from bench to bedside and back: history of a special Escherichia coli strain with probiotic properties, FEMS Microbiology Letters 363 (2016).
[22] S. Bhusari, S. Sankaran, A. del Campo, Regulating Bacterial Behavior within Hydrogels of Tunable Viscoelasticity, Advanced Science 9 (2022) 2106026.
[23] D.K. Roper, W. Ahn, M. Hoepfner, Microscale Heat Transfer Transduced by Surface Plasmon Resonant Gold Nanoparticles, The Journal of Physical Chemistry C 111 (2007) 3636-3641.
[24] M. Almada, B.H. Leal-Martínez, N. Hassan, M.J. Kogan, M.G. Burboa, A. Topete, M.A. Valdez, J. Juárez, Photothermal conversion efficiency and cytotoxic effect of gold nanorods stabilized with chitosan, alginate and poly(vinyl alcohol), Materials Science and Engineering: C 77 (2017) 583-593.
[25] B. Ali, I. Siddique, H. Ahmad, S. Askar, Influence of nanoparticles aggregation and Lorentz force on the dynamics of water-titanium dioxide nanoparticles on a rotating surface using finite element simulation, Sci Rep 13 (2023) 4702.
[26] B. Ullah, U. Afzal, A. Waheed, U. Khan, W. Emam, H.A.E.-W. Khalifa, Significance of nanoparticle aggregation for thermal transport over magnetized sensor surface, Nanotechnology Reviews 13 (2024).
[27] Y. Wang, Z. Gao, Z. Han, Y. Liu, H. Yang, T. Akkin, C.J. Hogan, J.C. Bischof, Aggregation affects optical properties and photothermal heating of gold nanospheres, Scientific Reports 11 (2021) 898.
[28] M. Puertas-Bartolomé, I. Gutiérrez-Urrutia, L.L. Teruel-Enrico, C.N. Duong, K. Desai, S. Trujillo, C. Wittmann, A. del Campo, Self-Lubricating, Living Contact Lenses, Advanced Materials 36 (2024) 2313848.
[29] V. Heiskanen, M.R. Hamblin, Photobiomodulation: lasers vs. light emitting diodes?, Photochemical & Photobiological Sciences 17 (2018) 1003-1017.

5.3 Thermoplasmonic stimulation in hydrogel waveguides

This chapter reports on optical waveguides with gold nanorods (AuNRs) embedded in segments of varying lengths and numbers. The waveguides are hydrogel optical fibers based on PluDA. The colloidal stability of AuNRs with CTAB and biocompatible BSA[1] ligands is evaluated, as colloidal stability influences their photothermal heating properties (see section 3.4.7.2). Then, the photothermal response of the nanocomposite segments in the waveguides is analyzed.

5.3.1 Introduction

Although there are reports of gold nanoparticles integrated into waveguides, these mainly focus on biosensors that exploit LSPR for applications in drug delivery and neural stimulation (see section 3.4.6). In these studies, nanoparticles are typically coated on the fiber tip, surface, or contained in the surrounding matrix.[2] For instance, Choi et al. embedded gold nanoparticles in hydrogel-based optical fibers and achieved photothermal heating using green laser light.[2]

We used a novel design and embedded nanoparticles in discrete segments within the waveguides, which offers distinct advantages. Segmenting the nanoparticles ensures localized photothermal heating, enabling precise control over temperature gradients within the waveguide. This segmentation is particularly beneficial for deep tissue applications, where light penetration is limited beyond the NIR transparency depth. The waveguides are capable of propagating light to targeted areas, overcoming this limitation. (see section 3.4.1 and 3.4.6). By concentrating AuNRs in defined regions, the design minimizes unnecessary heating of non-targeted areas, thereby enhancing efficiency and safety. To the best of my knowledge, no reports specifically evaluate the photothermal stimulation of segmented hydrogel-based waveguides.

The AuNR@CTAB were embedded in single segments featuring lengths of 2 mm and 5 mm. Double-segmented waveguides consisted of two 2 mm segments separated by a 2 mm gap. Photothermal analysis of these configurations provides insights into temperature distribution and light propagation within the waveguide. This analysis is crucial for understanding the heat generation and dissipation mechanisms, which inform the design of efficient and safe waveguides for biomedical applications. While studies exist on plasmonic heating and thermoplasmonic stimulation using optical fibers integrated with gold nanoparticles (see section 3.4.6), most focus on their application rather than detailed temperature profiling.

Core-shell structured waveguides were also fabricated with the same core diameter as the single-segment waveguides and a shell thickness of 0.5 mm. The shell layer functions as a

cladding layer (see section 3.4.6), preventing light loss due to the higher refractive index of surrounding tissues compared to the hydrogel core. This feature enhances the potential applicability of these waveguides in host body environments, making them viable for minimally invasive therapeutic and diagnostic applications.

5.3.2 Materials and methods

This section outlines the materials and experimental methods employed in this work. The characterization of AuNRs and the setup for photothermal stimulation of waveguides is described.

5.3.2.1 Materials

Gold nanorods (length: 41 nm, diameter: 10 nm) capped with CTAB and BSA (AuNR@CTAB and AuNR@BSA) in water were purchased from Nanopartz Inc. (Canada). The PluDA hydrogel based waveguide fiber (50 mm × 1.5 mm) with AuNR@CTAB composite segments was provided by Dynamic Biomaterials (INM – Leibniz Institute for New Materials, Germany). The segments were 2 mm and 5 mm in length for the single segmented waveguides. The double-segmented waveguides consisted of two segments with each 2 mm lengths and a gap of 2 mm. The core-shell waveguides had core dimensions of 50 mm × 1.5 mm with a shell coating of a thickness of 0.5 mm.

5.3.2.2 UV-VIS spectroscopy of gold nanorods in waveguide precursor mixture

Suspensions of AuNR@BSA and AuNR@CTAB (10% v/v) were mixed into the PluDA waveguide precursor (23% w/v). The precursor gel was transferred to a standard cuvette and maintained at 4 °C in its liquid phase. Gelation was induced at room temperature by waiting for 5 minutes. The absorbance spectrum was recorded between 400 nm and 1000 nm using a UV-VIS-NIR spectrophotometer (Cary 5000, Agilent, Germany). For comparison, the absorbance spectra of AuNR@BSA and AuNR@CTAB suspensions in water were also measured to evaluate the impact of the matrix change on their colloidal stability.

5.3.2.3 Setup for photothermal stimulation of waveguides

A continuous wave (CW) laser (CNI, China) with an excitation wavelength of 808 nm and adjustable power ranging from 100 mW to 6 W was used. The laser light was coupled into a 400 µm core diameter SMA 905 multimode fiber (CNI, China) and directed through a collimator (FOC-01, CNI, China). The laser beam spot diameter was set to 5 mm. The

collimated light passed through a laser line mirror (Thorlabs, Germany) and was split by a beam splitter (BP 208, Thorlabs, Germany) into two paths: one directed toward a black-and-white camera for visualizing the light and aiding in its alignment, and the other towards an objective (RMS4X - 4X, Thorlabs, Germany) focusing the light into a beam spot of 1 mm. The laser light was aligned and focused onto the tip of the waveguide using a stage (GNL20, Thorlabs, Germany). Temperature changes upon irradiation were monitored using an infrared camera (VarioCam@HD 980 S, Infratech, Germany), positioned 10 cm above the waveguide. The sample was placed in a cuvette (704.003-OG, Hellma, Germany) filled with water to prevent drying during photothermal treatment.

5.3.3 Results and discussion

AuNRs with CTAB and BSA ligands were characterized in hydrogel matrices using UV-VIS spectroscopy to evaluate their colloidal stability. AuNR@CTAB is a widely available and commonly used type due to its production via the seed-mediated growth method. This method facilitates the controlled growth of AuNRs with varying aspect ratios, where CTAB molecules adsorb onto the gold surface through van der Waals interactions, forming a bilayer.[3] This bilayer provides a positive surface charge, stabilizing the particles through electrostatic repulsion and preventing aggregation in water. AuNR@BSA, on the other hand, is selected for its biocompatibility, which is discussed in chapter 5.2. Photothermal analyses were conducted on core waveguides with varying nanocomposite segment configurations and lengths. Additionally, core-shell waveguides were introduced, and their photothermal performance was systematically investigated.

5.3.3.1 Characterization of gold nanorods in waveguide precusor

PluDA waveguides were shaped into fiber geometries using a 3-D printing process. The AuNR composite PluDA precursor was crosslinked via UV-light during printing to integrate plasmonic particles for thermoplasmonic responsiveness. In this section, the AuNRs within the precursor are analyzed.

I evaluated CTAB-coated (AuNR@CTAB) and BSA-coated (AuNR@BSA), both obtained from Nanopartz (Canada), as candidates for photothermal sensitizers. Their colloidal stability in the waveguide precursor was evaluated using UV-VIS-NIR spectroscopy (Figure 5- 11).

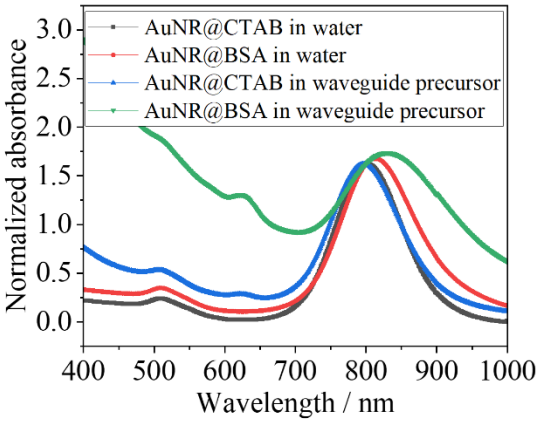

Figure 5- 11: Normalized absorbance of AuNR@CTAB and AuNR@BSA in water and in waveguide precursor obtained by UV-VIS-NIR-spectroscopy.

The L-LSPR of AuNR@CTAB changed little when transferred from water (805 nm) to the waveguide precursor (801 nm), with the full width at half maximum (FWHM) increasing slightly from 112 nm to 116 nm. This indicates that AuNR@CTAB remains colloidally stable within the waveguide. In contrast, AuNR@BSA exhibited a significant redshift of the L-LSPR from 820 nm to 833 nm, accompanied by a 30% broadening of the FWHM. These observations suggest that AuNR@BSA experiences slight agglomeration within the waveguide matrix due to changes in the local refractive index and weaker stabilization mechanisms. Due to these findings, AuNR@CTAB was selected for the photothermal activation of the waveguides.

While CTAB is known for its cytotoxic properties, this issue can be addressed by incorporating a protective core-shell structure, as discussed in section 5.3.3.3. In this design, the core contains AuNR@CTAB, while the shell encapsulates bacteria, effectively isolating the cytotoxic CTAB from the living components, making it a promising geometry for Engineered Living Materials (ELMs). Although bacteria are not included in the shell in this chapter, the presented core-shell structures demonstrate a potential configuration for ELMs by showcasing their feasibility and stability without the biological components.

5.3.3.2 Photothermal response of segmented waveguides

The 3-D-printed waveguides were cylindrical fibers with a length of 50 mm and a diameter of 1.5 mm. Each waveguide included one or two segments with incorporated AuNR@CTAB at a concentration corresponding to an optical density (OD_{10mm}) of 2. Laser light with a wavelength of 808 nm and a power density of 2 W/cm² was focused and coupled into the tip of the waveguide using an objective lens, enabling light propagation through the waveguide. The embedded nanorods in the segments absorbed the coupled light and converted it into heat thermoplasmonically.

This section investigates the temperature distribution generated by thermoplasmonic heating for different segment configurations. Segments with lengths of 2 mm and 5 mm, as well as a double-segment configuration (two 2 mm segments separated by a 2 mm gap), were analyzed. The waveguides were placed in a cubic cuvette filled with water, ensuring the waveguides remained hydrated and minimizing thermal gradients caused by ambient air. Temperature distributions were measured using an infrared camera positioned above the setup. The temperatures obtained here are surface temperatures of the water which is 0.5 mm above the waveguides surface.

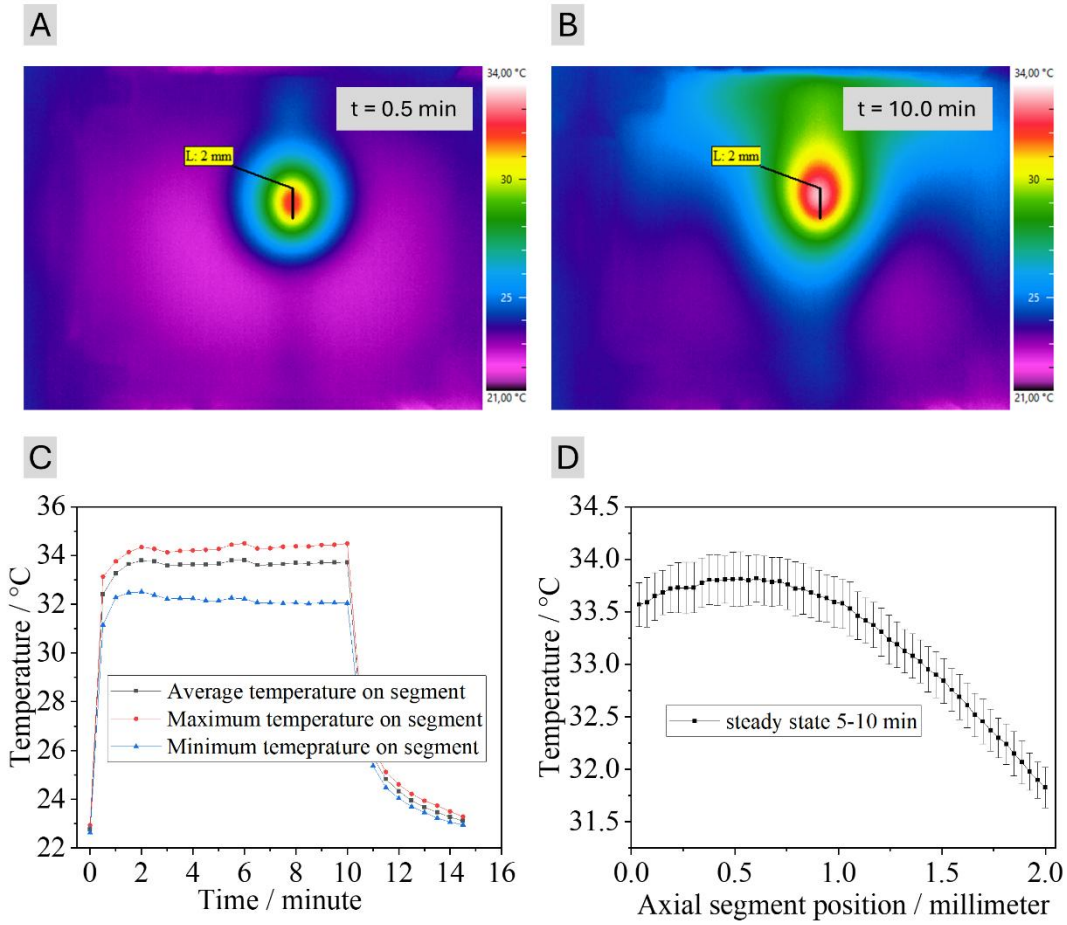

Figure 5- 12: Thermal analysis of a waveguide with one nanocomposite segment with length of 2 mm. A)+B) Thermal image of waveguide during plasmonic heating at irradiation time t = 0.5 min at initial state (A) and at t = 10 min at steady state (B). The black line represents the estimated nanocomposite segment. C) Temperature profile of the minimum, average and maximum temperature in the segment. At t = 0 min the laser is switched on resulting in the plasmonic heating of the segment in the waveguide. The laser is switched off at t = 10 min resulting in temperature decay to ambient temperatures. D) The steady state temperature between 5 min – 10 min is plotted in the function of the axial segment position of 2 mm.

A waveguide with a segment of 2 mm length (and width of 1 pixel ≙ 0.04 mm) containing AuNR@CTAB was irradiated with coupled laser light resulting in localized thermoplasmonic heating within the segment. An infrared camera was used to measure the temperature distribution on water´s surface. The coupled light enters the waveguide tip and propagates through it, with the entrance position appearing as lateral position 0 mm in the thermal analysis

(Figure 5- 12). Although the segment position was not directly visible due to water covering the waveguide, the infrared camera recorded the water's surface temperature, which resulted from heat diffusing from the segment in the waveguide. To accurately define the segment length, the initial heating phase ($t = 0.5$ min, Figure 5- 12 A) was used, as the generated temperature rise was still low, minimizing thermal gradients and allowing the temperature distribution to appear symmetric. At this point, the segment position was identified and marked using a predefined 2 mm scale bar (Figure 5- 12 A). This predefined segment line in (Figure 5- 12 A) provides minimum, average, and maximum temperatures, allowing assessment of heat distribution and axial temperature gradients. Understanding these temperature gradients ensure that waveguide-based thermoplasmonic systems can be optimized for heating and controlling thermoplasmonic stimulation in potential biomedical applications.

The waveguide was irradiated for 10 minutes, resulting in a steady-state temperature distribution after 2 min. A minimum, average and maximum segment temperature of about 32 °C, 33 °C and 34 °C was reached, respectively (Figure 5- 12 C). Thus, the temperature range within the segment at steady state was 2 °C. When the laser was switched off, the segment returned to its initial temperature after cooling for approximately 4 minutes.

As the light propagates through the waveguide, it interacts with the nanorods in the segment. The AuNR@CTAB absorbs the light and converts it into heat, causing localized heating within the segment. Due to their strong plasmonic absorption properties, the nanorods absorb a significant portion of the light passing through the segment. As a result, the front part of the segment, which is closer to the light entry point, exhibits a higher temperature than the back as shown in Figure 5- 12 D. The axial temperature variation across the segment was 2 °C (Figure 5- 12 D)

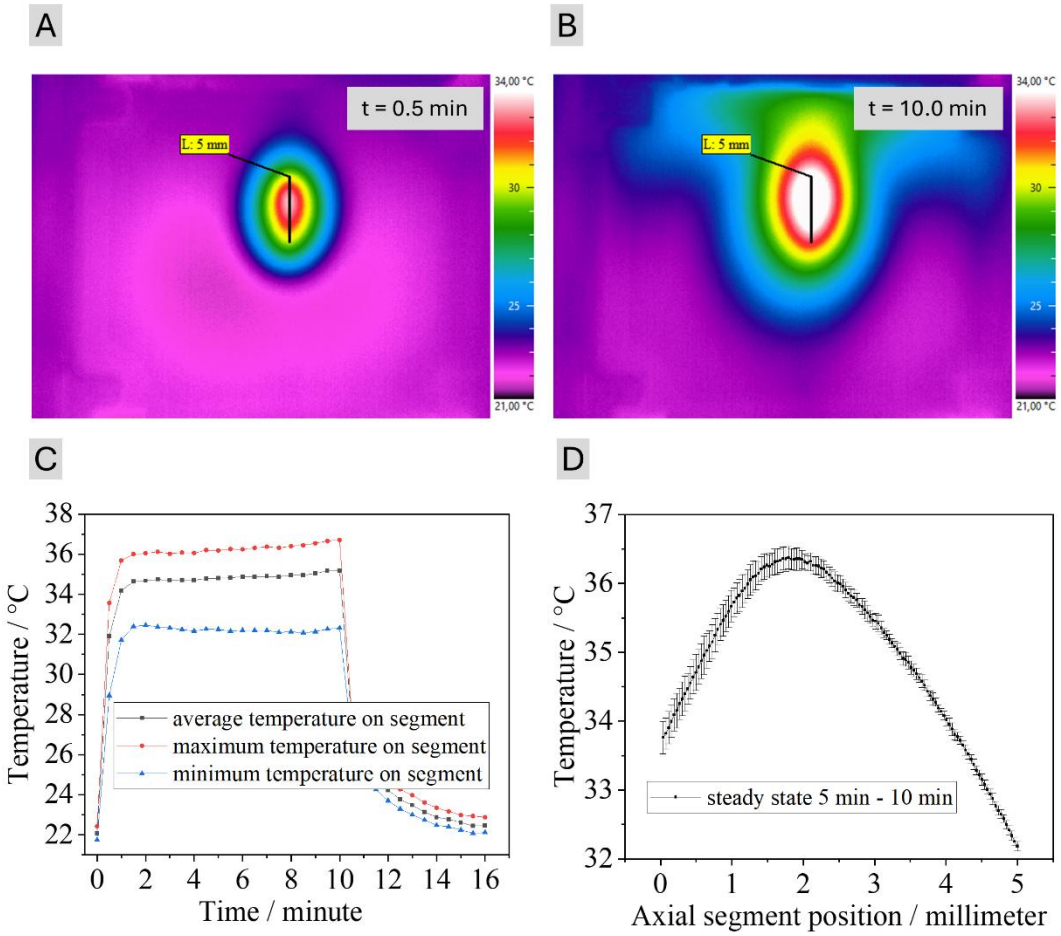

Figure 5- 13: Thermal analysis of a waveguide with one nanocomposite segment with length of 5 mm. A)+B) Thermal image of waveguide during plasmonic heating at irradiation time t = 0.5 min at initial state (A) and at t = 10 min at steady state. The black line represents the estimated nanocomposite segment. C) Temperature profile of the minimum, average and maximum temperature in the segment. At t = 0 min, the laser is switched on, resulting in the plasmonic heating of the segment in the waveguide. The laser is switched off at t = 10 min resulting in temperature decay to ambient temperatures. D) The steady state temperature between 5 min – 10 min is plotted in the function of the axial segment position of 5 mm.

Next, the temperature variation was evaluated for a waveguide with a 5 mm segment containing AuNR@CTAB. The axial position of the segment, depicted in Figure 5- 13 A, was predefined to cover the symmetric temperature distribution observed at t = 0.5 min, using the same procedure as for the 2 mm segment. Note that, for longer segments, such as the 5 mm configuration, the temperature distribution already exhibited slight asymmetry at t = 0.5 min. This effect arises because most of the coupled light is absorbed at the segment's entry point, reducing the amount of light available for absorption further along the segment. As a result, the temperature distribution becomes less uniform along longer segments, with more pronounced differences in heating between the entry and exit regions. As segment length increases, this spatial variation in absorption becomes more pronounced, introducing greater uncertainty in precisely defining the segment position.

The steady state infrared image at t = 10 min is shown in Figure 5- 13 B. Thermoplasmonic heating increased the segment´s surface temperature from an initial 22 °C to steady-state

minimum, average and maximum temperatures of 32 °C, 34 °C and 36 °C, respectively after about 2 min of irradiation. These values mark the temperature range in the segment. The initial temperature was restored approximately 4 minutes after the laser was switched off at t = 10 min (Figure 5- 13 C).

The steady state axial temperature profile, plotted in Figure 5- 13 D, provides insights into light propagation and nanorod absorption along the 5 mm segment. The light first interacts with nanorods at the segment's entry point (axial position 0 mm), where the temperature is among the highest. As the light propagates through the segment, its intensity decreases due to absorption by the nanorods, leading to a gradual temperature reduction towards the segment's end.

The extended segment length increased the light-particle interaction, resulting in a broader heat distribution. The axial temperature gradient across the 5 mm segment was 4.5 °C, approximately 2.2 times higher than in the 2 mm segment. Furthermore, the longer segment contributed to an expanded heated area beyond the waveguide, as a larger portion of the segment was heated, facilitating the spread of heat over a greater area.

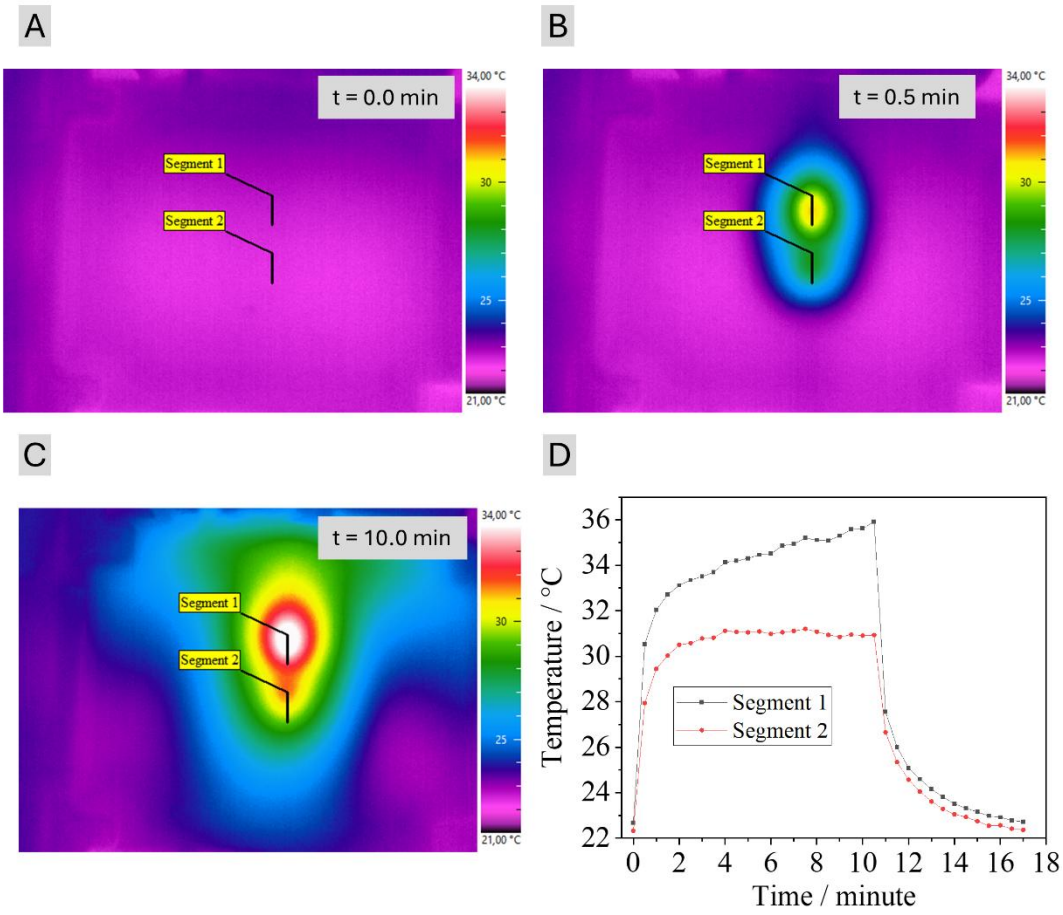

Figure 5- 14: Thermal analysis of waveguide with two nanocomposite segments each with length of 2 mm and a gap of 2 mm. The coupled light passes first through segment 1 and then travels further to segment 2. A)+B+C) Thermal image of waveguide during plasmonic heating at initial states of t = 0 min (A) and t = 0.5 min (B) and at steady state at t = 10 min (C). The black lines represent the estimated segments with a length of 2 mm. D) The maximum temperature profile of segment 1 and of segment 2 is plotted in function of time. At t = 10 min the laser is switched off.

The waveguide was modified to include two AuNR@CTAB segments, each 2 mm length, separated by a 2 mm gap infrared camera imaging revealed heating phenomena distinct from those observed in single-segmented waveguides, providing additional insights into waveguide properties and light interaction with AuNR@CTAB. Infrared images at t = 0 min and t = 0.5 min are shown in Figure 5- 14 A and B, respectively, with steady state images at t = 10 min in Figure 5- 14 C. The black lines in the images indicate the positions of the two segments, each 2 mm in length. The laser-coupled light enters the waveguide from above the image and first interacts with segment 1.

The maximum temperatures increase in segment 1 and segment 2 were 13.3 °C and 8.7 °C, respectively, at t = 10 min (Figure 5- 14 D). As the laser light travels through the waveguide, it interacts with the nanorods in segment 1, where some of the light is absorbed and converted into heat. The remaining light propagates through the gap, where no significant absorption occurs, and then reaches segment 2, resulting in additional heating due to the photothermal

conversion of nanorods. Heat dissipation from the segments into the gap also contributes to a temperature increase in this region.

The reduced temperature increase in segment 2, compared to segment 1, is attributed to the significant light absorption in segment 1, which diminishes the light intensity reaching segment 2. The temperature difference of the temperature increase between the segments after 10 minutes of irradiation is 4.6 °C. Unlike single-segmented waveguides with localized heating zones, the two-segmented waveguide creates two distinct heating zones, with the gap also being heated due to conductive heat transfer from the segments.

The optical density for the 2 mm path length in the segment is 0.4. According to Lambert-Beer's law:

$$E_\lambda = -\log_{10}\left(\frac{I}{I_0}\right) \tag{5- 1}$$

where E_λ is extinction, I_0 is the incident light intensity, and I is the transmitted light intensity. Since no optical scattering is assumed, E_λ is equivalent to OD. The fraction of remaining light intensity per 2 mm (I_{2mm}) after traveling through segment 1 is given by:

$$\frac{I_{2mm}}{I_0} = 10^{-0.4} \approx 0.4 \tag{5- 2}$$

Assuming, that the temperature increase in segment 2 is directly proportional to the light intensity reaching it (see equation (3- 24) and Figure 3- 4 C), and given that maximum temperature increase in segment 1 is $\Delta T_{\text{segment 1}}$ = 13.3 °C, the temperature increase in segment 2 $\Delta T_{\text{segment 2}}$ can be estimated as:

$$\Delta T_{\text{segment 2,calculated}} = \Delta T_{\text{segment 1}} \cdot \frac{I_{2\text{mm}}}{I_0} \tag{5- 3}$$

The calculation results in $\Delta T_{\text{segment 2,calculated}}$ = 5.3 °C. However, the experimental result is $\Delta T_{\text{segment 2}}$, experimental = 8.7°C and higher than expected from theoretical calculation. This discrepancy may arise from heat dissipation through the gap between the segments, contributing to additional temperature increase in segment 2.

5.3.3.3 Photothermal response of core-shell waveguides

The successful demonstration of plasmonic heating in nanocomposite waveguides provides a foundation for exploring more complex waveguide structures. By utilizing 3-D printing techniques, a secondary hydrogel layer was added to the gel fibers, resulting in core-shell geometries. These core-shell structures hold significant potential for therapeutic applications of

ELM waveguides. A related core-shell ELM structure was demonstrated by Dhakane et al., who used cylindrical geometries encapsulating bacteria in the core, with the shell providing a protective barrier to prevent bacterial leakage - a potential safety concern for host bodies in therapeutic applications.[4] Additionally, the shell layer serves as a cladding material, as described in section 3.4.6, enhancing the light-guiding efficiency.[2]

Core-only waveguides are insufficient for delivering light over organ-scale distances (>10 cm for humans) because the refractive index of tissues (1.33–1.51) is comparable to or higher than that of the core material, leading to light escape.[2] To address this, the shell layer in this work was designed with a lower polymer content than the 23% w/v PluDA core, ensuring a lower refractive index than the core's reported 1.36.[5] This refractive index gradient enables efficient light confinement and propagation. The core-shell waveguides presented in this study extend this concept by integrating AuNRs as NIR-responsive nano-heaters in the core. This dual-functional design provides a platform for combining plasmonic heating with bacterial encapsulation in the shell, paving the way for innovative ELMs with potential applications in advanced therapeutic systems.

In this work, the core consisted of a 2 mm long segment containing AuNR@CTAB while the shell layer was pure hydrogel. However, for future ELM applications, the shell layer could encapsulate engineered thermoresponsive bacteria. This design offers a dual layer functionality, where the core serves as an NIR-sensitive heating zone, and the shell acts as a containment layer for bacterial components, preventing direct contact with the host environment.

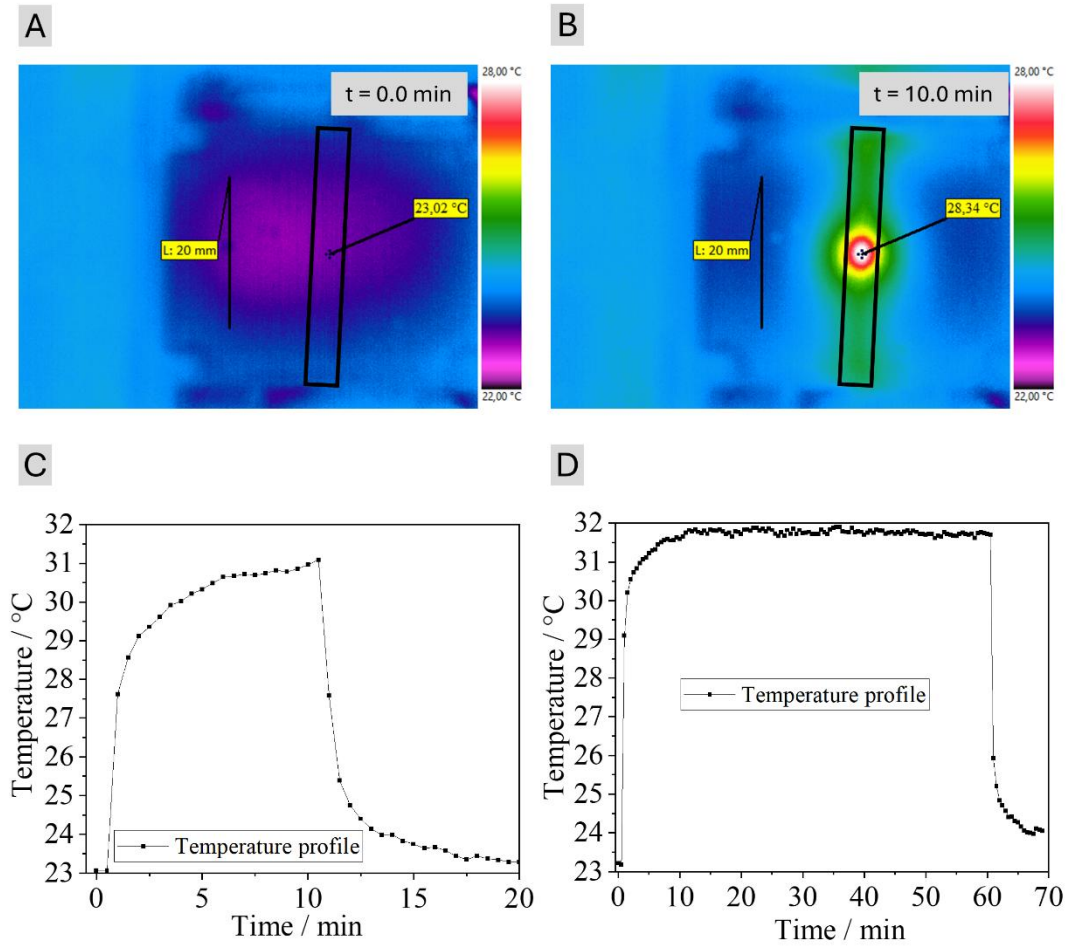

Figure 5- 15: Thermal analysis by infrared camera of core-shell waveguides. The core has one nanocomposite segment with the length of 2 mm. A)+B) Thermal image of core-shell waveguide at initial state of t = 0 min (A) and at steady state ate t = 10 min (B). The black rectangular represents the estimated waveguide position in the cuvette. The black line is the scale bar of 20 mm. The marked point is the maximum generated temperature during the plasmonic heating. C)+D) The maximum generated temperature profile for irradiation time of 10 min (A) and of 60 min (B) in function of time C) The laser is switched on at t = 0.5 min and switched off at t = 10 min with a following cooling period time of 10 min. Temperature profile reveals that steady state is reached after about 5 min and after laser turned off, the temperature decays in ambient temperature. D) The laser is switched on after t = 0.5 min and switched off at t = 60.5 min with a cooling period of 10 min.

The core-shell waveguide had a length of 50 mm and total diameter of 2.5 mm. The core diameter was 1.5 mm and the shell coating thickness was 0.5 mm. It was placed in a glass cuvette (50 mm × 50 mm × 50 mm) that was filled with water till its surface was covered to prevent it from drying out. The laser light (808 nm, 2 W/cm^2) was focused through an objective on one side of the waveguide. Light enters from above in the thermal images in Figure 5- 15 A and B. The temperature was monitored with an infrared camera at a defined point which represents the maximum temperature during steady state (Figure 5- 15 B). The recorded temperature is the surface temperature of the system, in this case water´s surface temperature.

The AuNRs within the core absorbed the light and plasmonically converted it into heat. The temperature distributions were measured with an infrared camera positioned above the waveguide. Initially, the waveguide maintained a temperature of 23 °C, in thermal equilibrium with the surrounding environment. Upon laser irradiation, a steady-state temperature with a

maximum temperature of 31 °C was reached after approximately 5 minutes of irradiation, corresponding to an 8°C increase. The laser was switched off after 10 minutes, with the temperature returning to ambient conditions after a cooling period of 10 minutes (in Figure 5- 15 C).

This temperature rise is below that of core waveguides with 2 mm segments (section 5.3.3.2), which showed higher maximum temperatures under identical conditions (in Figure 5- 15 C). Note that the infrared camera measures the surface temperature of the water, while the heat generated in the core must pass through both the 0.5 mm shell layer and the 0.5 mm water layer before reaching the surface, introducing an additional 0.5 mm radial heat path compared to the core-only waveguides. The Pluronic hydrogel in the shell has a lower thermal conductivity than water ($k_{\text{hydrogel}} < k_{\text{water}} \sim 0.6$ W/m·K)[6], resulting in slower heat dissipation and a reduced surface temperature. Furthermore, the hydrogel shell contributes to heat dissipation through the axial dimensions, further diminishing the temperature measured at the surface.

For potential therapeutic applications involving light- and thermoresponsive ELMs, longer irradiation durations are required to allow sufficient time for bacterial production of therapeutic molecules. For instance, the cylindrical ELMs described in Chapters 5.1 and 5.2 required heating durations of 30 min to 240 min for mCherry and PCQ production by *ClearColi* and *E. coli* Nissle 1917, respectively. To evaluate the stability of the core-shell waveguides under extended heating, a 60 min heating experiment was performed (in Figure 5- 15 D). Steady-state temperature was achieved after approximately 5 min, with minimal fluctuations observed over the remaining heating period. This stability demonstrates that the surrounding water effectively prevents the waveguide from drying out, confirming the potential of core-shell waveguides for photothermal applications in ELM systems.

5.3.4 Conclusion and outlook

This chapter shows that plasmonic heating of segmented waveguides is possible. Coupled laser light with initial power density of 2 W/cm^2 and wavelength of 808 nm travels through the core and core-shell waveguides and being absorbed by the AuNR@CTAB composite segments resulting in heat conversion observed by temperature increase via infrared camera. First, the core waveguide with a segment length of 2 mm and 5 mm was plasmonically heated. Along the axial direction, the temperature decreased by 2 °C in the 2 mm segment and by 4.5 °C in the 5 mm segment. Core waveguide with two segments each length of 2 mm with a gap of 2 mm revealed a maximum temperature difference between the two segments of about 6 °C during irradiation at steady state. The reduced temperature increase in segment 2 is attributed to the

lower light intensity reaching this region, as a portion of the incoming light is already absorbed in segment 1 due to the strong LSPR of rods. Core-shell waveguides were plasmonically heated for 60 mins with stable steady state temperatures. The empty shell layer gives the opportunity for engineered bacterial encapsulation, and thus for the application as ELM in therapeutics.

As future directions, the encapsulation of thermoresponsive bacteria in the shell layer opens the possibility for therapeutic ELMs shaped as fibers. The waveguide fiber would bring an additional feature; ultra deep photothermal activation of ELMs in host bodies. Even, 808 nm light is in biological transparency window, the penetration in deeper tissues higher than 3 mm beneath the skin tissue is restricted due to its attenuation in tissue components.[7] The waveguide fiber can be implanted in host bodies and transport the light in deeper tissues due to its optical properties giving the possibility to reach organs.

Bibliography

[1] M. Tebbe, C. Kuttner, M. Männel, A. Fery, M. Chanana, Colloidally Stable and Surfactant-Free Protein-Coated Gold Nanorods in Biological Media, ACS Applied Materials & Interfaces 7 (2015) 5984-5991.
[2] M. Choi, M. Humar, S. Kim, S.H. Yun, Step-Index Optical Fiber Made of Biocompatible Hydrogels, Adv Mater 27 (2015) 4081-4086.
[3] A.M. Alkilany, L.B. Thompson, S.P. Boulos, P.N. Sisco, C.J. Murphy, Gold nanorods: Their potential for photothermal therapeutics and drug delivery, tempered by the complexity of their biological interactions, Advanced Drug Delivery Reviews 64 (2012) 190-199.
[4] P. Dhakane, V.S. Tadimarri, S. Sankaran, Light-Regulated Pro-Angiogenic Engineered Living Materials, Advanced Functional Materials 33 (2023) 2212695.
[5] J. Feng, Y. Zheng, Q. Jiang, M.K. Włodarczyk-Biegun, S. Pearson, A. del Campo, Elastomeric Optical Waveguides by Extrusion Printing, Advanced Materials Technologies 7 (2022) 2101539.
[6] F. Xin, Q. Lyu, A Review on Thermal Properties of Hydrogels for Electronic Devices Applications, Gels 9 (2022).
[7] Y. Chu, X.-Q. Xu, Y. Wang, Ultradeep Photothermal Therapy Strategies, The Journal of Physical Chemistry Letters 13 (2022) 9564-9572.

6 Conclusion

This thesis demonstrates the potential of thermoplasmonic stimulation as a versatile and efficient tool for activating engineered living materials (ELMs) for therapeutic applications, including gene expression stimulation of *E. coli* strains. Utilizing gold nanorods (AuNRs) as plasmonic agents in hydrogel matrices, their ability to convert near-infrared (NIR) light into localized heat with high photothermal conversion efficiency (PCE) was showcased. Through systematic experimentation and optimization, ELMs capable of producing functional peptides and proteins under controlled photothermal stimulation were developed, thereby advancing the field of responsive biomaterials.

In Chapter 5.1, a bilayer ELM system was designed, integrating AuNRs in a Pluronic-based hydrogel layer and thermoresponsive bacteria in a separate layer. NIR irradiation of the AuNR layer induced precise thermal gradients, which diffused to the bacterial layer, activating protein production in a localized manner. This setup demonstrated the importance of spatial and temporal control over bacterial activation, achieving consistent protein expression across the bacterial population. The findings highlighted the adaptability of the system for therapeutic applications, such as controlled drug delivery and biosensing, while adhering to safe power density levels under the Maximum Permissible Exposure (MPE) limit for human tissues.

Building on this, Chapter 5.2 introduced a single-layer ELM system, where AuNRs and bacteria were embedded together in a PVA-VS hydrogel matrix. This configuration enabled more direct heating of the bacteria by placing them in the same layer as the AuNRs, significantly reducing the required power density for achieving bacterial activation within the desired temperature range (38–44°C) while maintaining biocompatibility. The engineered *E. coli* Nissle 1917 strain was employed to produce QK peptide-bearing PCQ proteins, a VEGF mimetic known to promote angiogenesis for wound healing. By replacing cytotoxic CTAB-stabilized AuNRs with biocompatible BSA-stabilized AuNRs and substituting the bacterial strain with the probiotic *E. coli* Nissle 1917, a safer and more effective system was developed. The PCQ production was quantified using a luminescence-based assay, revealing a total PCQ concentration of 6.9 ± 3.7 nM during 30 minutes of stimulation. Notably, the concentration of diffused proteins in the supernatant, which is therapeutically relevant, was 2.7 ± 1.6 nM, aligning with values reported for effective wound healing. This chapter demonstrated the feasibility of achieving therapeutic protein concentrations within significantly shorter treatment times compared to conventional methods, highlighting the potential of thermoplasmonic ELMs for biomedical applications.

Chapter 5.3 explored the integration of thermoplasmonic systems into hydrogel waveguides, advancing the functional design of ELMs for light-guiding applications. AuNRs were embedded in segmented core and core-shell hydrogel waveguides, enabling the targeted propagation of NIR light for localized heating. The results showcased efficient light confinement and thermoplasmonic activity, with the potential to stimulate bacterial activity in deeper tissue environments. The core-shell architecture can potentially improve light-guiding efficiency and thermal management, offering a robust platform for developing next-generation therapeutic ELMs. The innovative use of segmented waveguides and core-shell designs expanded the understanding of light-heat interactions in nanocomposite systems and provided a framework for future applications of thermoplasmonic materials in complex biological environments.

This work represents a significant contribution to the field of ELMs by pioneering the integration of AuNRs into bacterial hydrogels for therapeutic applications. It establishes a novel approach for employing thermoplasmonics to activate engineered bacteria, introducing a robust framework for the precise control of ELM activity. The study provides comprehensive insights into the design and optimization of AuNR-sensitized hydrogels for biological applications, addressing critical aspects such as colloidal stability, photothermal efficiency, and biocompatibility. By leveraging heat-responsive genetic circuits in combination with thermoplasmonic stimulation, this research achieved rapid and efficient production of angiogenic peptides, underscoring the potential of ELMs for localized wound healing. This approach offers a more efficient and scalable alternative to conventional methods, ranging from peptide production in single-layer hydrogels to advanced waveguide geometries that facilitate light-guided thermoplasmonic activation. Furthermore, this study demonstrates the feasibility of using thermoplasmonic systems for controlled gene expression in engineered bacteria, laying a foundation for broader applications in therapeutic and responsive biomaterials. It emphasizes the importance of balancing safety and efficiency in biomedical applications, providing critical insights and guidelines for designing future ELMs to meet clinical and practical demands.

Despite the significant advancements, this study acknowledges several limitations. Variability in bacterial growth and temperature distribution within the hydrogel resulted in high error margins in peptide quantification, which highlights the need for improved control over experimental parameters. Additionally, the study focused solely on the production of the therapeutic PCQ within a simplified model system. Future investigations should explore the performance of these systems in more complex tissue models, assess the use of alternative bacterial strains, and evaluate the production of diverse therapeutic molecules. The scalability

of the current setup for large-scale or *in vivo* applications remains an open question, particularly regarding long-term stability, biodegradability, and biocompatibility. To enhance the versatility of engineered living materials (ELMs), future studies could integrate multi-stimulus systems, such as magnetic or acoustic fields, alongside thermoplasmonic activation. Incorporating non-invasive imaging techniques, such as real-time monitoring of bacterial activity and protein production, could further expand the utility of these ELMs in clinical settings. Optimizing laser wavelengths and gold nanorod concentrations is another avenue for improving system efficiency, particularly for applications in deep tissue environments. Additionally, the use of temperature monitoring systems, such as lanthanide-based upconverting nanoparticles, could enable precise, non-invasive measurement of the internal temperature within the ELM, allowing better prediction of bacterial activity ranges. Such advancements would address the limitations of infrared cameras and thermocouples used in this study and significantly enhance the precision and applicability of thermoplasmonic ELMs for therapeutic purposes.

In conclusion, this thesis advances the understanding and application of thermoplasmonic stimulation in engineered living materials, bridging the gap between nanotechnology and synthetic biology. By combining material design, genetic engineering, and precise thermal control, the findings contribute significantly to the field of responsive biomaterials and hold promise for translational applications in biomedicine.